Space Mission Planning, Trajectory Design, and Orbit Analysis for the Exploration of Planets, Moons, and Small Bodies of the Solar System

vorgelegt von

Kai Wickhusen, Dipl.-Ing.

ORCID: 0000-0003-2524-5285

an der Fakultät VI – Planen Bauen Umwelt
der Technischen Universität Berlin
zur Erlangung des akademischen Grades

Doktor der Ingenieurwissenschaften
– Dr.-Ing. –

genehmigte Dissertation

Promotionsausschuss:

Vorsitzender: Prof. Dr. Jens Wickert
Gutachter: Prof. Dr. Jürgen Oberst
Gutachter: Prof. Dr. Harald Hiesinger
Gutachter: Dr. Johannes Benkhoff
Gutachter: Prof. Dr. Enrico Stoll

Tag der wissenschaftlichen Aussprache: 19. März 2025

Berlin 2025

Zusammenfassung

Diese Dissertation entwickelt und analysiert Szenarien für die Erforschung kleiner Körper, Monde und Planeten des Sonnensystems durch Raumfahrzeuge. Ein Schwerpunkt dieser Arbeit liegt auf der orbitalen Bewegung von Raumfahrzeugen um Asteroiden, einschließlich binärer und dreifacher Asteroidensysteme, sowie auf der Bewegung um Planeten und deren Satelliten. Ein weiterer wichtiger Schwerpunkt liegt auf dem vollständigen Missionsdesign und den Transfer-Szenarien von Raumfahrzeugen für die Erforschung des Mars und seiner Monde.

Im Falle der Bewegung von Raumfahrzeugen in der Nähe kleiner Asteroiden müssen störende Kräfte wie der Strahlungsdruck der Sonne, der die Wirkung von Gravitationskräften übersteigen kann, berücksichtigt werden. Es werden Ergebnisse für die Bewegung von Raumfahrzeugen in sogenannten "Terminator-Orbits" um binäre Asteroiden wie 1996 FG_3 präsentiert. Ein besonders komplexes Modell des dreifachen Asteroiden 2001 SN_{263}, bei dem ein Hauptkörper von zwei kleineren umkreist wird, wird ebenfalls untersucht. Hier wird die Bewegung aller drei Körper mit einem numerischen Integrator modelliert, der die Bewegungsgleichungen unter Berücksichtigung der verschiedenen Störkräfte löst. Es wird gezeigt, dass Raumsonden in "Selbststabilisierenden Terminator-Orbits" auch in diesem komplexen Asteroidensystem potenziell stabil sind.

Ein weiterer Schwerpunkt dieser Arbeit lag auf der orbitalen Bewegung von Satelliten, die sich nahe an ihrem Mutterplaneten bewegen und durch diesen gestört werden, wie im Fall der Marsmonde Phobos und Deimos. Hier wurden die dynamischen Eigenschaften und die Stabilität sogenannter "Quasi-Satelliten-Orbits" sowie potenzielle Nahvorbeiflüge an den Monden und Landungsansätze untersucht. In diesem Zusammenhang wurden auch resonante Orbits um den Saturnmond Enceladus untersucht, der durch seinen großen Mutterkörper Saturn erheblichen Störungen ausgesetzt ist.

In diesem Zusammenhang wurde auch eine weitere Studie zur orbitalen Entwicklung und Lebensdauer der Raumsonde BepiColombo durchgeführt, die die Komplexität des Gravitationsfeldes von Merkur höheren Grades und höherer Ordnung berücksichtigt.

Zusätzlich präsentiert diese Dissertation die Entwicklung und Untersuchung einer vollständigen Mission zum Mars und seinem Satellitensystem. Diese Arbeit wurde im Rahmen des Vorschlags an die ESA (European Space Agency) "Dephine" durchgeführt, der die Erforschung der Marsmonde mit Schwerpunkt auf Deimos zum Ziel hatte. In dieser Arbeit wurden Startmöglichkeiten, Transfers und Ankunftsszenarien am Mars untersucht. Das technische Missionskonzept wurde entwickelt, einschließlich möglicher Datenraten und Stromanforderungen des Raumfahrzeugs. Das Missionskonzept wurde von der ESA positiv bewertet.

Abschließend untersucht diese Arbeit mögliche Transferbahnen zum Mars, die 1,5 Umläufe um die Sonne umfassen und Vorbeiflüge an den Mars-Trojanern ermöglichen, die Ziele von hohem wissenschaftlichem Interesse darstellen. Die Mars-Trojaner teilen sich die gleiche große Halbachse wie der Mars auf seiner Umlaufbahn um die Sonne, befinden sich jedoch etwa $\pm 60°$ vor oder hinter dem Mars und bewegen sich in Bahnen mit relativ hohen Inklinationen. Es wurde ein Szenario untersucht, in dem die Raumsonde, wie die vorgeschlagene Missionssonde Dephine, auf ihrem Weg zum Mars einen Vorbeiflug an einem Trojaner durchführt. Das Szenario zielte darauf ab, zusätzliche Ressourcen im Vergleich zu einer reinen Mars-Mission zu minimieren. In günstigen Fällen war ein kleiner zusätzlicher Impulse von etwa 0,07 km/s ausreichend, um Trojaner-Vorbeiflüge in die Mission einzubeziehen.

Abstract

This dissertation develops and analyzes scenarios for spacecraft exploration of small bodies, moons, and planets of the Solar System. One focus of this work is on spacecraft orbital motion around asteroids, including binary and triple asteroid systems, as well as motion about planets and about their satellites. Another important focus is on the full mission design and spacecraft transfer scenarios for the exploration of Mars and its moons.

In the case of spacecraft motion near small asteroids, perturbing forces such as Solar Radiation Pressure, which may exceed the effect of gravitational forces, must be taken into account. Results are presented for spacecraft motion in so-called "Terminator Orbits" around binary asteroids, such as 1996 FG_3. A particularly complex model of the triple asteroid 2001 SN_{263}, involving a main body orbited by two smaller ones, is also investigated. Here, the motion of all three bodies is modeled using a numerical integrator that solves the equations of motion with the various disturbing forces. It is shown that spacecraft in "Self-Stabilizing Terminator Orbits" are potentially stable even within this complex asteroid system.

Another focus of this work has been the orbital motion of satellites moving close to and experiencing perturbations from their parent planet, such as in the case of the Martian moons Phobos and Deimos. Here, we studied the dynamic properties and stability of so-called "Quasi-Satellite Orbits," as well as potential close flybys of the moons and landing approaches. In this context, we also investigated resonant orbits around Saturn's moon Enceladus, which experiences significant disturbances from its large parent, Saturn.

In this context, another study of the orbital evolution and lifetime of the BepiColombo spacecraft was carried out, involving the complexity of the higher-degree and higher-order gravity field of Mercury.

Additionally this dissertation presents the development and investigation of a full mission to Mars and its satellite system. This work was carried out in the context of the proposal to ESA (European Space Agency), "Dephine," which aimed to explore the moons of Mars, with a focus on Deimos. This work explored launch opportunities, transfers, and arrival scenarios at Mars. The technical mission concept was developed, including possible data rates and electrical power requirements of the spacecraft. The mission concept was positively evaluated by ESA.

Finally, this work studied potential transfer orbits to Mars that included 1.5 revolutions around the Sun, allowing for flybys of the Mars Trojans, targets of high scientific interest. The Martian Trojans share the same semi-major axis as Mars in its orbit around the Sun but are located approximately $\pm 60°$ ahead of or behind Mars, moving in orbits with relatively high inclinations. A scenario was investigated in which the spacecraft, such as the proposed mission probe Dephine, performed a flyby of a Trojan on its way to Mars. The scenario aimed to minimize additional resources compared to a nominal Mars-only mission. In favorable cases, a small additional delta-v (Δv) of about 0.07 km/s was sufficient to add Trojan flybys to the mission.

Contents

List of Figures

List of Tables

Chapter 1

Introduction

1.1 Motivation

When I started working at the Deutsche Zentrum für Luft- und Raumfahrt (German Aerospace Center (DLR)) in September 2010, the Department of Planetary Geodesy was already planning to propose a medium-sized mission for the Cosmic Vision call M3[1] of the European Space Agency (ESA).

The proposal was named Gravity, Einstein's Theory, and Exploration of the Martian Moons' Environment (GETEMME) (Oberst et al., 2012). I had to familiarise myself with the proposal process within a few months and had to organize important parts of the proposal in the background. With only a few months until the submission deadline in January 2011, I had to understand quickly what the overall concept of a mission proposal was. We managed to finish the proposal in time and submitted it for evaluation.

In the years 2011 and 2012 the proposal lead and I improved the mission proposal of GETEMME. Additionally I became involved in another Cosmic Vision proposal called Marco-Polo-R (Barucci et al., 2012). The mission proposal consisted of a medium sized spacecraft which should investigate scientifically interesting asteroids or Near-Earth Object (NEO).

I was asked to search for stable orbit solutions for the primary target of the mission (175706) *1996* FG_3 (Wickhusen et al., 2011). During analysis of possible orbit strategies several stable solutions were found for the primary and also for the secondary targets (162173) *1999* JU_3 Ryugu and (101955) *1999* RQ_{36} Bennu (Wickhusen et al., 2012; Hussmann et al., 2012).

Unfortunately, neither our GETEMME nor the Marco-Polo-R concept were selected for further investigation. Nevertheless, the work on these proposals had a significant impact on my future work at the German Aerospace Center:

- The results for the stable orbits which I found during the analysis were so important that we decided to publish them in a dedicated paper (Hussmann et al., 2012).
- The selected mission for M3 was the PLATO mission, which was also proposed by the Institute of Planetary Research and I am now working on this project as well
- The proposal team was quite happy with the work I did and wanted me to become the Project Manager of the following M4, M5, and F mission proposals.

The call for M4 came out in 2014 (ESA, 2014), and we focused strongly on improving our previous proposal, which was not considered due to a "very low level of mission definition". As a result, we changed the overall mission concept of GETEMME and improved orbit and data handling analyses. We also focused more on feasibility and were able to write a very promising proposal.

ESA evaluated the concept as very good, but in the end, we were ruled out again, but this time not due to an incomplete proposal, but due to cost estimation. According to the evaluation, our proposal would have exceeded the overall cost limit by approximately 20% including margin.

[1] The European Space Agency (ESA) has established the Cosmic Vision 2015-2025 program, which is the current planning cycle for ESA's space science missions. Scientist from ESA member states can submit their mission proposals as (F)ast, (M)edium or (L)arge missions, depending on the actual call.

The proposal lead and I decided to rework the overall concept. I emphasized to the team the importance of including professional cost estimation and spacecraft design in the proposal to realistically advance to the next round and compete for the call. The team lead followed the advice, and we engaged in deep discussions with the European aerospace company OHB. In the end, we were invited to a Concurrent Design Facility (CDF) in order to prepare our proposal with more details and to have a higher chance of succeeding.

ESA was quite happy with our proposal and gave us a very good evaluation. This time, we passed the technical evaluation and also the cost estimation. Our scientific leaders were invited to present the results of the scientific outcome. In the end, ESA agreed but selected a different mission as more scientifically valuable than ours.

In any case, with now more than four mission proposals for M- and F-class missions for ESA's Cosmic Vision program, I gained a lot of knowledge and experience in preparing a proposal. In particular, the interactions between the science and engineering groups, along with their differing views on the problem, made the development phase challenging in several aspects. The search for new scientific objectives and the challenges in providing a realistic mission concept led to several new ideas which were published in scientific journals. Through this, I was able to contribute to several scientific publications either as a co-author or as first author, and the idea to write this cumulative PhD thesis arose.

1.2 Scope of this thesis

In this thesis, the main scientific results are summarized that I have published or contributed to publications over the past years. The content is mainly based on the experience gained during the mission concept development and the development of new science cases. Furthermore, background information on the methods is provided and how they were applied to the mission concepts.

In addition to general methods for the development of mission concepts, this thesis focuses strongly on the orbital dynamics, trajectories, and maneuvers required to allow such missions. In all these concepts, I was often asked to provide background information about possible orbit scenarios including their stability and Δv demands.

In section 1.3, my scientific contributions and the corresponding publications from recent years are summarized and a brief overview is given.

1.3 Scientific publications

In total, I contributed to 10 scientific publications that are directly relevant to this Ph.D. thesis. Three of these peer reviewed articles are include in this cumulative thesis and the remaining seven are cited in the corresponding sections. For completeness, the 10 papers are summarized here, and a brief overview about the content and my contribution to it are given. The authors are given in the same order as they appeared on the publications.

1.3.1 Peer Reviewed Articles included in this Thesis

In this section the 3 papers which are included in this thesis are summarized.

Terminator Orbits around the Triple Asteroid 2001-SN263 in Application to the Deep Space Mission ASTER

This research article is included in this thesis in chapter 5
(Wickhusen et al., 2022a)
Authors: **Kai Wickhusen**, Antonio G.V. de Brum, Friedrich Damme, Alexander Stark, Jean-Baptiste Vincent, Hauke Hussmann, Jürgen Oberst
Journal: Acta Astronautica
Year: Published 2023

I was the corresponding author of the article and was responsible for performing the numerical calculations and developing the software and methods. I wrote the main parts of the text, especially the methods, results and discussion sections, but also large parts of the introduction. I generated most plots and found the results for stable regions. I also organized the structure of the paper and the contribution by the co-authors.

Trajectory Analysis for Combined Missions to Mars and its Trojan Asteroids

This research article is included in this thesis in chapter 6.
(Wickhusen et al., 2023)
Authors: **Kai Wickhusen**, Jürgen Oberst, Apostolos Christou, Friedrich Damme
Journal: Planetary and Space Science
Year: Published 2023

I was the corresponding author of the paper and responsible for performing the calculations, developing the software, and writing the main text. I generated the plots, evaluated the results, and discussed them.

DePhine – The Deimos and Phobos Interior Explorer

This research article is included in this thesis in chapter 7.
(Oberst et al., 2018a)
Authors: Jürgen Oberst, **Kai Wickhusen**, Konrad Willner, Klaus Gwinner, Sofya Spiridonova, Ralph Kahle, Andrew Coates, Alain Herique, Dirk Plettemeier, Marina Dıaz-Michelena, Alexander Zakharov, Yoshifumi Futaana, Martin Paetzold, Pascal Rosenblatt, David J. Lawrence, Valery Lainey, Alison Gibbings, Ingo Gerth
Journal: Advances in Space Research
Year: Published 2018

I was the project manager of the Dephine proposal and responsible for the technical aspects of the mission. My contribution to the scientific publication included the orbit and trajectory analysis (section 7.3). Additionally I organized the requirements and constraints of the payloads and was responsible for technical decisions regarding spacecraft design. I set up the mission timeline and calculated the available power and data rates. Additionally, I ran the numerical calculations of the Quasi-Satellite orbits about Deimos, simulated the close flybys and set up the 2:1 resonance scenario. Furthermore, I was responsible for calculating the maneuvers and the resulting delta-v demand, which was used as a primary input for the spacecraft design.

1.3.2 Co-Authored Peer Reviewed Articles with direct Relevance for this Thesis

My contributions to scientific publications that are directly related to this thesis are summarized in this section.

Periodic orbits for interferometric and tomographic radar imaging of Saturn's moon Enceladus

(Benedikter et al., 2022)
Authors: Andreas Benedikter, **Kai Wickhusen**, Hauke Hussmann, Alexander Stark, Friedrich Damme, Marc Rodriguez-Cassola, Gerhard Krieger
Journal: Acta Astronautica
Year: Published 2022

The paper focuses on possible radar applications in the context of Enceladus Explorer (EnEx) initiative. A significant part of the paper shows the result of searches for possible interferometric and tomographic acquisitions, which require spacecraft orbits with almost perfectly repeating ground tracks and sufficient inclination for providing access to the most interesting south polar region with its plumes. Unfortunately, the low Enceladus mass and its proximity to Saturn often lead to extreme instabilities for orbit inclinations beyond 60°. However, the paper shows that stable repeat orbits close to this inclination barrier exist.

I supported this research and ran the first simulation to search for stable orbit about Enceladus. Afterwards, I provided tools and methods to support the search for repeat orbits. These tools and methods are also described in this thesis. Details about the work are given in Sections 2.2.4 and 4.4.3.

Planetary polar explorer - the case for a next-generation remote sensing mission to low Mars orbit

(Oberst et al., 2022)
Authors: Oberst, Jürgen ; **Wickhusen, Kai** ; Gwinner, Klaus ; Hauber, Ernst ; Stark, Alexander ; Elgner, Stephan ; Grott, Matthias ; Fanara, Lida ; Hussmann, Hauke ; Steinbrügge, Gregor ; Lewis, Stephen ; Balme, Matthew ; Maugeri, Maurizio ; Diolaiuti, Guglielmina ; Karlsson, Nanna ; Johnsson, Andreas ; Ivanov, Anton ; Hiesinger, Harald
Journal: Experimental Astronomy
Year: Published 2022

The paper proposes the exploration of polar areas on Mars with a next-generation orbiter mission. The orbiter is intended to fly in a very low Mars orbit within the atmosphere for further investigation. The atmospheric drag will be continuously compensated for by an electric propulsion system.

I was the project manager for this concept. I developed the mission scenario and analyzed the trajectory and orbit. I calculated the drag, simulated the orbit, and specified the propulsion system and spacecraft design. Details about the Martian atmosphere are given in Section 2.2.1, and concept details are provided in Section 4.4.4.

Quasi-Satellite Orbits around Deimos and Phobos motivated by the DePhine Mission Proposal.

(Spiridonova et al., 2017)
Authors: Spiridonova, Sofya; **Wickhusen, Kai**; Kahle, Ralph; Oberst, Jürgen
Booktitle: Proceedings of the 26th International Symposium on Space Flight Dynamics
Year: Published 2017

This paper analyzes the spacecraft motion in quasi-satellite orbits first around Deimos and then around Phobos for the DePhine proposal.It presents the results of a numerical analysis of several quasi-satellite orbits solutions around the Martian moons.

For this paper I ran several simulations for Quasi Satellite Orbit (QSO)'s about Phobos and Deimos. Details can be found in section 4.4.1.

Size matters - The shell lander concept for exploring medium-size airless bodies

(Grimm et al., 2020)
Authors: Grimm, Christian D.; Witte, Lars; Schröder, Silvio; **Kai Wickhusen**
Journal: Acta Astronautica
Year: Published 2020

The paper analyzes possible design scenarios for small landers and how to land them on very small bodies with diameters between 10-50 km. For the paper Phobos was considered as the reference target. The paper classifies carry-on landers with respect to their touchdown and operational strategy and evaluates the constraints of ballistic deployments.

In cooperation with DLR Bremen, I was responsible for analyzing possible orbit and fly-by scenarios about the reference target Phobos as well as defining a spacecraft separation and landing scenario. Details of the work and methods used can be found in Section 4.4.2.

Encounter trajectories for deep space mission ASTER to the triple near Earth asteroid 2001-SN263. The laser altimeter (ALR) point of view

(Brum et al., 2021)
Authors: de Brum, A.G.V., Hussmann, H., **Wickhusen, K.**, Stark, A.
Journal: Advances in Space Research
Year: Published 2021

The Brazilian Space Agency planned to send a small spacecraft to investigate the triple asteroid 2001-SN263. The paper focuses on identifying suitable trajectories for the ASTER spacecraft in the encounter phase, when the main campaign will take place. This paper describes the effort undertaken with focus on the operations of the laser altimeter. Possible encounter trajectories were modeled and simulated to identify suitable approach parameters and conditions to accomplish the intended investigation.

In cooperation with the Federal University of ABC (UFABC, Brazil), I supported the search for possible encounter trajectories and mission scenarios. I analyzed the trajectories in terms of feasibility and available power. Additionally, I provided information about laser altimeters and helped analyzing its feasibility for this scenario. The paper is based on the ASTER mission and related to my publication Wickhusen et al. (2022a). Details are given in section 5.

Orbital evolution of the BepiColombo Mercury Planetary Orbiter (MPO) in the gravity field of Mercury

(Höschele et al., 2021)
Authors: Marina Höschele, Alexander Stark, **Kai Wickhusen**, Hauke Hussmann, Jürgen Oberst
Journal: Planetary and Space Science
Year: Published 2021

In the article, we analyze the impact of the uncertainties in the gravity field harmonic coefficients of Mercury on the orbital evolution of the Mercury Planetary Orbiter (MPO), part of the European-Japanese BepiColombo mission. In the paper the most recent estimation of the gravity field model of Mercury was used, which was determined from radio tracking data of the NASA spacecraft MESSENGER. Thereby we propagated the orbital evolution of MPO by means of plausible gravity fields compatible with the covariance matrix measured gravity field coefficients.

During my work as BepiColombo Laser Altimeter (BELA) operations manager, we frequently analyzed the MPO orbit and sought a detailed analysis of its evolution, which remains uncertain due to the uncertainties in the gravity field of Mercury.

For the paper, I ran numerical integrations, provided background information about the mission and the reference orbit. I defined the main objectives, and verified the results. More details about Mercury, BepiColombo and the results of the paper can be found in section 2.2.3.

Stability and evolution of orbits around the binary asteroid 175706 (1996 FG3): Implications for the MarcoPolo-R mission

(Hussmann et al., 2012)
Authors: Hauke Hussmann, Jürgen Oberst, **Kai Wickhusen**, Xian Shi, Friedrich Damme, Fabian Lüdicke, Valery Lupovka, Sven Bauer
Journal: Planetary and Space Science
Year: Published 2012

In the paper we analyzed possible operational scenarios for MarcoPolo-R mission targets. The paper presents stable orbit solutions known as terminator orbits.

For the article, I conducted numerical integrations, analyzed the trajectories, and found several stable orbit solutions. I generated most of the images, presented the results, and provided large parts of the text.

The paper is cited several times in this thesis as it served as an important starting point for my scientific investigations. Several details about the work are given in Sections 2.2.2 and 4.4.5

Chapter 2

Exploration of the Solar System

"E pur si muove" are famous words attributed the Italian mathematician and astronomer Galileo Galilei in 1633. These words can be translated to "And yet it moves" and refer to the Earth moving about the Sun. According to legend, Galileo said this after he was forced to withdraw his statement that the Earth actually moves around the Sun and is not the motionless center of the universe.

Indeed, the theory of a heliocentric (Sun-centered) universe was already formulated by Aristarchus of Samos in the 3rd century BC. However, his observations were not consistent with the ideas formulated by Aristotle and later Ptolemy, who considered the earth to be the central body (Pincock and Frary, 2008).

It took more than 1000 years until the heliocentric model was reconsidered as main explanation for the movement of the planets. In 1543, already 90 years before the famous words of Galilei , Nicolaus Copernicus published his book "De revolutionibus orbium coelestium" (english translation: On the Revolutions of the Heavenly Spheres)" which changed the way mankind looks at the universe (Schmeidler, 1998; Faure and Mensing, 2007).

The book of Copernicus can be considered as the starting point of an astronomical revolution, and since then several famous astronomers, physicists, and mathematicians have contributed to our understanding of the universe. Among them are scientists such as Johannes Kepler, whose name is still used for Kepler orbital elements (osculating elements), Isaac Newton, or Carl Friedrich Gauß (Faure and Mensing, 2007).

Today we know that our sun is by far the most massive body in our solar system, but it is just one star in billions of stars in the Milky Way and that our Milky Way is just one galaxy of billions of galaxies in the universe. Besides the growing information about our universe, we were also able to gain more and more detailed information about our Solar System. This was on hand due to the fact that telescopes around the world have become more and more powerful and that computers are able to store and calculate an unbelievable number of data. On the other hand, humans have also pushed the frontiers and made their first steps into space. In 1957, Earth's first artificial satellite, 'Sputnik,' was launched into space. Twelve years later, a dream of humanity came true with the Apollo 11 mission, marking the first human landing on the Moon, where Neil Armstrong took his historic steps (Rödel, 2014; Johnson, 2017).

Since Sputnik, the very first space probe, several follow-up missions were launched into space. A large number of satellites is orbiting earth today for all kinds of different purposes, among them satellites for communication, weather observations, GPS, military purposes or the International Space Station (ISS). In addition to these earth satellites, all planets of the solar system as well as several moons, asteroids, and comets have been visited and explored by human space probes. All this is possible due to modern space flight (Fortescue et al., 2005).

In the following section 2.1 I will give a brief introduction to spaceflight and the Tsiolkowsky equation and in section 2.2 Solar System Bodies are presented are relevant for this thesis.

2.1 Spaceflight

In 1903, spaceflight was still just a dream. That year Orville and Wilbur Wright made their first powered flight. It took more than 50 years before the first artificial satellite was launched into space. However, in the same year, a young Russian teacher published his ideas about what he called *"Reactive Flying Machines"*. In this publication, the basic concepts of spaceflight are described, and although he was not the first to publish on the topic, his equation is now known as the Tsiolkovsky formula or Tsiolkovsky rocket equation (Blagonravov, 1954; Fasoulas and Messerschmid, 2009):

$$v_{max} = v_e \ln \frac{m_w}{m_d}, \tag{2.1}$$

with v_{max} being the maximum achievable velocity of a spacecraft. This maximum achievable velocity depends primarily on the effective exhaust velocity v_e of the spacecraft. The total mass of the spacecraft (wet mass) m_w includes the propellant, while the total mass of the spacecraft without propellant is called dry mass m_d. With this fundamental formula, it was now possible to calculate the required propellant mass for traveling in space. For this purpose, the equation 2.1 can be reformulated so that the ratio between wet and dry mass is given by:

$$\frac{m_w}{m_d} = \mathrm{e}^{\frac{v_{max}}{v_e}}. \tag{2.2}$$

Equation 2.2 shows that the propellant requirement grows exponentially with the demand for maximum achievable velocity. Given the limited mass available for spacecrafts, the equation shows clearly that required v_{max} or more specifically Δv (see Section 4.1.1) should be minimized as much as possible.

An example of this exponential relationship is shown in Figure 2.1, using the technical parameters of the mission proposal DePhine as input (details in Chapter 7). The figure shows the exponential growth of the mass of the Spacecraft with increasing demand for Δv. This figure considers the constraints of the DePhine mission (Oberst et al., 2016). The DePhine spacecraft dry mass is $548kg$ and the exhaust velocity $v_e = 2780 m/s$ is a specific property of the selected standard MON/MMH[2] bi-propellant system. With these two input parameters, the resulting propellant mass to dry mass ratio can be calculated for any Δv demand.

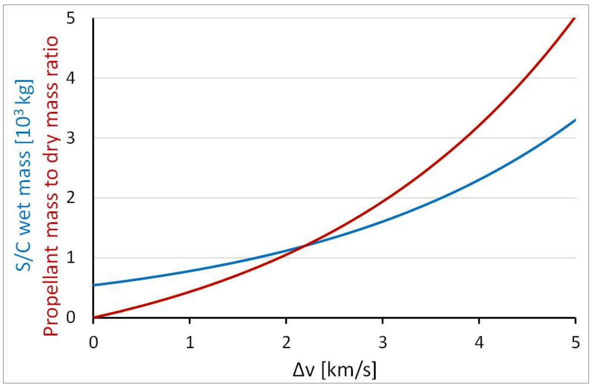

Figure 2.1: Exponential growth of spacecraft mass with Δv demand. The figure is based on the Deimos and Phobos Interior Explorer (DePhine) spacecraft, which has a dry mass of 548 kg and an exhaust velocity of 2.78 km/s (see chapter 7). The red curve depicts the ratio of propellant mass to dry mass as Δv increases, while the blue curve illustrates the total spacecraft mass growth. *Credit: Own work*

It is important to note that a Δv of $5 km/s$ already increases the overall spacecraft mass from $550kg$ to more than $3300kg$. The propellant mass in this case will be more than $2800kg$ leading to a wet to dry mass ratio of more than 5. Furthermore, the calculation doesn't take into account that such a high amount of propellant will most likely even increase the spacecraft dry mass as larger tanks and a bigger spacecraft structure will be required.

One could think that Δv demands of $5 km/s$ are not realistic, but this is not the case. For comparison, the final demand for the DePhine mission only for Mars orbit insertion and maneuvers to Phobos and Deimos was calculated to be more than $2 km/s$ (Oberst et al., 2018a). Other examples are a Hohmann-transfer (see section 4.1.2) from a 300 km Low Earth Orbit (LEO) to a Geostationary Orbit

[2]The propulsion subsystem uses a common approach with a mixed oxides of nitrogen (MON)/Monomethylhydrazine (MMH) bipropellant chemical system. For details, see Chapter 7

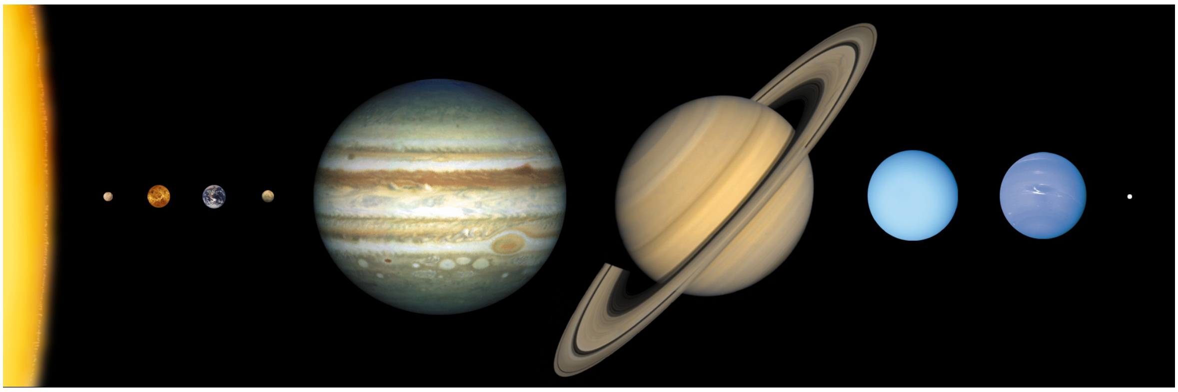

Figure 2.2: Image of the Solar System planets including the rim of the sun and the dwarf planet Pluto. Body diameters to scale. Bodies on Image: Sun, Mercury, Venus, Earth, Mars, Jupiter, Saturn, Uranus, Neptune, Pluto (from left to right) *Credit: NASA*

(GEO) which requires almost a Δv $\approx 4^{km}/_{s}$ and a Hohmann-transfer from a 300 km LEO to Jupiter transfer orbit requires more than $6.3^{km}/_{s}$ not taking into account the Δv demand for Jupiter orbit insertion (Fortescue et al., 2005).

It follows that impulsive maneuvers in space are very costly in terms of mass and financial budget. Therefore, maneuvers should be minimized as much as possible.

Another primary motivation for avoiding maneuvers in space is the scientific aspect. Once a propulsion system fires its engines, the orbit is no longer perturbed by only natural forces of space, such as gravity, atmospheres, or radiation pressures. However, determining the orbit of a spacecraft without perturbation by the propulsion system is often of great scientific interest. This approach enables the determination of key physical parameters—for example, gravity-field characteristics and atmospheric properties.

Consequently, one of the main motivations of this thesis is the reduction of impulsive maneuvers in space, either to reduce Δv demands or to allow better scientific investigation.

2.2 Bodies of the Solar System

The Solar System consists of celestial bodies in orbit about the central star: our Sun. With the Sun being the main attractor, eight major planets, dozens of dwarf planets and thousands of asteroids, comets, and other smaller objects orbit about this central star. The solar system is a huge and mainly empty place. The eight major planets are millions of kilometers apart from each other. The eight planets of the Solar System can be split into two groups: the terrestrial or rocky planets Mercury, Venus, Earth and Mars and the gas giants Jupiter, Saturn, Uranus and Neptune. A scaled image for size comparison of the planets can be found in Figure 2.2. It should be noted that several planets have moons and a large number of them have diameters of several hundred kilometers (Faure and Mensing, 2007).

In order to obtain a better relationship of the distances between the planets, the Astronomical Unit [AU] is defined as $1\,AU = 149\,597\,870\,km$ (nearly 150 Mio. km) and corresponds to the average distance between the geometric centers of Earth and the Sun (Faure and Mensing, 2007; Murray and Dermott, 1999). For larger distances, such as star-to-star measurements, lightyears are the typical distance unit, but since this thesis focuses on bodies within the Solar System, only [AU], [km], and [m] are used.

Today, in the year 2024, all planets of the Solar System have been visited by human space probes. Bodies that are relatively easy to reach have been visited more often than bodies that are more difficult to reach. A brief summary of solar system exploration missions is shown in Figure 2.3. Note that distance is not the primary constraint for readability. In fact, the orbital energy required for a transfer could be considered to be a key role. For instance, Mercury is comparably close to Earth, but much harder to reach than Mars (see Section 4.1.2).

In Figure 2.3 again the importance of Δv demand is shown. In the figure, all space missions to solar system bodies since the beginning of human space exploration are shown. Additionally, the Δv demand to reach each body is shown in reverse order. It can clearly be seen that the number of missions decreases with increasing Δv demand, while the number of mission increases with decreasing Δv demand. However, it is clear that the Δv demand is a very strong constraint for the selection of a target, but it is not the only one. Earth's moon has always been the number one target since the humans started to look at the sky and dreamed of visiting the stars one day. The moon, being the most prominent body in the sky at night, is obviously a primary target. Because of their extensive moon systems and complex atmospheres, Jupiter and Saturn are often regarded as higher-priority targets than Mercury. It must be taken into account that mission selection considers not only scientific value but also public outreach.

However, the strong inverse correlation between Δv and the number of missions, as well as Δv demand cannot be neglected. To prove this, the data points of figure 2.3 were used to calculate the Pearson correlation value r (Freedman et al., 2007). The result shows a clear value of $r = -0.85$ which proves a strong inverse correlation of the two. Due to the arguments presented in this thesis, I consider there to be a strong causality between the required Δv and the number of visitations, as additional Δv increase the mass, time and consequently the costs of a space mission significantly. It follows that missions to planets that are difficult to reach have only been visited a few times so far, although they might be of higher scientific interest.

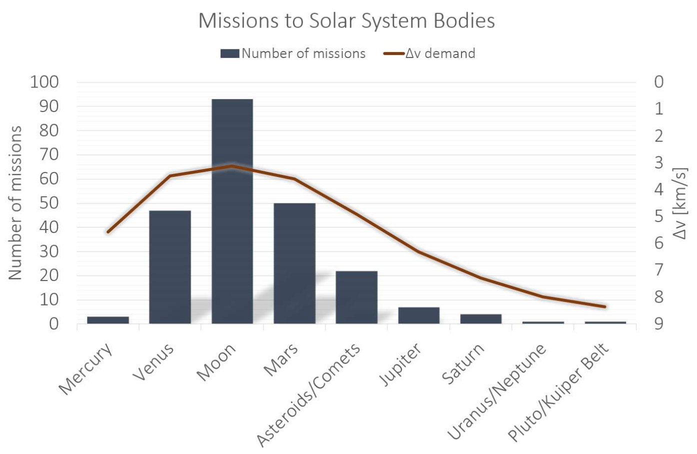

Figure 2.3: Number of Worldwide Space Missions to Solar System Bodies and reverse Δv demand. For the Δv calculation of asteroids and comets, Ceres was used as reference semi-major axis. The Δv requirements are for earth departures assuming a 300 km altitude circular Earth orbit (Fortescue et al., 2005); *Image is own work, with number of mission is taken from Osterhage (2021)*

In our mission proposals, we were most of the time strictly constraint by the mass and costs of a mission. The proposals for Medium (M)- and Fast (F)-Class missions, as well as the mission concept of the ASTER mission concept, did not allow for large masses or high Δv demands. Consequently we focused on the open science questions about reachable targets such as Mars, the Martian Moons, Martian Trojans, and asteroids. All of these targets could fit in a small or medium sized mission and were considered for the proposals. Additionally, our department and institute had strong scientific interest and expertise, and the selected targets received strong support. As I am also involved in the ongoing ESA missions to Mercury (BepiColombo), to the Moons of Jupiter (Jupiter Icy Moons Explorer (JUICE)) and the studies for a mission to Enceladus (EnEx), I supported publications that focused on these bodies, as shown in section 1.3.2.

In the following section I will give a brief overview about the bodies which are relevant for this PhD Thesis, as they were the selected targets of the proposed missions. Among them are the planets Mars and Mercury, several asteroids, and the Saturnian moon Enceladus.

2.2.1 Mars

As shown in Figure 2.3 Mars has hosted the most human-made spacecraft in its orbit, second only to Earth. In 1971 the first mission to Mars started. This mission was Mariner 9 and became the first spacecraft to orbit another planet (Duxbury and Callahan, 1989). Since then about 50 missions to Mars have been launched and more are about to come. Although not all of them succeeded, several of the missions were of great success and were able to shed light on highly scientific questions, such as the geological and atmospheric evolution of Mars. The reason why so many missions to Mars had been launched can be explained by mainly two reasons:

1. Mars, like Venus, is located close to the edge of the so-called habitable zone of the solar system (Urban, 2017). Thus, the chances to find water or even life on the planet were considered to be

higher than on other planets

2. Mars is one of the easier targets to reach in the solar system from Earth, after the Moon. Here again, the above mentioned Tsiolkovsky equation is of fundamental importance. In other words, the less propellant is needed to bring the spacecraft to its target, the more scientific instruments can be placed on the spacecraft instead. As a transfer orbit to Mars and the Mars orbit insertion have a comparably low demand for Δv, more instruments can be used to investigate the global question about the evolution of the solar system and the universe.

Mars is a terrestrial planet with a mass of 6.4185×10^{23} kg which corresponds to approximately 11 % of the Earth's mass. In contrast, its surface acceleration is approximately 1/3 of Earth. This difference in mass and surface acceleration is caused by the smaller radius of the Planet (see Table 2.1). Mars orbits the Sun at a distance of 1.5237 AU. Due to the small eccentricity, this distance varies between 1.381 and 1.666 AU over one Martian year, or 687 days (Barlow, 2009). The a brief summary of the orbital and physical properties of Mars is given in Table 2.1.

In the context of our studies I was mainly focused on the Martian Moons, the Martian Trojans, and the atmosphere of Mars, which are briefly described in the following subsections.

Table 2.1: Orbital and Physical Properties of Mars (Barlow, 2009)

Semi-major axis	1.5237 AU
Eccentricity	0.0933941
Sidereal orbit period	686.98 days
Solar day	24 h 39 min 35 sec
Mean equatorial radius	3,396.2 km
Mass	6.4185×10^{23} kg
Surface gravity	$3.69\times$ m/s^2

Martian Atmosphere

Mars has a very thin atmosphere compared to Earth, consisting mainly of carbon dioxide with small amounts of Nitrogen, Argon and trace amounts of oxygen (see Table 2.2).

The average atmospheric pressure on the surface of Mars ranges from 4 to 8 mbar, which is less than 1% of the pressure of Earth's atmosphere at mean sea level (Barlow, 2009).

Although the Martian atmosphere is very thin, the pressure at elevations between 80 and 150 km is comparable to the atmospheric pressure of the Earth at the same altitudes as shown in Figure 2.4. Even at altitudes between 150 and 300 km, the density of the Martian atmosphere still has an effect on the orbit of spacecraft that come this close.

The fact that this thin atmosphere causes a drag and consequently a decelerating force is explained in section 4.3.4 and 4.4.4. This drag is also used for the so-called aerobraking maneuvers which has already been used to save propellant on Mars missions. An example of this aerobraking technique is the 2001 Mars Odyssey mission (Saunders et al., 2004).

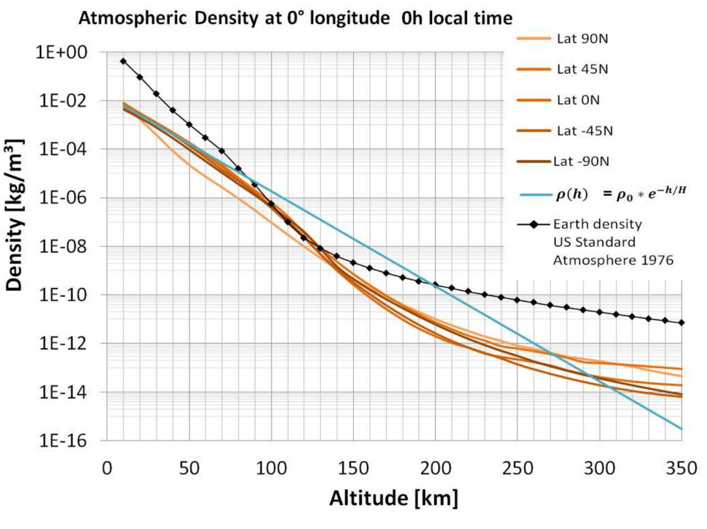

Figure 2.4: Atmospheric Density of Mars Over Altitudes at 0○ longitude 0h local time. The density profile is shown at different latitudes. *Image is own work as presented in Wickhusen et al. (2018) with data from Mars Climate Database ©LMD/OU/IAA/ESA/CNES Millour et al. (2018)*

Several missions to Mars have already been conducted, during which the Martian atmosphere was studied and analyzed in detail. Prominent examples include the Mars Global Surveyor (Albee et al., 2001) and the Mars Atmosphere and Volatile Evolution (MAVEN) missions (Jakosky et al., 2015). Nevertheless, open questions remain about the dynamics and evolution of the atmosphere, the seasons, and the polar caps. Based on these open questions, the proposal lead and I decided to propose a Mission to fly in a low Martian orbit. Details about the mission are given in section 4.4.4.

Table 2.2: Composition of the Martian Atmosphere (Franz et al., 2015)

Carbon Dioxide (CO_2)	94.9%
Nitrogen (N_2	2.6%
Argon (Ar)	1.9%
Oxygen (O_2)	0.2%
others	0.3%

Phobos and Deimos

Mars has two natural satellites or moons, called Phobos and Deimos. The two moons are relatively small in size, with diameters of only 26.8 km for Phobos and 15.0 km for Deimos, respectively. This small size and the irregular shape of the bodies is illustrated in Figure 2.5.

Both moons orbit Mars at a comparably short distance in nearly circular orbit and are in synchronous rotation (see Table 2.3). It is interesting to note that both satellites are evolving away from each other, with tidal strain energy causing a reduction of Phobos' semi-major axis and an increase of Deimos' semi-major axis (Spohn et al., 1998; Burns, 1992).

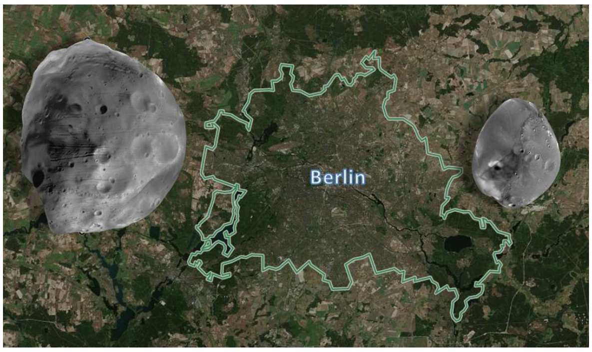

Figure 2.5: Scaled Illustration of Phobos and Deimos Relative to the Area of Berlin. *Credit: Own work, 3D Models of Phobos and Deimos provided by Konrad Willner (Willner et al., 2014), Berlin map taken from Google maps 2024 (Bilder © 2024 TerraMetrics,Kartendaten © 2024 GeoBasis-DE/BKG (©2009),Google)*

There is still an ongoing discussion about the origin of the two moons. Burns (1978) considered the two moons to be captured asteroids, due to their very low albedo, which is similar to C-class asteroids (see section 2.2.2). However, scientists nowadays also consider other options for their formation. Another prominent theory suggests that Phobos and Deimos may have formed from a debris disk that was formed by a giant impact (Rosenblatt et al., 2016). Most recently, Fornasier, S. et al. (2024) analyzed the reflectivtiy of the moons' surfaces and concluded that Phobos and Deimos could even be a captured binary comet. This illustrates that there are still several unanswered questions, and the moons remain of high interest to the scientific community.

Although Mars has been visited by human space probes more than any other Planet, its small moons have not been investigated in detail so far. The data we have from the moons come from various missions which primarily targeted Mars, such as Mars Express.

It should be noted that the Soviet Union Space Program and the successor, ROSKOSMOS, launched space probes to Phobos and even attempted to land on the moon. Unfortunately, all three missions, namely Phobos 1, Phobos 2, and Phobos-Grunt, failed, and only Phobos 2 was able to send very limited data. In summary, until today, there has been no successful mission to Phobos or Deimos and several questions about the moons remain unanswered (Duxbury et al., 2014).

Our mission proposals Getemme, PhoDEx and DePhine were focusing exclusively on the two moons and would have investigated several unanswered question such as:

- What is the origin of Phobos and Deimos and how did the two satellites evolve?
- What is the interior structure of Deimos and Phobos?

Table 2.3: Orbital and Physical Properties of Phobos and Deimos (Williams, 2023)

Property	**Phobos**	**Deimos**
Semi-major axis	9378 km	23459 km
Eccentricity	0.0151	0.0005
Orbital period	0.319 days	1.26 days
Inclination	1.08°	1.79°
Mass	10.6×10^{15} kg	2.4×10^{15} kg
Radius	11.2 km	6.3 km

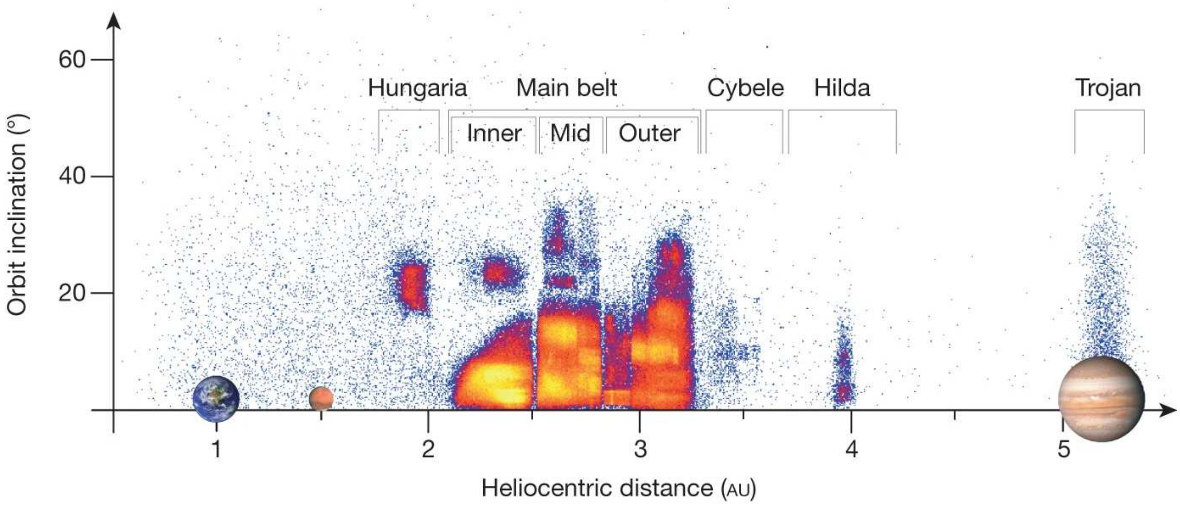

Figure 2.6: Location of asteroids and the Main Belt with respect to the Planets and the Sun, as well as the Orbital Structure of asteroid Inclinations and Number Density of Objects (Yellow represents the highest Number Density, blue the lowest). *Credit: (DeMeo and Carry, 2014)*

Although our proposals were not selected, the science questions formulated in the proposals are still of high interest. This can be proven by the upcoming Martian Moons eXploration (MMX) mission, which is going to be launched in 2026. This mission is a sample return mission, with Phobos as the primary target. It addresses several of the science questions that were also the main science questions in our proposal. A comparison with our mission proposal and Details about the MMX mission are discussed in section 8.1.

2.2.2 Asteroids

At the end of the 18th century, astronomers in Europe started the search for a new planet. Based on the Titus-Bode Law[3], they were mainly looking for this planet between the orbits of Mars and Jupiter and they were actually right. In 1801, Giuseppe Piazzi was the first astronomer to discover a new object (Schmadel, 2012) and he named this new planet Ceres. At that time, he did not know that this new object would become the first asteroid ever discovered (Serio et al., 2002; Cunningham, 2021).

In the following years, more objects were found in the region and until 1807, a total number of four asteroids were discovered. The three new objects were called (2) Pallas, (3) Juno and (4) Vesta. By 1851, a total number of 15 minor planets had been discovered, and this number increased to more than 50 by 1858 (Schmadel, 2012). Since then, the discovery of asteroids has continued to accelerate, and with advancements in sensors, computers, and spacecraft, it has become possible to detect smaller bodies with diameters of only a few tens of meters. As of February 2024, NASA and the Minor Planet Center (MPC) state that more than 1.3 million asteroids have been detected and are listed in their

[3]The Titus-Bode Law states that the radii R of the orbits of planets follow the law $R = 0.4 + 0.3 \times 2^n$, with $n = -\infty, 0, 1, 2, 4, 5$ for the at the time known planets Mercury, Venus, Earth, Mars, Jupiter, and Saturn. The apparently missing planet was searched for n=3 (Wynn-Williams, 2016)

databases (Bolles, 2024; IAU, 2024).

As mentioned before, most asteroids are relatively small bodies but, similar to the planets, they are in orbit about the sun. They are primarily, but not exclusively, located between Mars and Jupiter, in the so-called "main asteroid belt" or just "main belt" (Fisher and Erickson, 2013; NASA, 2024). An illustration of the locations of asteroids in the solar system can be found in Figure 2.6

It is common to classify the asteroids by their composition and location in the Solar System. The first and most widely used taxonomy of composition was originally specified by D. Tholen and divided into three main groups (Tholen, 1989; Michel et al., 2015):

- C-Types: Most asteroids are of this type, characterized as dark, carbonaceous objects.
- S-Types: Bodies of this group are primarily composed of silicon dioxide.
- X-Types: Tholen originally defined this group as an "umbrella" category, where asteroids have similar spectra but likely differ in composition.

In my studies, the composition of asteroids was of minor importance, as it primarily concerned geologists and the scientists who selected the target. Once the targets were selected, our focus shifted to reaching them, and for my studies, the classification by location was more important. The previously mentioned main belt asteroids were of minor importance, but I engage with some missions to these body groups. The more significant groups included Trojan asteroids and Near-Earth asteroids (NEAs). In addition to these, we also investigate binary and triple asteroids, which are systems of at least two bodies orbiting each other at close distances, typically a few kilometers. Binary asteroids can be found in the main belt, among the Trojans, and also as Near-Earth Asteroid (NEA)s. In the following a brief overview about all four asteroid groups is given.

Table 2.4: Properties of Selected asteroids which are Mentioned in this Thesis either as Mission Targets or for Comparative Purposes. Note: For binary or triple asteroids, parameters refer to the primary body. a: semi-major axis, e: eccentricity, i: inclination, d: diameter of the (main) body, GM: standard gravitational parameter times mass, class: orbital group classification, type: single/binary/triple (number of bodies that belong to the asteroid); Reference frame: heliocentric ecliptic and mean equinox/J2000;
Data taken from a) Fang and Margot (2012), b) Barucci et al. (2012), c) Watanabe et al. (2019), d) Goossens et al. (2021) e) Todd et al. (2013), f) Levison (2024), x) *JPL-SBD (2024) and IAU (2024)*

Name	**a** $[AU]$	**e**	**i** $[deg]$	**d** $[km]$	**GM** $[\frac{km^3}{s^2}]$	**class**	**type**
(153591) *2001 SN*$_{263}$ $^{(a,x)}$	1.987	0.48	6.69	2.5	6.1×10^{-7}	NEA	Triple
(175706) *1999 FG*$_{3}$ $^{(b,x)}$	1.054	0.35	1.99	1.4	1.4×10^{-7}	NEA	Binary
(162173) Ryugu $^{(c,x)}$	1.190	0.19	5.87	1.0	3.0×10^{-8}	NEA	Single
(101955) Bennu $^{(d,x)}$	1.13	0.20	6.0	0.5	4.9×10^{-9}	NEA	Single
(5261) Eureka $^{(e,x)}$	1.524	0.07	20.3	1.9	6.3×10^{-7} *	Trojan	Binary
(101429) *1998 VF*$_{31}$ $^{(e,x)}$	1.524	0.10	31.3	0.9	6.7×10^{-8} *	Trojan	Single
(121514) *1999 UJ*$_{7}$ $^{(e,x)}$	1.524	0.04	16.7	2.5	2.7×10^{-6} *	Trojan	Single
(311999) *2007 NS*$_{2}$ $^{(e,x)}$	1.524	0.05	18.6	0.8	5.0×10^{-8} *	Trojan	Single
(385250) *2001 DH*$_{47}$ $^{(e,x)}$	1.524	0.04	24.4	0.5	1.5×10^{-8} *	Trojan	Single
(10469) Krohn $^{(x)}$	2.349	0.11	6.4	2.5	7.5×10^{-7} *	Main Belt	Single
(152830) Dinkinesh $^{(f,x)}$	2.19	0.11	2.1	0.7	3.3×10^{-8}	Main Belt	Binary
(4) Vesta $^{(x)}$	2.36	0.09	7.1	525.4	1.7×10^{1}	Main Belt	Single

* No data for the mass was found in the literature, only the diameters and spectral types. Most Mars Trojan asteroids are classified as S-types, with only (121514) classified as an X-type (Todd et al., 2013). The mass was then calculated as $Volume \times Density$. For the volume, a homogeneous sphere with the specified radius was assumed, and density values of $2710 ^{kg}/_{m^3}$ for S-types and $5320 ^{kg}/_{m^3}$ for X-types were used (Krasinsky et al., 2002). For (10469) Krohn, no composition data was found. A C-type density ($1380 ^{kg}/_{m^3}$) was assumed, as this is the most common group of asteroids (Michel et al., 2015).

Main Belt asteroids

Main Belt asteroids constitute the largest number of asteroids. They are located roughly between 2 and 3.5 AU, forming a nearly flat ring (Fisher and Erickson, 2013). It is estimated that between 1.1 and 1.9 million asteroids with diameters of more than one kilometer are located in this region.

Main Belt asteroids come in all sizes, with diameters varying from a few meters up to several hundred kilometers, and can also vary significantly in shape and mass. The size distribution of Main Belt asteroids shows a clear exponential behavior. While only a few asteroids have diameters of more than 100 km, several thousand asteroids have diameters in the range of several hundred meters (Davis et al., 2002).

The very first discovered and largest asteroids (1) Ceres and (4) Vesta are located within the main belt, but also the small asteroid (152830) Dinkinesh, which has been visited by the Lucy spacecraft in November 2023 (Mottola et al., 2023). From my very personal point of view, the most important asteroid of the main belt is (10469) Krohn which is named after my beloved wife and mother of my children Dr. Katrin Krohn.

An interesting side note is that the first-ever discovered asteroid, (1) Ceres, was originally classified as a planet and later reclassified as an asteroid. However, in 2005, it was recognized that Ceres is a bit less than half the size of Pluto. With this size, the gravity of the asteroid is strong enough to pull it into a nearly round shape (Thomas et al., 2005). Due to this and the resulting hydrostatic equilibrium, the International Astronomical Union (IAU) decided in 2006 to change the classification of Ceres from an asteroid to a dwarf planet (Ekers and Gingerich, 2006). Ceres is therefore no longer considered a "nominal" asteroid but has maintained its ID (1) as the first asteroid.

Trojan asteroids

Trojans asteroids are a special group that share the orbit of a major planet around the Sun but do not collide with the planet. The reason for this is that these bodies are located in the naturally stable Lagrangian Points L_4 and L_5. These geometric points are named after the astronomer Joseph-Louis Lagrange, who was able to find analytical solutions to the general three-body problem. L_4 and L_5 are points that form equilateral triangles with the center of gravity of the two main bodies in a three-body problem, which are usually the Sun and a planet or a planet and its moon (Fasoulas and Messerschmid, 2009; Ley et al., 2009).

Due to the fact that Trojans at Lagrangian Points L_4 and L_5 form equilateral triangles with the planet and the Sun, they are generally either leading (L_4) or trailing (L_5) the planet by 60deg. The positions of the Lagrangian Points are shown in Figure 2.7.

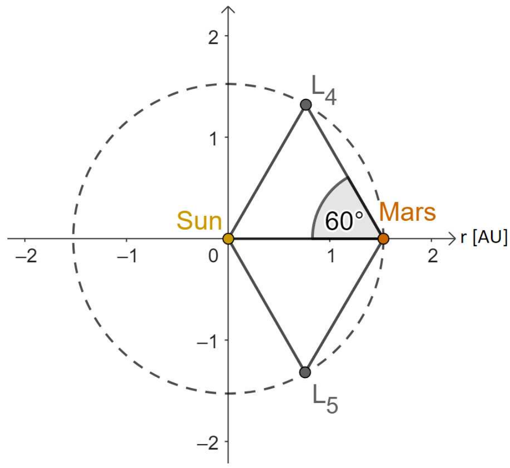

Figure 2.7: Lagrangian Points of the Sun-Mars System. The majority of known Martian Trojans is librating about the trailing L_5 and only one about the leading L_4. *Credit: Own work, created using GeoGebra [https://www.geogebra.org/calculator].*

A consequence of this geometry is that all Trojans have the same semi-major axis as the planet they share the orbit with. The other orbital elements, such as the inclination, longitude of ascending node, or eccentricity, can vary significantly, but by definition, the semi-major axis has to be the same and consequently also the orbital period around the Sun (see Table 2.4).

The most famous Trojan group is probably the one associated with Jupiter, as shown in Figure 2.6. The asteroid (588) Achilles was discovered and confirmed to be a Jupiter Trojan at the beginning of the 20th century. It was the first-ever discovered Trojan asteroid, and since then, the total number of Trojans has increased significantly to more than 10,000 (Nicholson, 1961; Li et al., 2023).

In 2021, the National Aeronautics and Space Administration (NASA) launched the Lucy mission with the objective of investigating seven primitive bodies near both the L4 and L5 Lagrange points of Jupiter. Lucy is the first mission ever to study a diverse selection of Trojan asteroids with diameters ranging from roughly 1 km to 100 km (Levison et al., 2021).

Besides Jupiter also Neptune, Uranus, Mars and even Venus and Earth are confirmed to have Trojan companions (Santana-Ros et al., 2022). In this thesis I focus exclusively on the Trojan asteroids of Mars.

By February 2024, nine Martian Trojans were officially confirmed by the Minor Planet Center (IAU, 2022a). These bodies are relatively small in diameter, ranging from only a few hundred meters to a few kilometers. The properties of the most prominent Mars Trojans are summarized in Table 2.4, and additional details can be found in Table 6.1. The publication presented in chapter 6 focuses on visiting the Martian Trojans and combining it with a mission to Mars and the moons of Mars.

Near-Earth Asteroids (NEA's)

As can be derived from their name, Near-Earth Asteroid (NEA)'s or Near-Earth Object (NEO)'s are small bodies with orbits close to that of Earth. 'Close' in this case should be understood from an astronomical point of view, as even asteroids with a closest approach of 40 million kilometers to Earth's orbit are considered 'near-Earth.' NEA's are therefore classified by their orbital distance to the Sun and, more importantly, to Earth's orbit. According to the official definition, asteroids with a perihelion distance of < 1.3 AU are considered Near-Earth asteroids (Michel et al., 2015; Scheeres, 2012). The group is further divided into four different types —Atiras, Atens, Apollos, and Amors— based on finer distance specifications (Scheeres, 2012). An overview of these types and their differentiation can be found in Table 2.5. About 90% of all discovered NEOs belong to the Amor or Apollo categories (Binzel et al., 2015).

Table 2.5: Near-Earth asteroids Classifications (Scheeres, 2012; Binzel et al., 2015); q: perihelion distance, Q: aphelion distance, a: semi-major axis

Group	Description	Definition
NEAs	Near-Earth asteroids	$q < 1.3AU$
Atiras	NEAs whose orbits are contained entirely within the orbit of Earth	$a < 1.0AU$ $Q < 0.983AU$
Atens	Earth crossing NEAs with semi-major axis smaller than earth	$a < 1.0AU$ $Q > 0.983AU$
Apollos	Earth crossing NEAs with semi-major axis larger than earth	$a > 1.0AU$ $q < 1.017AU$
Amors	Earth-approaching NEAs with orbits exterior to Earth's but inferior to Mars'	$a > 1.0AU$ $1.017 < q < 1.3AU$

In February 2024, the Center for Near-Earth Object Studies (CNEOS) reported that a total of 34,394 NEAs are known, of which 33 are Atiras, 2,718 are Atens, 19,488 are Apollos, and 12,155 are Amors (Chodas et al., 2024). Due to improved observation campaigns, the total number of known bodies has increased significantly in recent years, as has the interest in them. Binzel et al. (2015) identifies several reasons for this high interest:

1. By definition, these asteroids come close to Earth and are consequently potential hazards that could cause civilization-threatening impacts.
2. Their close proximity allows easier access for space missions, as already explained in section 2.1 and shown in Figure 2.3
3. Different observational techniques are possible for Earth-based observers to investigate these objects when they are close to Earth.

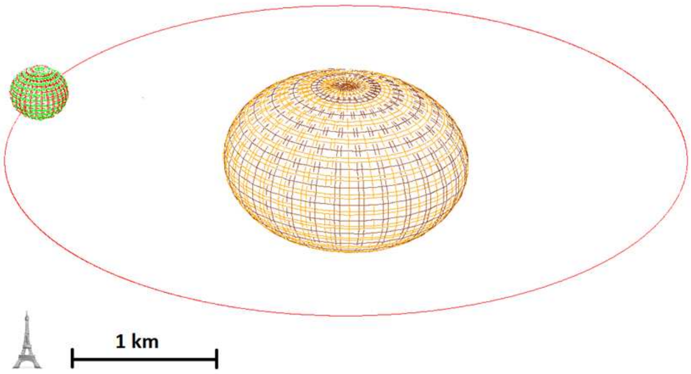

Figure 2.8: Scaled model of binary near-earth asteroid 1996FG_3 as used in our calculation. A scaled Eifel Tower is include for size comparison. Details about the binary can be found in table 2.4 *Image is own work as published in (Wickhusen et al., 2012)*

Figure 2.9: Image of asteroid Dinkinesh and Its Moon Salem taken by the Lucy spacecraft. *Credit: NASA/Goddard-/SwRI/Johns Hopkins APL*

Binary and Triple asteroids

A significant number of asteroids form a system with a main body and at least one additional body orbiting it. Asteroids with two bodies orbiting each other are called binary asteroids. In this thesis, two asteroid systems belong to this group: the Near-Earth Asteroid 1996 FG_3 and the Martian Trojan (5261) Eureka (see Table 2.4). An illustration of the model of 1996 FG_3, which we used in Hussmann et al. (2012), is shown in Figure 2.8.

In November 2023, the Lucy spacecraft visited asteroid (152830) Dinkinesh during a short flyby. The images showed that this main belt asteroid is also at least a binary asteroid. The small companion was named Salem. However, in some images, it appeared that the moon itself might consist of two bodies, which could either be orbiting each other or could be a special type of contact binary (Menne, 2023). The corresponding image showing Dinkinesh and its moon Salem is presented in Figure 2.9.

In addition to binary asteroids, where two bodies orbit each other, systems with three bodies also exist. In our study on terminator orbits (Wickhusen et al., 2022a), we focused on the triple (or trinary) asteroid 2001 SN_{262}, which is also a NEA. It had long been assumed that asteroids with four or more bodies exist, and in 2022, the first-ever discovery of a quadruple (four-body) asteroid was confirmed (Berdeu et al., 2022).

Although we also considered single asteroids, our studies often focused on binary and triple asteroids, with the most massive body of such a system being denoted as the 'primary.' The smaller bodies were then denoted as 'secondary' and 'tertiary' bodies. This approach is also followed throughout this thesis.

An alternative notation in relevant publications is 'Alpha,' which is used as a synonym for 'primary,' and 'Beta' and 'Gamma' for 'secondary' and 'tertiary,' respectively.

The number of discovered binary and triple near-Earth asteroids has increased significantly over the last years as well as the number of known large main-belt asteroids with satellites. Based on current measurements, it is assumed that approximately 15% of all asteroids (main-belt, Trojans or NEOs) are binary objects (Pravec et al., 2006). By August 2024 a total number of 407 asteroids with at least one companion have been identified so far (Johnston, 2024).

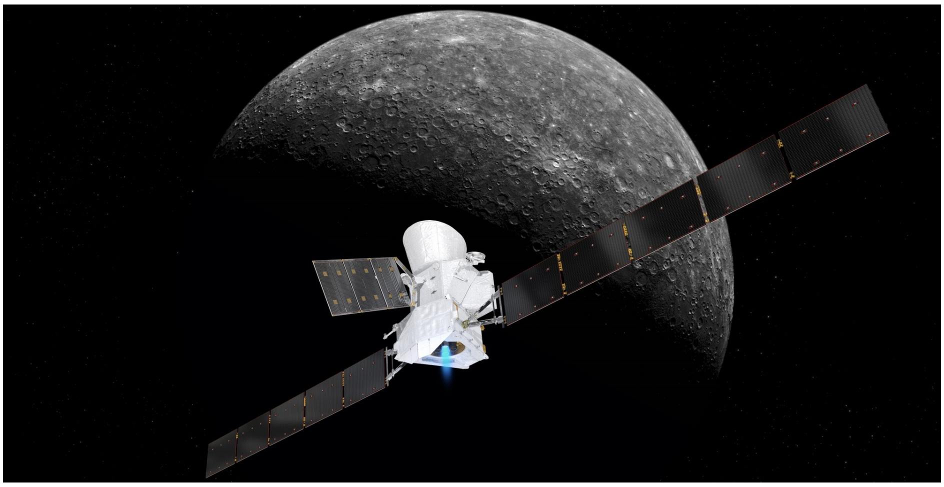

Figure 2.10: Computer generated image of BepiColombo on its way to Mercury. *Credit: ESA*

2.2.3 Mercury

Mercury is the smallest planet in our Solar System with a radius of $2,439.7$ km, which corresponds to 0.38 earth radii and it is also the planet closest to the Sun. It has a semi-major axis of 0.38 AU, which results in an orbital period of 88 days around the Sun. Mercury is tidally coupled to its orbital period around the Sun. The planet rotates 1.5 times around its own axis during one full orbit around the Sun. This leads to a 3:2 resonance and a Mercury solar day that lasts 176 Earth days (Podbregar and Lohmann, 2014).

Mercury is also a rocky planet, but in contrast to Venus, Earth, and Mars, it has no atmosphere. Its surface is comparable to that of Earth's Moon and is covered with impact craters. Due to its rotational state, the absence of an atmosphere, and its close proximity to the Sun, the surface temperatures of the planet range from $-170°C$ to $+430°C$ (Podbregar and Lohmann, 2014).

The orbit of Mercury has a semi-major axis that is relatively close to that of Earth (90 million kilometers difference) and comparable to the semi-major axis difference between Earth and Mars (80 million kilometers). However, due to its proximity to the Sun, it is far more difficult to get into orbit about Mercury than Mars, as missions to this planet require very high Δvs (Podbregar and Lohmann, 2014). For details, see Figure 2.3.

So far, only two space probes have been sent to Mercury for exploration. The first was Mariner 10, which visited Mercury for the first time in 1974 but did not enter orbit around it. The second mission, MESSENGER, reached Mercury almost 40 years later and was able to enter a highly elliptical polar orbit around the planet (Osterhage, 2021).

With only two missions to Mercury so far, and only one mission in orbit around it, there are still several unanswered questions that should be investigated in the future. Currently, a new mission is on its way to Mercury, which is ESA's BepiColombo. The spacecraft en route to Mercury is shown in Figure 2.10. My personal involvement in this mission as an operator of the laser altimeter BELA led to contributions to scientific publications about this upcoming mission. In Thomas et al. (2021), I provided the operational concept, and in Steinbrügge et al. (2018), I set up the operational procedure, performed the tests, and generated the test data.

However, the most important publication related to BepiColombo and this thesis is Höschele et al. (2021). In this paper, we analyzed the orbital evolution of BepiColombo during its one-year nominal mission lifetime and an additional year of extended lifetime. The paper addresses the uncertainties in the known gravity field of Mercury. The strong perturbations caused by this gravity field lead to a continuous reduction in the pericenter altitude of BepiColombo. This altitude is crucial for the mission in Mercury's harsh thermal environment. The uncertainties in Mercury's gravity field can cause significant variations in the pericenter altitude. Starting at an altitude of 480 km above the surface, the pericenter could drop to 400 km in the best case and fall below 100 km in the worst case after two years Höschele et al. (2021).

The results of this Paper had been considered by ESA and possible scenarios two avoid critical altitudes were discussed afterwards.

2.2.4 Enceladus

Enceladus is a geologically active Saturnian moon of considerable scientific interest. It has a diameter of about 500 km and is geologically active.

So far, only four space probes have visited Saturn and its moons. The NASA-ESA joint mission Cassini-Huygens was a milestone mission that yielded numerous discoveries (Osterhage, 2021). The highest-resolution images of Enceladus currently available were acquired by the Cassini mission (see Figure 2.11). It was also the Cassini mission that led to the discovery of plumes on Enceladus, ejecting gas and ice particles in the south pole area. Cracks within the ice crust in this region and the presence of complex organic molecules have put Enceladus in the spotlight of the planetary science community and made it a prime target in the search for extraterrestrial life (Schenk et al., 2018; Benedikter et al., 2022; Konstantinidis et al., 2014).

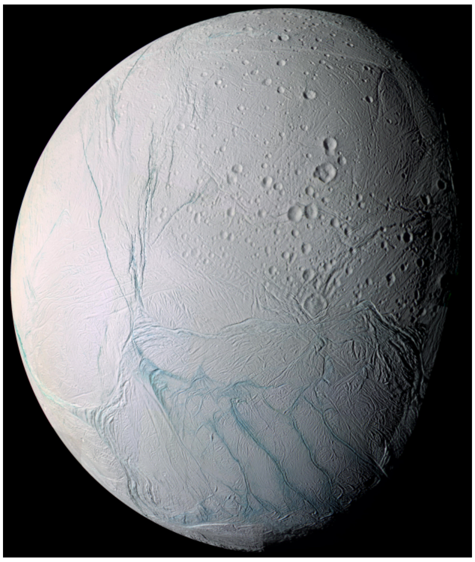

Figure 2.11: Surface Features of Saturn's Moon Enceladus. The image was taken by the Cassini mission and shows the south pole area. *Credit: NASA/JPL/Space Science Institute*

There is strong evidence that Enceladus has a subsurface ocean of liquid water beneath its ice crust. Thomas et al. (2016) used measurements of control points across the surface of Enceladus to determine the satellite's precise rotation state. They showed that a forced physical libration of 0.120 is too large to be consistent with Enceladus's core being rigidly connected to its surface. This study provided evidence for the presence of a global ocean rather than a localized polar sea. Enceladus is therefore one of the best candidates for a potentially habitable ocean world in our Solar System (Spencer and Nimmo, 2013; Thomas et al., 2016).

The German Aerospace Center (DLR) has also studied possible missions to Enceladus since 2012. In cooperation with several Universities a mission concept was developed which includes a lander to land close to the plumes. After landing on the surface, an ice-penetrating melting robot shall melt itself towards the ocean for analyzing ice and water samples. The mission concept was named Enceladus Explorer Initiative (EnEx) (Konstantinidis et al., 2014).

Our department and I have been involved in this mission study since 2016. Already in 2017, we contributed to the research with the Enceladus geodetic framework (Oberst et al., 2017). As part of this research, I analyzed the illumination conditions in the polar area and determined the best time frames for the landing. Although, in retrospect, the results could have been expected, I was still surprised that regions at the south pole would be permanently in light for more than 8 years. The time frame even increases to almost 14 years, but during this additional time, Saturn will regularly cast a shadow on the areas. It was also noted that the distance to the Sun varies between approximately 9 to 10 AU, and the incoming radiation from the Sun will consequently be about 80 to 100 times lower than the radiation on Earth. In the end, this sums up to $13 - 17\frac{W}{m^2}$ solar radiation, not taking into account the surface angle at the landing site (Oberst et al., 2017).

In the following years we had a joint EnEx cooperation with DLR in Oberpfaffenhofen. One major objective of this study were possible repeat-pass orbits about Enceladus. Due to the very strong gravity of Saturn, the relative small semi-major axis of Enceladus and its small gravity, highly inclined solutions or even repeat-pass orbits were not easy to find. We performed a systematic analysis and were able to find the required solutions (Benedikter et al., 2022).

Afterwards an Enceladus study funded by ESA was started and we are still developing concepts for this study. One goal of the study is analysing highly inclined low-altitude orbits, finding scenarios for station keeping and analysing the required Δv demand. Details about the orbital studies can be found in Section 4.4.3

Chapter 3

Mission Design

Experience from multiple mission proposals shows that the preparation process consistently requires the definition of certain key components. Through review of state-of-the-art literature such as (Fortescue et al., 2005; Falkner et al., 2007; Montenbruck and Gill, 2000), the main work packages were condensed into the following six major blocks:

1. Definition of science objectives
2. Definition of mission goals and requirements
3. Selection of payloads
4. Definition of trajectory and orbit
5. Concept design of the spacecraft
6. Cost estimation

The preparation of a scientific mission proposal should always begin with the definition of science objectives, which outline what the mission aims to investigate. This information is then used to derive the mission requirements and constraints in the second step. In the third step, the appropriate payloads (instruments) are selected to gather the necessary data required for answering the scientific questions.

When the first steps are finalized, the trajectory and orbit requirements can be defined, taking into consideration the requirements and constraints of the payloads, mission concept, and science objectives. The fifth step involves developing a preliminary spacecraft design, which serves as the foundation for the final step: cost estimation. This estimation considers the full mission concept to determine its cost implications.

Figure 3.1: The Mission Design Iteration Cycle as developed during the various mission proposals: GETEMME, PhoDEx, DePhine, and Planetary Polar Explorer. *Credit: Own work*

The first iteration through the six steps often results in inconsistencies and a cost estimation that exceeds the budget. This requires restarting the process at a previous step, sometimes even the first step, to re-evaluate the science questions. The process is an iteration cycle and several steps may have to be repeated and refined to arrive at a final concept that can address the science questions while staying within the budget constraints.

In some cases, the iterations may lead to the conclusion that the concept is either technically infeasible or not feasible within the given cost constraints.

3.1 Science Objectives

The definition of scientific objectives is the starting point for a science-led mission proposal, such as the Cosmic Vision M- or F-class mission. These objectives must address the fundamental questions about the Solar System and the Universe.

In the context of the Cosmic Vision program, the ESA has established a framework for all possible scientific questions (ESA, 2014). Proposals funded by this program must answer one or more of the following questions:

1. What are the conditions for planet formation and the emergence of life?
2. How does the Solar System work?
3. What are the fundamental physical laws of the Universe?
4. How did the Universe originate and what is it made of?

Based on this framework, we have defined specific, high-priority scientific questions related to asteroids and small bodies, which are explained in more detail in section 2.2 and explicitly addressed in section 7.2.

3.2 Mission Requirements and Constraints

The mission requirements and constraints are directly derived from the science objectives. They define the goals that the mission must achieve to be successful.

Each mission has its own specific objective and, consequently, its own specific requirements. For instance, in our Dephine proposal, we aimed to answer the question of what the bulk densities and porosities of Phobos and Deimos are. To address this, Dephine needed to determine the global shape and volume of the moons with high precision. This required special instruments like a camera, radar, and radio science experiments as the minimal payload (see Section 3.3). "A specific mission requirement for that scientific objective consisted of low-velocity fly-bys at close ranges.

Once the science objectives, mission requirements, and payloads have been iterated, a so-called Science Traceability Matrix needs to be set up to relate the three blocks to each other. With this Matrix, each scientific question and goal, along with the mission objectives, can be broken down into corresponding measurements.

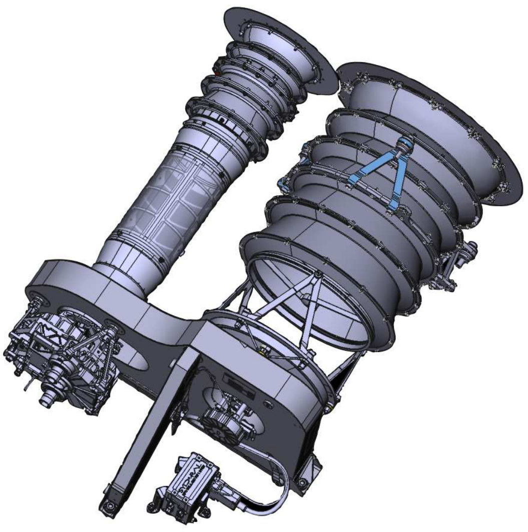

Figure 3.2: The BepiColombo Laser Altimeter BELA instrument for the BepiColombo mission, which will arrive at Mercury in the year 2025. See also Section 2.2.3. *Credit: DLR/University of Bern*

3.3 Instruments (Payloads)

The instruments or payload of a science mission are the tools that collect data and help us understand the conditions on the corresponding planets or small bodies. These instruments or payloads detect or sample the environment and provide insights into these conditions.

In our proposals, the payload always consisted of scientific instruments. These instruments must collect all scientific data within a predefined time frame to answer the scientific questions that are the primary focus of the mission.

Common examples of instruments are cameras, spectrometers, magnetometers, particle detectors, radars, and laser altimeters. In our proposals, we often included these instrument types as they were optimal candidates to answer the scientific questions. Laser altimeters, in particular, are of high interest to us as our department is responsible for the laser altimeters BELA and GALA (see Figure 3.2).

With the payloads, the basic demands for resources like power, data rates, and pointing accuracy, as well as orbit properties, illumination requirements, and operational distances, are already defined. For instance, a camera typically operates only in illuminated regions and tends to generate large amounts of data, while a laser altimeter can only operate up to a certain distance and requires a lot of power.

However, each payload is selected for a specific reason and is used to answer important scientific questions. As a consequence, the payloads also impose requirements and constraints that must be taken into account. These requirements and constraints, in turn, must be iterated several times to reach an acceptable compromise.

3.4 Trajectory and Orbit Analysis

With inputs from the three previous steps, a preliminary trajectory and orbit design can be performed, taking into account the resulting requirements and constraints. It is difficult to find a general approach to account for these, as they often highly depend on the specific payloads and mission. Each payload and spacecraft unit typically has its own dedicated demand for resources such as power, data rates, pointing, operational altitudes, thermal operational range, etc. A camera, for example, requires an illuminated surface to operate properly, while a laser altimeter requires a certain minimum altitude for return pulse detection. (Thomas et al., 2021).

Another important aspect of the orbit design phase is the illumination conditions. Solar radiation is of fundamental importance for powering a spacecraft, especially since ESA (almost) exclusively uses solar panels for generating electric power in space. Although other concepts exist, solar panels are the most common method for generating electric power for spacecraft. Other alternatives, such as Radioisotope Thermoelectric Generators (RTGs), have only minor importance and have so far only been used on NASA missions to the outer planets (Ambrosi et al., 2019).

Furthermore, the distance to Earth has a direct impact on the available data rate. Although power generation and antenna gains can be increased with larger solar panels or antennas, the overall gain decreases proportionally to the square of the distance from the Sun or Earth, respectively (Fortescue et al., 2005). Additionally, a very low orbit around the target body can often result in regular shadow phases, affecting both solar radiation and communication links.

The last, but probably most important, aspect of trajectory and orbit design is the Δv analysis. As already shown in section 2.1, each additional propulsive maneuver has an exponential impact on the required propellant and, consequently, on the overall mass. It is therefore crucial to minimize the total Δv demand to reduce the overall spacecraft mass.

3.5 Spacecraft Design

The spacecraft bus itself has no direct scientific purpose. Instead, it serves as the main structure that enables the payload to collect the required data and transmit it to Earth. The spacecraft must deliver the payload to the correct location, provide power, ensure proper pointing, manage data, and maintain the instruments within the correct temperature range. Consequently, the spacecraft bus consists of the following main components (Fortescue et al., 2005; Berlin, 2014):

1. On-Board Data Handling and Storage or On-Board Computer (OBC)
2. Power Generation and Distribution System
3. Telemetry, Tracking and Control (TT&C)
4. Thermal Control System
5. Attitude Control System
6. Structure and Mechanics
7. *Propulsion System*

In the ESA Cosmic Vision proposals, the spacecraft design was always the responsibility of industry partners, not the scientific institutes. The proposals needed to define a specific spacecraft concept, but ultimately, the industry had to decide what was feasible and what was not. The design is significantly constrained by the understanding of the requirements. Therefore, it is extremely important to define the requirements clearly and precisely and to focus exclusively on the actual demands. However, it is not always possible to reduce the demands and requirements to the essential design rules.

This point is especially important, as the spacecraft is the fundamental part of the space mission. If a critical failure occurs during flight, it could jeopardize the entire mission and result in a complete loss. Prominent examples of such total losses are mentioned in Section 2.2.1, where three missions were launched towards the moons of Mars, but all of them failed, leading to a complete loss of the mission.

Furthermore, the fundamental importance of spacecraft design is evident in the cost estimation. ESA's guidelines for an M-class mission proposal allocate 40% of the entire budget to industry partners for the definition, design, and construction of the spacecraft (ESA, 2014).

In any case, the current method of expressing scientific needs, formulating scientific requirements, selecting payloads, and defining a reference spacecraft design is the best approach we know so far, and thus we continue to follow this path.

3.6 Cost Estimation

Cost estimation was the most challenging objective during our concept development phases. For the second proposal, Phobos and Deimos Explorer (PhoDEx), I was responsible for providing a full cost estimation for the project. The predecessor proposal, "GETEMME," was not accepted due to incomplete cost estimations and a low level of definition. Therefore, a better method for estimating costs had to be developed.

The launch costs for the former Soyuz Fregat launcher were provided by ESA and fixed at 75 million euros, while the operations costs (mission + science) were estimated at 100 million euros (ESA, 2014). However, calculating the industrial costs for the spacecraft was more challenging. A precise calculation of the building costs was not feasible with the limited resources available. The best solution to this problem was to compare previously flown missions to Mars with our concept.

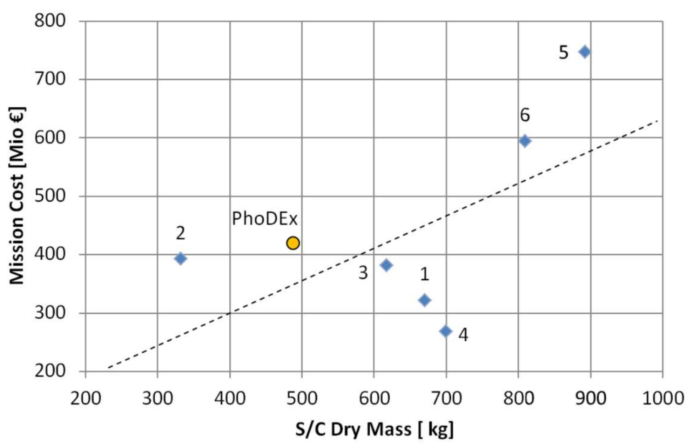

Figure 3.3: Mission Cost Estimation Comparison Diagram of the PhoDEx Proposal. (1) Mars Global Surveyor NASA, (2) Mars Odyssey NASA, (3) Mars Express ESA, (4) Venus Express ESA, (5) Mars Reconnaissance Orbiter NASA, (6) MAVEN NASA *Credit: Own work as published in (Oberst et al., 2014)*

First, I searched for details about Mars Express (MEX), which was the best reference mission for our proposal. The total costs for the MEX spacecraft bus were given as 150 million euros (ESA Public Relations Division, 1999), with a dry mass of 666 kg (Chicarro et al., 2004). Using these values, I calculated the cost per mass ratio to be 0.225 M€/kg. Since we assumed that several components of MEX could be reused, we estimated that the price per kilogram would be comparable for PhoDEx. We assumed that each dry mass kilogram of the spacecraft would cost 0.25 M€ and derived the total costs to be 117 M€, or 36% of the estimated 325 M€ Costs at Completion without margin (Oberst et al., 2016). This result aligned with the provided reference value of approximately 38% (ESA, 2014).

On top of this, we assumed a margin of 30%, leading to a total sum of 423 M€. This value was then used in a subsequent step, where I compared it with the actual costs at completion of already flown missions. We searched for missions that were comparable in terms of expected mission duration, target, and dry mass. The results are shown in 3.3. With the cost estimation per dry mass for PhoDEx being above the average of the six reference missions, the team was confident that we had a reliable cost estimation.

Unfortunately, ESA did not evaluate our cost estimation as we did, and they assumed a significantly higher amount of 270 M€ for the spacecraft bus. Consequently, our entire concept would exceed the M4 cost cap of 450 M€. As a result, the PhoDEx proposal was ruled out at the first step of the evaluation process.

After the evaluation, the proposal lead and I reviewed the results and iterated the process. We concluded that a cost estimation by an industry partner with a precise spacecraft model would be required. As it was planned to get in contact with OHB for a concurrent design study, it was also the best opportunity to ask for a detailed cost estimation.

With the spacecraft components defined during the study and a professional cost estimation for development costs and margins, we were able to provide a detailed estimation of the costs. It should be noted that OHB also adopted my idea of comparing the cost estimation with previously flown missions, and we generated an updated diagram.

The results were then included in the DePhine proposal (Oberst et al., 2016) (see also chapter 7) and convinced the technical and programmatic evaluation team that the DePhine mission would fit within the budget of an M-class call of the Cosmic Vision program.

Chapter 4

Trajectory and Orbit Design

4.1 Impulsive Maneuvers in Space

As already explained in Section 2.1, impulsive maneuvers in space are often very costly in terms of Δv and propellant. Nevertheless, they are almost always required for corrective maneuvers during the cruise phase, orbit insertion, station keeping, inclination changes, or changes of orbit around the target body. This section provides an overview of how general trajectory and orbit maneuver calculations can be performed.

4.1.1 Delta-v Calculation

Delta-v or Δv is a physical quantity commonly used to describe an impulsive maneuver. It represents the amount of velocity change required to perform the maneuver. It should be noted that the impulse is generally assumed to be instantaneous, and the fact that a propulsion system burn will always take a certain amount of time is typically neglected in the calculation. However, this approximation is usually sufficient for a preliminary trajectory or orbit maneuver analysis. Calculating the required Δv is straightforward (Curtis, 2010):

$$\vec{v_i} = \vec{v_t} - \vec{v_c}, \tag{4.1}$$

$$\Delta v = |\vec{v_i}|, \tag{4.2}$$

where v_c is the current velocity vector of the spacecraft and v_t is the target velocity vector. From a geometrical point of view, Δv is the length of the vector $\vec{v_i}$, which connects the current velocity vector with the desired target velocity vector (see Figure 4.1). The vector $\vec{v_i}$ also indicates the required direction of the impulse during the maneuver, i.e., the propulsion system must fire in the $-\vec{v_i}$ direction.

Once all the main maneuvers required during a mission are determined, all Δv's must be summed up to calculate the total demand (Fasoulas and Messerschmid, 2009). This value, with margin, is then a mandatory input for the Tsiolkovsky equation 2.2 in order to determine the overall spacecraft mass. It is a key input value for the design of the spacecraft, as it significantly constrains the overall available dry mass.

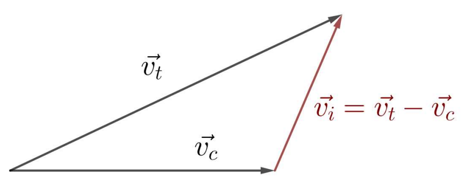

Figure 4.1: Required velocity vector $\vec{v_i}$ to change from current velocity $\vec{v_c}$ to the target velocity $\vec{v_t}$. *Credit: Credit: Own work, created using GeoGebra [https://www.geogebra.org/calculator]*

Impulsive maneuvers and Δv calculations can be used to change any osculating element, although some elements require a specific position in orbit to be changed correctly. For example, an inclination change of a polar orbit is not possible while being directly above the pole.

In our studies, impulsive maneuvers were mainly used to change the semi-major axis and eccentricity (which includes orbit insertion maneuvers), as well as to change the inclination or longitude of the ascending node. The remaining two Keplerian elements, argument of periapsis and mean anomaly, were not considered in the trajectory analysis performed in the papers (see Chapter 6, 7 and Section 4.4.4).

In the triple asteroid paper (Section 5), the inclination and the longitude of the ascending node were specifically varied to rotate the orbital plane of the probe in space. However, in this particular case, changing these two elements required only very minor amounts of Δv due to the very low gravity of the asteroids.

4.1.2 Hohmann Transfer

Space vehicles often need to be transferred from one orbit to another with a different altitude or semi-major axis. If only a single maneuver is performed, the initial and final orbits will intersect at the position where the maneuver was executed. Therefore, at least two maneuvers are required to transfer a spacecraft between two orbits that do not intersect each other (Fortescue et al., 2005).

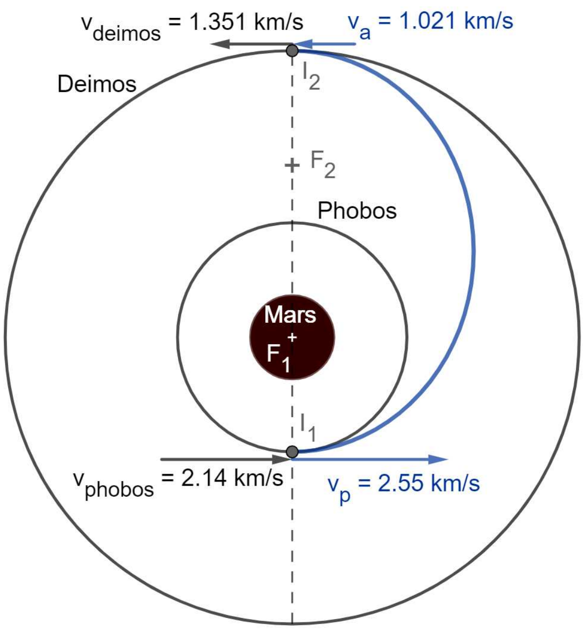

Figure 4.2: A Hohman transfer from a Quasi-Satellite orbit about Phobos to a Quasi-Satellite Orbit about Deimos. All distances are to scale. Δv's are calculated with equations 4.3, 4.4 and 4.5. Orbits of Phobos and Deimos are assumed to be circular and coplanar. The overall Δv demand to raise the orbit from Phobos to Deimos sums up to $0.747 km/s$. *Credit: Own work, created using GeoGebra [https://www.geogebra.org/calculator]*

The Hohmann transfer is often used to transfer space vehicles from a circular orbit at low altitude (e.g., Low Earth Orbit (LEO)) to another circular orbit at high altitude (e.g., Geostationary Orbit (GEO)) or the vice versa (Ley et al., 2009). In our studies for PhoDEx and DePhine, we used the Hohmann transfer to move the spacecraft from a Quasi Satellite Orbit (QSO) around Phobos to a QSO around Deimos, as both moons orbit Mars in an almost circular orbit. Details of this transfer are shown in Figure 4.2. Details about QSO's are given in Section 4.4.1.

In most cases, the minimum energy and thus Δv demand for transferring a spacecraft to another orbit can be determined using a Hohmann transfer. The velocities required for the two maneuvers of a transfer can be calculated using the vis-viva equation. In the first step, one calculates the initial speed of the spacecraft at the point where the maneuver is to be performed. For a circular orbit, this is given by (Fortescue et al., 2005):

$$v_c = \sqrt{\frac{GM}{r_c}}, \tag{4.3}$$

where v_c is the tangential speed of the spacecraft on its orbit, GM is the gravitational constant times the mass of the main body, and r is the orbital radius. To raise the semi-major axis for an intersection with the target orbit, a first maneuver, in this case, a pericenter kick, has to be performed. Afterwards, when the new apocenter is reached, another maneuver is required to enter the new circular orbit. The tangetial velocities of the intersecting ellipse are given by (Ley et al., 2009):

$$v_p = \sqrt{GM\left(\frac{2}{r_p} - \frac{2}{r_p + r_a}\right)}, \tag{4.4}$$

$$v_a = \sqrt{GM\left(\frac{2}{r_a} - \frac{2}{r_p + r_a}\right)}, \tag{4.5}$$

where v_p and v_a are the pericenter and apocenter speeds. The distances r_p and r_a are the pericenter and apocenter radii, respectively, with $r_p + r_a = 2a$, where a is the semi-major axis of the ellipse.

4.2 Lambert's Problem

The Lambert Problem is a fundamental problem in modern celestial mechanics used to determine an orbit connecting two points in space while satisfying a trajectory constrained by time. The concept behind this theorem was formulated in the 18th century by Johann Heinrich Lambert and formally solved in the 19th century by the renowned Joseph-Louis Lagrange (Lancaster and Blanchard, 1969). During the 1960s, when the space race to the Moon reached its peak (Schefter, 2000), possible solutions to the Lambert Problem were studied intensively, and to this day, more than 60 authors have proposed solutions to the problem (de la Torre Sangrà and Fantino, 2021). In this section, a general overview of solving Lambert's problem is provided, along with a brief summary of the Izzo algorithm (Izzo, 2015), which was used in the Martian Trojans paper (Wickhusen et al., 2023) (see chapter 6).

4.2.1 Overview

The Lambert Problem is primarily a simplified two-body problem, where a main attractor (typically the Sun) is used to calculate an orbit connecting two position vectors in space at different times ($r(t_1)$ and $r(t_2)$). Lambert's Theorem provides a solution for such cases (Roa, 2017). For instance, if one plans to travel from Earth to Mars within a specific timeframe of 100 days, the Lambert Problem can provide a feasible transfer orbit, although it would require a significant amount of Δv to achieve.

As stated by Jordan (1964), the Lambert Theorem can be expressed as a functional equation, "the form of which depends upon the energy per unit mass of the body in motion and certain geometrical conditions." The energy per mass ratio (E) of a body is then given by the formula:

$$E = \frac{1}{2}v^2 - \frac{\mu}{r}, \tag{4.6}$$

with r being the distance from the origin of the central force to the body, v the velocity of this body at r, and $\mu = GM$, where μ is the gravitational parameter (gravitational constant times the mass of the central body).

Based on this equation, a spacecraft launched from Point P_1 (at positional vector $r(t_1)$), three different energy conditions can occur:

- $E < 0$ and thus $v_1 < \sqrt{\frac{2\mu}{r_1}}$ (ellipse),
- $E > 0$ and thus $v_1 > \sqrt{\frac{2\mu}{r_1}}$ (hyperbola),
- $E = 0$ and thus $v_1 = \sqrt{\frac{2\mu}{r_1}}$ (parabola).

For transfers within the solar system, we use only elliptical transfers, focusing only on cases where $E < 0$. In these cases, a general procedure for solving Lambert's problem consists of the following steps (de la Torre Sangrà and Fantino, 2021):

1. computing the geometric parameters of the transfer;
2. initial guessing for the free parameter and iterating on the transfer time equation until convergence
3. computing the velocity vectors.

4.2.2 The Geometric Parameters of Lambert's Problem

In this section, the general geometric concept used to solve Lambert's Problem is explained, using an Earth-Mars transfer as an illustrative example to enhance understanding and visualization of the results. For a spacecraft launching from P_1 (Earth) on an elliptical trajectory to P_2 (Mars), one needs to take into account the launch date (t_0) and the arrival date (t_1).

During this travel time, the target (Mars) will also move along its orbit around the Sun. Consequently, the position of the target depends only on the time.

Figure 4.3 illustrates the first three steps in constructing a geometric solution for Lambert's problem, using an Earth-Mars transfer as an example. In the first step (4.3a), the departure and arrival times

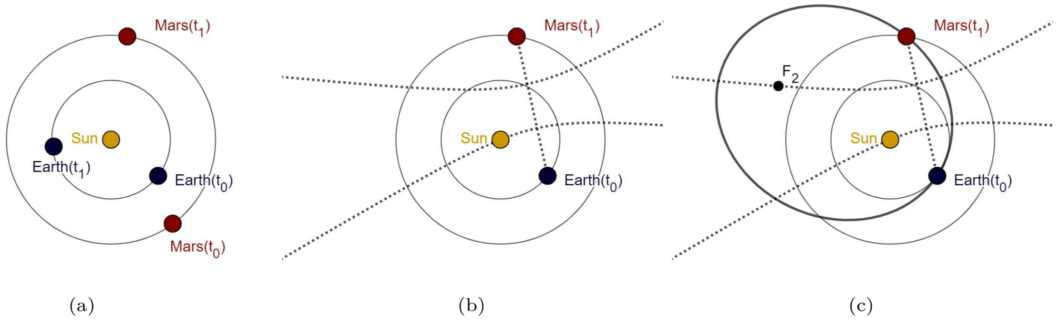

Figure 4.3: Geometric way to construct possible transfer ellipses for an exemplary Earth-Mars Transfer. a) Initial orbit geometry, b) construction of a hyperbola, c) defining a secondary focus for transfer ellipse definition. Details are given in section 4.2.2. *Credit: Own work, created using GeoGebra [https://www.geogebra.org/calculator]*

(Earth at t_0 and Mars at t_1) are defined, and the corresponding positions of the two bodies relative to the main attractor (the Sun) are determined. In the second step (4.3b), a hyperbola is drawn with Earth at departure and Mars at arrival as the two foci, and the Sun as a point on the hyperbola. This hyperbola defines the possible transfer ellipses, with the Sun as the first focus (attractor) and any point on the opposite hyperbola as the second focus. The final step determines either Mars at arrival or Earth at departure as a point on the ellipse (4.3c).

4.2.3 Transfer Time of the Arc

Once the geometric parameters of Lambert's Problem have been determined, the semi-major axis a must be calculated based on a given transfer time or Time of Flight (TOF). While the transfer time for a full or half ellipse depends only on the gravitational parameter (GM) and the semi-major axis, an analytically correct solution can be found. Calculating the time for only partial arc transfers is more challenging, as no analytical solution exists (Fasoulas and Messerschmid, 2009).

The Time of Flight we are interested in is the difference between the departure time and the arrival time. In Figure 4.3, this time is defined as follows:

$$\Delta t = t_1 - t_0. \tag{4.7}$$

However, the goal is to find the corresponding semi-major axis based on the Time of Flight. Peet (2023) and Izzo (2015) suggest determining the chord and the semi-perimeter, which are defined as follows:

$$c = |\vec{r_1} - \vec{r_0}|, \tag{4.8}$$

where $\vec{r_0}$ is the position on the transfer ellipse at the departure time t_0 and $\vec{r_1}$ the position at the arrival time t_1. With these two positions, the chord c of the triangle formed by $\vec{r_0}$, $\vec{r_1}$, and c can be calculated and is shown in Figure 4.4.

Afterwards the semi-perimeter s of this triangle can be calculated:

$$s = \frac{c + r_0 + r_1}{2}. \tag{4.9}$$

Now the two auxiliary angles α and β can be defined:

$$\sin\left(\frac{\alpha}{2}\right) = \sqrt{\frac{s}{2a}}, \tag{4.10}$$

and

$$\sin\left(\frac{\beta}{2}\right) = \sqrt{\frac{s-c}{2a}}. \tag{4.11}$$

With these two angles the semi-major axis and the Time of Flight can be related to each other. This can be done by using a modern Formulation of Lambert's Equation (Peet, 2023):

$$\Delta t = \sqrt{\frac{a^3}{GM}} \left(\alpha - \beta - (\sin\alpha - \sin\beta) \right), \tag{4.12}$$

where a is the semi-major axis of the wanted transfer ellipse and Δt the TOF as defined in Equation 4.7. GM is the standard gravitational parameter which consists of the gravitational constant times the mass of the central body which is the sun in the examples of Figure 4.4.

Unfortunately, in this equation, Δt is clearly defined for a given semi-major axis a, but in the case of Lambert's Problem, Δt is given, and we are searching for the corresponding a. According to Fasoulas and Messerschmid (2009), the equation cannot be solved analytically in this situation and must be solved numerically. There are several numerical methods to solve Lambert's Equation, and Peet (2023) suggests the following:

1. Newton Iteration
2. Series Expansion
3. Bisection

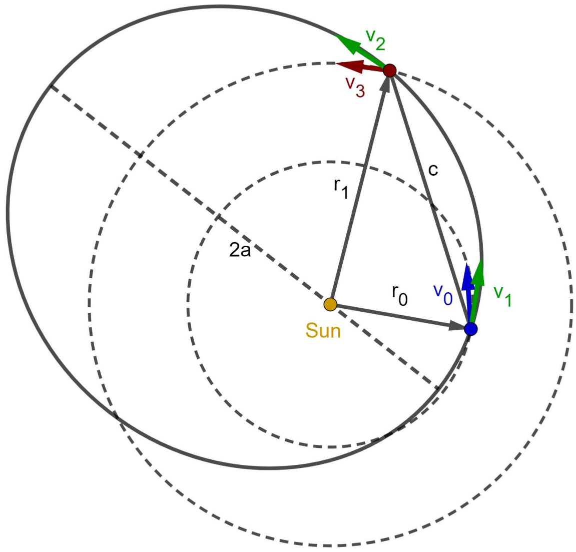

Figure 4.4: Geometric relation between the departure position r_0 at time t_0, the arrival position r_1 at time t_1 and the chord c of the triangle. Additionally four velocity vectors v_0, v_1, v_2 and v_3 are shown. In this image, v_0 is the original velocity on the initial orbit and v_1 the target velocity of the transfer ellipse, v_2 is the arrival velocity of the spacecraft and v_3 the target velocity. *Credit: Credit: Own work, created using GeoGebra [https://www.geogebra.org/calculator]*

Besides these, there are several other algorithms, each with its own advantages and disadvantages. Today, computational speed and accuracy are likely the most important factors when selecting a numerical algorithm.

In Izzo (2015), the problem was revisited, and the author suggested a new algorithm for solving the Time of Flight. Izzo introduced a new variable representing all problem classes, which is used to express the TOF equation. In this new formulation, the time of flight curves have two oblique asymptotes, which are mostly approximated by piecewise continuous lines. Additionally, he provided a new first-guess method to reduce the overall iteration time.

In de la Torre Sangrà and Fantino (2021), nine different numerical Lambert solvers were analyzed, and it was concluded that the Izzo (2015) algorithm 'exhibits the best ratio between speed, robustness, and accuracy.' For that reason, and due to its ability to include multi-revolutions in the algorithm, we selected it for our calculations.

4.2.4 Computing the Velocity Vectors

Once the semi-major axis for the given Time of Flight is determined, the full ellipse is defined. With this, the Izzo (2015) algorithm calculates four velocity vectors, which are required for determining the two impulsive maneuvers and the Δv demand. These four vectors are:

1. v_0: initial velocity on initial orbit at $\vec{r_0}(t_0)$
2. v_1: departure velocity on transfer ellipse also at $\vec{r_0}(t_0)$
3. v_2: arrival velocity on transfer ellipse at $\vec{r_1}(t_1)$
4. v_3: target velocity on target orbit also at $\vec{r_1}(t_1)$

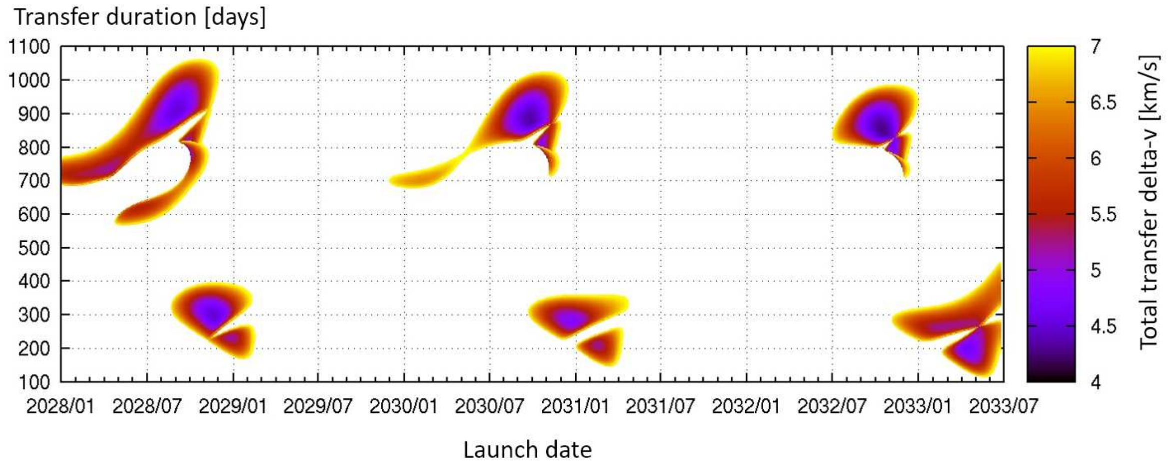

Figure 4.5: Contour or Porkchop Plots for a Earth-Mars Transfer as used for Mission Analysis during DePhine Concept Development. The x-axis gives all possible launch dates between the years 2028 and 2033. On the y-axis, the required cruise time is shown. The map itself consists of islands with different Δv demands. All transfers with a Δv demand higher than $7km/s$ are not shown. Note: The islands with transfer duration of 400 days or less are direct transfers, while the ones with 600 days and more include more than one revolution about the sun. *Credit: Own work as used for the Dephine mission definition.*

The four vectors and the transfer ellipse are shown in Figure 4.4. With the Equation 4.2 it is now possible to determine the overall Δv demand:

$$\Delta v = |\vec{v_1} - \vec{v_0}| + |\vec{v_3} - \vec{v_2}| \tag{4.13}$$

4.2.5 Visualization of the Results

Once all previous steps of solving Lambert's problem are complete, a solution for an orbit connecting two points in space at given times is found. The resulting Δvs provide the overall demand for this specific trajectory. All steps are then repeated for different launch dates and different arrival dates. Consequently, the departure and arrival time space is scanned, typically with equidistant time steps of 1 or 2 days. For each departure-arrival time combination, a total Δv demand is determined and plotted on a map, typically as contour or color-coded information (Burke et al., 2010).

The resulting plot is a contour plot with the x-axis representing the departure date and the y-axis representing the arrival date or alternatively the transfer duration (see Figure 4.5). This contour plot is also called a porkchop plot and shows curve levels of equal Δv or characteristic energy (C3).

During the development of Phodex and Dephine, we also considered not only the direct transfers from Earth to Mars but also those that include an additional revolution around the Sun. In Figure 4.5, the three areas above 600 days of transfer duration represent the solutions for these additional revolutions. Although these transfers last approximately 400-700 days longer, they offered partially better Δv demands at the cost of longer operation times. However, this longer transfer also allowed for possible flyby scenarios at the Martian Trojans, which are presented in Chapter 6.

4.3 Numerical Integration

At the department of planetary geodesy, a numerical integrator has been developed for solving trajectories of planets, asteroids, particles, or spacecraft in space (Hussmann et al., 2012; Höschele, 2022; Benedikter et al., 2022; Wickhusen et al., 2022a). This integrator is able to solve the equations of motion and was used to simulate orbits around asteroids, particularly for the Triple Asteroid paper (Section 5) and for verification of the results in the Martian Trojan paper (Section 6).

The integrator solves the equations of motion using SPICE. SPICE is a toolkit provided by Navigation and Ancillary Information Facility (NAIF) and was built to assist scientists and engineers involved in modeling, planning, and executing activities needed to conduct planetary exploration missions (Acton, 1996; Acton et al., 2018). We used the toolkit to retrieve solar system data, such as ephemerides, reference frames, and planetary constants. With this data, a precise simulation of small bodies or spacecraft in the solar system is possible by solving the following equation of motion (Montenbruck and Gill, 2000):

$$\ddot{\vec{r}}(t) = -\frac{GM}{r^3}\vec{r}(t) + \ddot{\vec{r}}_{ht}(\vec{r},t) + \sum_{sb}\ddot{\vec{r}}_{sb}(\vec{r},t) + \ddot{\vec{r}}_{srp}(\vec{r},t) + \ddot{\vec{r}}_{drag}(\vec{r},\dot{\vec{r}},t), \tag{4.14}$$

where $\vec{r}$ is the position of the body or spacecraft relative to the center of gravity of the main body, $\dot{\vec{r}}$ is the spacecraft's velocity, and $\ddot{\vec{r}}$ is its acceleration, respectively. The gravity caused by the main attractor is given by the GM value, representing the body as a point mass. The second term $\ddot{\vec{r}}_{ht}$ in equation 4.14 accounts for deviations from the spherical gravity field of the main body (higher-order terms). Perturbing gravity forces caused by other bodies besides the main body are represented by the third term $\ddot{\vec{r}}_{sb}$. The position of these bodies is typically extracted from the DE421 SPICE kernel for each given time step (Folkner et al., 2014). The penultimate term of the equation, $\ddot{\vec{r}}_{srp}$, represents the solar radiation pressure, which is of high importance when the mass of the primary body is relatively small, while the last term $\ddot{\vec{r}}_{drag}$ accounts for atmospheric drag.

Depending on the given constraints of the mission, some terms can be neglected and not included in the calculation. For the calculation of stable orbits around the triple asteroid $2001SN_{263}$ (see Chapter 5 atmospheric drag was neglected, but solar radiation pressure was of high importance. On the other hand, during the simulation of our Low-Mars-Orbiter proposal (see section 4.4.4), atmospheric drag was highly significant, while solar radiation pressure had a negligible effect.

This equation of motion (Equation 4.14) is a differential equation. An analytical solution is currently not available, so it must be solved numerically. For that, different numerical methods are included in the integrator software. We primarily used an explicit Runge–Kutta method of the eighth order after Dormand and Prince, as well as an implicit Adams multi-step method (Hussmann et al., 2012). Both methods were suitable for the given problems, and the results did not depend on a specific choice of integration method.

4.3.1 Higher-Order Terms of the Gravity Field

The gravity of a main attractor is typically not a point mass but an inhomogeneously distributed field, where regions with higher density and mass cause stronger acceleration than others. For a first approximation around Earth or Mars, the point mass approach is usually sufficient. However, for more complex problems, such as orbits around asteroids or when flying very close to the main body, a complex gravity field can have a significant impact on the results. The following section explains the implementation of the gravity model.

The gravitational potential U of a body's mass distribution affects the spacecraft depending on its location. The location of the spacecraft is expressed in geographic coordinates (distance r, latitude ϕ, longitude λ) with respect to the center of gravity. The formula used in the equation of motion 4.14 is provided by Montenbruck and Gill (2000) and Scheeres (2012):

$$\ddot{\vec{r}}_{ht} = \nabla U = \frac{\partial U}{\partial r}\vec{u}_r + \frac{1}{r}\frac{\partial U}{\partial \phi}\vec{u}_\phi + \frac{1}{r\cos\phi}\frac{\partial U}{\partial \lambda}\vec{u}_\lambda, \tag{4.15}$$

with

$$U(r,\phi,\lambda) = \frac{GM}{r}\sum_{n=0}^{\infty}\sum_{m=0}^{n}\frac{R^n}{r^n}P_{nm}(\sin(\phi))(C_{nm}\cos(m\lambda) + S_{nm}\sin(m\lambda). \tag{4.16}$$

In Equation 4.15 $\vec{u}_r, \vec{u}_\phi$, and $\vec{u}_\lambda$ denote the unit vectors of the r, ϕ, λ basis of the body-fixed spherical coordinates. The unit vector $\vec{u}_r$ points along the radius vector of the satellite, $\vec{u}_\phi$ in the direction of increasing north and $\vec{u}_\lambda$ in the direction of increasing east. The gravitational potential of the planetary body is then represented through spherical harmonics in Equation 4.16, where GM is again the gravitational constants times the mass of the body and R denotes its normalized radius (e.g. the mean radius). C_{nm} and S_{nm} are spherical harmonic coefficients (or Stokes coefficients) of degree n and order m. P_{nm} are the Associated Legendre Functions that can be defined by the closed-form relationship (Scheeres, 2012):

$$P_{nm}(\sin\phi) = \cos^m\phi\sum_{i=0}^{\frac{n-m}{2}}\frac{(-1)^i(2n-2i)!}{2^n i!(n-i)!(n-m-2i)!}\sin^{n-m-2i}\phi. \tag{4.17}$$

4.3.2 Perturbations by Secondary Bodies

Secondary bodies, which are included as perturbers in the numerical integration, are simulated as point masses and are implemented similarly to the primary body as GM_{body}, where M is the mass of each corresponding body. Perturbations by these secondary bodies can have a strong effect on orbital stability. This is especially the case when the primary body, which the spacecraft is intended to orbit, has a relatively low mass compared to the perturbing body and is in the vicinity or sphere of influence of this perturbing body. Moons in orbit can be particularly affected by this circumstance. Here, I want to highlight two studies where the orbit of a spacecraft around a moon became unstable due to the strong perturbing forces of the planet.

In the first case, I investigated orbits around the Martian moons Phobos and Deimos. Due to the relatively low mass of these moons and their short distance to Mars (see Table 2.3), only so-called Quasi-Satellite Orbits (QSO) were found to be stable. I conducted numerical scans of these orbits and found several solutions suitable for the PhoDEx (Oberst et al., 2016) and DePhine missions (Chapter 7). Details about the calculations can be found in Section 4.4.1.

The second case is the simulation of spacecraft orbits around Enceladus, one of Saturn's moons. In this study, we also searched for stable orbits around the moon. Here, similar to the moons of Mars, the perturbing planet (Saturn) is too close and has a gravity field that is too strong for orbits to be stable around the moon at high inclinations. However, unlike Phobos and Deimos, Enceladus is a larger body with a radius of approximately 250 km. Nevertheless, for a spacecraft with a semi-major axis of 500 km, the gravitational perturbation force caused by Saturn is only about one order of magnitude weaker than the force caused by Enceladus's GM. The orbits became unstable within a relatively short time frame, and the goal was to find stable periodic with comparably high inclinations (Benedikter et al., 2022). Details are given in Section 4.4.3.

4.3.3 Solar Radiation Pressure

Solar radiation pressure results from the Sun's electromagnetic radiation exerting a force on objects in space. This force can cause acceleration and is considered a non-conservative force acting on surfaces. When light is received, it transfers its momentum to the body, and the outcome depends on whether the light is absorbed or reflected. Most surfaces have a specific ratio of absorption and reflection, with some surfaces having a higher tendency to reflect light and others to absorb it. In calculations, it is important to consider the reflectivity of a surface, as a partially reflective surface would require multiplying the force by its reflectivity (Fortescue et al., 2005).

In our papers, we used typical reflectivity values of 0.8 for high-reflecting surfaces (such as Multi-Layer Reflective Insulation (MLI)) of the main body and 0.058 for low-reflective solar panels (Leem et al., 2013). In our models we consider only specular reflection of solar photons; diffuse reflection is neglected.

Due to this solar radiation pressure, the space probe experiences a force which perturbs its orbit and orientation. The acceleration $\ddot{\vec{r}}_{sb}$ caused by solar radiation pressure for a plane surface reflecting

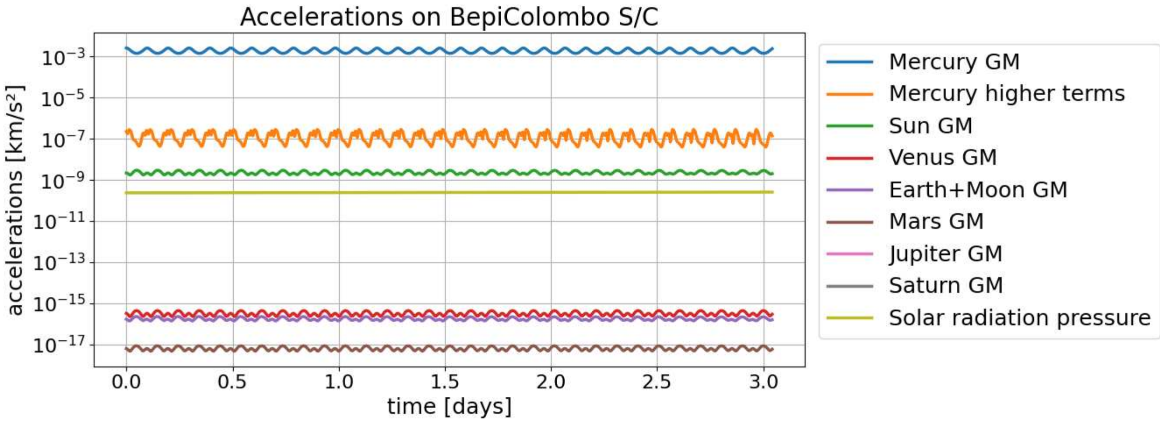

Figure 4.6: Overview of simulated acceleration acting on the BepiColombo spacecraft model in orbit about Mercury. The time frame was chosen such, that the spacecraft does not enter the shadow of Mercury. *Image is own work with data and model as published in (Höschele et al., 2021)*

one fraction and absorbing the other fraction of the incoming light is given by Montenbruck and Gill (2000):

$$\ddot{\vec{r}}_{srp} = -\nu P_{ref}\left(\frac{1AU}{d_{sun}}\right)\frac{S}{m_{sat}}\cos\theta[(1-\epsilon)\vec{e}_{sun} + 2\epsilon\cos(\theta)\vec{n}] \tag{4.18}$$

where ν is the shadow function ($\nu = 0$: umbra, $\nu = 1$: sunlight, $0 < \nu < 1$: penumbra), $P_{ref} = 4.56 \times 10^{-6}\,\mathrm{Nm}^2$ is the solar radiation pressure at 1 AU, d_{sun} is the distance from the surface to the Sun, S is the surface area, m_{sat} is the space probe's mass, θ is the illumination angle, ϵ is the reflectivity of the surface, $\vec{e}_{sun}$ is the direction to the Sun, and $\vec{n}$ is the surface normal.

The shadow function $\nu = 1 - A/(\pi a^2)$ has to be calculated for the given spacecraft position and the constellation of celestial bodies considered. The area A is the occulted segment of the Sun, and a is the apparent diameter of the Sun. The constellation of bodies is calculated using SPICE routines at the given epoch. The solar radiation pressure, which has to be computed at every time step, depends on the absolute distance to the Sun and on the mass-to-area ratio of the spacecraft.

For large bodies, the effect of solar radiation pressure is negligible. The acceleration caused by the gravity of the main body in these cases is several orders of magnitude higher than the solar radiation pressure. However, for small bodies such as asteroids with diameters of only a few kilometers, solar radiation pressure becomes a very important disturbance that must be taken into account during orbit calculation. This fact is illustrated in Figures 4.6 and Figure 5.2. In Figure 4.6, the accelerations on the BepiColombo spacecraft are simulated. It can clearly be seen that the force caused by the central GM of Mercury is by far the strongest and approximately 4-6 orders of magnitude higher than the accelerations caused by the higher-order terms of Mercury's gravity field and the GM of the Sun. Although Mercury is the planet closest to the Sun, the accelerations due to solar radiation pressure are approximately 7 orders of magnitude lower and have an almost negligible effect.

In contrast to BepiColombo in orbit around Mercury, a spacecraft in orbit around a small body such as 2001 SN_{263} is strongly perturbed by solar radiation pressure. As shown in Figure 5.2, the solar radiation pressure in this case is the second largest acceleration and only one order of magnitude less than the central GM of the asteroid. In such a case, the nominal orbit can become unstable quickly, and only Self-Stabilized Terminator Orbits could allow a stable orbit solution (for details, see Section 4.4.5).

4.3.4 Perturbations by Atmospheric Drag

A very strong non-gravitational perturbation acting on a spacecraft can be caused by the atmosphere of a planet. Depending mainly on the atmospheric density and the altitude of the Spaceraft (S/C), a dominant atmospheric force, called drag, acts in the opposite direction of the spacecraft's velocity. In our simulations, we used the following formula for modeling atmospheric drag (Mostaza Prieto et al., 2014):

$$\ddot{\vec{r}}_{drag}(r) = -\frac{1}{2}\rho(r) \times \dot{\vec{r}}(r)^2 \times C_D \frac{A}{m}. \tag{4.19}$$

Here, $\ddot{\vec{r}}_{drag}$ denotes the acceleration acting on the spacecraft, r is again the distance of the spacecraft to the center of mass, and $\rho(r)$ the atmospheric density at that altitude. The orbital velocity of the spacecraft at the corresponding altitude is given by $\dot{\vec{r}}$. The drag coefficient C_D represents the resistance of the spacecraft body to the atmosphere and is influenced by factors such as the shape and material of the spacecraft surface, as well as gas-surface interaction. Finally, A/m represents the cross-sectional area-to-mass ratio of the spacecraft.

While the orbital velocity, mass, cross-sectional area, and drag coefficient of a spacecraft can be predicted with reasonable accuracy, the density of a planet's atmosphere is much harder to forecast. In fact, according to Höschele (2022), the atmospheric density of Mars at an altitude of 150 km can vary between $[10^{-11}; 10^{-9}]\ \frac{kg}{m^3}$, resulting in a difference of almost a factor of 100 in acceleration.

As a result, an accurate model of the aerodynamic forces experienced by a spacecraft in the Martian atmosphere cannot be developed due to imprecise knowledge of the physical properties of the atmosphere, as well as the interaction of neutral gas and charged particles with the spacecraft's surface, as mentioned in Höschele (2022).

In this case, we focused on the best, worst, and average cases in order to create a reasonable scenario for flying a spacecraft in low Mars orbit. This scenario was then used to present our Low Mars Orbiter concept in Wickhusen et al. (2018) and to publish the results as the "Planetary Polar Explorer" in Oberst et al. (2022). More details can be found in Section 4.4.4.

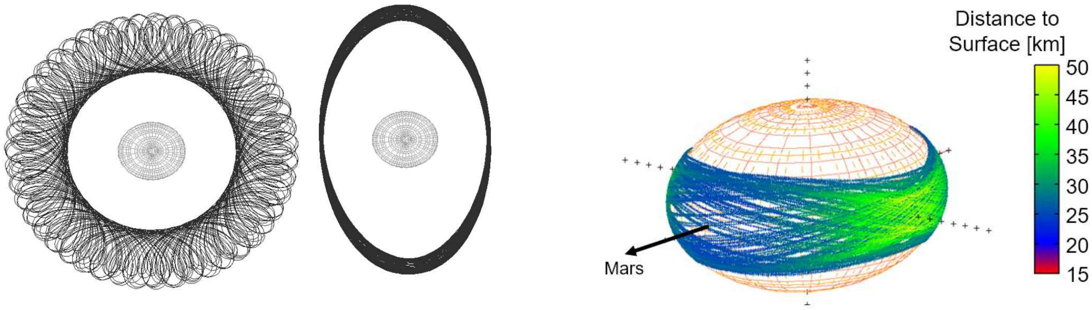

(a) Left: A Quasi Satellite Orbit about Phobos in an inertial Reference Frame. Right: The same orbit shown the Phobos Co-Rotating References Frame.

(b) Ground Track of the Same Quasi-Satellite Orbit, Shown on the Surface of a 3-Axial Ellipsoid Model of Phobos.

Figure 4.7: Different Views on a Quasi-Satellite Orbit Around a 3-Axial Ellipsoid Model of Phobos. *Credit: Own work*

4.4 Orbits in Strongly Perturbed Environment

4.4.1 Quasi-Satellite Orbits (QSO)

Objects in a Quasi Satellite Orbit (QSO) move in a specific 1:1 mean-motion resonance, in which the object librates around the longitude of its associated body. In simple terms, a body and its Quasi Satellite (QS) orbit a larger body and share the same semi-major axis but have slightly different eccentricities. In this way, both objects can remain in resonant motion around the main body (Mikkola and Innanen, 1997; Wiegert et al., 2000).

QSOs are a special form of the circular restricted three-body problem. These orbits are often chosen when the mass of the body to be orbited is too small in comparison to its primary body. In such cases, the perturbations by the larger body are too strong to allow nominal Keplerian orbits around the actual body. One of the most prominent examples of these QSOs is the Phobos/Mars constellation. An example of a QSO around Phobos is shown in Figure 4.7a.

Phobos orbits Mars at a distance of only 9378 km. It is a small body with principal axes radii between 9 and 13 km, and this small size results in a low mass of only 1.06×10^{16} kg. Comparing it to Mars, which has a mass of 6.4169×10^{23} kg, Mars is approximately 60 million times heavier than Phobos (Williams, 2023). This, combined with the small semi-major axis of Phobos, makes nominal Keplerian orbits around the moon impossible.

The case is similar for Mars' second moon, Deimos. Although it is farther away from Mars, its smaller size leads to comparable results.

For our mission proposals PhoDEx and DePhine, several scenarios were calculated in which the spacecraft would orbit Phobos or Deimos. In both cases, the only suitable solutions found were QSOs. The challenging part was the required high inclination of the orbits, which was intended to allow full coverage of the surface of Phobos and Deimos. Unfortunately, no stable orbit with a high inclination was found. The highest inclination found was approximately 45°.

In order to still allow full coverage of the poles, we included short impulsive maneuvers in the timeline, which enabled close flybys over the poles of Deimos. Due to the special situation in QSOs, these maneuvers required only a small amount of Δv. Details are given in Section 7.3.3.

4.4.2 Landing from QSO

As part of the PhoDEx and DePhine proposals, we also studied landing a small package the size of a shoebox on the surface of Phobos. The optimal lander for such a scenario would be a package similar to Mascot, in collaboration with DLR-Bremen, who were responsible for the development of Mascot (Ho et al., 2017).

I set up the constraints for landing a package on the surface and provided the orbital path and close flyby scenarios. The idea was to perform a small "braking" maneuver from the QSO around Phobos (see Figure 4.9). We developed this basic flyby landing concept already during the PhoDEx proposal (Oberst et al., 2014).

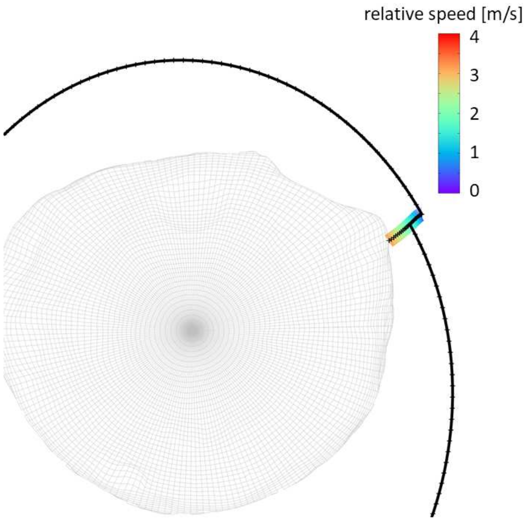

Figure 4.8: Landing Scenario for a Small Spacecraft on Phobos. The marker on the trajectory are one minute steps. *Credit: Own work with Phobos shape model provided by K. Willner (Willner et al., 2014) and published in (Grimm et al., 2020)*

After the proposal was not selected for further investigation, a more detailed plan for the flyby and landing concept was developed, which was then used as a reference case for the DePhine proposal. Unfortunately, the entire concept of landing a package on Phobos had to be removed due to the strict cost cap of an M-class mission (Oberst et al., 2016).

However, DLR Bremen remained very interested in the concept of landing a small package on Phobos, and a cooperation began. After several simulations, I found scenarios where only 5-7 m/s of Δv would be required for the braking maneuver and a close approach to the surface. During this close flyby, when the spacecraft reached the closest distance and the desired position above the surface, the spacecraft would perform a short braking maneuver to come to a full stop relative to the surface. The spacecraft would then immediately start falling towards the moon, but due to its low gravity, the entire fall would last more than 30 minutes before the spacecraft would hit the surface (see Figure 4.8) at a comparatively low speed of approximately $3^{m}/_{s}$.

In the resulting brake and release scenario, the spacecraft would have to perform three main actions in less than half of the falling time, i.e., in approximately 15 minutes:

1. reduce relative speed to zero (approximately $10^{m}/_{s}$)
2. release the landing package for a free fall landing
3. accelerate relative speed to original one (approximately $10^{m}/_{s}$)

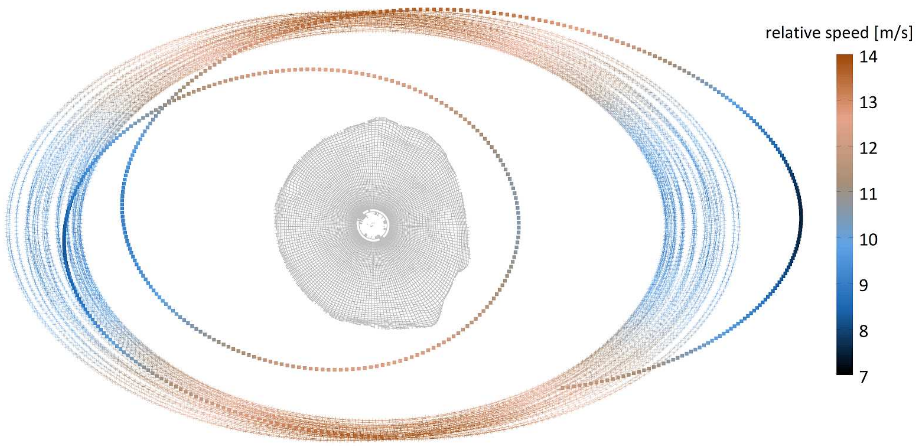

Figure 4.9: Close Flyby Maneuver from a Quasi Satellite orbit about Phobos. *Credit: Own work with Phobos shape model provided by K. Willner (Willner et al., 2014)*

By this, the spacecraft would almost return to the trajectory it was on during the close approach. My simulations showed that even small guidance and steering errors would not lead to a critical change in the trajectory and that it would be possible for the spacecraft to return to the original QSO with only one additional maneuver of approximately 7-20 m/s (Grimm et al., 2020).

4.4.3 Orbits about Enceladus

Compared to Saturn, Enceladus is a very small moon of roughly 500 km in diameter and orbits Saturn at a relatively short semi-major axis of $238400km$. Enceladus has a $GM = 7.2^{km^3}/_{s^2}$ which is very

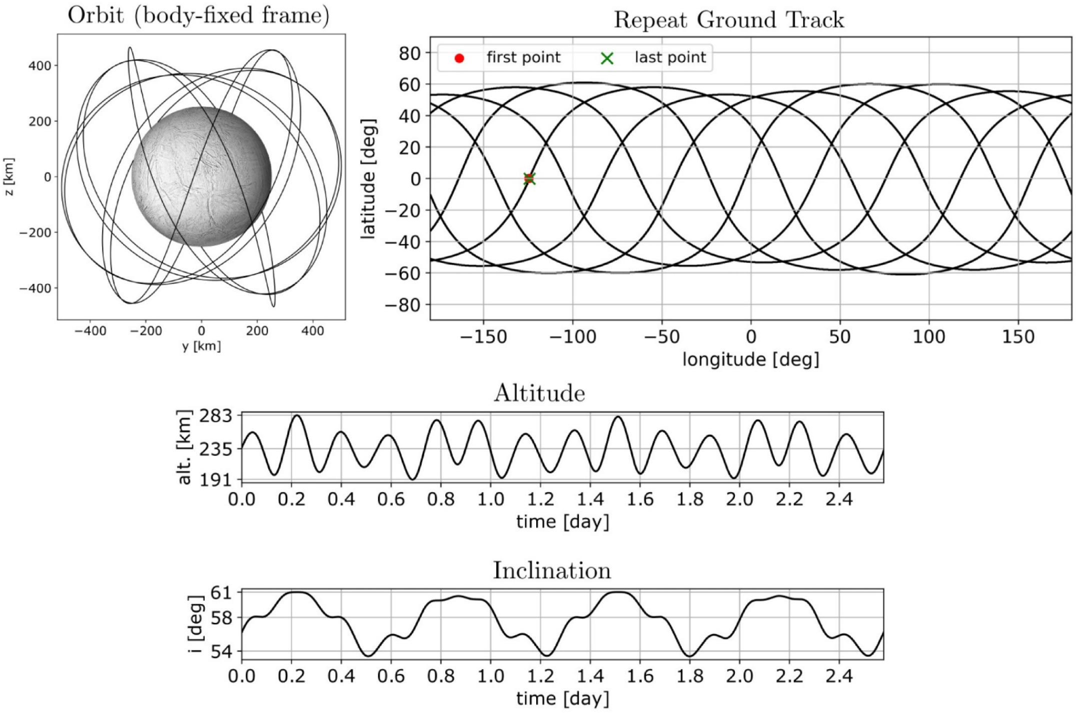

Figure 4.10: Repeat-Pass Orbit Around Enceladus with a mean inclination of approximately 58° and a mean altitude of 235 km, *Credit: (Benedikter et al., 2022)*

small compared to Saturn, which has a $GM = 3.8 \times 10^7 km^3/s^2$ (Jacobson, 2022).

Similar to orbits around Phobos and Deimos, nominal Keplerian orbits around this moon are not possible. However, similar to Quasi-Satellite Orbits around Phobos and Deimos, special stable orbits around Enceladus can be found. As already shown in the section about QSOs (4.4.1), orbits in the orbital plane of Enceladus around Saturn are possible, but inclinations of 60° or more lead to extreme instabilities. This so-called "Kozai mechanism" causes the spacecraft either to crash onto the surface of Enceladus or to leave its sphere of influence (Kozai, 1962; Benedikter et al., 2022).

Unfortunately, one of the most interesting regions on Enceladus is the south pole area, which is geologically very active, with plumes of water ice being injected into space (Spencer and Nimmo, 2013; Konstantinidis et al., 2014). A remote sensing or lander mission would therefore require a highly inclined or even polar orbit to investigate this region.

In the context of the EnEx[4] initiative, we searched for stable resonant orbits for radar applications (Benedikter et al., 2022). Besides the requirement to find orbits with high inclinations, we also had to look for resonant orbits. The interferometric and tomographic data acquisitions with radar required orbits with almost perfectly repeating ground tracks. In the paper, we used the same grid search strategy that we used in Hussmann et al. (2012) and Wickhusen et al. (2022a) for identifying highly stable, periodic orbits that satisfy the repeating ground track requirement. The identified orbits provide sufficient inclination and long-term stability to sustain the required repeat characteristic for up to a few hundred days (Benedikter et al., 2022). A resulting orbit is shown in Figure 4.10.

On the 25th of March 2024, and by coincidence one day after this section was written, ESA announced their plan to go to Enceladus with the very first planetary L-class mission of the new Voyage 2050 program (ESA Media Relations, 2024). The circumstances and more details about this new Enceladus mission are discussed in Chapter 8.

[4]The Enceladus Explorer (EnEx) space mission is to search for extraterrestrial life on Saturn's moon Enceladus. Scientists and engineers in the Enceladus Explorer Initiative are therefore developing new technologies to make this mission possible.

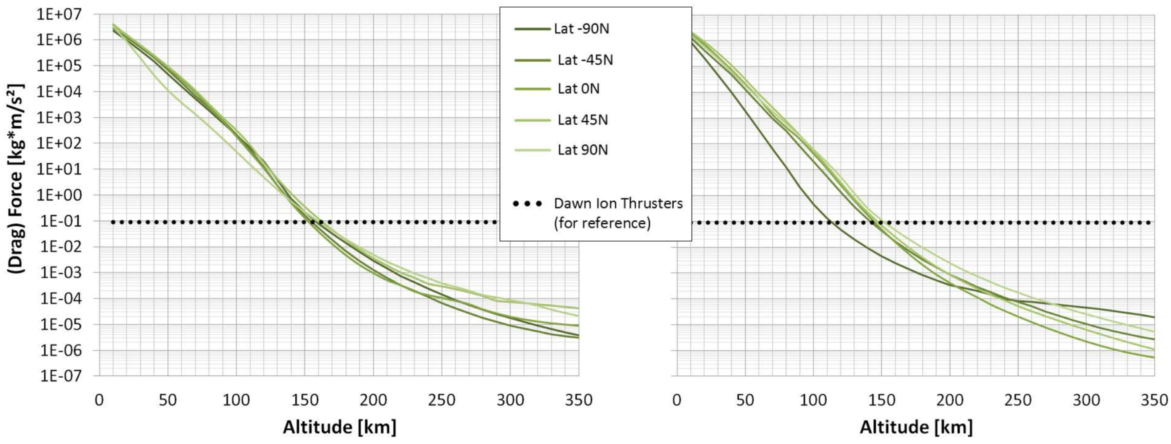

Figure 4.11: The Drag Force Caused by the Martian Atmosphere over Different Altitudes. For comparison, the possible force provided by the DAWN propulsion system is shown. The left Figure shows the drag at perihelion and the right Figure at aphelion. *Image is own work with data from Mars Climate Database ©LMD/OU/IAA/ESA/CNES Millour et al. (2018) and was presented at EPSC 2018 (Wickhusen et al., 2018).*

4.4.4 Continuous Drag Compensation by an Electric Propulsion System

In 2018, ESA launched a new Call for Ideas for the Voyage 2050 program. This new program is the successor to the highly successful Cosmic Vision program and is planned for missions in the time frame 2035-2050. In the context of this Call for Ideas, we designed a new mission proposal named "Planetary Polar Explorer" (Oberst et al., 2022).

The concept consisted of a Next-Generation Remote Sensing (ESA M-Class) mission to Mars, involving a spacecraft in circular Low Mars Orbit (LMO) ($\leq 150km$). One of the key technical aspects of the concept is the usage of an electric propulsion system. Besides the transfer to Mars,the propulsion system will also continuously compensate for the drag of the Martian atmosphere. This drag force acts in the opposite direction of the spacecraft velocity and decelerates the spacecraft. This "braking" leads to a continuous reduction of velocity and consequently of its altitude and lifetime. Similar to equation 4.19, this drag force F can be expressed by the formula (Montenbruck and Gill, 2000):

$$F(h) = \frac{1}{2}\rho(h) \times v(h)^2 \times C_D A, \tag{4.20}$$

where h represents the altitude of the S/C, ρ the density of the atmosphere and v the velocity of the spacecraft. The drag coefficient C_D represents the interactions of the spacecraft with the atmosphere while A is the cross-sectional area of the S/C.

The parameters C_D and A are primarily influenced during the construction of the spacecraft and can therefore be considered constant. We set $C_D = 2.0$, which is a conservative value according to Fortescue et al. (2005), and $A = 41\,\mathrm{m}^2$, which is the cross-sectional area of the DAWN spacecraft (Thomas et al., 2011b). The different cross-sectional areas due to different attitudes are neglected for the moment. It should be noted that we selected the DAWN spacecraft as a reference because it has an electric propulsion system capable of delivering 91 mN.

The resulting drag force depends then only on the altitude of the spacecraft. For the proposal we used a standard density model of the upper Martian Atmosphere, which is defined by (Fortescue et al., 2005):

$$\rho(h) = \rho_0 \times \mathrm{e}^{h/H}, \tag{4.21}$$

where $\rho_0 = 0.02{}^{kg}/{}_{m^3}$ is the reference density and $H = 11.1$ km is the scale height (Williams, 2023). The velocity can easily be determined using the vis-viva equation (Fortescue et al., 2005):

$$v(h) = \sqrt{GM \times \left(\frac{2}{r} - \frac{1}{a}\right)}, \tag{4.22}$$

where GM is the standard gravitational parameter of Mars (for the mass of Mars, see Table 2.1), $r = r_{mars} + h$ is the distance of the spacecraft to the center of mass, and a is the semi-major axis.

With these equations, we had a fully analytical solution, which showed the expected results. By lowering the altitude, the velocity increased as well as the atmospheric density. However, the effect of both was very different. For a spacecraft altitude between 100 km and 200 km, the spacecraft relative velocity varies only slightly between 3.5 km/s and 3.45 km/s. The density, on the other hand, decreases exponentially with increasing height (Wickhusen et al., 2018; Oberst et al., 2022).

However, we realized that the simple density model was not truly representative of the Martian atmosphere, so we considered a more realistic numerical model provided by the Mars Climate Database (MCD). Using these values, we were able to calculate the minimum possible altitude that could be compensated by the DAWN electric propulsion system to be $h = 150\,\text{km}$. Details of the results are given in Figure 4.11.

4.4.5 Self-Stabilizing Terminator Orbits

In astronomy, the terminator is a closed line that separates the day and night sides of a planetary body. This line moves across a body as it rotates. For spherical bodies, this line is a circle that has the same angular period as the synodic day of the body. For Earth, in its body-fixed reference frame, the mean angular movement of the terminator is exactly 24 hours (Meeus, 1997).

However, during Earth's movement around the Sun, the terminator also follows the Sun. Considering the basic geometry of the terminator, the plane of the terminator circle is perpendicular to the incoming radiation. Therefore, the plane will make one full 360° rotation over one year.

In order to follow the rotation of the terminator over one year, a spacecraft needs to fly in an orbit where the longitude of the ascending node is not fixed inertially but rotates. In other words, it requires a nodal precession of 360° per year. For Earth, this is achieved by taking advantage of the J_2 effect. This effect, caused by the second-degree spherical harmonic coefficient J_2 (or C_{20}, see Section 4.3.1), describes the oblateness of the central body and leads to a drift of the longitude of the ascending node. These orbits are the well-known sun-synchronous orbits, although they do not lie in a plane perpendicular to the incoming radiation (Chobotov, 2002; Montenbruck and Gill, 2000).

Terminator orbits around small bodies, such as asteroids, work a little differently. The requirement remains the same: the orbital plane of the spacecraft needs to have the same rotational rate as the precession of the terminator. However, due to the small mass and often irregular shape of small asteroids, the spacecraft cannot take advantage of the J_2 effect. Furthermore, the incoming solar radiation is relatively strong compared to the mass of the asteroid. As explained in Section 4.3.3, the Solar Radiation Pressure (SRP) can have a significant impact on the orbit of a spacecraft, especially when the gravity of the main body is very weak. This is typically the case for asteroids with diameters in the range of a few kilometers (see acceleration diagram in Figure 5.2). The SRP in these cases causes a very strong perturbation, which often results in the spacecraft either crashing onto the surface or escaping from its sphere of influence (Scheeres, 1999).

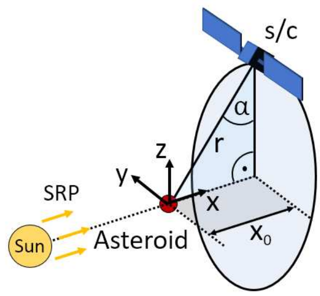

Figure 4.12: Sketch of Terminator Orbits Around Small Asteroids. x_0 denotes the small offset away from the center of gravity and α is the displacement angle. *Sketch is own work*

To compensate for this, flying in a terminator orbit around small bodies is often the only way to place a spacecraft in a stable orbit. Here, the J_2 effect is counteracted by the solar radiation pressure, which acts as a continuous non-conservative force on the orbit. It leads to a continuous offset of the orbital plane from the center of gravity. This displacement in the anti-sunward direction, x_0, is shown in Figure 4.12 and can be calculated with the following formula (Bookless and McInnes, 2006):

$$x_0 = \frac{a_{srp}}{GM} r^3, \tag{4.23}$$

where a_{srp} is the acceleration of the spacecraft caused by the solar radiation pressure. The distance from the center of mass of the asteroid to the spacecraft is given by r, and the product of the asteroid's mass and the gravitational constant is given by GM.

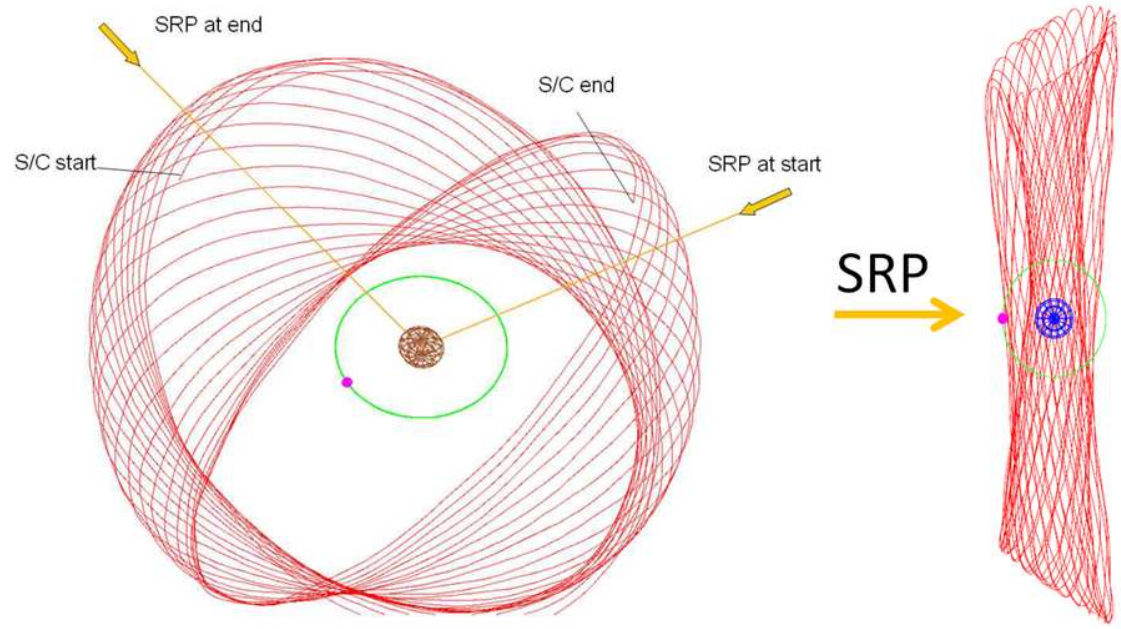

Figure 4.13: Self-Stabilized Terminator Orbit Around Binary Asteroid 1996FG_3, left: orbit in inertial reference frame, right: same orbit in co-roating reference frame with x-axis always pointing towards the sun and consequently in opposite direction of the solar radiation pressure and y-Axis pointing in flying direction. *Image is own work, taken from (Wickhusen et al., 2012) and published in (Hussmann et al., 2012)*

During our search for stable orbits around the asteroids 1996 FG_3, (162173) Ryugu, and (101955) Bennu in support of the Marco-Polo-R mission proposal, only terminator orbits in the vicinity of the asteroids were found that fulfilled the requirements and constraints. The resulting reference orbit from the study is shown in Figure 4.13 in both inertial and co-rotating reference frames (Wickhusen et al., 2012; Hussmann et al., 2012).

The same approach in search for stable orbits was then also followed for the Brazilian space mission ASTER to the triple Asteroid 2001 SN_{263}. By applying the same methods developed during my studies for terminator orbits about the binary 1996 FG_3, we could easily identify the pertubation strengths caused by the secondary and tertiary body and the solar radiation pressure. The results were published in Wickhusen et al. (2023) and are included in this thesis in section 5.

Chapter 5

Terminator Orbits around the Triple Asteroid 2001-SN263 in Application to the Deep Space Mission ASTER

Research Paper I

Published version, 2022 in Acta Astronautica
https://doi.org/10.1016/j.actaastro.2022.06.029

Kai Wickhusen [a], Antonio G.V. de Brum [b], Friedrich Damme [c],Alexander Stark [a], Jean-Baptiste Vincent [a], Hauke Hussmann [a], Jürgen Oberst [c]

a. German Aerospace Center (DLR), Institute of Planetary Research, Rutherfordstr. 2, D-12489, Berlin, Germany

b. Federal University of ABC, SBC, São Paulo, Brazil

c. Technical University Berlin, Institute of Geodesy and Geoinformation Science, Strasse des 17. Juni 135, D-10623 Berlin, Germany

Abstract

We search for stable orbits in the vicinity of the triple asteroid system, 2001-SN263, which will be target of the deep space mission ASTER, currently under study by the Brazilian space agency (AEB). Our numerical simulations include gravitational forces caused by the three bodies of 2001-SN263, higher-order terms of the primary's gravity field, planetary perturbations and solar radiation pressure. Due to the low gravity of the triple system, the spacecraft's motion becomes complex and the faint gravity forces of the secondaries are exceeded by radiation pressure from the Sun. However, we show that the so-called "terminator orbits" within the asteroid system at distances between 6-10 km to the primary body can be found. A spacecraft parked in such orbit will stay within the system for several months without the need to adjust its trajectory. Additionally, these stable orbits will allow investigating the entire primary body including its poles as well as the two secondary bodies. We also show that a laser altimeter, which is part of ASTER's primary payload, will benefit significantly from these terminator orbits.

5.1 Introduction

The inner Solar System is populated by a large number of small bodies, the Near-Earth Objects (NEOs), approaching or crossing the orbits of the terrestrial planets. More than 28,000 NEOs have already been discovered and hundreds of new ones are discovered each year (IAU, 2022b). These

objects are believed to be remnants from the formation of the Solar System about 4.6 billion years ago. Some NEOs follow trajectories, which cross Earth's orbit – and can possibly collide with our planet. Depending on their size and velocity, such collisions may have dramatic consequences for Earth's ecological system or the human population (Gritzner et al., 2006; Rumpf et al., 2017). It is obvious that our knowledge on the physical properties, the dynamics and evolution of NEOs is critical.
Much knowledge about the structures and dynamics of NEOs can be obtained from multiple NEO systems. A large fraction of the NEOs (15%) are binaries, i.e., systems featuring a primary object orbited by a smaller secondary (Margot et al., 2002; Fang and Margot, 2012; Margot et al., 2015). While the origins of such binaries are still being discussed, their formation can be explained if the asteroids in question are invoked to have "rubble pile" structures, implying that the asteroids consist of loosely bound material instead of monolithic structures. Small asteroids are observed to undergo a spin-up due to the YORP (YarkovskyO'Keefe-Radzievskii-Paddack) effect (Rubincam, 2000). With increasing spin, centrifugal forces may cause a disruption and release of particles that can then re-accrete to form one or several small satellites (Walsh et al., 2008). Alternatively, satellites may form by single catastrophic disruptions (Jacobson and Scheeres, 2011) . The YORP-effect in binary systems (termed BYORP) may also modify the asteroids' orbits within the system, leading asteroids to be locked in spin-orbit resonance (Ćuk and Burns, 2005). Also, tidal effects may be important. Tidal interaction between the primary and secondary may affect the semi-major axes and eccentricities of the orbits resulting in the secondary's escape or tidal decay (e.g.(Walsh and Jacobson, 2015)). Tidal disruption during close planetary encounters may support the formation of binaries or multiple asteroid systems (Margot et al., 2002) – or it may be responsible for disruption of the system. A combination of the YORP or BYORP effects, chaotic orbital evolution and tidal effects can lead to the formation of unique triple systems (Jacobson and Scheeres, 2011), which may reveal even more information about the formation of multiple NEOs.
The first identified triple asteroid 2001 SN263 was discovered in 2001 and initially classified as a binary system. In 2008 the "Amor-type" object (approaching the Earth's orbit without crossing it) was observed by the planetary radar station of Arecibo, in Puerto Rico, which led to the discovery that 2001 SN263 was in fact a triple system (Nolan et al., 2008). This was the first triple NEO known at that time. In 2009, a second triple system, 1994 CC, was identified (Brozović et al., 2011). Furthermore, in 2017 the NEO 3122 Florence was identified as the third triple system, when it had an Earth flyby (see: NASA, JPL Center of Near Earth Object Studies (CNEOS): Radar reveals two moons orbiting asteroid Florence, Sep 1, 2017).
The analysis of the observational data of 2001 SN263 (Becker et al., 2015; Becker et al., 2009) suggested that the primary is approximately a spheroid with an equivalent diameter of about 2.6 km ($2.8 \times 2.7 \times 2.5$ km) and smaller companions, about 700 m and 430 m in diameter orbiting at distances of 16.6 and 3.8 km, respectively. Here, we follow the nomenclature adopted by Fang and Margot (2012), referring to the central (most massive) body as Alpha, to the second most massive body as Beta and to the least massive body as Gamma.
Dynamical solutions for the two triple systems, 2001 SN263 and 1994 CC were presented by Fang and Margot (2012). Using numerical integrations of the N-body problem and radar observations as constraints, they derived the masses of the components, the J_2 gravitational harmonic of the central body, and orbital parameters of the satellites (Table 5.1).

The interest in the first identified triple system 2001 SN263 increased significantly when the Brazilian Space Agency (AEB, Agência Espacial Brasileira) announced ASTER, a rendezvous mission to explore this unique target (Sukhanov et al., 2010; Macau et al., 2011). Besides being Brazilian's first deep space mission it will also be the worldwide first mission to a triple asteroid system (Brum et al., 2021).
Several Missions to NEA's such as Hayabusa and Hayabusa 2 have be successfully completed in the last years (Tsuda et al., 2013; Yano et al., 2006). The OSIRIS-Rex mission has successfully completed its science operation in the vicinity of (101955) Bennu and is currently on its way back to earth (Lauretta et al., 2017). New mission such Dart and Hera are currently developed or are already on the way to their target and will be the first rendezvous missions to a binary system (Cheng et al., 2018).
Hayabusa 1, Hayabusa 2 and Osiris-Rex consisted of remote sensing phase where the asteroids were studied from different hovering and fly-by positions. After studying the asteroids remotely, the spacecrafts left their safe hovering positions and approached the surfaces of their targets for short touch-an-go landing. The spacecrafts collected samples of surface materials and returned or will return

Table 5.1: Orbital elements and physical properties for the primary and secondaries for the 2001 SN263 system. Values for the secondaries are given with respect to the primary asteroid Alpha. Mass, mean diameter, and density are taken from Becker et al. (2015). Semi-major axis, eccentricity, inclination, argument of pericenter, longitude of ascending node, and mean anomaly at epoch, are all referred to MJD 54509 in the equatorial J2000 frame. Given errors are 1-σ formal errors. Following Fang and Margot (2012), we refer to the central (most massive) body as Alpha, to the second most massive body as Beta and to the least massive body as Gamma (regardless of orbit position). Rotation periods are taken from Becker et al. (2017). The J_2 values for Beta and Gamma were derived from their shapes assuming a homogeneous density distribution (see Section 5.3.2).

	Alpha (primary)	Gamma (inner)	Beta (outer)
mass, 10^{10} kg	917.466 ± 2.235	9.773 ± 3.273	24.039 ± 7.531
mean diameter, km	2.5 ± 0.3	0.43 ± 0.12	0.77 ± 0.14
mean density, g/cm^3	1.1 ± 0.2	2.3 ± 1.3	1.0 ± 0.4
J_2	0.013 ± 0.008	0.003	0.007
pole orientation (ecliptic):			
ecliptic latitude β, deg	309 ± 15		
ecliptic longitude λ, deg	-80 ± 15		
pole orientation (ICRF/J2000):			
right ascension α, deg	281.97		
declination δ, deg	-58.20		
semi-major axis, km		3.804 ± 0.002	16.633 ± 0.163
inclination, deg		165.045 ± 12.409	157.486 ± 1.819
argument of pericenter, deg		292.435 ± 53.481	131.249 ± 21.918
longitude of asc. node, deg		198.689 ± 61.292	161.144 ± 13.055
mean anomaly, deg		248.816 ± 11.509	212.658 ± 10.691
orbital period, days		0.686 ± 0.00159	6.225 ± 0.0953
rotation period, hours	3.4256 ± 0.0002	16.4000 ± 0.0004	13.4300 ± 0.0001

these samples back to earth safely (Tsuda et al., 2013; Yano et al., 2006; Lauretta et al., 2017). In contrast to these mission and due to the small size of the spacecraft and mission constraints, the science phase of the ASTER mission will consist only of two different remote sensing phases. During the first phase, the spacecraft will be in a hovering position at 50 km from the primary body. The second phase will consist of a terminator orbit phase with a very low demand for maneuvers. A touch down or even are sample return is not foreseen and would exceed the mission requirements.
The motion of the Aster spacecraft will become complex near the small asteroids system 2001 SN263, where the faint gravity forces are possibly exceeded by radiation pressure from the Sun. Additionally, the secondary bodies cause a strong perturbation when the spacecraft gets closer to the system. However, families of orbit-like motion models exist (McInnes, 1997), including the well-known "terminator orbits", where particles move in circular or slightly elliptic paths, with the orbit normal vectors in line with the Sun direction (Scheeres, 1999; Hussmann et al., 2012).The terminator orbits are members among a family of stable motion patterns, the so-called "Quasi-Terminator Orbits" (Bookless and McInnes, 2006; Giancotti et al., 2014). In 2013 Scheeres et al. (2013) showed that terminator orbits about the asteroid (101955) Bennu are possible and Hesar et al. (2017) determined the robustness against maneuver errors. Then, in 2019 Osiris-Rex entered a terminator orbit about a NEA for first time and proved that these orbits are not just theoretically feasible (Lauretta et al., 2017).
For the ASTER spacecraft, terminator orbits are an optimal solution to investigate the three bodies remotely from a relatively short distance. Additionally, staying in the terminator orbits will require no or very few maneuvers which reduces the demand for operations and propellant.
Several studies on orbits around the asteroid 2001 SN263 have been conducted in the last years. Prado (2014) considered in his model perturbations due to the oblateness of the main body, Alpha, the gravity field of the two satellite bodies, the Sun, the Moon, the asteroids Vesta, Pallas and Ceres and all the planets of the solar system, without taking the SRP (solar radiation pressure) into account. Their results show that, when compared to elliptical and equatorial orbits, an internal orbit is the best choice, especially when this orbit is circular and polar (less perturbed). Araujo et al. (2012, 2015) characterized stable regions around the components of this triple system. Through numerical integration they found two stable regions near Alpha and Beta, respectively, and another region, much beyond the satellites. In addition, retrograde orbits - even though not perfect for remote sensing -

were found to be stable. Also without considering the SRP, in their works they point out orbits that are approximately polar, circular and internal (region between Gamma and Beta) as favourable for a mission of exploration inside the triple system. The stability of orbits in the 2001 SN263 system has been investigated also using (semi-) analytical theories taking into account perturbations by solar radiation pressure (Masago et al., 2016; Silva Neto et al., 2016; Cavalca et al., 2017). More recently, Sanchez and Prado (2019) conducted a search for less-disturbed orbital regions to place a spacecraft around the system considering gravity forces and solar radiation pressure. Although they have not considered inclined orbits in this research (this subject is indicated for future studies), only planar ones, their results, presented as perturbation maps, show how the SRP dramatically changes the stability regions around the system. They also provide information on the consumption of propellant to keep a spacecraft as close as possible to a Keplerian orbit in those identified orbital regions. Obrecht et al. (2020) used evolutionary algorithms to search for stable orbits in the vicinity of the triple system. The authors solved a restricted four-body problem including the gravity attraction by Alpha, Beta and Gamma as well as the solar radiation pressure. Where applicable, the results of their work could be confirmed by our simulations, but a large range of additional solutions are presented in this paper.

In this study we search for stable orbits within the triple asteroid system 2001 SN263. In particular we investigate the possibility of moving in terminator orbits which are stable over a period of at least one month. The study focuses particularly on the mission ASTER and takes the requirements and constraints of the mission into account (Macau et al., 2011; Perna et al., 2014).

The paper is organized in 5 sections. In Section 5.2 we give details on the Aster mission, the triple asteroid system and terminator orbits. Section 5.3 summarizes the methods which were used to determine stable areas. In Section 5.4 we show the results, including stable areas with exemplary orbits and in the last Section 5.5 the implications of the derived results are discussed.

5.2 The ASTER Mission

The Brazilian space agency plans to launch a small spacecraft called "ASTER" to investigate the triple Asteroid 2001-SN263. The spacecraft will arrive at the asteroid in December 2024 (backup date: September 2027) and start its first science operation phase (Brum et al., 2021). During this first phase the Asteroid is observed from a larger distance at 50 km from Alpha. At the end of this phase, the spacecraft performs maneuvers to get into the system and is positioned on a stable orbit within the system, i.e. between the main and the outer body. During this second phase, maneuvers of the spacecraft shall be avoided. This requirement in combinations with the science requirements makes terminator orbits an optimal choice for this second phase.

To move safely within the system, it is critical for the spacecraft to identify and characterize regions of stability and instability (i.e., where collision or escape are imminent). Furthermore, observational and operational strategies to explore all three asteroids critically depend on availability of stable spacecraft orbits (i.e., orbits that do not requiring expensive correction maneuvers).

Besides the technological motivations, the main scientific goal is the unprecedented on-site characterization of this very interesting triple Asteroid. Inside the selected exploration window, a main exploration campaign is being planned to focus the investigations on the biggest asteroid (Alpha). In terms of scientific goals, the investigation will shed light on the formation of this triple system, and each of its main three asteroids will be separately investigated as to dynamic and orbital properties, shape, size, volume, mass distribution, mineral composition, surface topography and texture, gravitational field and rotation speed. The nominal science phase of the ASTER mission is planed to last for 4 month. Based on current design studies, the spacecraft will have a total launch mass of 150 kg (Goretov et al., 2018). The main body is a cube with side lengths of 0.5 m each and a total solar cell area of $20m^2$. The spacecraft model, which was used in the simulations is illustrated in Figure 5.1

5.2.1 The ASTER Laser Rangefinder

In 2011 a laser altimeter was selected to be part of the primary payload (Brum et al., 2011). The instrument was named ALR (ASTER Laser Rangefinder). The altimeter data to be collected by the ALR will be used to determine the morphology of the asteroids (sizes and shapes), essential for precise determination of their masses and densities. The instrument will acquire data for the characterization of the topographic features on the surfaces (craters, boulders, etc.). The topographic profiles to be constructed will be used in the production of digital elevation models of the surfaces with resolutions of about 10 m horizontal, and 10 m (altitude $D < 50$ km) to 1 m ($D \leq 10$ km) vertical, in illuminated and non-illuminated regions. A minimum of 50% coverage of the surface of the main body Alpha, is required for the main exploration campaign, when all attention is going to be focused on this asteroid. The instrument will also support the fine determination of the orbits and the modelling of gravitational parameters. As additional capacities, the instrument is planned to be also applicable in the navigation, supporting spacecraft maneuvers in the proximity phase, and in the calibration of other instruments (imaging camera and infrared spectrometer). A review of the ALR design can be found in Brum and Cruz (2017) containing a more elaborated description of the instrument configuration and the values of key parameters of its operation. To verify the performance in realistic scenarios the simulator software *ALR_Sim* for the environment and operation of the instrument was developed (Brum et al., 2015b,a). After a more complete characterization of all three bodies in the system was published (Becker et al., 2015), the planning of the mission was further enhanced (Winter et al., 2020; Brum et al., 2021). Modelling of the test trajectories, the joint dynamics and the operation of the instrument was made and integrated in simulator software *ALR_Sim_Tracks* specially created for this purpose.

5.2.2 Equatorial and polar coverage

A study on possible encounter trajectories for the first part of the science phase has been carried out by Brum et al. (2021). A favourable encounter trajectory at 50 km from the primary body was identified and characterized, together with predictions of the results (coverage) attainable by the ALR along this trajectory. The mentioned predictions show that a minimum of 58% coverage of the surface of Alpha can be achieved with superior quality (better than the minimum expected, in terms of vertical (less than 2 m) and horizontal (about 10 m) resolution, which are controllable through the insertion of a very small inclination in the encounter trajectory of the spacecraft, and through optimization of the laser pulse frequency). Although satisfactory, according to the science goals of the mission, the achieved results also indicate that the attainable coverage will focus mostly on central areas of Alpha (around its equator), leaving the regions around both poles unexplored. Additionally, simulations also show the unavailability of obtaining altimetry data of the poles from different positions inside any encounter trajectory in the scenario of this mission.

To ensure the coverage of the areas around the poles, a second complementary exploration campaign is discussed and proposed in this paper. Once the altimetry data of the poles in this second part of the main campaign is attained and added to the data acquired in the first part (central region), a global model of the asteroid surface could be built with improved quality. This will fulfil the main goal of the ALR with respect to asteroid Alpha in the main campaign.

This paper describes the search conducted to identify internal orbits in the system that would favour the exploration of the poles (from the laser altimeter point of view) and that could accommodate the permanence of a spacecraft with minimum use of station keeping for a short period of time, of at least 1 month.

5.3 Methods

5.3.1 Numerical integration

The spacecraft trajectories around the triple asteroid are calculated with a numerical integrator, which solves the equation of motion. Taking into account the relevant forces that are acting on the spacecraft we solve the following general equation (Montenbruck and Gill, 2000):

$$\ddot{\vec{r}} = -\frac{GM_\alpha}{r^3}\vec{r} + \ddot{\vec{r}}_{ht,\alpha} - \frac{GM_\beta}{r_\beta^3}\vec{r}_\beta - \frac{GM_\gamma}{r_\gamma^3}\vec{r}_\gamma + \sum_{sb}\ddot{\vec{r}}_{sb} + \ddot{\vec{r}}_{srp} \tag{5.1}$$

with $GM_\alpha = 6.12327 \times 10^{-7}\mathrm{km}^3/\mathrm{s}^2$ being the standard gravitational parameter of the primary body and $\vec{r}$ and $\ddot{\vec{r}}$ being the spacecraft's position and acceleration, respectively. The reference frame is centered at the center of mass of the primary body.

The main acceleration acting on the spacecraft is caused by the primary body of the asteroid system. The first term of the equation includes the GM-value of the primary body, GM_α as a point mass. The second term of equation 5.1, $\ddot{\vec{r}}_{ht,\alpha}$, includes the higher order Stokes coefficients of the primary's gravity field. The secondary and tertiary body are represented by the third and forth term of the equation. Both are included as point masses with their corresponding GM values, GM_α and GM_β. Additionally the large Solar System bodies, such as Sun and Jupiter are also include as perturbing forces in $\ddot{\vec{r}}_{sb}$. The last term takes into account the solar radiation pressure acting on the spacecraft. This acceleration is extremely important in the low-gravity environment of small asteroids.

The acceleration $\ddot{\vec{r}}_{sb}$ caused by solar radiation pressure for a plane surface reflecting one fraction and absorbing the other fraction of the incoming light is given by (Montenbruck and Gill, 2000):

$$\ddot{\vec{r}}_{sb} = -\nu P_{ref}\left(\frac{1AU}{d_{sun}}\right)\frac{S}{m_{sat}}cos\theta[(1-\epsilon)\vec{e}_{sun} + 2\epsilon cos(\theta)\vec{n}] \tag{5.2}$$

where ν is the shadow function ($\nu = 0$: umbra, $\nu = 1$: sunlight, $0 < \nu < 1$: penumbra). $P_{ref} = 4.56 * 10^{-6}Nm^2$ is the solar radiation pressure at 1 AU, d_{sun} the distance from the surface to the sun, S the surface area, m_{sat} the space probe's mass, θ the illumination angle, ϵ the reflectivity of the surface, $\vec{e}_{sun}$ sun the direction to the sun, and $\vec{n}$ the surface normal. $\nu = 1 - A/(\pi a^2)$ has to be calculated for the given spacecraft position and constellation of celestial bodies considered. A is the occulted segment of the sun and a the apparent diameter of the sun. The constellation of bodies is calculated using SPICE routines at the given epoch. The solar radiation pressure, which has to be computed for every time-step depends on the absolute distance to the sun and on the mass-to-area ratio of the spacecraft.

In our simulation the so called box-wing model for S/C geometry was used. It is composed of a cubic shaped with 6 surface areas and two solar panel areas which are orientated perpendicular towards the solar radiation. The bottom surface of the spacecraft's main body cube is always nadir pointing. The spacecraft model is shown in Figure 5.1 . Based on the information provided spacecraft reference design document Goretov et al. (2018) the surface areas are defined as:

- 6x 0.25 m^2 (with a reflectivity value of 0.8)
- 2x 10 m^2 (with a reflectivity value of 0.058 or 0.21)

For the simulation two spacecraft scenarios were defined. In the first scenario a S/C with a mass of 150 kg, i.e. with full tank and low reflectivity of 0.058 for the solar radiation pressure was used (**heavy S/C**). In this scenario the solar radiation pressure has a lower effect as in the the second scenario, where the Xenon tank are empty and and the total mass is reduced to 80 kg (**light S/C**). Additionally we assumed a solar panel with less efficiency and a higher reflectivity of 0.21, leading to a higher force caused by SRP.

In summary, the following accelerations were used as force or perturbing force in our model:

- GM of the primary body of the Asteroid (Alpha)
- higher terms of the gravity field of the primary body up to degree and order 20

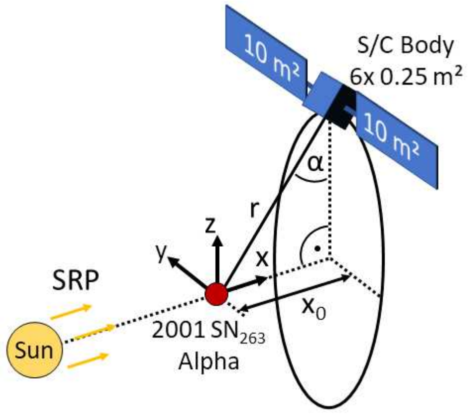

Figure 5.1: Illustration of the sun oriented co-rotating reference frame and the spacecraft model used in the simulation. The spacecraft is positioned on a displaced terminator orbit in anti-sun or x direction. The spacecraft model consist of a solar panel area of 20 m^2 which is always oriented towards the sun. The bottom side of the spacecraft main body is always nadir pointing. The x-axis of the reference frame is always parallel to the incoming solar radiation and the z-axis perpendicular to the heliocentric orbital plane of 2001SN263.

- GM's of the secondary and tertiary body (Beta and Gamma)
- GM's of solar system bodies (Sun, Mercury, Venus, Earth+Moon Barycenter, Mars, Jupiter, Saturn)
- Solar radiation pressure (one heavy S/C scenario and one light S/C scenario)

All modeled accelerations acting on the S/C in an 8 km reference orbit are shown in Figure 5.2. It shows that the higher terms of the primaries gravity field as well as the planets of the solar system have only a very small effect and can be neglected. The same applies on accelerations caused by Beta's and Gamma's higher terms gravity field.

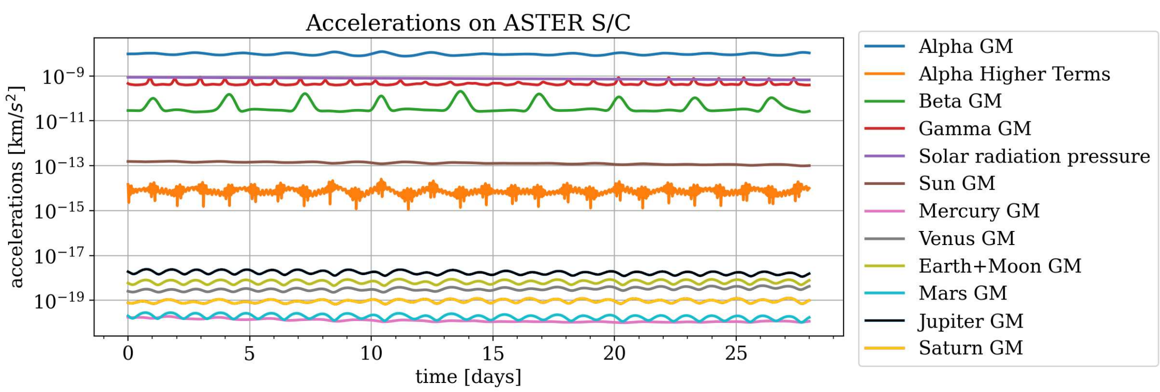

Figure 5.2: Accelerations acting on the S/C in the reference orbit (at 8 km initial distance from primary, heavy s/c, see 5.3.1)

It is well know that the stability of spacecraft orbits in the environment of low-gravity NEO's depend on the direction of the incoming solar radiation pressure Scheeres (1999). Stable orbits are found when their orbital plane is chosen to be perpendicular to the incoming radiation. However, to assess the gravitational effects of the secondaries we ran a full scan over the three orbital elements which define mainly the position of the orbital plane relative to the primary body. The following orbital elements were varied:

- a: semi-major axis, range: [2 km - 15 km]
- i: inclination , range [0° - 90°]
- Ω: longitude of ascending node, range [0° - 180°]

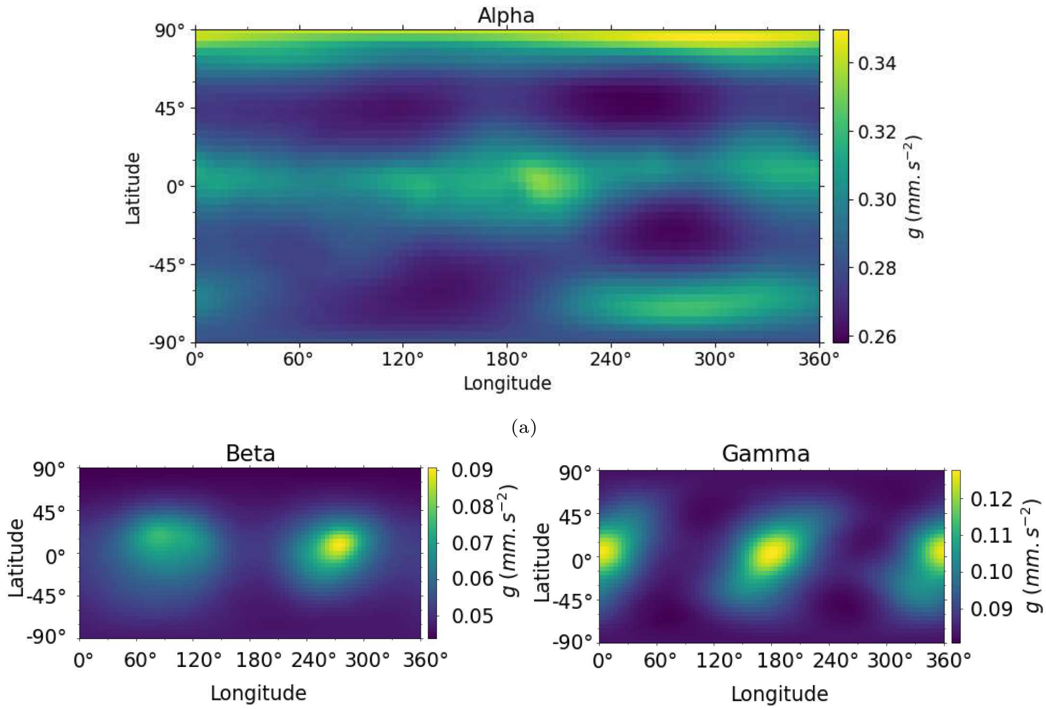

(a)

(b)

(c)

Figure 5.3: Gravitational acceleration calculated on a sphere circumscribing each asteroid. This field is approximated with spherical harmonics and expanded to further distances.

5.3.2 Shape and gravity fields

The gravitational field of all three bodies of $2001SN_{263}$ was modeled in two steps. First, a polyhedral approach was used to integrate the gravitational acceleration contributed by the mass distribution inside the object. Afterwards a volume discretization from Cheng et al. (2012) was used to integrate over volume elements where each polyhedron is defined by a triangular facets of the shape model, and the center of the shape. This integration is equivalent to the classical approach of Werner and Scheeres (1996) for shapes with more than 10 000 facets, but faster to compute. We considered each object to be homogeneous, with the density of each volume element being equal to the bulk density of the asteroid (i.e. $\rho_\alpha = 1100$ kg/m^3, $\rho_\beta = 1000$ kg/m^3, $\rho_\gamma = 2300$ kg/m^3). Although fast, this method requires an integration over each facet for every calculation, and is not suited for long term orbital calculation. We run this analysis once to get a reference gravitational field, calculated on the circumscribing sphere for each object.

In a second step, this reference field was replaced with a spherical harmonics approximation. This is done with the python library SHTOOLS Wieczorek and Meschede (2018) which provides a well tested implementation of this conversion. In short, the gravitational field calculated in the first step from the irregularly sampled shape is expanded into spherical harmonics using a least-squares inversion (function: `pyshtools.expand.SHExpandLSQ`).

As a test, the gravitational acceleration on the reference interface was recalculated from this spherical harmonics expansion and compared it to the polyhedral model from step 1. It showed that using a maximum degree/order of 20 is sufficient for an accurate description of the gravitation field. The mean residual difference between the spherical harmonics approximation of the gravitational acceleration and the value determined by the polyhedral integration is equal to 0.002 %, with a standard deviation of 0.48 %. When applying the same approach to the gravitational potential, the spherical coefficient C_{20} gives us the oblateness factor J_2. We find $J_{2,\alpha} = 0.015$, which is within the range proposed by Becker et al. (2015). Using the same approach $J_{2,\beta} = 0.007$ and $J_{2,\gamma} = 0.003$ were determined. With the resulting gravity field coefficients, we are able to determine the acceleration caused by this field. The results are summarized in Figure 5.3

5.3.3 Track simulation of the ASTER Laser Ranger

The study aims to identify orbits sufficiently stable for a period of approximately 1 month to allow optimal laser operation from an almost constant distance with the possibility to cover at least 50% of the surface of the asteroid and to scan to pole areas with a laser altimeter. The expected results for the research campaign, in terms covered area with laser altimetry shots, footprints sizes and spacing between successive footprints are provided. The analysis consists of two main steps. The first step involves the search for stable orbits which allow laser ranging from an almost constant distance. This can be satisfied with a terminator orbit. For the second step a simulator software, called *ALR_Sim_Tracks* was developed Brum et al. (2021). This software allows a deeper understanding of the details of the instrument operation and facilitating the definition of parameters during the design phase. The simulation procedure carried out with use of this tool is described in the following.

i) Trajectories and orbits: for the simulations, spacecraft and asteroid orbits were generated for the period from 12h of 07/Feb/2025 to 12h of 07/March/2025 (Ephemeris Time - ET, 60 sec spaced data), in the Sun centred ecliptic J2000 frame.
The position and velocity vectors of asteroid Alpha are given by $\vec{R}_{ast}(t) = (X_{ast}, Y_{ast}, Z_{ast})$, and $\vec{V}_{ast}(t) = (VX_{ast}, VY_{ast}, VZ_{ast})$. The position and velocity vectors of the ASTER spacecraft when it follows the reference orbit are denoted by $\vec{R}_{sc}(t) = (X_{sc}, Y_{sc}, Z_{sc})$, and $\vec{V}_{sc}(t) = (VX_{sc}, VY_{sc}, VZ_{sc})$. The program will accept any trajectory as input data. In this scenario, the 8 km reference orbit (see Figure 5.8) was given as input data.

ii) Modelling of asteroid Alpha's physical and dynamic features (Becker et al., 2015): 2001SN263 Alpha is modelled as a ellipsoid with the following main axes: $(d_x, d_y, d_z) = (2.5, 2.4, 2.1)$ km). Its rotation period is set to 3.4 hours and the pole direction (ecliptic longitude and latitude): $(\lambda, \beta) = (309, -80) \pm 15$ deg (see also Table 5.1.)

iii) Laser altimeter simulation: When the spacecraft is in a terminator orbit around asteroid Alpha, the nadir pointing condition is used as reference case, i.e. the instrument line of sight points towards the body's center of mass. For each emitted laser pulse (modelled as a line pointing from the spacecraft in the direction of the asteroid's center of mass) the intersection with the asteroid's surface is calculated. The determined intersection point is identified and the footprint size is calculated. The list of all footprints is stored for later analysis.
The following instrument parameters were assumed:
- **Divergence angle (θ_{div})**: this parameter directly affects the footprint size. The planned size of the footprint is 5 to 10 m (radius), at 10 km. To have such footprints, values from 500 μrad to 650 μrad (half cone) are considered for this angle.
- **Pulse repetition frequency (PRF)**: this parameter directly affects the spacing between successive footprints in a surface scan, named along-track distance (ATD), consequently affecting the quality of the surface mapping in terms of horizontal resolution.

From the ALR preliminary design, the reference PRF value is 1 Hz and, associated to this operation rate, the data generation rate is 12 bytes/sec (Brum et al., 2011; Brum and Cruz, 2017). However, previous results of this research pointed to the possibility of using smaller PRF values (e.g. 1/20 Hz) as sufficient to get the desired coverage. Nevertheless, 1 Hz was chosen as PRF in the simulation. The LIDAR instrument on board mission Hayabusa-2 mission also had a maximum PRF of 1 Hz (Mizuno et al., 2017) and can was considered as reference case.

With these inputs, the scanning of the asteroid surface by the laser altimeter is simulated for the complete time frame. The list of all points of intersection, called footprint centres, is generated. From the analysis of this list and associated data the results of the simulated exploration campaign are extracted. Each footprint has its position, distance, minimum radius and minimum covered area calculated. The analysis of the distribution of points and covered areas over the target surface allows to predict the type of coverage (qualitative and quantitative) that will be obtained for the inputs used.

5.4 Results

Our analytical evaluation and our numerical calculation show that stable orbits can be found in the vicinity of the triple asteroid. Especially at distance between 6 to 10 km from the primary, large stable areas have been identified. With a semi-major axis of approximately 8 km +-2 km, the optimal solution are between the orbits of the the secondary and the tertiary body. These orbits could be of high scientific interest for studying this complex 3-body asteroid.

5.4.1 Analytical predictions

Due to the numerous perturbing forces acting on the S/C numeric integration is necessary for orbit simulation. But analytical predictions can help limiting the regions where stable or even frozen orbits may occur.
Perfectly circular terminator orbits occur only in a very reduced model: the two-body problem plus a constant pressure force originating form a unmoving sun. An orbit with constant distance r to the asteroid must have an orbital plane displaced behind the asteroid (see Figure 5.1). The displacement x in anti-sun direction is given by Bookless and McInnes (2006):

$$x \quad = \quad \frac{a_{srp}}{GM} \; r^3 \; . \tag{5.3}$$

With a_{srp} denoting the acceleration caused by the pressure force and GM central force of asteroid mass M. If distance r is big the orbit becomes unbound. Linear stability can be inspected by introducing small initial perturbations $x + \delta x$ and $r + \delta r$ to the orbit solution Bookless and McInnes (2006). As result we get a limit on the distance r of a stable circular terminator orbit:

$$r \quad < \quad \sqrt{\frac{GM}{3a_{srp}}} \tag{5.4}$$

This is a easy to use criteria for terminator orbit size, but only valid for time intervals where the asteroids movement about the sun can be neglected.
To study longtime effects The Augmented Hill Three-Body Problem introduces the eccentric orbit of the asteroid around the sun. Orbit approximations found by averaging the effects of solar radiation pressure over one orbit of the S/C, were always stable and periodic Scheeres (1999). Also the S/C orbit liberates around a sun-synchronous state, e.g. a terminator orbit will rotate the orbit normal to follow the sun. The eccentricity changes periodically with the same period T as the liberation of the orbit plane.
Unstable orbits will only occur if the eccentricity is too high and the S/C is to close to the surface or the averaging method is not applicable. Small orbits become more eccentric and we get a lower bound for orbit size. The eccentricity of a frozen terminator orbit (no liberation) described in Scheeres (1999) was used to find the lower bound in Figure 5.4 to avoid hard landing. Large S/C orbits have a higher period P for one revolution over which we averaged. Is $P \geq T$ the method is invalid. Sun-synchronous orbits of this size are necessarily unstable and were blown away by SRP in numeric simulations. Through numeric experiments we are sufficiently confident in the averaging method as long as:

$$4.1 \times P \quad < \quad T \tag{5.5}$$

In Figure 5.4 this criteria in used to give a maximum semi-mayor axis for stable sun-synchronous orbits.

5.4.2 Frozen terminator orbits

For carefully chosen initial states the orbit does not liberates around a sun-synchronous state. In the co-rotating frame of the asteroid this orbit is ’frozen’. Due to interactions with the asteroids shadow we do not consider the frozen orbits with $i = 0°$. Again, by averaging the effects of solar radiation pressure over one orbit of the S/C, the works of Scheeres (1999) give us the constant orbital elements

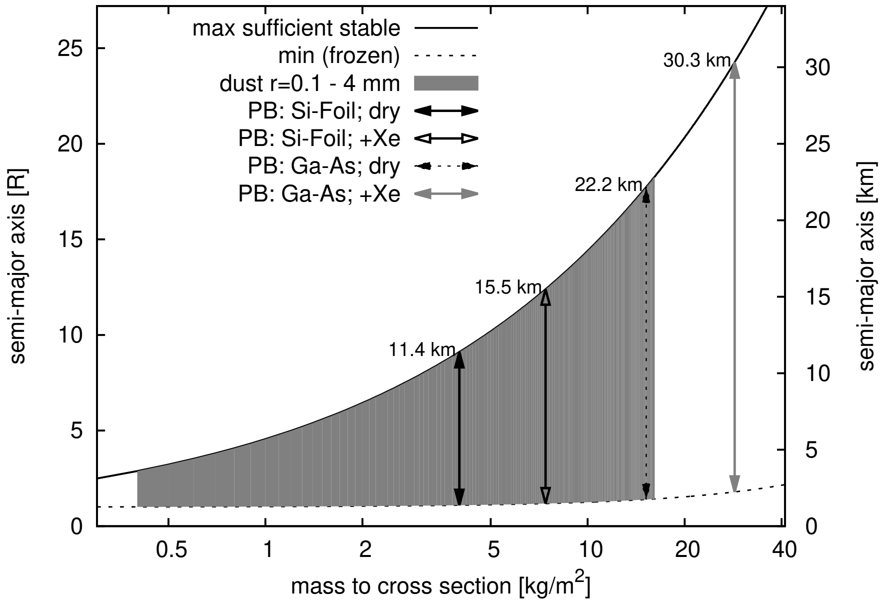

Figure 5.4: Semi-mayor axis (in km or primary asteroid radius R) of stable and periodic orbits depending on orbiter mass to cross section. The area between the upper and the lower curve is the region were stable terminator orbits can be found. Reference values are given for different ASTER case models and grains of dust; ASTER dry mass 80 kg; xenon (Xe) capacity is 70 kg; effected area with Si-foil photoelectric battery: $20.25m^2$, with Ga-As photoelectric battery: $5.25m^2$; total reflectively of S/C and dust is 0.093 (0.8 ASTER main body, 0.058 Ga-As panel, 0.0844 Si-foil); dust is assumed to be spherical; secondary bodies of 2001Sn263 are not considered

of a frozen orbit:

$$\begin{aligned} i = \quad \Omega = & \quad \pm 90^\circ \\ \omega = & \quad \mp 90^\circ \\ e = & \quad \cos\psi \end{aligned} \tag{5.6}$$

With the constant ψ defined by the relation of asteroid gravity, centripetal force and SRP:

$$\tan\psi \quad := \quad \frac{3a_{srp}}{2\nu'_{\text{hel}}}\sqrt{\frac{a}{GM}} \tag{5.7}$$

If SRP is weak, then $\psi \to 0$ and if SRP is strong relative to gravitational forces, then $\psi \to 90°$. ψ is constant because solar distance is canceled out from $a_{srp}/\nu'_{\text{hel}}$ in Eq. (5.7).
It is important to remember that the solutions for a, e, i, ω and Ω in Eq. (5.6) are averages over one orbit and are referring to the co-rotating frame. Frozen and other terminator orbits still have a displacement x in anti-sun direction, positioning the orbital plane behind the small body. Even if the average inclination i is frozen at 90° the actual inclination must differ to account for the displacement x. For a frozen terminator orbit the optimal initial offset is Takahashi and Scheeres (2020):

$$x_0 \quad = \quad \frac{a_{srp}}{GM}\; a^3\; (1-e)(1+\frac{e}{4}) \quad \text{if } \nu_0 = 0 \tag{5.8}$$

This offset is consistent with the result Eq. (5.3) in the static 2-body problem. x_0 has the factor a_{srp} and therefore is anti-proportional to the square of the changing solar distance. Our numerical simulations, in Figure 5.5, show that the displacement x will adapt to this changes consistent with Eq. (5.8), keeping the other elements frozen.
In an algorithm in Takahashi and Scheeres (2020) the frozen eccentricity was improved by using an 'effective' semi-major axis $a' = a(1 + a^4 a_{srp}^2/GM^2)^{3/2}$ to calculate frozen eccentricity e using Eq. (5.6, 5.7). The 'effective' semi-major axis is defined to be consistent with the velocity $\dot{r}$ of the displaced orbit.

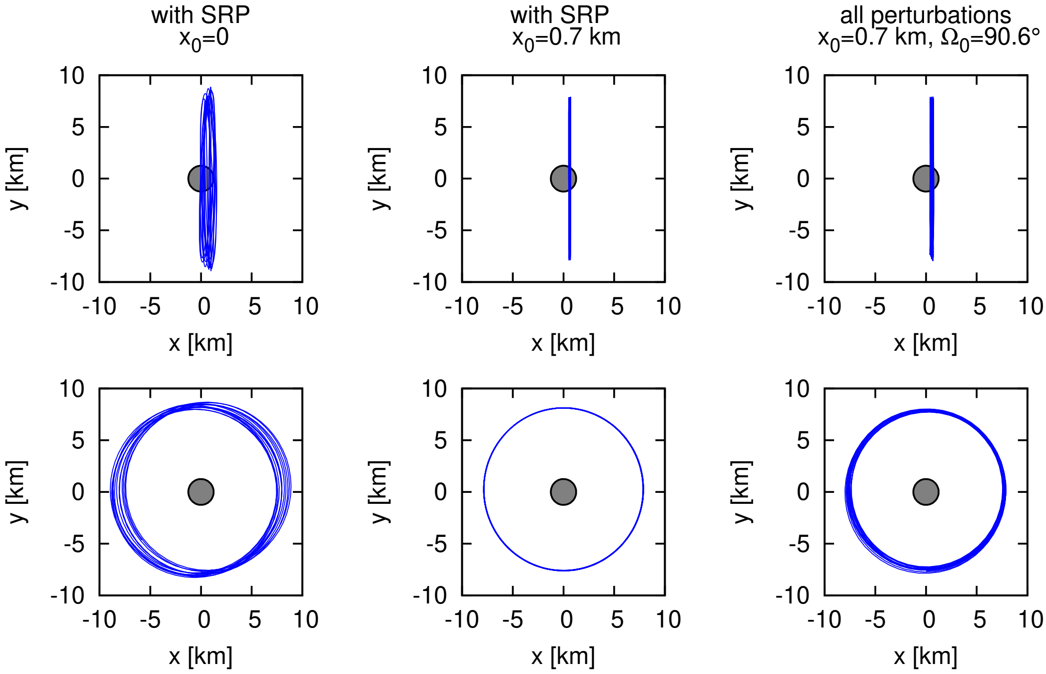

Figure 5.5: Numeric simulation for light s/c (80 kg, refelctivity = 0.21), see also 5.3.1. Frame is co-rotating with Sun-asteroid line x, z orientated along the asteroid's orbit normal and y orthogonal to x and z. Initial state: $i = 90°$, $\Omega = 90°$, $\omega = -90°$ and anomaly $\nu = 0°$. Over the 30 days of integration solar distance rises from $1.27AU$ to $1.44AU$. **Left:** Frozen eccentricity $e = 0.0325$ chosen according to Eq. 5.6. **Middle:** Augmented frozen eccentricity $e = 0.0323$ and shift of orbit in anti-sun direction x_0 chosen according to Takahashi and Scheeres (2020) algorithm 2. **Right:** all perturbations are included in simulation, in particular moonlet gravity. Elements $e = 0.091$ and $\Omega_0 = 90.6°$ adapted to compensate for moonlet gravity.

Perturbing effects from the J2 and J3 term of the asteroid gravity on the frozen state (Figure 5.5) were too small in the simulation to be noticeable. Therefore we did not apply the corrections to the inclination and eccentricity to compensate for the J2 and J3 term proposed in Takahashi and Scheeres (2020). But eccentricity and ascending node Ω were mortified in the simulation in Figure 5.5 to compensate for moonlet gravity. Frozen terminator orbits are strictly periodic therefore particularly robust to initial state and dynamics perturbations in the numerical experiments of Broschart et al. (2010).

5.4.3 Orbital stability

The orbit stability is defined as (dist$_{max}$ - dist$_{min}$) / dist$_{init}$ to the primary body, i.e. maximal distance over one month - mininal distance over one month divided by the initial distance. This criteria is comparable to the keplerian eccentricity, i.e. if the eccentricity stays below a certain value, the orbit would also be considered as stable. However in the vicinity of the such a triple asteroid where the secondary and tertiary bodies play an important role and the solar radiation pressure is one of the strongest forces acting on the space, a nominal eccentricity is hard to determine. Thus, we used and absolute distance criteria. Additionally, minimizing the eccentricity and consequently the absolute distance variation, will give better results for the laser altimeter. In Figures 5.6 and 5.7 a hypothetical value of 0 would lead to a spacecraft orbiting the primary body in a perfect circle. Of course, this is an unrealistic scenario and is not obsevered in our simulation, but in the best cases we obtain a value of less than 0.2. In this case, at an exemplary initial distance of 8 km, the spacecraft would mainly stay at this distance and have a variation better than ± 0.8 km in total. In other words, in this case the orbital distance would vary between 7.2 km and 8.8 km.

The numerical simulations suggest the existence of optimal stable regions in distances of about 6 to

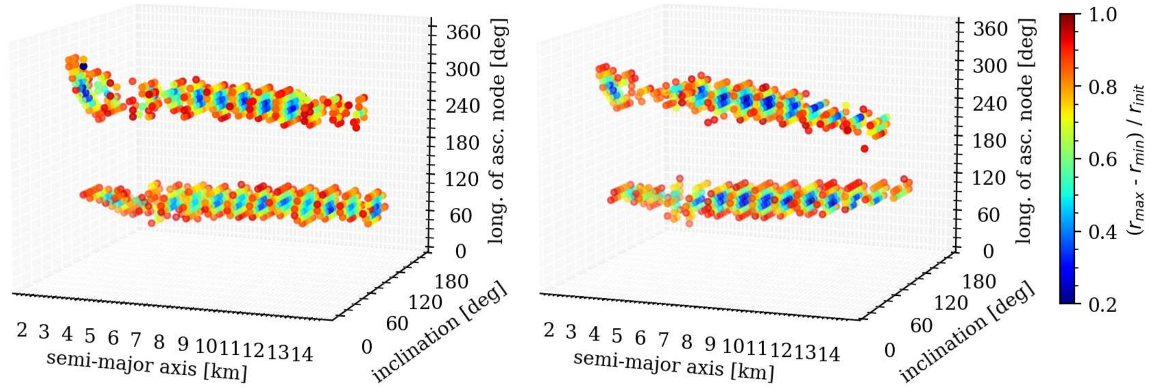

Figure 5.6: Stability results for initial distances between 2 km to 14 km from the primary body. **Left**: heavy s/c (150 kg, reflectivity = 0.058), **Right**: light s/c (80 kg, reflectivity = 0.21), see also 5.3.1. Each point of the Figure represents an orbit which is stable over 30 days. Reference Frame: ICRF/J2000. The stability is defined by maximal distance to primary over 30 days minus minimal distance divided by initial distance. A detailed overview of the planes at semi-major axis = 6, 8 and 10 is found in Figure 5.7

10 km from the primary body. In Figure 5.6 the results of the simulations are shown. In these areas, the spacecraft may stay in a stable orbit for at least one month with no or very little need of additional station keeping maneuvers. Our simulation show that both cases with strong (light spacecraft) and low (heavy spacecraft, see Section 5.3.1) accelerations caused by solar radiation pressure will allow finding stable regions but located differently in the three dimensional space (inclination, longitude of ascending node and semi-major axis). In both cases an initial distance of 8 km to the primary will allow getting in to a stable orbit.

5.4.4 Results of the laser tracks simulator software

The predicted exploration results for the second part of the main campaign and the implication on the laser ranging are presented in this subsection. This second part, consisting of the terminator orbit phase, is used to simulate the laser altimeter tracks and simulate its coverage. For this purpose, the reference terminator orbit at 8 km distance from the primary was used (see Figure 5.8). The following setting were applied for the simulation:

- Epoch: 07/Feb/2025 to 07/March/2025 (60 sec spaced data).
- Instrument: divergence angle (θ_{div}; half cone) = 650 μrad; PRF = 1 Hz.
- Spacecraft: nadir pointing (instrument points to Alpha's center of mass).

Figure 5.8 shows the ASTER spacecraft in its reference orbit within in the triple Asteroid system at 8 km difference from the primary body during the exploration period considered in this simulation. It shows that the s/c completes only 13 orbits around the main body during this period. For a fixed period of investigation, this reduced number cannot be raised because it depends only on the chosen reference orbit. In this case, the coverage attainable depends on the chosen distance and on the asteroid dynamics. To improve the coverage from the 13 orbits depicted in Figure 5.8, the quality of the altimetry data to be collected by the laser altimeter must be raised. To do that, a high PRF is indicated. In this case, 1 HZ means an ATD (Along Track Distance) smaller than 1 m (0.1 - 0.7 m) for footprint diameters of about 8.9 m. The coverage of the surface is simulated by splitting the surface area in 180x360 deg^2 elements. Afterwards each surface element is evaluated and the number of laser shots within this element is counted. The coverage of the surface of Alpha attained in the whole complementary exploration campaign is represented in Figure 5.10 in terms of a flat latitude-longitude map with the number of altimeter measurements per area. This Figure shows a remaining uncovered cap around the south pole. In this simulated case, the central values assumed for the spin axis of Alpha (ecliptic longitude and latitude) are (λ, β)=(309, -80) (see Table 5.1). In fact, because of the large uncertainty in the current knowledge about the direction of the spin axis ($\pm$15 deg (Becker et al., 2015)), one cannot guarantee a perfect coverage of both poles. However, inside this uncertainty margin, it is possible to achieve a better situation regarding the complete coverage of the poles. Nevertheless, unless the mentioned uncertainty is reduced, there is no guarantee that the desired coverage will

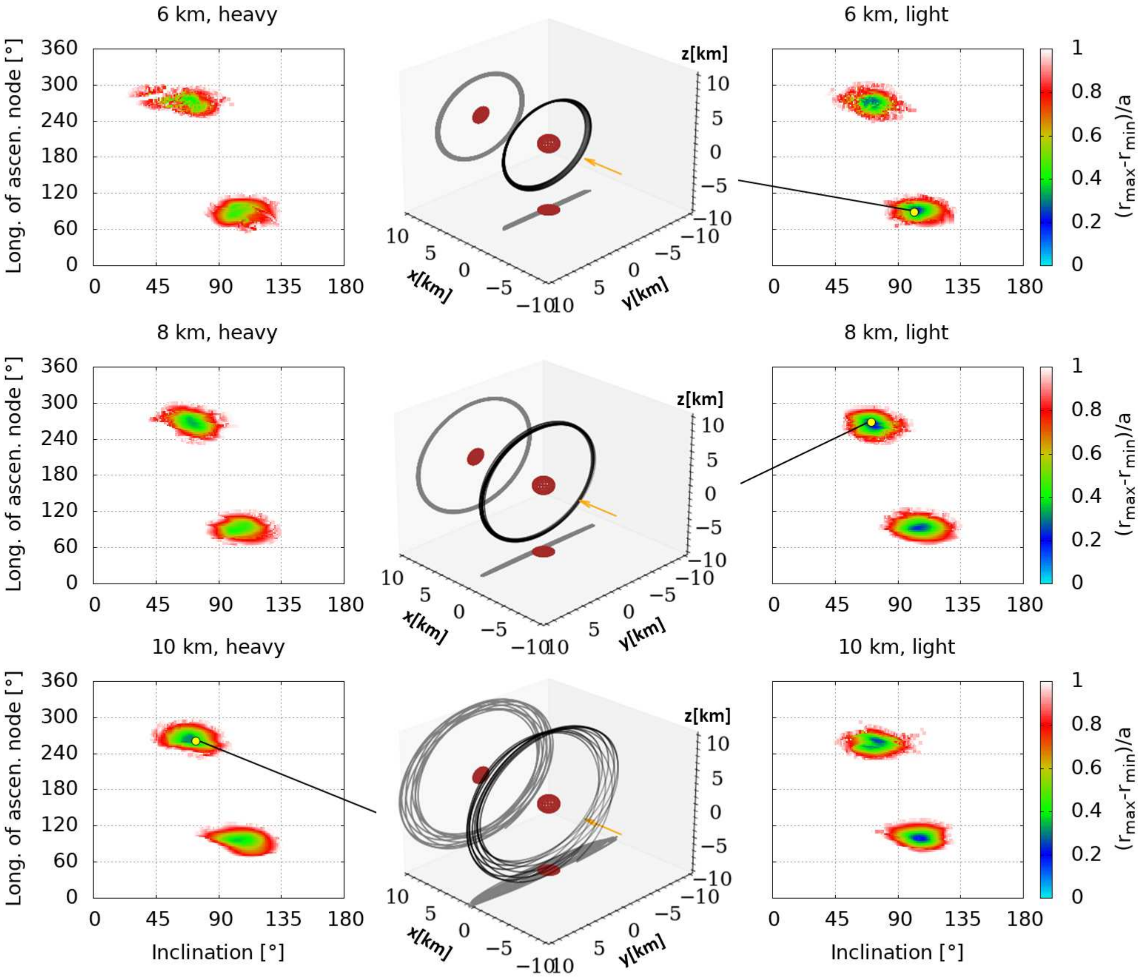

Figure 5.7: Detailed stability results for initial distances at 6, 8 and 10 km. See also Figure 5.6. **Left**: heavy s/c (150 kg, reflectivity = 0.058), **Right**: light s/c (80 kg, reflectivity = 0.21), see also 5.3.1. Each point of the Figure represents an orbit which is stable over 30 days. Reference Frame: ICRF/J2000, reference plane: earth mean equator. The stability is defined by maximal distance to primary over 30 days minus minimal distance divided by initial distance. **Middle**: Three exemplary orbits for 6, 8 and 10 km initial distance. Frame is co-rotating with Sun-asteroid line x, z orientated along the asteroid's orbit normal and y orthogonal to x and z. The orange arrow represents the incoming radiation. Each orbit is referenced to the corresponding points in the color coded map. Each three dimensional orbit and the primary body are projected to the xy- and yz-plane for a better visualisation. The orbits of the secondary bodies are not shown, although they were included in the simulations. A detailed view of the 8 km orbit including the orbits of the secondaries is shown in Figure 5.8

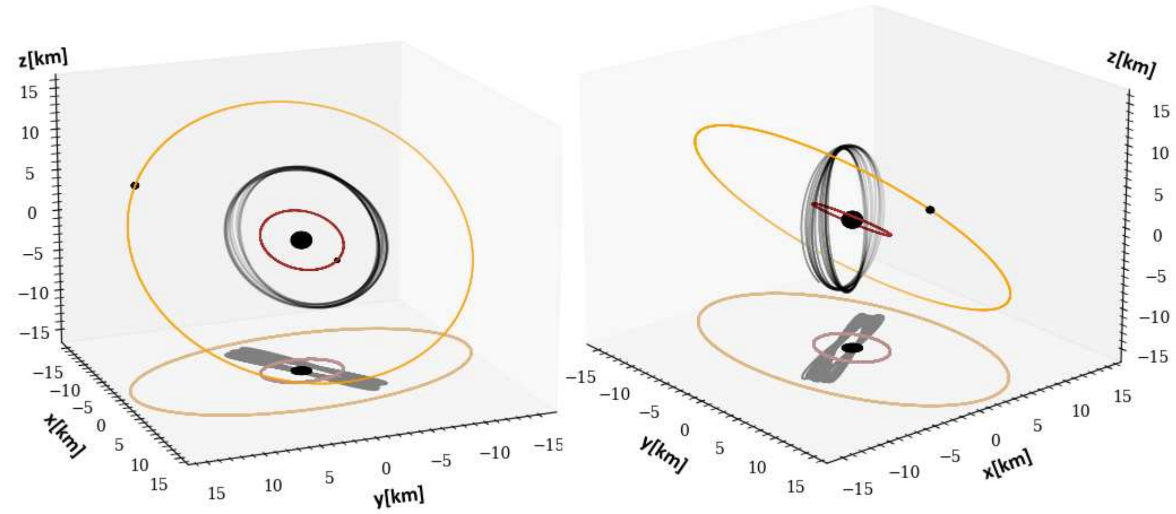

Figure 5.8: Two different perspectives of the ASTER spacecraft in its reference orbit within in the triple Asteroid system at 8 km difference from the primary body (black line). The time frame is 1 month. This orbit is identical to the 8km orbit shown in Figure 5.7. Orbits of the secondary bodies (red and orange) and their starting position at epoch 07/Feb 12:00 are also shown. Body size and orbtial radii are in correct scale. For a better visualisation, the orbits are also projected to the xy-plane. Reference Frame: Heliocentric Ecliptic J2000 frame.

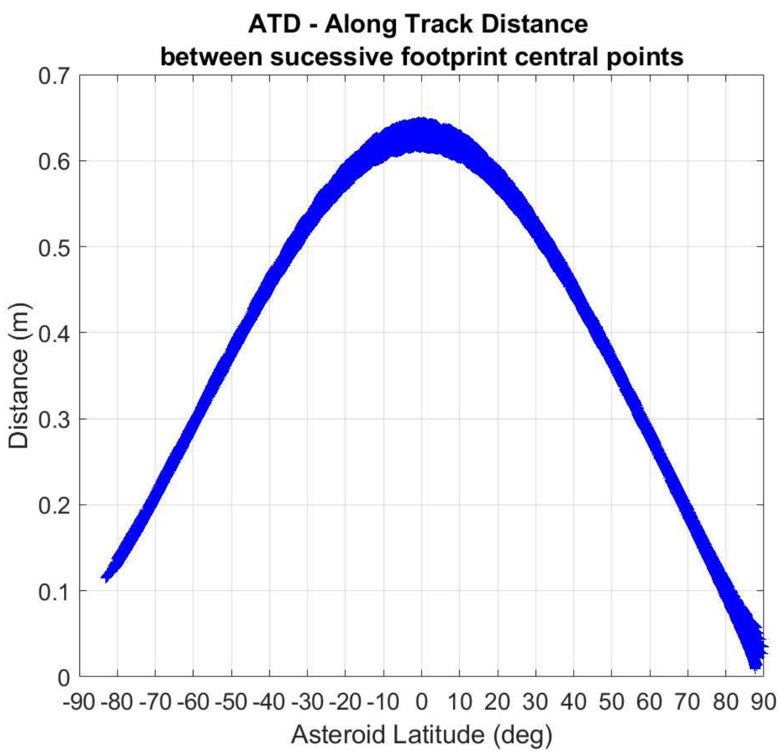

Figure 5.9: ATD for the simulated reference T.O. when PRF=1 Hz and θ_{div}=650 μrad. The calculated footprint diameter in this case measures 9.0±1.5 m. ATD values directly influence the horizontal resolution.

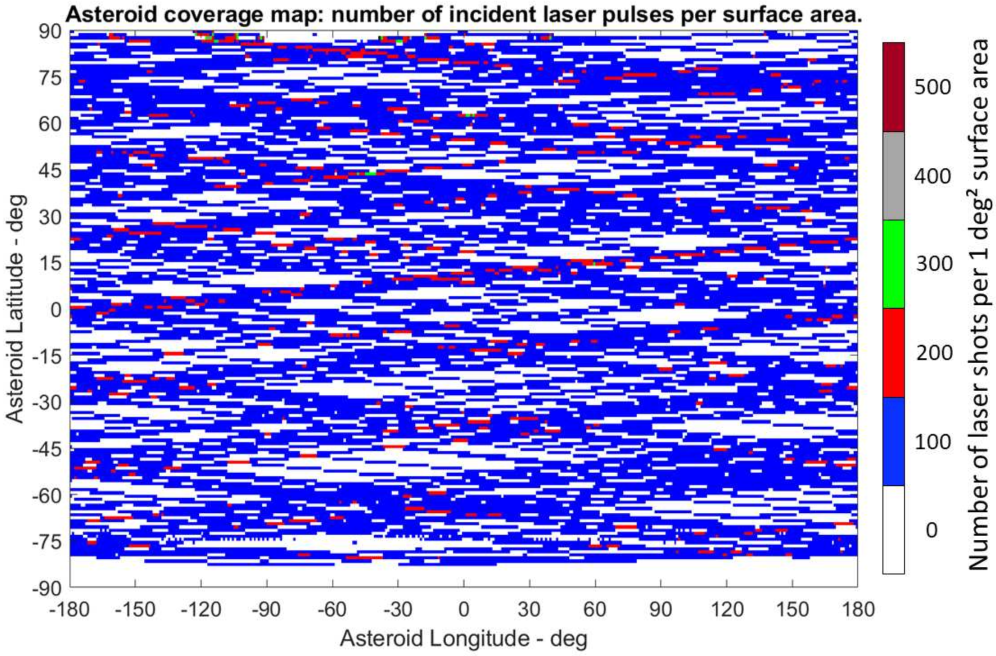

Figure 5.10: The coverage attained is presented through a flat latitude-longitude map of the density of altimetry measurements per area of 1x1 degrees on the surface of asteroid Alpha. Parameters are: PRF=1Hz, θ_{div}=650 μrad.

actually occur. Because of this fact, the availability of an "off-nadir" attitude mode is recommended for this mission.

5.5 Discussion and conclusions

In this paper we have confirmed that stable terminator orbits exist about Asteroid 2001 SN263. In application to the ASTER mission we found several optimal terminator orbits which fulfill the requirements in terms of coverage and stability. Additionally, we showed that the gravity fields of Beta and Gamma have only a negligible effect on stability while the higher terms of the primary body's gravity field play an important role.
The simulation focuses on operations in Feb 2025 as specified in the mission concept document but can also be applied on the backup date in September 2027 or any other date, when the asteroid is at a similiar distance to the sun. Due to the high eccentricity of the Alpha's heliocentric orbit, the solar radiation pressure will vary significantly over time. Consequently, if the arrival occurs near aphelion, the solar radiation pressure will be less than in the current scenario and the overall stability will be different.
Nevertheless, the orbits give good results for the current mission scenario. The small eccentricity of the stable orbits allow the generation of homogeneous remote sensing data set. Especially the laser altimeter will benefit from the almost constant altitudes. Additionally, the orbits are located in a sweet spot between the primary, secondaries and the solar radiation pressure and allow a precise gravity determination as no station keeping maneuvers will be required.
For carefully chosen initial states, in particular an initial eccentricity, frozen orbits exist in the model composed of sun, primary asteroid, S/C and Solar Radiation Pressure. This model does not account for the secondaries effect on s/c orbit. By analytical means we found initial conditions for frozen orbits. Numerical integration of frozen orbits are presented in section 5.4.2 and examples are visualized in Figure 5.5.
Terminator orbits at distances between 6 and 10 km were identified as suitable to conduct the second part of the ASTER science campaign. This orbit, named here simply as '8 km reference terminator orbit', is nearly circular and stays perpendicular to the incoming solar radiation at an average distance from Alpha's center of mass of about 8 km (presented in Figure 5.8).
The results also showed that a terminator orbit at a distance of approximately 2 km from the primary body Alpha ($<$ 1km from the surface) is possible (see Figure 5.7). However, this orbital region was not analyzed in detail as it would require a precise navigation through unstable areas were the effects of Gamma could cause critical instabilities. Additionally the specified stability zones between 6 and 10 km are an optimal choice to fulfil the science and laser requirements.
With the selected reference orbit at 8 km, laser ranging simulation could be performed. The results were used to analyze the exploration with the laser altimeter ALR under the described circumstances. In the case of a nadir pointing spacecraft, results point to a good coverage of low and high body latitude regions, with smaller concentration of measurement spots per area in central regions (white spots in Figure 5.10) and an increased one on the poles. However, depending on the primary's spin axis orientation (the uncertainty on this parameter is $\pm$15 deg), a small cap of uncovered area will probably remain over both, or at least one pole (the south one, in this simulation conditions). Because of that, to guarantee complete coverage of both poles, an important requirement for the attitude system of the s/c is the need to include an off-axis operation mode capability. This search has also pointed out that Terminator Orbits (Hussmann et al., 2012) are the most promising orbits for the achievement of the desired additional coverage of the poles of asteroid Alpha. Additionally, an observation of the primary and secondaries from a comparably close distance will also be possible.
This fact, combined with the very first investigation of a triple asteroid mission will allow collection of completely new scientific data and shed light on the evolution of asteroids. This complementary exploration campaign of about 1-month with use of a terminator orbit and focused on the poles of asteroid Alpha is suggested to follow the first part of the main campaign which will use an encounter trajectory and focus on the central regions of Alpha.

Acknowledgements

The authors of this paper would like to thank two anonymous reviewers for their very helpful and constructive comments. Coauthor Antonio de Brum wishes to demonstrate his gratitude to the São Paulo Research Foundation - FAPESP, which supported his participation in this research (grant 2018/22672-4), also to the Planetary Research Institute of the German Aerospace Centre, in Berlin, where the research was conducted, and to the Federal University of ABC, in São Paulo, Brazil. Coauthor Friedrich Damme received funding by the Deutsche Forschungsgemeinschaft (DFG - German Research Foundation) for his research on sun-synchronous orbits. This research has made use of
- NASA's Astrophysics Data System
- data and/or services provided by the International Astronomical Union's Minor Planet Center and
- the scientific software shapeViewer (www.comet-toolbox.com).

References

All references were moved and collected in the Bibliography

Chapter 6

Trajectory Analysis for Combined Missions to Mars and its Trojan Asteroids

Research Paper II

Published version, 2023 in Planetary and Space Science
https://doi.org/10.1016/j.pss.2023.105649

Kai Wickhusen [a], Jürgen Oberst [b], Apostolos Christou [c], Friedrich Damme [b]

a. German Aerospace Center (DLR), Institute of Planetary Research, Rutherfordstr. 2, D-12489, Berlin, Germany

b. Technical University Berlin, Institute of Geodesy and Geoinformation Science, Strasse des 17. Juni 135, D-10623 Berlin, Germany

c. Armagh Observatory and Planetarium, Armagh, Northern Ireland, United Kingdom

Abstract

While standalone missions to the Trojan Asteroids of Mars are costly, we analyze flyby scenarios of Mars Trojans, which can be achieved in combination with missions to Mars. We find several trajectory options within the time window 2025-2050, which allow flybys at seven of the known Trojan asteroids located at L5 (trailing by approximately 60 degrees behind Mars) with a low demand for additional delta-v of 0.02 to 1 km/s compared to a nominal Mars mission. On the other hand, the minimal cruise duration from Earth to the Trojan and from the Trojan to Mars adds up to at least 2 years as more than one revolution about the sun is required for the spacecraft. For the unique L4 Trojan no practical trajectory solution was found. All Trojans have a significant inclination of more than 10 degrees relative to the orbital plane of Mars, which implies high flyby velocities (v = 6 - 13 km/s) for spacecraft approaching from within this plane.

6.1 Introduction

In the context of ESA's Cosmic Vision program, we proposed DePhine – the Deimos and Phobos Interior Explorer – for a rendezvous with the Martian satellite system. DePhine , proposed to be launched in 2030, would explore the origin and evolution of the two Martian Satellites (Oberst et al., 2018a) During the development, the idea of a mission to the Trojan Asteroids of Mars in combination with a mission to the Martian Moons arose.

In recent decades, several successful missions have been conducted to investigate small asteroids with diameters of only a few kilometers. Notable examples include the Hayabusa missions and Osiris-Rex (Lauretta et al., 2017; Tsuda et al., 2013; Yano et al., 2006). Currently, only one mission, Lucy, is en route to study Jovian Trojans. It is expected to arrive at the first Trojan in 2027, making it the first mission to explore Trojan asteroids in the solar system (Khan et al., 2023). Consequently, studies of the Martian Trojans and comparing them with the Moons of Mars is a completely new scientific frontier and would be of significant scientific interest.

Unfortunately, the high inclinations (IAU, 2022a) of the Martian Trojans make rendezvous missions very challenging and costly. As an alternative we looked for possible flyby scenarios at Martian Trojans on the way to Mars. The objective was to find trajectories, which connected Earth, Martian Trojans and Mars at a very low demand for delta velocities (delta-v) and consequently a low demand for propellant, or even no demand for additional propellant in the best case.

The paper is organized as follows: In Section 6.2 we give a short overview of the Martian Trojans and their properties. In section 6.3 we present the methods that were used to find the best trajectories and in section 6.4 we summarize the results. The conclusions and discussion are presented Section 6.5.

6.2 Mars Trojans

Trojan asteroids are commonly associated with outer solar system planets, but only a small population, if any, have been discovered for terrestrial planets of the Inner Solar System (Dotto et al., 2008; Hui et al., 2021). Trojans librate around the so-called Lagrangian points L4 and L5, leading (L4) or trailing (L5) a planet by 60deg, respectively (Robutel and Souchay, 2010) (see Figure 6.1).

The first Martian Trojan (5261) Eureka was discovered in 1990 librating about L5 (Bowell et al., 1990; Mikkola et al., 1994). In 2005 four Martian Trojans were officially confirmed; Scholl et al. (2005) demonstrated that the population is stable, with estimated orbital lifetime on the order of the age of the Solar System.

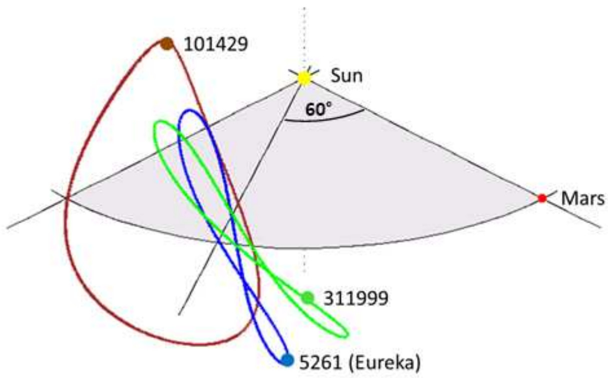

Figure 6.1: The orbital paths of the three Martian Trojan asteroids, "5261 Eureka", "1998 VF_{31}", and "2007 NS_2" are illustrated in a 3D view of the trailing quadrant. The paths are shown in a Sun-Mars co-rotating reference frame, spanning a period of one Martian year.

By the end of 2022 nine Martian Trojans have been confirmed, eight of them located at L5 and one at L4 (Christou et al., 2017; IAU, 2022a). Seven of the eight L5 Trojans are considered to belong to a genetic family, most likely originating from (5261) Eureka (Ćuk et al., 2015), with its diameter of 1.79 km being the largest. Compositional data show that (5261) Eureka belongs to an olivine-dominated, A-type taxonomic class of asteroids. Consequently, Polishook et al. (2017) suggested that the parent body of the Eureka cluster originated from Mars and was ejected from the planet due to a large impact. This raised speculations that the Trojans represent samples from Mars. (5261) Eureka itself has a small yet unnamed companion S/2011 (5261) (Johnston, 2019; Koehn et al., 2014), which makes Eureka a particularly attractive exploration target.
All Trojans have only small eccentricities, but high inclinations relative to the ecliptic (Table 6.1), posing a challenge to resource management of spacecraft missions. Due to these high inclinations, Trojans like Eureka rise up to more than 0.5 AU above the ecliptic (see Figure 6.2). Consequently, flybys are recommended at the time when the Trojan passes through the ecliptic.

Table 6.1: Osculating elements of nine Martian Trojans used in this study (IAU, 2022a).
a: semi-major axis, e: eccentricity, i: inclination, Ω: longitude of ascending node, ω: argument of perihelion, M: mean anomaly, Ln: Lagrange Point, epoch: 2022-08-09. Reference frame: ecliptic and mean equinox/J2000.

	a [AU]	e []	i [deg]	Ω [deg]	ω [deg]	M [deg]	Ln []
5261 Eureka	1.524	0.065	20.3	245.0	95.5	204.57	L5
1998 VF31(101429)	1.524	0.100	31.3	221.3	310.6	0.41	L5
1999 UJ7 (121514)	1.524	0.039	16.7	347.4	48.5	288.69	L4
2007 NS2 (311999)	1.524	0.054	18.6	282.5	176.9	88.76	L5
2001 DH47 (385250)	1.524	0.035	24.4	147.4	17.6	21.53	L5
2011 SL25	1.524	0.114	21.5	9.4	53.3	114.83	L5
2011 SC191	1.524	0.044	18.7	5.8	196.4	332.42	L5
2011 UN63	1.524	0.065	20.4	223.5	165.3	160.50	L5
2011 UB256	1.524	0.071	24.3	58.8	7.6	121.39	L5

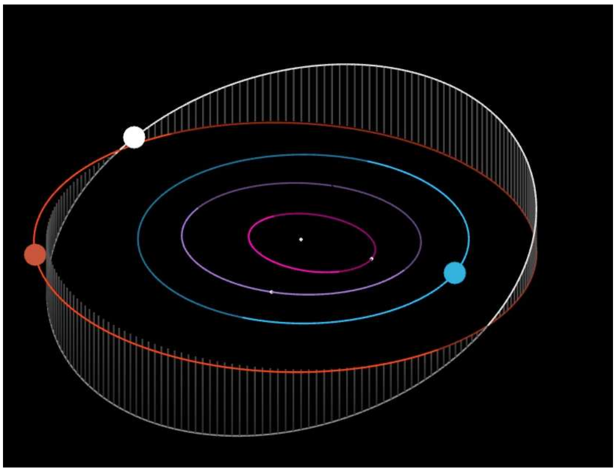

(a)

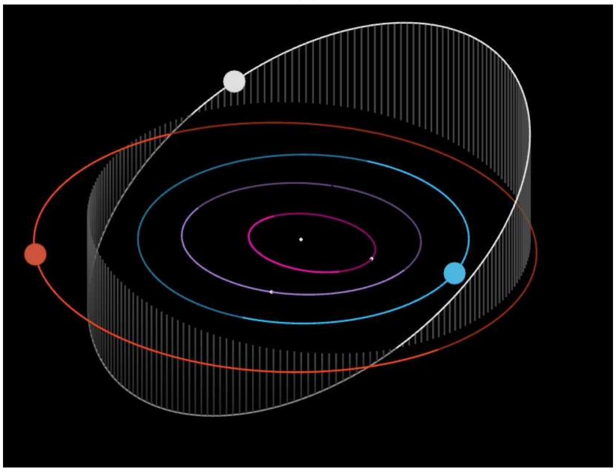

(b)

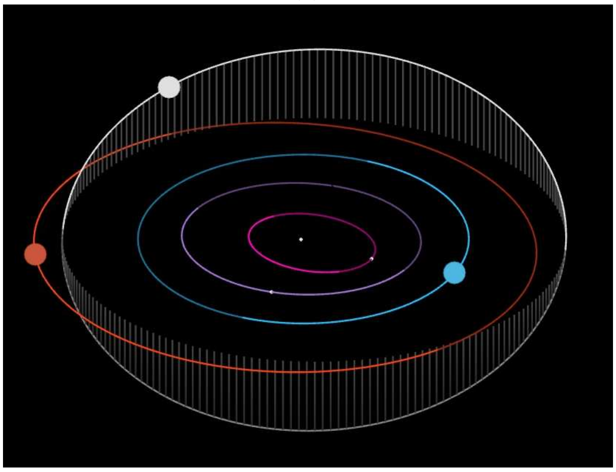

(c)

Figure 6.2: Orbits of the four inner planets of the solar system and three Martian Trojans (same as in Figure 6.1); Blue: Earth, red: Mars, white: Trojan; Reference Frame: ecliptic and mean equinox/J2000; epoch: 2034-06-15; a: 5261 Eureka, b: 1998 VF_{31} (101429), c: 2007 NS_2 (311999). Drop lines of the trojan orbits are used to show the elevation about the ecliptic. Images generated with JPL's SSD orbit viewer tool [https://ssd.jpl.nasa.gov/tools/orbit_viewer.html] .

6.3 Method

Spacecraft transfers to Mars are common practice and all available launch windows up to the year 2045 have been analyzed in detail Burke et al. (2010); Sergeyevsky and Cunniff (1987). In this paper we analyze trajectories from Earth to Mars involving flybys at Martian Trojans. Consequently, we first search for trajectories from Earth to each Trojan and then from this Trojan to Mars.
For the study we focus on solving Lambert's problem to search for transfer trajectories with low requirements for delta-v. Solving Lamberts problem is a method for determining spacecraft trajectories but it has limitations such as only assuming gravitational forces, assuming the spacecraft is a point mass, and needing precise initial conditions. Nevertheless, the results give a very good estimate about the required delta-v demand which are required for a mission. Details about the lambert solver are given in section 6.3.2.

6.3.1 Ephemeris Data

To calculate a trajectory from Earth to Mars with a flyby at the Martian Trojans, the positions of each body at given times are needed. The positional information for Earth and Mars is extracted from recent ephemeris data DE431 (Folkner et al., 2014), conveniently stored in the format of SPICE kernels (Acton et al., 2018; Acton, 1996), available from JPL's SPICE website (NAIF, 2019). Ephemeris kernels (SPK) for the Trojans were downloaded from, JPL's HORIZONS tool (JPL, 2022).

6.3.2 Solving Lambert's Problem

We search for physically possible trajectories connecting two position vectors within a given time of flight. We assume an unperturbed two-body problem, with the sun as central body. The issue is well known as the so-called "Lambert's Problem" or sometimes referred to as the "orbital boundary value problem" (Izzo, 2015). For solving the Lambert problem, we used the so-called "Izzo2015"-algorithm (Biscani and Izzo, 2019; Biscani et al., 2010), which conveniently delivers the velocity vectors of the spacecraft at the beginning and end of the orbit arc.
In our model we access the solver twice, as we search for a three-impulse model for connecting three positions in space. The first impulse is used to obtain a transfer trajectory from Earth to a Martian Trojan. The second maneuver is then used to adjust the spacecraft trajectory from the Martian Trojan to a Mars transfer. With the last impulse we model the orbit insertion at Mars.
In our calculation we allow multiple revolutions about the sun for both, the transfer to the asteroid as well as the transfer from the asteroid to Mars. This implies rather long transfer times, significantly longer than the typical direct Hohmann-type transfers from Earth to Mars (within approx. 9 months). The calculation is performed by scanning through a two-dimensional space with the first dimension being the launch date and the second dimension being the transfer duration (which constrains the time of arrival).
For each launch and arrival date the position and velocity vectors (state vectors) of Earth and the Trojan are determined. All calculations were repeated for trajectories from the Trojans to Mars.
The solution of Lambert's Problem readily yields the required velocity increments for each transfer.
As a result we obtain the so-called "porkchop plots" (Woolley and Whetsel, 2013). To limit the possible transfer scenarios, we constrained the launch dates to a range between January 2025 and Dec 2045 and to transfer durations between 100 and 1200 days. The time discretization (step size) was set to 1 days for both, launch date and transfer duration. The simulations are performed for each Martian Trojan individually.

Modeling the Launch and transfer to a Trojan

As a first step we modeled the launch from Earth and the transfer to the Trojan. Assuming constraints as in ESA's M7-class mission call, we adopted an Ariane62 for launch from the Guyana spaceport, where, reliable performance data on maximal S/C launch mass and delta-v were available (ESA, 2021). Hence, from given results of Lambert's problem (v_{inf} and the declination of launch asymptote) connecting Earth and the Martian Trojans, we were able to determine the feasible launch dates. We assumed a direct insertion into a transfer orbit by the launcher. After the launch the remaining two maneuvers have to be established with the onboard S/C propulsion system.

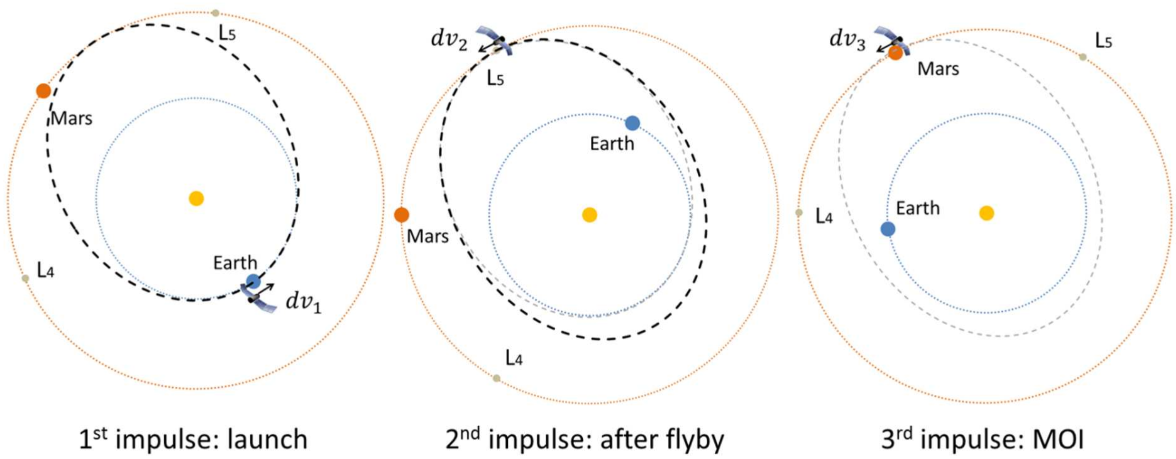

Figure 6.3: Overview of the three impulses

Flyby impulse

After the launch and the interplanetary cruise, the S/C will reach a Martian Trojan. Shortly after the flyby at a Trojan a second maneuver is performed. The maneuver adjusts the orbit in such way that the trajectory of Mars is intersected (see Figure 6.3, 2nd impulse). Again, Lambert's problem is solved for a trajectory from the Trojan to Mars. Here, the flyby date is used as the start date. Again, all possible transfer durations from 100 to 1200 days are scanned through with a step size of two days. The mass of the Trojans is neglected.

Mars orbit insertion (MOI)

The final maneuver is used for Mars Orbit Insertion (MOI). The required delta-v for a C3=0 orbit insertion (i.e. parabolic orbit) is determined. The distance to the surface at closest approach is set to 200 km, i.e. 3590 km pericenter distance for a mean Martian radius of 3390 km (Seidelmann et al., 2007).

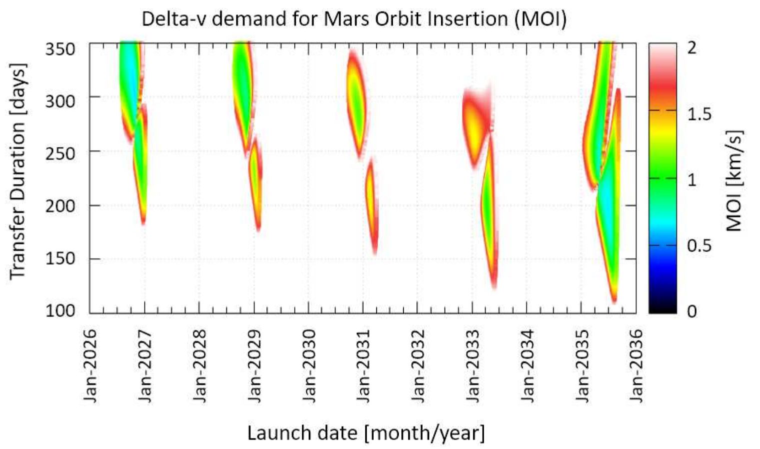

Figure 6.4: Δv demand for mars orbit insertion at a parabolic orbit with C3=0 for a nominal earth-mars mission. The shown launch dates from Earth are limited to a Δv demand of less than 7km/s.

To allow a delta-v comparison between a nominal Mars mission and the scenarios proposed here, we determined values for Mars orbit insertion of a nominal mission. Direct Earth-Mars missions typically require approximately 0.6-1 km/s or more for Mars Orbit insertion (Burke et al., 2010; Morley et al., 2004). Additionally, we used our Lambert solver to determine the required delta-v. The results are shown in Figure 6.4 and confirm that the typical delta-v demand is at least 0.6 km/s. We know that this value is very mission depending, but we chose it to allow a better comparison between the two scenarios.

Consequently, the delta-v demand for flyby and MOI shown in this paper minus 0.6 km/s give the required additional delta-v compared to a nominal mission to Mars. For example, a launch window for Trojan 311999 in August 2034 (see section 6.4.4) requires 0.6 km/s for the flyby maneuver and Mars orbit insertion. With a typical delta-v demand of 0.6 km/s for MOI, the delta-v difference is 0 km/s compared to a nominal

Mars mission. However, this does not necessarily imply that the delta-v for the flyby maneuver is 0 km/s, but a maneuver at the Trojan can also lead to a reduced delta-v demand for MOI. In this example, the flyby delta-v is 0.07 km/ while the MOI delta-v is 0.53 km/s.

Trajectory Results

After calculating the three previous steps the overall Δv demand for the transfer to Mars is determined by summing up the required Δv of all three maneuvers. As a result, we get a 3-dimensional porkchop plot with the first axis showing the launch date, the second axis the transfer duration from Earth to the Trojan and the third axis showing the transfer duration from the Trojan to Mars. To reduce complexity, only total transfer times from the two transfer legs were considered. Besides, we only consider total Δv requirements.

With the above-mentioned time frame and time discretization this leads to 1.1 Billion different trajectories which have be analyzed for each Trojan. Consequently, we have 9.9 Billion trajectories in total (see section 6.4).

6.4 Results

In order to visualize the results, we consider best results only, i.e. the shortest transfer and lowest total Δv demand. Specifically, we set the sum of Δv for maneuver 2 (flyby) and maneuver 3 MOI to $\leq 2km/s$. The results for all Martian Trojans are shown in Figure 5, including all launch dates and transfer scenarios that meet these conditions.

The results show that all flybys occur close to the points where the Trojans pass through the ecliptic (and the orbital plane of Mars), where the S/C trajectories do not require costly Δv for inclination changes. Unfortunately, this is also the point where the Trojans have the highest vertical velocity relative to the ecliptic. Their inclinations between 16.7 and 31.3 degrees lead to high flyby velocities between approximately 6 and 13 km/s. These high vertical velocities can be seen as the main reason why a direct rendezvous with the Trojans is very costly in terms of Δv. A spacecraft would have to perform maneuvers to adjust its velocity to match that of the Trojans.

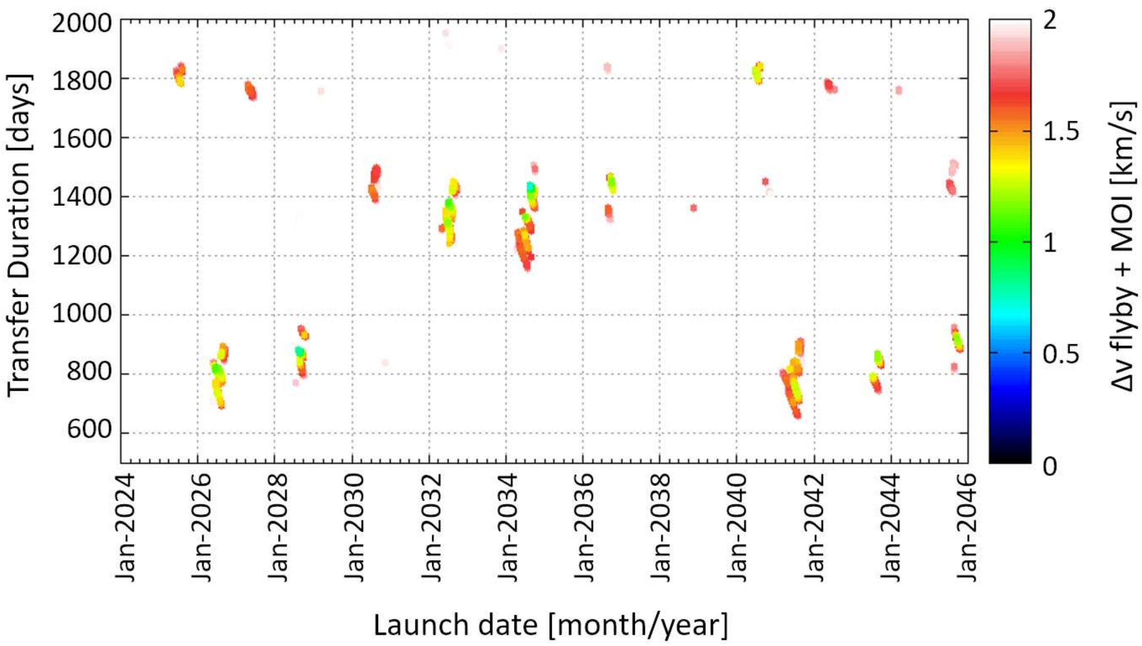

Figure 6.5: Contour plot with all available launch dates and corresponding transfer times for all 8 trailing Trojans (for the leading Trojan, see section 6.4.3). The color coding shows the required delta-v sum for the maneuver after the Trojan flyby and for Mars Orbit insertion with C3=0

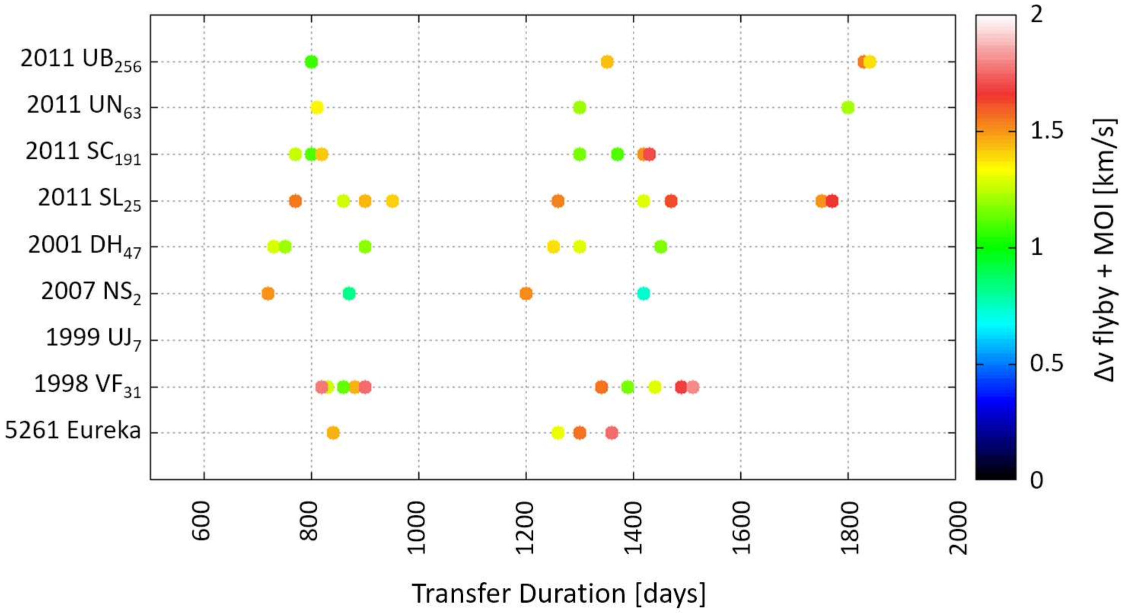

Figure 6.6: Transfer times for each launch window with a flyby at a Trojan. The color coding shows the required delta-v sum for one maneuver after Trojan flyby and for Mars Orbit insertion with C3=0.

Figure 6.6 summarizes the available scenarios for each Trojan. Especially the points with transfer times < 1000 days and delta-v demand $\leq 1.5km/s$ are the most interesting for a possible mission.

Short mission durations reduce costs for operation and the overall spacecraft life time can be reduced. Secondly the Δv demands have a direct impact on the spacecraft mass as higher Δv's require more propellant.

In the following subsection we show the results for the most interesting targets. Launch windows for all Trojans are summarized in the Annex. The launch window dates in the tables give only the year and month of the optimal launch date. The launch windows have typically a timeframe of ± 7 to 10 days leading to a size of approximately 2-3 weeks.

6.4.1 5261 (Eureka)

From the scientific point of view, Eureka is the most interesting target. Unfortunately, 5261 Eureka is not the easiest target to reach. In terms of Δv and duration the optimal launch date is in Jun 2041 with a total transfer time of 2.3 years. The spacecraft would require a Δv of at least $1.01^{km}/_{s}$ for maneuver after Trojan flyby and Mars Orbit insertion. An earlier alternative are the launch windows in 2032. Within approximately 3.5 years it would be possible to fly by at Eureka and enter Mars orbit with moderate Δv demand of $1.27 - 1.40^{km}/_{s}$. For Eureka we find different transfer opportunities within our constraints, which are summarized in Table 6.2.

Table 6.2: Launch window for (5261) Eureka

Launch Window	mean Flyby date	mean Mars Arival	Aprox. Transfer Duration [days]	optimum Δv $[^{km}/_{s}]$
May 2032	Jun 2034	Nov 2035	1284	1.40
Jul 2032	Jun 2034	Jan 2036	1270	1.27
Nov 2038	Feb 2041	Oct 2042	1452	1.35
Jun 2041	Jan 2042	Nov 2043	840	1.01

Table 6.3: Launch window for (101429) *1998 VF*$_{31}$

Launch Window	mean Flyby date	mean Mars Arival	Aprox. Transfer Duration [days]	optimum Δv [km/s]
Aug 2026	Nov 2027	Mar 2029	950	0.97
Aug 2028	Sep 2029	Jan 2031	870	1.20
Aug 2030	Jul 2033	Nov 2034	1550	1.04
Aug 2032	May 2035	Sep 2036	1500	0.95
Sep 2034	Mar 2037	May 2038	1335	1.01
Sep 2036	Feb 2039	May 2040	1390	1.34
Aug 2041	Nov 2042	Apr 2044	970	1.16
Sep 2043	Oct 2044	Nov 2045	800	0.98

6.4.2 101429 (1998 VF31)

1998 VF31 offers many launch options almost every two years in the specified time frame. The launch date in August 2026 offers a low transfer time of 2.6 years and a low Δv demand of less than $1^{km}/_{s}$. A good alternative for 101429 is the launch date in Sep 2043 with a transfer time of 2.4 years and Δv demand of $0.98^{km}/_{s}$.

It is worth mentioning that Aug 2026 together with Sep 2043 are the best launch window for 2007 NS2 in terms of delta-v and transfer duration (see Table 6.3).

6.4.3 121514 (1999 UJ7)

No trajectory solution was found for Trojan 121514, located at the leading Lagrange Point L4.

This can be understood by a quick analysis of the spacecraft orbital transfer scenarios:

Note that the semi-major axes and the orbital periods of all Mars Trojans are identical to those of Mars ($a_{mars} = 1.5AU; 687days$). Also note that the transfer ellipse of a spacecraft on its way from Earth to a Mars Trojan has a perihelion distance at approximately the mean Earth distance of 1 AU and an aphelion distance of approximately the mean Mars distance of $1.52AU$. Consequently, the semi-major axis and the orbital period on this transfer ellipse can be calculated as $a_{EM} = 1.26AU$ and $T = 518days$ (i.e, 169 days less than the orbital period of Mars). The mean angular velocity of Mars and his Trojans is $\omega_{mars} = {}^{360°}/_{687d} = 0.524°/_{d}$.

Assuming that the S/C does not perform any maneuvers after a flyby at the L5-Trojan (approx. 60° trailing behind Mars) and just “stays” on its transfer orbit. As the spacecraft needs 169 days less for one full revolution about the sun it will be 88° ahead, i.e., 28° ahead of Mars, when intersecting the planet’s orbit again. Consequently, for a Mars intersection after one orbit, only a minor course correction (slight increase of the semi-major axis) is required.

For the L4 Trojan (moving approx. 60° ahead of Mars) the situation is less fortunate. The S/C has to increase its semi-major axis significantly to become “slower” than Mars and to intersect the planet after one revolution. Hence, such missions will be far from the resource margins used in this paper.

6.4.4 311999 (2007 NS2)

From the technical point of view, 311999 can be considered the best target. Especially the launch window in 2028 offers short transfer duration of 2.4 years with a low Δv demand of $0.59^{km}/_{s}$. This trajectory also offers a very special case, where the impulse maneuver at the Trojan is (almost) not required. The Δv required for bringing the spacecraft on course towards Mars is only $0.02^{km}/_{s}$.

The launch window in Aug 2034 requires almost the same amount of Δv, but this launch window allows only trajectories lasting at least 3.8 years.

311999 is also the only asteroid for which total transfer duration of less than 2 years is possible. The launch window in 2041 allows a very fast transfer but at a high demand for Δv.

This concludes that 311999 could be considered the best option in terms of costs and technical feasibility. However, only 3 launch windows have been found for the asteroid in this study (see Table 6.4.

Table 6.4: Launch window for (311999) 2007 NS_2

Launch Window	mean Flyby date	mean Mars Arival	Aprox. Transfer Duration [days]	optimum Δv [km/s]
Aug 2028	Jan 2029	Jan 2031	900	0.59
Aug 2034	Aug 2036	Jul 2038	1450	0.60
Jun 2041	Mar 2042	May 2043	710	1.50

6.5 Summary

In this paper we show that transfers from Earth to Mars involving a flyby at a Mars Trojan are possible with low demands for additional delta-v between 0 and 1.0 km/s, compared to missions involving Mars only.

From a scientific point of view, (5261) Eureka would be the most interesting target for such a flyby mission. A flyby at Eureka would be possible, but the conditions are not optimal. Details for Eureka are summarized in section 6.4.1. Significantly better trajectories were found for 2007 NS_2. In terms of mission duration and required delta-v, 2007 NS_2 offers the best options for a flyby mission (see section 6.4.4). It is also interesting to note that there are no solutions for 1999 UJ_7, which is the only Trojan located at L4. An explanation for this issue can be found in section 6.4.3. Finally, 101429 (1998 VF_{31}) is the Trojan for which the highest amount of solutions was found.

We propose a flyby of 311999 (2007 NS_2), which offers two launch opportunities (August 2028 and August 2034) and transfer options with an overall Δv demand about 0.6km/s for the flyby maneuver and Mars orbit insertion. The required Δv in both cases is comparable to a nominal mission to Mars. The additional demand is negligible, but the transfer duration is increased significantly.

Unfortunately, the interesting binary Trojan (5261) Eureka is difficult to reach. The trajectories found (launch in July 2032) require about 1.3km/s Δv (0.5km/s for the flyby maneuver) and an overall cruise of 1270 days. A flyby at Eureka increases the overall cost, due to the high required propellant mass and the long operation times.

We propose alternative missions with low demand for propellant and cruise time for 101429 (1998 VF_{31}) with a launch in September 2043; 385250 (2001 DH_{47}) with a launch in July 2041; (2011 SC_{191}) and (2011 UB_{256}) both with a launch window in July 2026.

Our mission scenarios are constrained by the performance of the launcher. In particular, the asymptote of the departure trajectory of the Ariane 6.2 launched from Kourou (Section 6.3.2) is strictly limited to high- or to negative declinations. It is conceivable to place the S/C in a low Earth orbit or in a geo-transfer orbit. Then, the required Δv for a transfer to the Trojans would have to be provided by the S/C itself. This would lead to higher mass allowance but increase the overall Δv requirements. However, a new analysis of the Δv budget would be required.

In addition, the 3-impulse model we used in our simulation (where we use only one course correction shortly after the flyby) is not optimized yet. Correction maneuvers during cruise could increase the available payload mass and reduce Δv demands.

The model we used in the simulation is an enhanced 2-body problem in principle, involving the spacecraft orbiting about the sun. We find that perturbational forces such as gravity of other planets and nonconservative forces such as solar radiation pressure will have only a small impact on the trajectory and the overall results of this paper.

Author Statement

I, Kai Wickhusen, served as the corresponding author and was responsible for performing the calculations, developing the software, and writing the main text. Jürgen Oberst provided supervision for the paper, offered feedback, and contributed to the conceptualization and methodology. Friedrich Damme, an expert in space flight dynamics, helped with the methodology and software development, and also assisted with validation. Finally, Apostolos Christou, provided a list of Trojans with secure orbits, the current state of knowledge on their orbital and physical properties and their scientific significance.

Declaration of competing interest

The authors declare that they have no known competing financial interests or personal relationships that could have appeared to influence the work reported in this paper.

Data availability

Data will be made available on request.

References

All references were moved and collected in the Bibliography

Annex

The following Table 6.5 summarizes all launch Windows with a Δv demand $\leq 1.8^{km}/_{s}$.

Table 6.5: Summary of all possible transfer scenarios

Trojan	Launch Window	mean Flyby date	mean Mars Arival	Aprox. Transfer Duration [days]	optimum Δv [$^{km}/_{s}$]
2011UN63	Jun 2025	Sep 2028	Jun 2030	1800	1,38
2011UN63	Jun 2032	May 2034	Feb 2034	1300	1,2
2011UN63	Jul 2040	Oct 2043	Jun 2045	1800	1,22
2011UN63	Jun 2041	Dec 2041	Sep 2043	810	1,34
2011UB256	Jul 2025	Nov 2028	Aug 2030	1830	1,54
2011UB256	Jul 2026	Dec 2026	Sep 2028	800	1,08
2011UB256	Jul 2032	Jun 2034	Mar 2036	1350	1,43
2011UB256	Aug 2040	Nov 2043	Aug 2045	1840	1,38
2011SL25	Aug 2026	Aug 2027	Dec 2028	860	1,27
2011SL25	Mai 2027	Jul 2030	Mar 2032	1750	1,51
2011SL25	Sep 2028	Jul 2029	Apr 2031	950	1,4
2011SL25	Aug 2030	Mar 2033	Aug 2034	1470	1,62
2011SL25	Aug 2032	Feb 2035	Jul 2036	1420	1,29
2011SL25	Mai 2034	Mar 2036	Oct 2037	1260	1,53
2011SL25	Apr 2041	Nov 2041	Jun 2043	770	1,54
2011SL25	Aug 2041	Aug 2042	Jan 2044	900	1,44
2011SL25	Mai 2042	Aug 2045	Mar 2047	1770	1,65
2011SC191	Jul 2026	Sep 2027	Oct 2028	800	1,1
2011SC191	Jul 2030	Apr 2032	Jun 2034	1420	1,51
2011SC191	Jul 2032	Mar 2035	Apr 2036	1370	1,1
2011SC191	Jul 2034	Jan 2037	Mar 2038	1300	1,16
2011SC191	Jul 2041	Sep 2042	Oct 2043	820	1,42
2011SC191	Jul 2043	Jul 2042	Sep 2045	770	1,25
2011SC191	Jul 2045	May 2048	Jun 2049	1430	1,7
385250	Jul 2026	Jun 2027	Jul 2028	730	1,28
385250	Jul 2032	Dec 2034	Jan 2036	1300	1,29
385250	Jul 2034	Nov 2036	Dec 2037	1250	1,38
385250	Sep 2036	Sep 2038	Sep 2040	1450	1,17
385250	Jul 2041	Jun 2026	Aug 2043	750	1,2
385250	Sep 2045	Mar 2046	Mar 2048	900	1,18
311999	Sep 2028	Feb 2029	Jan 2031	870	0,82
311999	Mai 2034	Jul 2036	Sep 2037	1200	1,52
311999	Sep 2034	Aug 2036	Jul 2038	1420	0,73
311999	Mai 2041	Mar 2042	May 2043	720	1,5
101429	Aug 2026	Nov 2027	Feb 2029	880	1,45
101429	Sep 2028	Oct 2029	Dec 2030	830	1,27
101429	Sep 2030	Jul 2033	Sep 2034	1490	1,68
101429	Sep 2032	May 2035	Aug 2036	1440	1,29
101429	Sep 2034	Apr 2037	Jun 2038	1390	1,16
101429	Sep 2036	Feb 2039	May 2040	1340	1,55
101429	Aug 2041	Dez 2042	Feb 2044	900	1,75
101429	Sep 2043	Oct 2044	Jan 2046	860	1,13
101429	Aug 2045	Sep 2046	Nov 2047	820	1,78
101429	Sep 2045	Jul 2047	Jul 2049	1510	1,80
5261	Mai 2032	Jun 2034	Nov 2035	1300	1,55
5261	Jul 2032	Jun 2034	Dec 2035	1260	1,3
5261	Nov 2038	Feb 2041	Aug 2042	1360	1,75
5261	Jun 2041	Jan 2042	Oct 2043	840	1,45

Chapter 7

DePhine – The Deimos and Phobos Interior Explorer

Research Paper III

Published version, 2018 in Advances in Space Research
https://doi.org/10.1016/j.asr.2017.12.028

Jürgen Oberst [a,b], Kai Wickhusen [a], Konrad Willner [a], Klaus Gwinner [a], Sofya Spiridonova [c], Ralph Kahle [c], Andrew Coates [d], Alain Herique [e], Dirk Plettemeier [f], Marina Diaz-Michelena [g], Alexander Zakharov [h], Yoshifumi Futaana [i], Martin Pätzold [j], Pascal Rosenblatt [k,o], David J. Lawrence [l], Valery Lainey [m], Alison Gibbings [n], Ingo Gerth [n]

a. German Aerospace Center (DLR), Institute of Planetary Research, Rutherfordstr. 2, D-12489, Berlin, Germany
b. Technical University Berlin, Institute of Geodesy and Geoinformation Science, Strasse des 17. Juni 135, D-10623 Berlin, Germany
c. German Aerospace Center (DLR), Space Flight Technology, D-82234 Oberpfaffenhofen-Wessling, Germany
d. Mullard Space Science Laboratory, University College London (MSSL-UCL), Holmbury St Mary, Dorking RH5 6NT, UK
e. Univ. Grenoble Alpes, CNRS, IPAG, F-38000 Grenoble, France
f. Technische Universität Dresden, Professur für Hochfrequenztechnik, Würzburger Str. 35, D-01187 Dresden, Germany
g. Space Programs and Space Sciences Department, Instituto Nacional de Tecnica Aeroespacial (INTA), Madrid 28850, Spain
h. Space Research Institute of the Russian Academy of Sciences, Profsoyuznaya ul. 84/32, 117997 Moscow, Russia
i. Swedish Institute of Space Physics, Box 812, SE-98128 Kiruna, Sweden
j. Rheinisches Institut für Umweltforschung, Universität zu Köln, D-50931 Köln, Germany
k. Royal Observatory of Belgium (ROB), Belgium
l. Space Department, The Johns Hopkins University, Applied Physics Laboratory, 11100 Johns Hopkins Road, Laurel, MD 20723, USA
m. Institut de Mecanique Celeste et de Calcul de Ephemerides, Observatoire de Paris, UMR 8028 du CNRS, UPMC, 77 Av. Denfert-Rochereau, F-75014 Paris, France
n. OHB System AG, Universitätsallee 27-29, D-28359 Bremen, Germany
o. Present address: Advanced Computing Research Institute - Sciences de la Terre (ACRI-ST), 260, route du Pin Montard - BP 234 - F-06904 Sophia Antipolis Cedex, France

Abstract

DePhine – Deimos and Phobos Interior Explorer – is a mission proposed in the context of ESA's Cosmic Vision program, for launch in 2030. The mission will explore the origin and the evolution of the two Martian satellites, by focusing on their interior structures and diversity, by addressing the following open questions: Are Phobos and Deimos true siblings, originating from the same source and sharing the same formation scenario? Are the satellites rubble piles or solid bodies? Do they possess hidden deposits of water ice in their interiors? The DePhine spacecraft will be inserted into Mars transfer and will initially enter a Deimos quasi-satellite orbit to carry out a comprehensive global mapping. The goal is to obtain physical parameters and remote sensing data for Deimos comparable to

data expected to be available for Phobos at the time of the DePhine mission for comparative studies. As a highlight of the mission, close flybys will be performed at low velocities, which will increase data integration times, enhance the signal strength and data resolution. 10–20 flyby sequences, including polar passes, will result in a dense global grid of observation tracks. The spacecraft orbit will then be changed into a Phobos resonance orbit to carry out multiple close flybys and to perform similar remote sensing as for Deimos. The spacecraft will carry a suite of remote sensing instruments, including a camera system, a radio science experiment, a high-frequency radar, a magnetometer, and a Gamma Ray/Neutron Detector. A steerable antenna will allow simultaneous radio tracking and remote sensing observations (which is technically not possible for Mars Express). Additional instrumentation, e.g. a dust detector and a solar wind sensor, will address further science goals of the mission. If Ariane 6–2 and higher lift performance are available for launch (the baseline mission assumes a launch on a Soyuz Fregat), we expect to have greater spacecraft mobility and possibly added payloads.

7.1 Introduction

DePhine – the Deimos and Phobos Interior Explorer – has been proposed as M-class mission in the context of ESA's Cosmic Vision program, with the spacecraft projected for launch in 2030. The mission will explore the origin and the evolution of the Martian natural satellites and will also contribute to the general questions of planetary formation and the workings of the solar system. Up to the present day, the origins of Phobos and Deimos are uncertain. They may have co-accreted with the parent planet (Safronov and Vitjazev, 1986), or formed from Martian impact basin ejecta (Citron et al., 2015; Craddock, 2011; Rosenblatt and Charnoz, 2012; Rosenblatt et al., 2016). Alternatively, they may represent captured primitive asteroids or comets (Burns, 1992). Clues on the origins of the satellites may come from comparative studies of whether Phobos and Deimos are true siblings, originate from the same source and share the same formation scenario and history. Other clues may come from investigations of the interior structures of the satellites, e.g., to resolve whether the satellites are rubble piles or solid bodies, or whether they possess hidden deposits of water ice in their interiors.

The DePhine spacecraft will initially enter a quasi-satellite orbit of Deimos to carry out a comprehensive remote-sensing campaign. The spacecraft will then move into an orbit in resonance with Phobos to carry out multiple flybys and to perform remote sensing experiments similar to those for Deimos to enable comparative studies. The spacecraft will carry a suite of remote sensing instruments, including a camera system, a radio science experiment, a high-frequency radar, a magnetometer, and a Gamma- Ray/Neutron spectrometer (GRNS). In addition, the spacecraft will be equipped with dust detectors and a solar wind sensor.

7.2 Science Cases

The mission aims at investigations of the origins of the two satellites, by an in-depth study of the diversity of Deimos and Phobos. Quite naturally, the mission will first focus on Deimos, to obtain its physical parameters and characteristics, at a level comparable to information already available for Phobos. In particular, we wish to determine the properties of the Deimos soil to enable comparisons with Phobos samples, expected to be available at the time of DePhine from the upcoming Phobos sample return missions such as MMX (Fujimoto et al., 2017; Kuramoto et al., 2017). In addition, the mission will focus on the interior structures of both satellites.

7.2.1 Science Case 1: Interior Structure of Deimos and Phobos

The DePhine spacecraft will address the question of interior structure by various techniques, including gravity field mapping to high degree and order, direct radar observations to infer the structure of the upper layers of the moons, studies of rotational dynamics, magnetic sounding, and gamma-ray/neutron flux detections.

Mass and Gravity Field

The knowledge of the gravity field when combined with other bulk parameters, such as shape, volume, bulk density, porosity, and water ice content are key information for models of internal mass distribution, structure, composition, and Deimos/Phobos origins. Using data from X-band radio tracking during recent spacecraft flybys, especially by Mars Express (Andert et al., 2010; Pätzold et al., 2014b; Rosenblatt et al., 2008), the mass of Phobos has been estimated as 1.065 ± 0.016 x 10^{16} kg (Pätzold et al., 2014a). The higher degree and order terms of the gravity fields (e.g., the C_{20} and the C_{22} terms) of Phobos suffer from large uncertainties (Pätzold et al., 2014b), due to the faint gravity signatures, the high spacecraft flyby speeds and the large flyby distances. Besides, even though the Phobos ephemeris has improved over the years (Lainey et al., 2007; Jacobson, 2010), the Phobos positions relative to the spacecraft during the flybys were poorly known. For Deimos, only rough mass estimates from the early Viking flybys and from secular modeling are available, i.e., 1.51 ± 0.04 x 10^{15} kg (Jacobson, 2010).

DePhine will move in "quasi satellite orbits" (see description later in the text), close to Deimos and Phobos, supported by optical navigation. Benefitting from a state-of-the art radio science experiment, even small spacecraft trajectory perturbations are revealed by the Doppler shift of the radio carrier. Effects of non-gravitational perturbations, e.g. solar radiation pressure and atmospheric drag as well as spacecraft control maneuvers (or wheel-off-loadings), will be carefully modeled in the process.

While the current knowledge of Phobos' mass has an uncertainty of about 18% (and higher order gravity parameters have uncertainties larger than the actual derived values) (Pätzold et al., 2014a,b), the DePhine radio tracking will determine the mass at an accuracy of 0.01%, the second degree and order gravity field coefficients at 1% accuracy and the degree and order five gravity field coefficients at 50% accuracy.

Shape and Rotation

Early attempts to derive Deimos and Phobos shape models were based on Mariner 9 and Viking TV camera images. These included tri-axial ellipsoids (Duxbury, 1974) or spherical harmonics representations. Duxbury (1991) determined over 300 control points, to solve for a Phobos shape model represented by of a spherical harmonics function with degree and order 8. Primarily based on limb as well as terminator observations by Simonelli et al. (1993); Thomas (1989) derived a 2° x 2° gridded shape model. The models have a relative accuracy ranging between ±70 m and ±50 m with locally larger uncertainties due to limited surface coverage. Willner et al. (2010); Willner et al. (2014) produced Phobos shape models using image data from the High Resolution Stereo Camera (HRSC) (Jaumann et al., 2007) and the Super Resolution Channel (Oberst et al., 2008) on-board the Mars Express spacecraft. A gridded Digital Terrain Model (DTM) (grid spacing: 100 m; relative accuracy: 25 m) and a spherical harmonic model (degree and order 45) were derived (Willner et al., 2014). With improved shape models, Phobos is estimated to have a volume of 5742 ± 35 km^3 (Willner et al., 2014). The volume of Deimos has been determined from Viking images as 1017 ± 130 km^3 (Thomas, 1993).

Both, Deimos and Phobos are in a locked rotation. Owing to their odd shapes and their slightly elliptic orbits, the satellites are undergoing physical librations. The librational amplitude of Phobos was determined from direct observations and control point tracking by Mars Express and Viking Orbiters (Burmeister et al., 2014; Oberst et al., 2014; Willner et al., 2010) as well as from the effect on Phobos' orbital motion (Jacobson, 2010; Lainey et al., 2021). Reported libration amplitudes vary from 0.99° to 1.2° ± 0.15°, corresponding to a displacement at the equator of approximately 230 to 280 m. For Deimos, moving at larger distance from Mars in an orbit of smaller eccentricity, the amplitude of libration is predicted from the given orbit, gravitational interaction with Mars, and the shape model as 0.2° (20 m at the equator) (Rubincam et al., 1995), which remains to be verified.

DePhine will survey Deimos systematically and globally with a higher resolution than any other spacecraft before, which will result in higher-accuracy on both, shape and rotation parameters. For example, DePhine will allow to derive volume estimates for Deimos with uncertainties in the order of 1% and better (currently above 10%) and a first observation of the librational motion of Deimos will be possible. For Phobos, DePhine will collect high-resolution topographic data, especially during the very close and low-velocity flybys, which will refine our shape models and fill gaps in our current coverage.

Interior Models

Our current knowledge about the interiors of Deimos and Phobos is almost entirely based on indirect conclusions from estimates of mass, shape, and rotation. From the improved mass and the volume of Phobos and Deimos, the bulk densities of the two satellites have been estimated as 1.860 +/- 0.02 g/g/cm^3 (Willner et al., 2014) and 1.48 $\pm$ 0.22 g/cm^3 (Rosenblatt, 2011) respectively, suggesting that their interiors have a high porosity and/or contain water ice (Avanesov et al., 1991; Murchie et al., 1991). The respective required porosity ranges are between 10-30% (Murchie et al., 1991) and 33-66% (Rosenblatt, 2011), which are comparable with porosities of small-sized asteroids (Britt et al., 2002). This attests to an accretion process in which large blocks form an initial core with abundant voids that smaller debris are unable to fill and would support origin scenarios from a planetary debris disk (Citron et al., 2015; Craddock, 2011; Rosenblatt and Charnoz, 2012; Rosenblatt et al., 2016). The low density can also be explained by sufficient water ice in the satellite interiors, depending on rocky material density and porosity. Detection of ice repositories would provide a strong constraint on the moons origins. However, neither the proportions of rock and water nor the origin of Deimos and Phobos can be constrained by the bulk density alone (Pätzold et al., 2014a; Rosenblatt, 2011). Phobos' shape models together with models of rock-water ice mixtures have been used to predict moment of inertia coefficients of the satellite (Willner, 2009; Rosenblatt et al., 2009). These may be tested against observed Phobos libration amplitudes and gravity field coefficients, following dynamic theories by Borderies and Yoder (1990). However, the observed shape models, libration amplitudes and the (poorly constrained) gravity parameter C20 can be brought in agreement with a wide variety of compositional models including a homogeneous mass distribution. Also, knowledge of obliquity, i.e., the tilt of the rotational axis with respect to the orbit plane is critical, which is currently assumed to be zero. The DePhine mission will improve our knowledge on the interior structure, mass distribution, shape, and volume by various techniques leading to improvements in uncertainty i.e. for the bulk density of Deimos by at least 10% to 1% or better.

Subsurface Structure

In order to discriminate among the various formation scenarios of the Martian satellites, sophisticated experiments directly observing the interior are needed that constrain the subsurface structure and bulk compositional elements (Herique et al., 2018). Secondary radar echoes were revealed by MARSIS on Mars Express (Picardi et al., 2004) during Phobos flybys, but analyses of the data remained inconclusive. Shape models of Phobos were used to produce simulations of radar backscattering to separate surface from subsurface echoes (Plettemeier et al., 2009). Unfortunately, no echoes could be positively identified as coming from the subsurface. This can be attributed to the comparably large flyby distances to Phobos and the high relative velocities between spacecraft and target of 3 km/s limiting the performance of MARSIS by short effective integration times. The horizontal resolution of MARSIS in combination with the irregular shape of Phobos resulted in a Signal to Noise Ratio (SNR) of 25 dB in this best case, while a SNR of 50 dB has been achieved with MARSIS on a flat Mars surface under similar conditions. In addition, Phobos' fragmentation might be invisible to the MARSIS radar as fragment block sizes might be smaller than the applied wavelength (50–150 m). Furthermore, rocks with high metal content and carbonaceous chondrites are materials known with high dielectric loss properties resulting in possible signal absorption by Phobos' loose material.

The DePhine spacecraft will overcome the issues experienced with Mars Express flybys. The quasi synchronous orbit allows for longer integration times as the relative velocity will be in the order of less than 5 m/s. The radar package consists of a high frequency and low frequency channel optimized for the DePhine mission (see Section 7.4.1).

Magnetic field measurements can be used to support subsurface sounding and determine the conductivity or resistivity of the body's interior based on the induced response to the variable environment (Constable and Constable, 2004). The measurements indicate the intensities and spatial variability of remnant magnetic characteristics of the exposed surface as well as rocks down to several kilometers below the surface (Veselovsky, 2004). The detection of a remnant magnetic signature on these moons would support the hypothesis of an impact-related formation scenario, during which magnetized crustal rocks (Acuna et al., 1999) were ejected from Mars as a consequence of the large impact event, and re-accreted in orbit (Citron et al., 2015; Ramsley and Head, 2013a; Rosenblatt et al., 2016). In contrast, the lack of a magnetic signature would give arguments in favour of the captured asteroids formation scenario. For example, magnetic investigations during the Rosetta mission document that primitive planetary rocks, such as the carbonate chondrite of 67P/Churyumov-Gerasimenko, do not have any significant remnant magnetism (Auster et al., 2015).

Measurements of the intensity and orientation of the remnant magnetic signatures will allow us a mapping of minerals with remnant magnetism for both moons. In concert with shallow surface radar and gravity data the magnetometer measurements will improve the knowledge on compositional variations of different types of rocks as well as ice and/or voids (e.g. Basilevsky et al. (2014); Pieters et al. (2014)). This will support advanced models of the moons' structures and new scenarios for their origins.

Bulk chemistry

The competing theories for the formation and early evolution of Mars' moons make distinct predictions for their present-day surface composition (e.g., Murchie et al. (2015)), and measurements of elemental compositions can distinguish between competing hypotheses of Phobos' and Deimos' origin (7.1).

Gamma-ray and neutron spectrometer measurements can therefore test the existing formation models for Phobos and Deimos. For example, measurements of Fe, Si, and O concentrations can place Phobos and Deimos on the plot of Fig. 1, which discriminates between the differentiation state of materials (i.e. achondrites vs chondrites), and by extension, separates out different formation scenarios. Measurements of additional elements (H, Mg, and K) as well as thermal, epithermal, and fast neutrons (Elphic et al., 2016) can provide the additional information needed to constrain the formation scenarios of Phobos and Deimos.

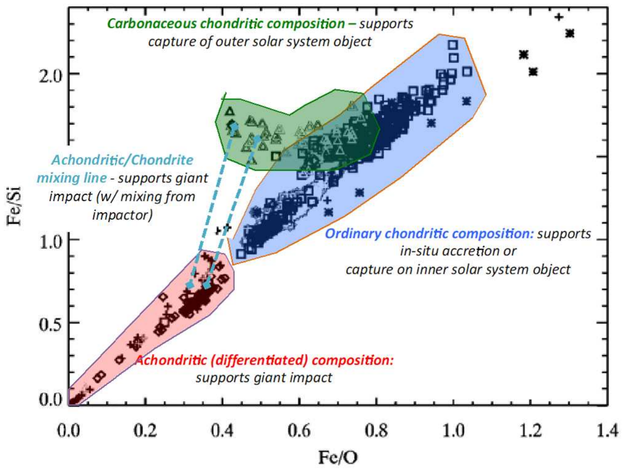

Figure 7.1: Measurements of Fe, Si, and O to distinguish between competing hypotheses of Phobos' and Deimos' origin. Figure adopted from Peplowski et al. (2015).

Gamma-ray and neutron spectroscopy represent established techniques for characterizing the elemental composition to tens of centimeters depth of planetary surfaces from orbit (see Section 7.4.4). Detected gamma-ray and neutron fluxes are converted to elemental concentrations using standard techniques (Lawrence et al., 2013; Peplowski et al., 2012). Note that DePhine currently does not foresee carrying a spectrometer, which would map the abundance of mineral compounds of very-near-surface regolith layers only.

7.2.2 Science case 2: Deimos and Phobos diversity

Perhaps the one most intriguing single observational fact in the question for the origin of the Martian satellites is that there exist two of them – not more and not less! Comparative studies of the two satellites will very much help understanding their formation. Are the two satellites siblings that have originated from the same source and by the same process? Or did they form separately through different events at different times?

The two satellites are generally similar but also strikingly different in some details. Both move in near-circular near equatorial orbits about Mars. However, Phobos is moving deep inside the Mars-synchronous orbit (subject to tidal decay and disruption), whereas Deimos is moving safely outside the synchronous orbit. The spectral characteristics of Phobos and Deimos – spectral slopes and absorption bands – are similar (Fraeman et al., 2014). Also, both satellites show a low albedo (Pieters et al., 2014). However, the bulk densities differ substantially (Murchie et al., 2015). The visual appearance of the surface morphologies are quite different as well. Currently, meaningful comparisons between the two satellites are difficult, as the data volumes and knowledge is far more limited for Deimos. The comparative studies are aggravated as both satellites are affected differently by their environments. Phobos moves deep in the gravity field of Mars and is much affected by gravitational interaction in the satellite system. Mars ejecta is certainly deposited on Phobos and may or may not have formed the prominent groove structures (Murray and Heggie, 2014; Murray and Iliffe, 2011; Ramsley and Head, 2013a,b). Both, Phobos and Deimos are differently affected by the meteoroid bombardment from various solar system sources. Solar wind interacts with the surfaces in complex ways and is responsible for effects of space weathering.

Orbital motions and gravitational interactions

The orbits of Phobos and Deimos are highly indicative for various dynamic parameters of the Martian satellite system. Because the static gravitational field of Mars is well constrained today, it is the gravity fields of the moons themselves, simultaneously with their physical libration, that will be accurately quantified from the satellites' secular orbital motion. DePhine data will tightly constrain the gravity fields of the bodies.

Meteoroid flux from crater statistics and dust impact detections

Small and large meteoroids from various solar system sources intercept the Martian satellite system, as attested by the large numbers of impact craters on Mars, Phobos, and Deimos. While the impact craters represent a powerful tool to study surface ages, craters can also be used to study the characteristics of the impactor population (Christou et al., 2014). As Phobos and Deimos are both locked in their orbits, impact rates and speeds vary across the surfaces of the satellites.

Christou et al. (2014) simulated the production of craters on Phobos from the sporadic flux of Mars-crossing asteroids and comets predicting a significant difference in the crater production rate on the leading and trailing hemisphere of Phobos. While the current crater statistics (limited by strong observational biases in the image data) do not support such a difference, accurate global crater counts by DePhine down to the smallest sizes will constrain this important effect. For unknown reasons, Deimos presents a lower number of large-sized impacts than Phobos (Thomas et al., 1992, 1996).

Mars and its satellites should also intersect a number of meteoroid streams produced by comets. However, the predicted timing and geometry of the stream encounters (see Christou et al. (2014) and references therein) have not been observationally confirmed to-date. Such streams affect the Martian upper atmosphere in a measurable way (Grebowsky et al., 2002; Molina-Cuberos et al., 2003), as was directly observed during the recent close encounter of comet C/Siding Spring with Mars. Our observations will constrain the flux of exogenous material to the Martian atmosphere and surface, including the delivery of organic compounds. DePhine will study the meteoroid encounters by using two complementary techniques: On one hand, we will study the crater population and size frequency distributions of craters on both satellites by imaging. We will search for hemispheric asymmetries in the distributions of the craters. On the other hand the dust detector in orbit will allow us to directly measure the mass distributions and motion vectors of smaller meteoroids.

Ejecta production, re-accumulation, and ring formation

Large blocks and boulders of meter-scale cover the surface of Phobos, probably representing ejecta from impacts at the large end of the size scale, in particular from formation of crater Stickney. However, due to the observations from varying spacecraft ranges, only small areas on Phobos could be imaged at sufficient resolution for detection of blocks and boulders. In fact, almost all data have been obtained during a unique Phobos flyby of the Mars Reconnaissance Orbiter in 1998 (Thomas et al., 2000). DePhine, under suitable lighting conditions, will enable surface coverage for both moons with a globally uniform image resolution (<4 m/pixel; see Section 7.4.2. Thus, in contrast to previous missions, DePhine images will provide unbiased maps of block abundances, which will allow us to test hypotheses for the sources of blocks and the dynamics of their emplacements.

In addition to the above-mentioned bombardment by meteoroids (10^{-18} g $<$ mass $<$ 10^{2} g, velocity of about 15 km/s), the surfaces of Phobos and Deimos are exposed to solar ultraviolet radiation, solar wind plasma, and cosmic rays. The sputtering causes dust particles from the regolith to be ejected from the surface and to escape. With ejection larger than escape velocity (about 10 m/s for Phobos and about 6 m/s for Deimos), but smaller than the orbital speed of the moons (V_{Ph} = 2.1 km/s for Phobos and V_D = 1.35 km/s for Deimos), particles should remain trapped in the Martian satellite system. Theoretical models (Banaszkiewicz and Ip, 1991; Ip and Banaszkiewicz, 1990; Ishimoto and Mukai, 1994; Juhasz and Horanyi, 1995; Kholshevnikov et al., 1993; Krivov and Hamilton, 1997) suggest that these dust grains form rings or tori along the orbits of the satellites.

Although the existence of such dust rings near Phobos/ Deimos orbits has been predicted more than 40 years ago (Soter, 1971), no confirmed observations of rings or tori are available. Evidence for the presence of a dust or gas in the moons' orbits, related to a possible outgassing from their surfaces, may come from magnetic field observations. Fanale and Salvail (1989) did not find any evidence for outgassing from Phobos. With no detection of oxygen ions from a distance of 100 km, the upper limit for Phobos outgassing is set at $<10^{20}$ s^{-1}. A detection was reported by Dubinin et al. (1990, 1991) and Baumgärtel et al. (1998) using the Phobos-2 magnetometer data. On the contrary, Øieroset et al. (2010) found no direct evidences in the Mars Global Surveyor magnetometer data to support the idea of a significant outgassing or dust escape from the Phobos surface. More direct observations attempts by cameras also have remained inconclusive. The cameras on Viking 1 Orbiter and the Hubble Space Telescope (HST) lacked the required sensitivity (Krivov et al., 2006), while the Mars Express SRC (Super Resolution Channel) suffered from image blur and straylight (Oberst et al., 2008). DePhine is moving in favorable rendezvous orbits for new efforts to detect dust rings by its onboard camera. The spacecraft data will deliver new models and bounds for volatiles near the surface and outgassing. Also, DePhine will study the population of micrometeoroids by means of a dust detector. Encounters with meteoroid streams will temporarily bolster the ejecta production rate from the surfaces of the moons. In turn, this will generate a proportionate enhancement on the density of the Phobos/Deimos dust tori (Zakharov et al., 2014) and lead to increased impact rates on the detector.

Ejecta from Mars

Phobos and Deimos, moving close to Mars, almost certainly have accumulated Mars ejecta in the past. Dynamic studies suggest that regolith may contain 0.0002% to 0.025 of Mars material (Chappaz et al., 2012; Ramsley and Head, 2013a), with the thickness of deposited regolith layers varying from the near to the far side (Thomas et al., 2000). Hence, space explorers have identified Phobos and Deimos as targets, from where recovery of Martian samples may be comparably straightforward.

Investigators suggest that the various families of Phobos grooves may have formed as a result of such ejecta (Murray and Heggie, 2014). Alternatively, grooves may be surface manifestations of a global fracture pattern that pervades Phobos' interior (Asphaug and Melosh, 1993; Fujiwara and Asada, 1983). Recent theoretical work has reproduced similar formations on Vesta as the result of shear deformation following a large impact (Stickle et al., 2015; Scully et al., 2014). We will test this scenario by determining the internal structure of Phobos by radar. Like in the case of the craters, the current statistics of grooves suffer from observational biases. Also, with the current limited observational data, no grooves have been identified on Deimos. The camera will carefully map the surfaces of the two satellites to establish unbiased catalogs and maps of grooves. Using crater statistics, we may identify the sequence of groove formations and families of common origin. Spectral data and albedo patterns, which represent different mineral and physical properties of the regolith, will help in the mapping of the grooves (Longobardo et al., 2015). Studies of groove morphology will allow us to test their proposed origins.

Using radar mapping from orbit, we will assess regolith thickness for Phobos and Deimos, and variations of regolith thickness of near and farside. Using GRNS (Gamma Ray and Neutron Spectrometer) mapping from orbit, DePhine will be able to constrain the abundance of Mars material in the regolith, as GRNS may be able to discriminate between chemical compositions on the near- and farside, polar, and equatorial areas.

Regolith formation

Studies of the Phobos' surface by OMEGA spectrometer on Mars Express (Fraeman et al., 2012; Gondet et al., 2010) reveal that the surface is covered by a thick regolith layer, which appears rather uniform. In fact, the surface on Deimos appears smoother than the surface of Phobos, implying that morphologic features on Deimos have been gardened more effectively by impact ejecta and mass movements or that they simply never formed. The DePhine camera system will study the morphology of the Martian satellites to determine regolith characteristics, and to identify creep or mass wasting processes. Using the radar and GRNS experiments, DePhine will measure regolith thickness, its porosity, and elemental abundances. Multiple imaging at different phase angles will be used to study photometric properties for interpretations of the physical properties of the surface regolith. The DePhine mission will provide the first opportunity to study the nature of space weathering effects on the Martian Moons. The HFC (High-Frequency Channel) radar will permit to study the relevant surface processes on these objects. The presence of large grains and blocks (cm to m) as well as peculiar regolith processes (migration, sorting) can be determined through the HFC observables (presence of layering, variation in the intensity of the radar echo, presence and distribution of radar scatters in the subsurface).

Tidal interaction and processes

The orbit of Phobos is known to decay due to tidal interaction with its parent planet Mars (Bills and Comstock, 2005; Burns, 1978). Hence, Phobos is experiencing increasing tidal forces, associated with accelerated rotation rate and centrifugal forces, which have been demonstrated to affect surface processes (Davis et al., 1981; Thomas, 1993). Studies of Mars Express high-resolution image data suggest that the evolution of Phobos' dynamic environment has triggered landslides on crater walls (Shi et al., 2016), perhaps as recently as within the past 10^8 years. The effects may be responsible for observed asymmetries for many of the Phobos' craters. Unfortunately, detailed studies of the surface of Phobos – not to mention Deimos – are hampered by the limited resolution and coverage of spacecraft images as well as the limited topographic data. DePhine will provide new and updated shape models for Deimos and Phobos, respectively, along with gravity field models, from which slopes (and evolution of dynamic slopes over time) may be determined. We will search for slopes near angle of repose and associated landslides. We will use high-resolution imaging to provide a complete global mapping of landslides associated with crater statistics to determine ages of such landslides and the associated time scales of processes.

Solar wind interaction

The surfaces of Deimos and Phobos are exposed to the solar wind. Multispectral observations reveal obvious effects of "space weathering" in areas where recent resurfacing is known to have exposed fresh material. Spacecraft spectral measurements for the surfaces of the satellites reveal two materials distinguished mainly by slope of the spectral continuum: a "redder" unit that dominates and is also present on Phobos, and a "bluer" unit excavated from depth on Phobos by the formation of Stickney crater (Murchie and Erard, 1996; Murchie et al., 1991; Rivkin et al., 2002; Thomas et al., 2011a). Both Phobos' redder unit and Deimos indicate absorptions due to Fe-phyllosilicate near 0.65 µm (Murchie et al., 2008) and possibly olivine/pyroxene near 1 µm (Gendrin et al., 2005). Thermal infrared spectra show emission features consistent with phyllosilicates (Giuranna et al., 2011). Unfortunately, multispectral data for Phobos (not to mention Deimos) are limited in spatial resolution and do not show the needed details of fresh surface exposures on impact craters or mass wasting features. While DePhine does not carry a spectrometer system, the spacecraft onboard camera with its multiple color channels will be able to identify "red" and "blue" units and outline their extent at high spatial resolution. Thus, we may resolve local resurfacing events and improve our understanding of space weathering effects. By studying color variations in the context of geologic settings, it will be possible to understand whether observed color variations are related to exogenous or endogenous processes.

As part of studying the diversity of Deimos and Phobos, DePhine will also more directly study the solar wind interactions. The two satellites are small non-conductive rocky bodies and normally expected to fully absorbing plasma impinging on them. However, recent Lunar missions, Chandrayaan-1 and Kaguya, discovered that the lunar regolith reflects only few % protons (Saito et al., 2008), but backscatters up to 20% hydrogen (Wieser et al., 2009). A similar effect may be expected for the regolith surfaces of the Martian satellites. Indeed, backscattered protons were tentatively observed during a Phobos flyby of Mars Express from a distance of ∼500 km, with a backscattered efficiency of 0.5–10% (Futaana et al., 2010). Surprisingly, no such disturbance was observed during the closest-ever flyby on December 29, 2013, 07:09 UT at a distance of 58 km from the center of Phobos. This may be due to low solar wind speed and Phobos being likely inside the induced magnetosphere. Hence, the interaction of Phobos and Deimos with the environment and how plasma interacts with their regolith surfaces remains to be established.

Further clues on how plasma interacts with the regolith surfaces and on surface weathering processes may come from magnetic field investigations. Solar wind sputtering is a significant mechanism, which may alter surface properties (Murchie et al., 2014; Pieters et al., 2000) and release surface material to contaminate the surrounding environment as, e.g., in case of Mercury's polar regions (Paral et al., 2010). Also, a local field produced by magnetic anomalies could affect the surface properties as seen in the form of "swirls" on the Earth's Moon (Bhardwaj et al., 2015). However, the data coverage of currently available magnetic field observations for Phobos and Deimos is very limited and longer period observations from quasiorbital motion are needed in order to see the relevant magnetic signatures. The magnetometer will also measure intensities and variation of external magnetic field of the satellites at different distances over the time of the mission. Such external magnetic signatures are generated by the interaction of the moons ionospheres with the solar wind (e.g. Baumgärtel et al. (1998); Øieroset et al. (2010); Poppe et al. (2015)). The results of these measurements will contribute to the interpretations of the ionosphere composition derived from analyses of other instruments data and the dust analysis (Zakharov et al., 2014). DePhine will address the question of how the solar wind interacts with Phobos' regolith and how this might depend on solar activity or surface characteristics.

7.3 Mission profile

7.3.1 Launch and cruise

We anticipate a launch by ESA's future Ariane 6-2 vehicle, but unfortunately confirmed data about the Ariane 6-2 lift performance are not yet available for reliable mission planning at this stage. We adopt a Soyuz-Fregat launcher as the baseline, with which we can achieve a mission, which is technically feasible and which can accomplish all science goals well within the cost cap of the M5 program (550 Mio Euro). If Ariane 6-2 with improved performance becomes available, we propose an upgrade and modified mission profile (see further below).

The DePhine spacecraft will be launched into a Mars Transfer Orbit (MTO) with 1.5 revolutions about the sun. With the general time window given for the M5 mission opportunity (and with reasonable delta v), this is the only viable transfer solution. Our baseline launch is on September 23, 2030, with hyperbolic excess velocity $v_{inf} = 3.727$ km/s and a Declination of the Launching Asymptote (DLA) of -1.8°. At this launch opportunity, the Soyuz launch vehicle will be able to inject a total S/C mass of ∼1493 kg into MTO (including launch error margin). Several other opportunities for launch exist in 2030, days before and after the nominal launch date, which feature quite similar transfer time and spacecraft carrying capacity. No mission opportunity exists until two years after (2032), when a launch window opens again, which we consider as a backup. Here again, mission profile and spacecraft performance are similar to the nominal mission scenario.

While the Earth departure velocity will be provided by the launch vehicle, mid-course corrections and orbit insertion are performed through spacecraft thrusting maneuvers. For Mars capture with C3 = 0 km^2/s^2 (parabolic orbit), a total velocity increment (Δv) of 670 m/s is required. We add a margin of 10% for "gravity loss" (accounting for non-zero duration of thrusting maneuvers) and other uncertainties. We choose an initial elliptical 300 km x 150,000 km orbit (height above ground) about Mars (similar to the arrival orbit of Mars Express) and perform a small inclination change to match Mars' equatorial plane, which requires an additional 81 m/s, to which we add a margin of 5%. This leads to a total Δv of 822 m/s, required for full orbit insertion. Mars orbit insertion is on January 30, 2033.

7.3.2 Science mission baseline

In this initial high elliptical orbit, maneuvers are performed, which will adjust inclination, raise the periapsis and circularize the orbit of the spacecraft to enable a Deimos rendezvous and begin its science mission in March 2033. After 10 months of operations at Deimos, DePhine will change from its near-circular into an elliptic Mars orbit to carry out repeated encounters with Phobos for another 9 months. The mission will end in September 2034, just before Mars enters superior conjunction, when communication with Earth is disrupted. The total mission duration is 4 years (see 7.2).

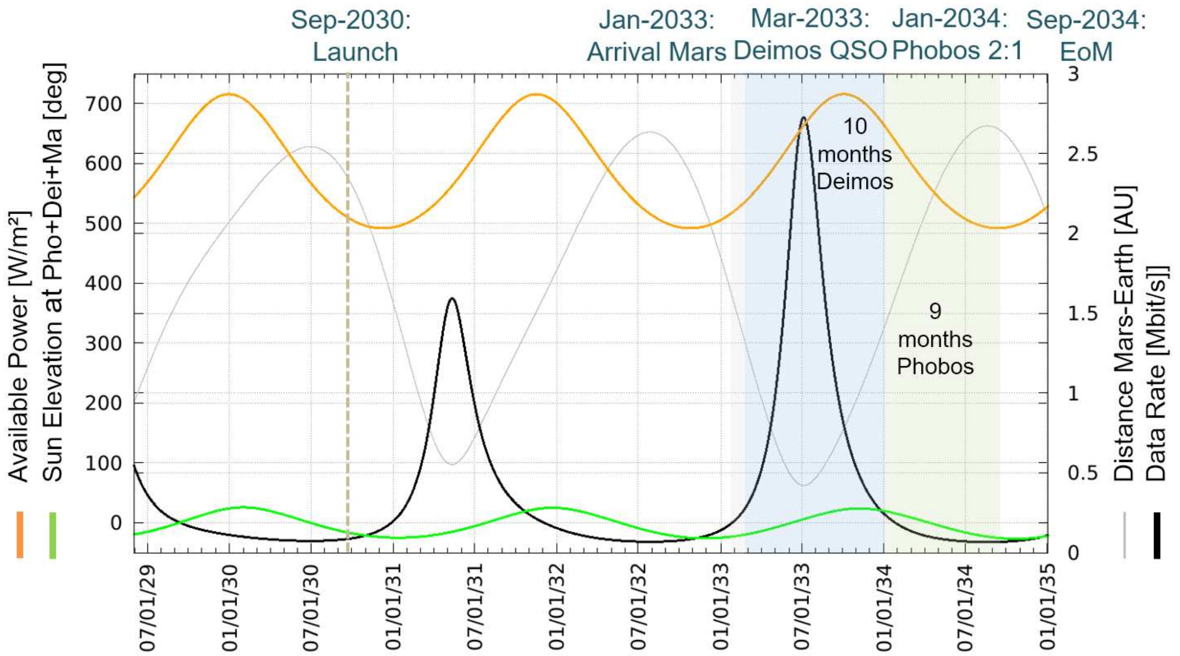

Figure 7.2: Mission timeline

7.3.3 Deimos Quasi-Satellite orbit

Due to the low mass of the Martian satellites and the strong perturbation by Mars' gravity field, it is not possible to orbit the moons directly. Instead, DePhine will move in Quasi-Satellite Orbits (QSOs), which are in 1:1 resonance with the satellite orbits aboutMars, but have slightly different inclinations and eccentricities. The orbital parameters of the Deimos QSOs are chosen such that the distance from the surface to DePhine will vary between 8 and 12 km, at relative speeds of 2–3 m/s and such that sub-spacecraft points move between 30° latitudes North and South ("quasi" inclination of 30°). Our numerical simulations, which were carried out using a variety of Deimos gravity field models, planetary perturbations, and radiation pressure effects, reveal that this orbit is stable over time scales of more than one year. Therefore, only minimal orbit correction maneuvers are needed during this phase. The spacecraft will gradually approach Deimos from the arrival orbit to finally enter the QSO. Approach distances to Deimos will be reduced, as the mission proceeds and gravity field knowledge of Deimos improves.

During the QSO mission phase, the spacecraft will carry out special flyby maneuvers of Deimos at

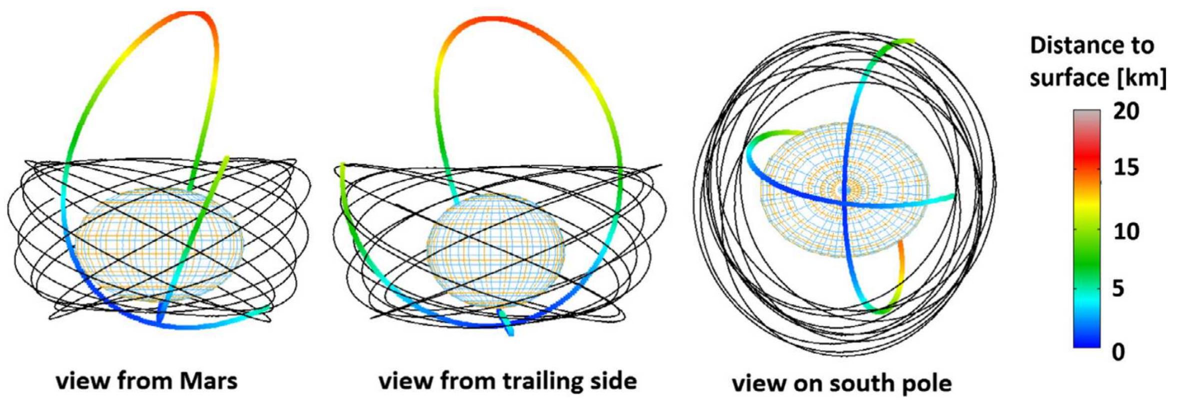

Figure 7.3: Quasi-Satellite Orbit and example of flyby maneuver (distance to surface, color-coded). (For interpretation of the references to color in this figure legend, the reader is referred to the web version of this article.)

selected orbital/- solar phases, which enable approaches within 1–2 km at flyby speeds of 3–4 m/s. Each flyby requires a small thrusting maneuver with a typical Δv of 5–8 m/s. The flyby "event" lasts about 3–5 h, after which the spacecraft returns to the stable QSO (see Figure 7.3). During the flybys, the radar, magnetometer, gamma-ray and neutron spectrometer as well as the camera will operate simultaneously, while the spacecraft will maintain the radio link with Earth for performing the radio-science experiment. This will require the spacecraft attitude guidance to maintain instrument pointing at Deimos, while maintaining Earth pointing of the steerable antenna. In the mission baseline we foresee ten flybys, requiring 86 m/s of Δv.

The simultaneous radio tracking and image data acquisition allow us to make precise reconstructions of the flyby trajectories with respect to the targets. Otherwise, as in the case of Mars Express, currently the only spacecraft to carry out Phobos flybys on a regular basis, the flyby trajectory must be reconstructed from the tracking data before and after the flyby in combination with target ephemeris knowledge, a procedure sensitive to systematic errors.

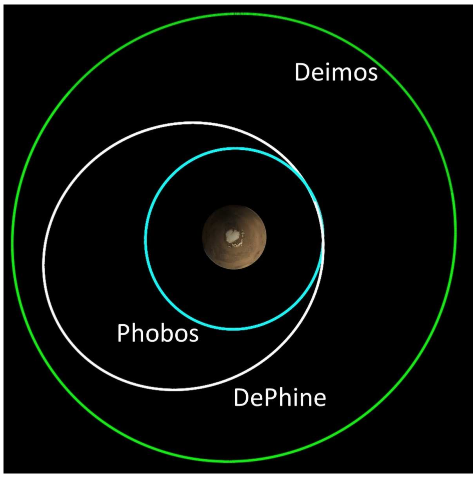

Figure 7.4: DePhine orbit (white) in 2:1 resonance with Phobos, with respect to the orbits of Deimos (green) and Phobos (blue). (For interpretation of the references to color in this figure legend, the reader is referred to the web version of this article.)

7.3.4 Phobos phase

After the Deimos phase, DePhine will perform thrusting maneuvers, to move from the near-Deimos circular orbit to an eccentric orbit, chosen to be in 2:1 resonance with the orbit of Phobos (pericenter of 9238 km and an apocenter of 20,510 km) (Figure 7.4). We foresee approximately 45 Phobos flybys within a mission phase of 1 month (1.5 flybys per day) at moderate speeds of approximately 450 m/s (considerably less than the typical Mars Express Phobos flybys at speeds of approximately 3 km/s).

At the beginning of this mission phase, we will begin with safe flyby distances to Phobos of ∼500 km. Benefitting from the flyby tracking experience and improving Phobos ephemeris data that will be obtained, we will then reduce the distance until DePhine achieves flybys below 50 km with respect to the center of Phobos. Small thrusting maneuvers near apocenter will allow us to change the flyby geometry, i.e., the intersection of the spacecraft trajectory with the so-called b-plane (the plane attached to the target, perpendicular to the spacecraft trajectory), which will allow us to carry out flybys over polar areas (typically more difficult to achieve from the QSOs). The closest approach will occur either slightly before or after S/C pericenter passage allowing us to realize different approach geometries (Figure 7.5). Remaining propellant permitting, flyby distance of 10 km, implying a small risk of collision, may be achieved at the end of the mission.

7.4 Onboard instruments

The DePhine spacecraft shall carry seven instruments: a Shallow Subsurface Radar (SSR), a Wide Angle Survey Camera (WASC), a Deimos Magnetometer (DeMag), a Gama Ray and Neutron Spectrometer (GRNS), the Gravity Radio Science Investigation of the Martian Moons (GRIMM), theeXtra Small Analyzer of Neutrals – 2 (XSAN-2) and the Dust In the Martian EnviRonment (DIMER).

7.4.1 Shallow subsurface radar – SSR

The SSR transmits radar waves to the surface of the Martians moons and will analyze the reflected and refracted sounding waves, to obtain information about the surface and internal structure of Deimos and Phobos (Herique et al., 2018). The radar is a dual channel radar consisting of a High-Frequency Channel (HFC) covering a frequency range from 300 to 3000 MHz and a Low-Frequency Channel (LFC) operating at 60 MHz with 20 MHz bandwidths. The design is optimized for DePhine's operation with altitudes ranging from 30 to 1 km and low orbital speed.

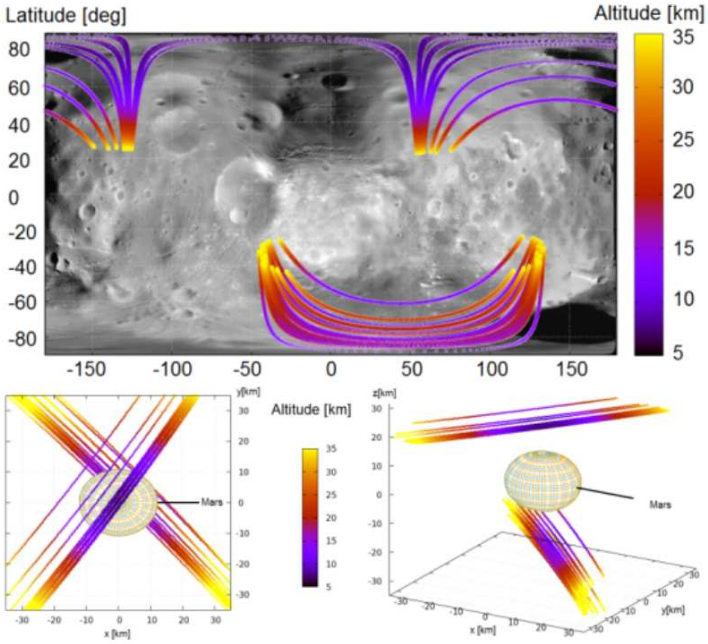

Figure 7.5: Polar flybys at Phobos. Spacecraft ground tracks in the body-fixed (top) and inertial reference frame (bottom).

The High Frequency Channel will provide 2D radar images processing echoes from the surface and the first tenth of meters of the regolith in nominal mode. It will be able to detect layers, embedded rocks or possible water ice with depth depending decametric vertical resolution. By multiple coverage we will achieve the vertical resolution needed to image embedded structures: for DePhine, we foresee 3D tomography with metric resolution, which will require approximately 40 observation passes and acquisition sequences with different observation geometries. The reduction and correct 3D interpretation of the data will benefit from the high-resolution (a few meters or less) Digital Terrain Models (DTMs) of Deimos, delivered by the DePhine camera and associated photogrammetric image processing. Altimeter modes at higher frequencies are implemented to provide target ranges for both science and real-time navigation with a resolution of up to 6 cm. This information will contribute to shape model, surface roughness estimation, S/C orbit restitution, as well as to studies of Deimos' and Phobos' dynamical state.

The Low Frequency Channel will enable probing of the first few hundred meters of Deimos and Phobos and will allow us to assess whether the observed geological structures have vertical extensions. LFC will be able to detect hidden blocks, boulders or voids, which would hint at a rubble pile interior, critical information for possible formation scenarios.

The SSR consists of an electronic unit and an antenna system facing the surface. The electronic unit delivers a set of adjustable frequencies from 300 MHz to 800 MHz in HFC nominal mode and up to 3 GHz in the extended band. The fully polarimetric antenna system transmits a circular polarized signal and receives the returned signal in two perpendicular linear polarizations. Both signals are amplified, sampled, phase-calibrated and combined to co- and cross polarized signals in the two-channel receiver chain on board. The LF Channel is based on the bistatic Low-Frequency Radar (LFR), under development for the Asteroid Impact Mission (AIM) by ESA. It is a BPSKcoded radar operated at 60 MHz with a 10–20 MHz bandwidth corresponding to the monostatic mode of LFR on the AIM orbiter. The antennas will be accommodated on the S/C instrument deck. The typical half-power beam width of more than 90° is limiting the pointing requirement to about ±10° or less.

7.4.2 Wide Angle Survey Camera – WASC

The Wide Angle Survey Camera (WASC) instrument uses a frame sensor array in combination with a wide angle lens for Deimos and Phobos imaging. The main science goal is the mapping of geological

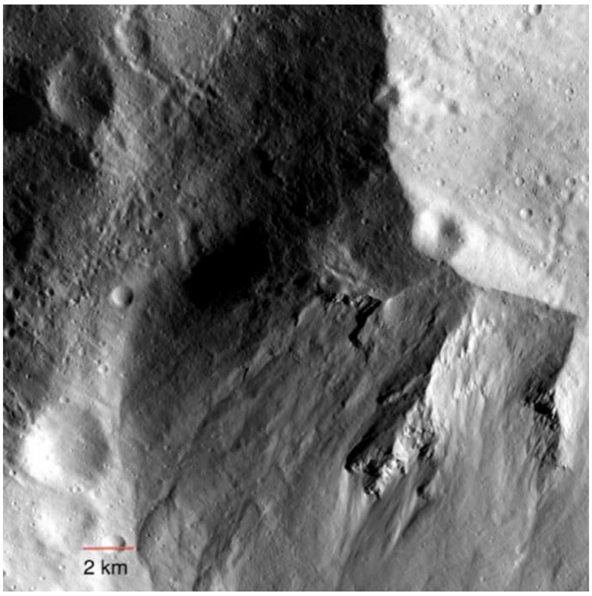

Figure 7.6: Rim of Matronalia Rupes on Vesta, example image from the Dawn framing camera (See Figure 7.7). Source: Planetary Data System F1b_FC21A0015600_11361133030F1A.

structure and diversity. The instrument will have a multispectral capability (including near-infrared) for compositional information. The camera will also carry out astrometric observations and will contribute significantly to spacecraft optical navigation, in particular on flyby sequences.

WASC will regularly take stereo sequences, which will be realized by overlapping nadir-pointed images, taken in close temporal succession, along the ground track of the spacecraft. While we benefit from the large field of view of WASC (25°), this allows us a significantly reduced operational effort. Image blocks will provide stereo information of equally high quality both along and perpendicular to the flight direction. In combination with the high geometric stability of frame detectors, 3D point reconstruction from stereo analysis will be accurate to scales significantly smaller than the image resolution.

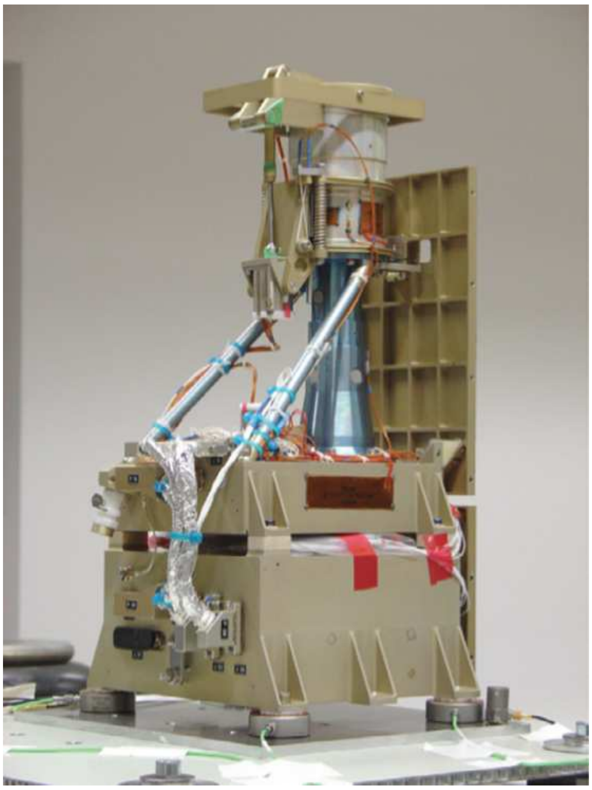

Figure 7.7: Dawn framing camera.

The instrument is derived and re-uses main components from the NASA Dawn mission's framing cameras (Dawn FC) (Sierks et al., 2011) (see sample image and camera laboratory model, Figure 7.6 and 7.7), which in turn is based on the design of the European Space Agency's Rosetta Landing Imaging System (ROLIS) (Mottola et al., 2007). A major modification for WASC is its increased field of view (larger by a factor of about 5 compared to Dawn FC).

WASC will be equipped with a refractive optics modified from the ROLIS camera of Rosetta (Mottola et al., 2007). The optics will be color-corrected and make use of radiation-tolerant glasses. With an effective focal length of 30 mm, it will project a square field of view (FOV) of 25° by 25° onto the Charge Coupling Device (CCD) detector. This translates to an image scale of 0.21

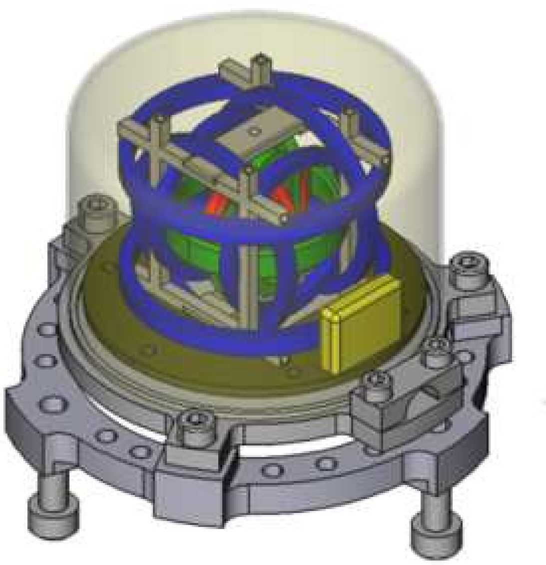

Figure 7.8: Fluxgate sensor MASCOT design (Herčík et al., 2017).

mrad per pixel. Image ground pixel size will be better than 4 m/pixel, on average, for global mapping (from 10 km distance), and as high as 90 cm/pixel on close flybys (2 km for close flybys of Deimos), gives a sampling of about 85 cm/pixel.

The detector in WASC is a 1 k x 1 k CCD with frametransfer architecture, which allows the implementation of electronic shuttering, avoiding a mechanical solution. Color imaging will be realized by a filter wheel, which comprises an 8-position Geneva drive, a stepping motor, a Hall-effect angle encoder, and a wheel with 8 positions (specific filters yet to be determined). WASC exploits a compact architectural design coupled with a framing detector, avoiding any scanning mechanism or operational requirement on the S/C to obtain images in different spectral bands and in stereo.

7.4.3 Deimos magnetometer – DeMag

Figure 7.9: DeMag boom.

DeMag represents a suite of magnetometry instruments. The main component is a three-axial vector compensated fluxgate magnetometer with a Mascot design ((Herčík et al., 2017), Figure 7.8). The principle of fluxgate magnetometers is based on measuring the induced field of a soft magnetic core which is excited by a periodic saturating magnetic field. Like a transformer the core is surrounded by a primary and a secondary coil. The primary coil is used to excite the core, and a secondary one measures the response. A third set of coils is providing a negative feedback to keep the sensor in linear regime. The information about the ambient magnetic field is acquired from the combination of the response and the feedback signals. The technological details of the secondary magnetometers have to be defined.

We foresee that two magnetic sensors are mounted on a deployable short (1 m) boom at the outer edges of the S/C structure for keeping interference level low and for enabling separation of s/c interferences by a dual sensor method (see 7.9).

7.4.4 Gamma Ray and Neutron Spectrometer – GRNS

Planetary gamma-rays and neutrons are created within near-surface material when galactic cosmic rays (GCR) collide with an airless or nearly airless planetary body. The GCRs liberate neutrons from elemental nuclei, which then generate gamma-rays via nuclear excitation reactions that are detected by sensors on orbiting (or landed) spacecraft. Bulk concentrations of a number of elements (e.g., Fe, Si, O, Mg, H) can be measured using these GCRinduced gamma-rays. In addition, the bulk concentration of some elements (e.g., K, Th, and U) can be measured using direct gamma-rays from their radioactive decay. Finally, GCR-induced planetary neutrons provide independent and complementary composition information through the three different energy ranges of thermal, epithermal, and fast neutrons. Thermal neutrons provide a measure of neutron absorbing elements (e.g., Fe and Ti), epithermal neutrons enable a determination of hydrogen concentrations and fast neutrons provide analysis of average atomic mass.

The goals of the Gamma-Ray and Neutron Spectrometer (GRNS) are to measure the elemental concentrations of Fe, Si, O, Mg, K, H, as well as thermal, epithermal and fast neutrons. The elemental concentrations are obtained with a relative statistical uncertainty of better than 20%. The neutron measurements enable the compositional characterization needed to distinguish between the various Phobos/Deimos formation scenarios.

In order to make these measurements, GRNS needs to acquire data from Phobos and Deimos from a distance of less than one body radii for at least 20 h per body. For the neutron measurements, the data can be acquired using standard neutron sensors that have spaceflight heritage from the Lunar Prospector, Mars Odyssey, Dawn, and MESSENGER missions.

The GRNS consists of four primary subsystems, namely a Gamma-Ray Spectrometer (GRS), a Neutron Spectrometer (NS), and two associated Data Processing Units (DPUs). The GRS is based largely on the MESSENGER GRS (Figure 7.10) (Goldsten et al., 2007), which is a High-Purity Ge HPGe gamma-ray sensor, which warrants precision measurements with a high signal-to-background ratio. The NS is based on the Lunar Prospector NS (Feldman et al., 2004) equipped with two 3He gas proportional counters that are used to measure thermal and epithermal neutrons.

7.4.5 Gravity Radio Science Investigation of the MartianMoons – GRIMM

The radio science experiment uses the radio link between the spacecraft and the ground station antennas on Earth for a precise mass and gravity field determination. The experiment shall be supported by optical navigation.

The attracting forces of the small moons and other nongravitational forces act on the spacecraft and change its trajectory and speed, which can be precisely extracted from the Doppler shift of the radio carrier frequency received on ground (for details see: Andert et al. (2010, 2015); Pätzold et al. (2011, 2014a,b)). The mass and gravity field of the body when combined with the body's volume and shape determined from camera observation, pose constraints on the bulk density and hint at the internal structure and composition and porosity considerations, as demonstrated during the Mars Express flybys of Phobos (Andert et al., 2010; Pätzold et al., 2014a,b) and the Rosetta flyby at asteroid 21 Lutetia (Pätzold et al., 2011).

The Radio Science experiment GRIMM relies upon the on-board radio subsystem, which includes two redundant transponders providing a coherent two-way X-band uplink/X-band downlink (X/X) radio link, two redundant Travelling Wave Tube Amplifier (TWTA), which amplify the X-band downlink radio signal generated by the transponder, and the High Gain Antenna (HGA), which receives and transmits the radio signal. A hydrogen maser in the ground station is used as the frequency standard for generation/acquisition of the uplink/downlink signal.

The HGA shall be pointed towards the Earth during GRIMM gravity operations. The orbiter will not perform AOCS (Attitude and Orbit Control System) operations during GRIMM operation.

7.4.6 eXtra Small Analyzer of Neutrals - 2 – XSAN-2

The eXtra Small Analyzer of Neutrals – 2 (XSAN-2) is a compact sensor for measuring neutrals (with energy > 10 eV; energetic neutral atoms, or ENAs) or ions released from the regolith. An entrance deflector can be switched on or off for rejection or detection of ions. Neutrals (and ions for deflector off) passing the deflector hit the conversion surface and are transformed to positive ions. These are guided to an electrostatic analyzer (ESA), which provides the energy determination. The ions enter a time-of-flight section (TOF), which provides a rough mass identification within the accuracy determined by the energy conversion. The instrument sensor will be equipped with a cover

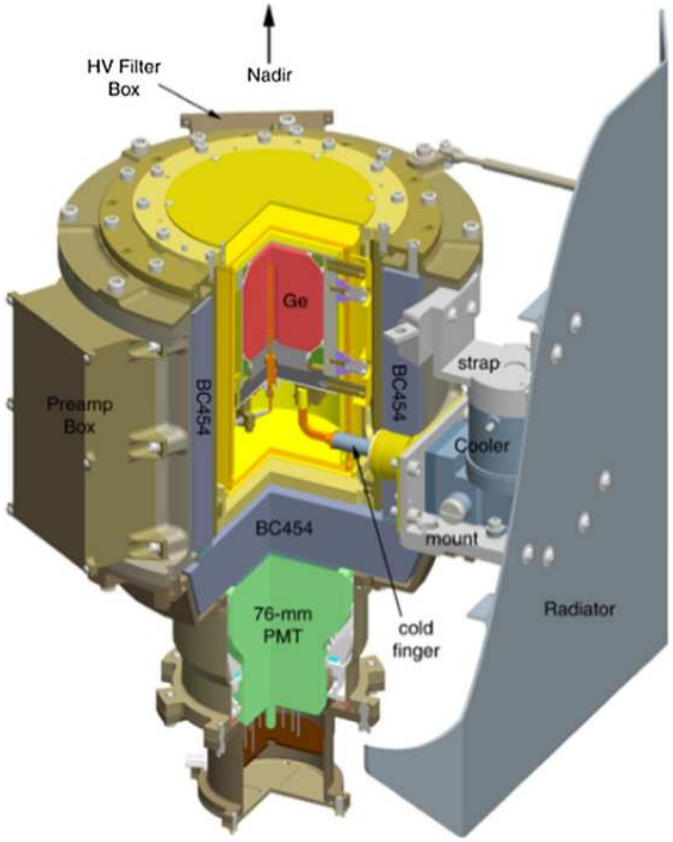

Figure 7.10: CAD model cutaway view of the GRS sensor (from Goldsten et al. (2007). The Germanium (Ge) crystal is highlighted in red. It is 5 cm in diameter and 5 cm in length. The intended view direction of the measurement is upward along the Ge detector centerline (same as the cut axis). (For interpretation of the references to color in this figure legend, the reader is referred to the web version of this article.)

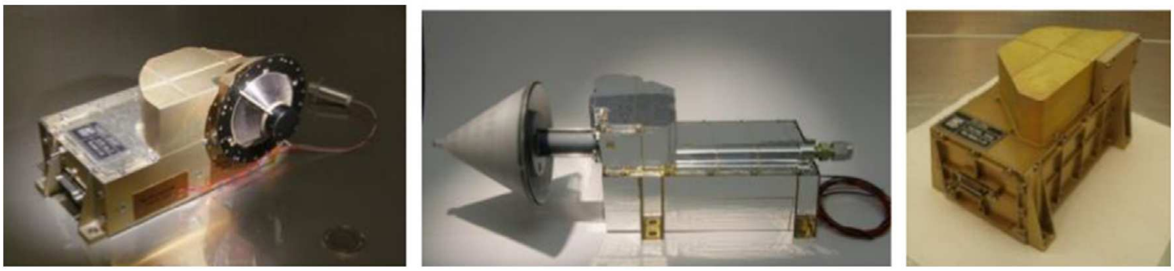

Figure 7.12: Selected flight models of the XSAN-2 series from left to right: Phobos-Grunt/DIM, BepiColombo/MIPA, PRISMA/PRIMA (Wieser and Barabash, 2016).

to protect the instrument's sensitive surfaces from contaminations during AIV (Assembly, Integration and Verification) and launch. The cover is opened when safe operations become possible.

XSAN-2 (Figure 7.11) is a slightly modified replica in a series (Figure 7.12) of small ion and neutrals spectrometers built for Chandrayaan-1 (2008), Phobos-Grunt (2011), and it is going to fly on the BepiColombo mission (2018). More detailed description is found in Wieser and Barabash (2016).

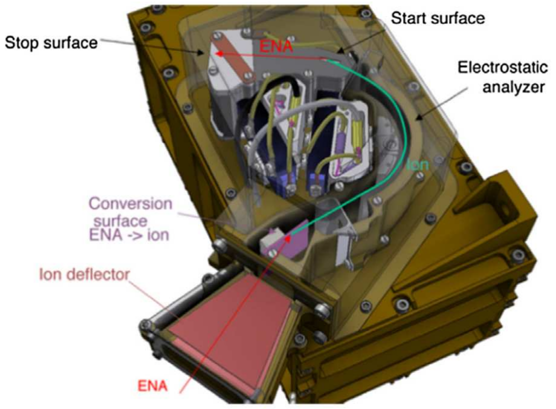

Figure 7.11: Cross section of the Analyzer of Neutrals (XSAN-2) and a sample trajectory of an Energetic Neutral Atom (ENA) to be detected.

7.4.7 Dust In the Martian Envi-Ronment – DIMER

The DIMER experiment is devoted to detecting dust particles in the Mars environment, which have been suggested to form dust tori associated with the orbits of the Martian moons. Besides, the experiment will address the question of the presence of electrostatic fields causing levitating and escaping of dust particles from the Martian moons. The instrument includes two identical blocks of impact sensors (IS1 and IS2) and 12 small sensors (10 g each) based on piezoceramic compounds mounted on the solar panel for registration of dust particles hitting the spacecraft (see Figure 7.13). DIMER will be able to measure impact impulse, mass, velocity, and charge of the impacting particles. The instrument is inherited from the Russian Lunar Dust Monitor (PmL), which will be a payload element on the Russian lunar landers scheduled for launch in 2019 and 2021. The PmL has passed all qualification tests (thermal, mechanical, electrical, functional, operation life time testing) and is now being manufactured. DIMER will use the sensor, electronics and mechanics developed for PmL.

7.5 Space segment

The scientific objectives of the DePhine mission can be fulfilled with a moderately complex space segment. The design has been confirmed with an internal phase 0 study, using the concurrent engineering design facilities at OHB System AG in Bremen, Germany. Subsystem trade-offs were considered and conservative assumptions were applied throughout the spacecraft design. At the time of writing, the performance of the Ariane 6 launcher is unknown. The mission has therefore been designed to be compliant with the known Soyuz launcher performance (i.e. uplift capability) from ESA's launch site in Kourou. The environmental loads, fairing dimensions, launch adapter and launcher-spacecraft interfaces were taken from the draft issues of the Ariane 6.2 user manual (Arianespace, 2016). Heritage is taken from previous NASA and ESA missions (Mars Global Surveyor, Mars Express, Rosetta, BepiColombo), and well-characterized concepts under study (Phobos Sample Return, MMX, AIM).

Figure 7.13: Impact sensor block.

Figure 7.14 shows the spacecraft in its deployed and launch configuration, respectively. The spacecraft has a total dry and wet mass of about 585 kg and 1210 kg at launch, including all margins. The payload contribution is about 40 kg. The delta-v demand requires about 545 kg of propellant. The launch adapter mass is 80 kg. A launch mass margin of about 12% (or more than 160 kg) as compared to the Soyuz performance makes the design robust towards any potential mass growth and towards uncertainties of the Ariane 6 class launcher. More detailed information on the spacecraft design is given in the M5 call science proposal (Oberst et al., 2016).

The top deck of the spacecraft is the dedicated payload panel, which points towards the nadir direction with respect to Deimos and Phobos. The solar array and HGA are accommodated on opposite sides of the spacecraft. This maintains the center of mass and limits the (low) disturbance torques in the Mars environment. The solar array can be rotated for Sun tracking (1 degree of freedom). The HGA is equipped with a two axis pointing mechanism to enable independent Earth-pointing capabilities. Mounting the HGA on a boom increases the pointing envelope and flexibility. Two propellant tanks, the helium tank and reactions wheels are mounted externally. Each are clad with micro-meteorite protecting Multilayer Insulation (MLI).

The spacecraft's structure is based around a central tube, which establishes the primary load bearing path. Additional shear webs and panels create compartments for internal accommodations and external mounting. The propulsion subsystem uses a common approach with a mixed oxides of nitrogen (MON)/Monomethylhydrazine (MMH) bipropellant chemical system. Large orbit maneuvers are performed with an apogee engine located at the bottom of the central tube. Two sets of small thrusters are used for attitude control and to perform small orbit maneuvers. Propellant is accommodated in three different tanks. A single MON tank is located in the central tube with two smaller MMH tanks mounted to its sides. Helium is stored in a smaller pressurized tank. The driving demand for the power subsystem occurs when the spacecraft is in its flyby mode. The payload and communication system (for the radio-science experiment) are operated simultaneous for several hours. The deployable solar array is mounted on a single wing, similar to Mars Global Surveyor. It provides sufficient power at a reduced mass. The battery is sized for launch and early operations, and the worst-case eclipse duration caused by Deimos in QSO.

The Guidance, Navigation and Control (GNC) subsystem includes a standard suit of star trackers, Sun sensors, reaction wheels, an Inertial Measurement Unit (IMU) and a navigation camera. The GNC strategy is based on ground-in-the-loop guidance and navigation, with minimal on-board GNC autonomy. Delta-differential one-way ranging and offline landmark matching occurs before the spacecraft performs its injection maneuver into its flyby trajectory. Heritage is taken from previous missions (Mars Express, Rosetta) and possible future missions (Phobos Sample Return, AIM, PILOT project). The communication subsystem is based on an X-band system, with a steerable HGA. This steerable antenna will allow simultaneous radio tracking and observations by the platform instruments, which is technically not possible for the current Mars Express, with its antenna hard-mounted on the spacecraft bus.

Data downlink, varying with Mars distance (Fig. 7.2), is realized via the 35 m antennas of ESA's ESTRACK. The data-handling subsystem implements a standard solution using an on-board computer, remote-terminal units and a solid-state mass-memory unit. The mass memory is capable of covering four days of science and house-keeping data. A simple passive thermal control subsystem is used with

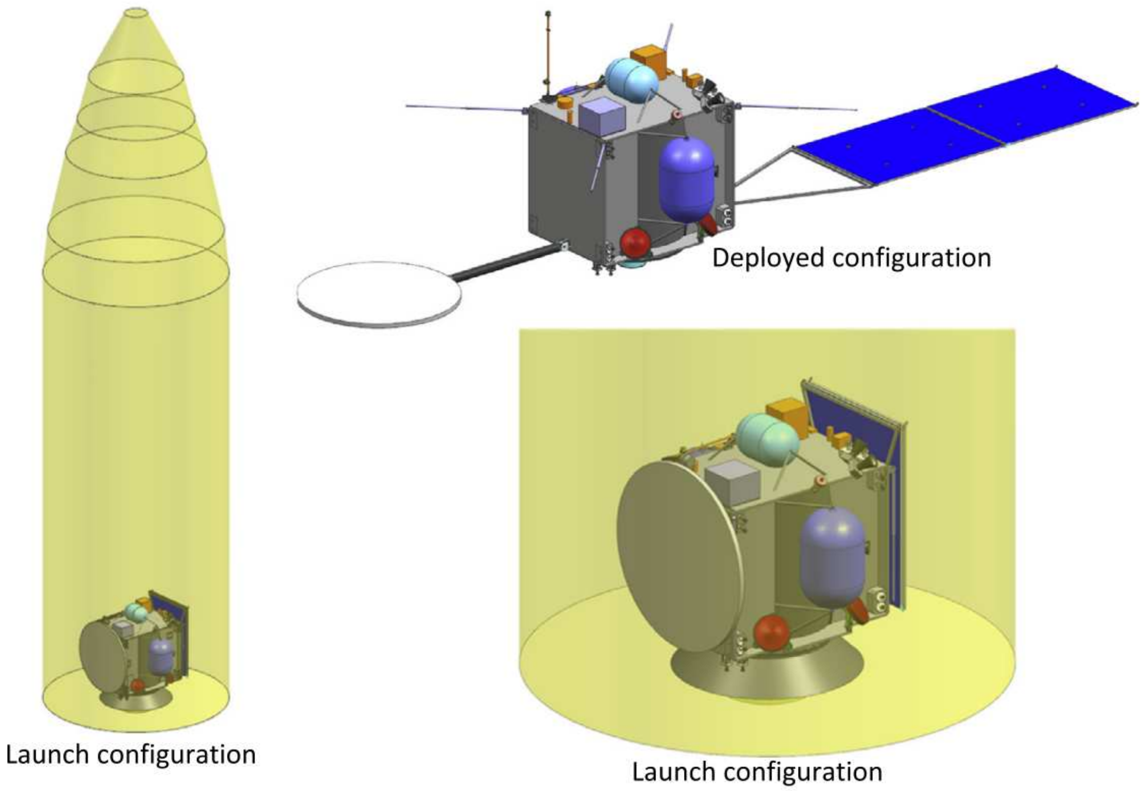

Figure 7.14: Spacecraft in its launch and deployed configuration [OHB]. Note the steerable HGA and solar array panels.

Table 7.1: Overview of Alternative Scenarios

Launcher	Scenario	Launch mass, kg	Margin, kg	Margin, %
Soyuz-FG	Baseline	1129	162	12%
	3:1 resonance	1119	172	13%
	Only 5 Deimos flybys	1113	178	13%
	ELECTRA UHF addition	1151	140	10%
Ariane 6-2	Dephine-A	1450	TBD	TBD Soyuz +12%
	GTO	1713	3287	66%
	GTO with propulsion stage	2531	2469	49%

a heater in a closed loop system.

While the mission baseline described above was analyzed in much detail, the feasibility of alternative mission concepts was also assessed. The different alternative mission configurations are summarized in table 7.1.

Mass could be saved, for example, if the number of flyby events were reduced, or if the spacecraft entered a longerperiod 3:1 Phobos resonance. The spacecraft could also first be injected into a GTO before its interplanetary transfer. Here, DePhine could be launched atop of Lisa-Pathfinder-derived propulsion stage (a jettison-able bi-propellant propulsion module) into GTO. This modified design, however, must be traded-off against increasing costs and complexity of the mission. This would avoid the redesign of the baseline structure and propulsion system to accommodate the increased delta-v. A dual-launch scenario on a co-manifested launcher might also be feasible.

Benefitting from the increased launcher performance of the Ariane 6.2, the nominal mission baseline can be upgraded ("DePhine-A"), resulting in a greater science return. For example, the spacecraft may go into a Phobos QSO after the resonant elliptical orbit. Entering the QSO requires the spacecraft to adjust its orbital parameters to match those of Phobos, at a significant cost of delta-v. In addition, an upgrade would allow the deployment of a small lander on Deimos. However, the added lander including deployment mechanisms and navigation capability, will add considerably to the launch mass of the spacecraft (Table 7.1). In fact, in these configurations, the total launch mass increases by 16% w.r.t. the baseline, and exceeds the Soyuz capability by 5%. The option would become feasible if the performance of the Ariane 6.2 increased moderately.

Acknowledgements

The mission and system design for DePhine was developed by a consortium composed of teams from German Aerospace Center (DLR) and OHB System AG, as well as of scientists from international institutes and organizations. The authors acknowledge the subsystem support of OHB's concurrent engineering facility.

References

All references were moved and collected in the Bibliography

Chapter 8

Synthesis and Discussion

This thesis was written in the context of mission concepts development, especially the mission proposals DePhine, PhoDEx, GETEMME, ASTER, Mars Polar Explorer and Mars TAstE. Most of these missions were proposed in context of ESA's Cosmic Vision Program, and only the ASTER mission is a proposal studied by the Brazilian Space Agency.

The focus of this thesis was mainly put on the exploration of Mars and its small moons as well as the exploration of small asteroids. Additionally, I briefly presented my contribution to the research of mission concepts for Enceladus, Mercury, and the moons of Jupiter.

In the following sections, the results of this scientific research are discussed and compared with actual and upcoming missions.

8.1 Missions to the Moons of Mars

Missions to the moons of Mars have already been launched before, but none of them have succeeded so far. Therefore, the first detailed exploration of the Martian moons will be a scientific highlight in the coming years. With our mission proposals, we addressed the open questions about origin and evolution of Phobos and Deimos.

First, our GETEMME proposal in 2011, then PhoDEx in 2014, and finally the DePhine proposal in 2016 focused on investigating the origin and evolution of the moons of Mars.

During concept development, the interaction with the engineering and science teams had always been one of the most challenging aspects. The science requirements derived from the science questions often led to very high Δv demands, high demands for spacecraft mass, and ultimately to costs that would have exceeded the overall budget. As a consequence, we had to iterate the concept several times, and with each iteration step, the result became more feasible. By the end of the iteration and with the submission of the mission concept or publication of the scientific manuscript, several goals had been adjusted.

For instance, in the GETEMME and PhoDEx proposals, we still included a small lander package that was intended to land on Phobos. Concepts for the package were developed, and a scientific paper regarding this landing package was published (Grimm et al., 2020). Such a small landing package would have strengthened the science case. Landing on Phobos or Deimos could have provided a completely different view of the moons' surfaces.

Unfortunately, the strict budget constraints of the M-class mission proposals did not allow for such a package. As PhoDEx was ruled out due to exceeding costs, we had to remove the lander from our DePhine proposal. As a result, the different iteration steps led to a successful technical and programmatic evaluation of the overall DePhine concept.

Although the lander concept was not included in the DePhine proposal, the development of this lander concept was still very useful. The results obtained in the studies are comparable to those of other small landers and may have influenced their development, such as the Rover IDEFIX onboard the MMX spacecraft (Ulamec et al., 2024).

The Martian Moons eXploration (MMX) mission is also comparable in several aspects to the concepts we developed over the last few years. The science objectives of DePhine and PhoDEx are still highly relevant, and several of them will be addressed by this upcoming mission, which is planned to be launched in November 2026. MMX constitutes a major milestone in Mars-moon exploration and is designed to address several of the key science questions identified in this study.

On the other hand, the MMX mission might also be one reason why the Dephine proposal was not selected in the end, due to the overlapping scientific goals between the two concepts. The MMX proposal was developed in approximately the same time frame as our Dephine proposal, and the results of the conceptual study of MMX were published in 2017 (Kuramoto et al., 2017). It is therefore worth analyzing the MMX mission and comparing it with the results we obtained during our concept development. Table 8.1 summarizes the key elements of the mission.

Kuramoto et al. (2022) states that MMX will carry out an extensive survey of both Martian moons. It addresses some of the biggest questions about the Martian moons, namely what their origins are and how they evolved. Additionally, the interactions with the space environment and material transport are questions that MMX addresses, similar to our proposals.

However, as shown in Table 8.1, the MMX spacecraft is significantly heavier and much more complex than the proposed Dephine and PhoDEx missions. This is especially evident since MMX is a sample return mission, where material samples from the surface of Phobos will be collected and brought back to Earth. One of the biggest challenges will be this sampling of surface material, as it requires a short landing of the spacecraft on the moon. Additionally, returning the samples to Earth requires a substantial amount of additional Δv (Kuramoto et al., 2022). Consequently, the MMX mission is a relatively ambitious exploration concept and comparable to a Large-class mission of ESA's Cosmic Vision program.

It should be noted that MMX is a mission led by the Japan Aerospace Exploration Agency (JAXA) with a contribution by DLR, the French Centre national d'études spatiales (CNES), and the National Aeronautics and Space Administration (NASA). The European contribution to the MMX mission is primarily focused on the small landing package called "IDEFIX" (Ulamec et al., 2024). Despite being a movable rover, the objectives and mission requirements of this small rover are also comparable to the objectives of the PhoDEx lander concept.

During the Dephine and PhoDEx concept development and also during the research in Grimm et al. (2020), I analyzed on possible delivery options. The question was how the landing package could be delivered to the surface of either Phobos or Deimos. During my research, the proposal team agreed on a free-fall delivery. The challenging aspect was always the trade-off between the release height and the risk of damaging or losing the spacecraft by getting too close to the surface of the moon.

I investigated several possible heights and their resulting impact velocities for Phobos. In Oberst et al. (2016), the team agreed on a release altitude of a maximum of 1 km. In Grimm et al. (2020), we agreed on an altitude range between 1 and 3 km. The resulting impact speed from an altitude of 1 km will be approximately 3 m/s with 10 minutes of free-fall time (see Figure 4.8). The impact energy was supposed to be absorbed by a crushable structure surrounding the lander.

In contrast, MMX will go very close to the surface of Phobos before releasing the landing package, with a maximum release altitude of 100 m. At this close altitude, the impact speed is significantly lower, and crushables are not required. As this is a sample return mission, the mother spacecraft will go very close to the surface and even land on it twice for surface sampling (Michel et al., 2022).

Another interesting similarity between MMX and Dephine are the flyby scenarios. The secondary targets of both missions will be visited via flybys. MMX will increase its semi-major axis again before leaving Mars. These maneuvers are then used to perform several flybys of Deimos. With Dephine, we wanted to visit Deimos first and then decrease the semi-major axis afterwards to get into a resonant orbit with Phobos.

A comparison of the mission scenarios shows that DePhine would have been a promising complement to MMX, because it was focusing primarily on Deimos.

Table 8.1: Comparison of mission parameters of the PhoDEx and Dephine proposal and the Martian Moons eXploration (MMX) mission (Oberst et al., 2014, 2016; Kuramoto et al., 2022)

	PhoDEx	**Dephine**	**MMX**
Primary target *secondary target*	Phobos and *Deimos*	Deimos and *Phobos*	Phobos and *Deimos*
Launch date (*backup*)	Oct 2024 (*Nov 2026*)	Sep 2028 (*Sep 2030*)	(*Sep 2024*) Nov 2026 *
Mission duration	3 years	4 years	5 years
S/C wet mass	1160 kg	1210 kg	4000 kg
Lander mass	44.1 kg	*no lander*	29.1 kg
Science goal 1	What is the origin of Phobos and Deimos and how did the two satellites evolve?		Clarify the origins of the Martian moons and constrain processes for planetary formation and material transport in the region connecting the inner and outer Solar Systems
Science goal 2	How do Phobos and Deimos interact with Mars and the space environment?		From the viewpoint of the Martian moons, clarify the driving mechanism of the transition of the Mars–moon system and add new knowledge to the evolution history of Mars

* By July 2024, it was already decided that the launch would take place on the backup launch date.

8.2 Missions to Martian Trojans

In contrast to a mission to the moons of Mars, a mission to the Martian Trojans is currently not foreseen by any space agency. No mission concepts or proposals to the Trojans of Mars were found in the literature, except for the Mars' Trojan Asteroids Explorer (MarsTAstE) proposal, which was our own proposal to an F-class call of the ESA. In this proposal, I was responsible for the project management and the mission analysis (Oberst et al., 2018b). More details about the proposal are given below.

Besides this proposal and the fly-by paper (Wickhusen et al., 2023), no other studies focusing on in-situ exploration of the Martian Trojans were found. The reason for this might be the challenging feasibility of a rendezvous mission. The relatively high inclination of the Trojans relative to the ecliptic makes such a rendezvous mission very difficult and costly. The scientific output compared to the required costs of such a mission cannot be easily justified. Therefore, a fly-by mission as proposed in this thesis might be a good option to collect at least some close-up data of these small bodies and use them for comparative studies with other small bodies..

On the other hand, the fly-by concept has two main disadvantages. The first one is the extended cruise time, which requires approximately 1-3 additional years compared to a nominal mission to Mars. This additional cruise time will also increase the overall mission cost, as such a long duration requires extended operation time and spacecraft lifetime.

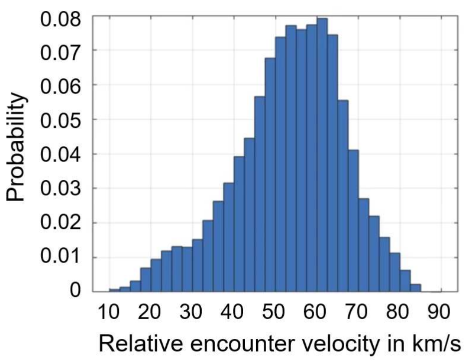

Figure 8.1: Relative velocities between the Comet Interceptor Spacecraft and possible comet targets. *Credit: (Jones et al., 2024)*

The other disadvantage is the relatively high fly-by velocities, which allow only short remote sensing sessions. This fact, in combination with the higher costs, makes such a mission challenging, but the investigation of these Trojan asteroids will still be of high scientific interest.

This second disadvantage is probably the most critical one. It might be hard to answer the most important science questions with the short flyby time. Indeed, the question of how many science questions can be answered with a short flyby scenario will be investigated in the near future, as we plan to analyze this case in more detail.

In any case, a literature study showed that there have already been missions and some are planned or on the way to their targets, which suffer from this same disadvantage but were selected for realization. Prominent examples are the 'New Horizons' mission, which had a fast flyby at Pluto, and the upcoming 'Comet Interceptor' mission by ESA, which is designed for a short flyby at a comet. The ESA mission Comet Interceptor provides a particularly suitable reference for comparison.

First of all, it is interesting to note that this mission was also proposed for the same F-call as our MarsTAstE proposal (Jones and Snodgrass, 2019).

Comet Interceptor is a comparably small mission and will be launched to the Sun-Earth Lagrangian point L2 as a co-passenger of ESA's M4 ARIEL mission. The spacecraft 'will remain at the L2 point until the right departure conditions are met to intercept a yet-to-be-discovered long-period comet (or interstellar body).' When a suitable comet is identified, the spacecraft will leave its waiting position and go onto an interception course. Once the comet interception position is reached, the true science operation will start for this short flyby. In the end, the entire mission is designed for a short flyby at a comet (Sánchez et al., 2021; Jones et al., 2024).

Now, the comets that will be selected as targets have high eccentricities and consequently very high velocities when they get close to the sun. The selected targets will have relative speeds to the spacecraft between 10-70 km/s, with most of them lying between 50-60 km/s, as shown in Figure 8.1 (Jones et al., 2024).

This means that the relative flyby speeds are approximately 5 to 10 times higher than those in the Mars Trojans flyby concept presented in this thesis. If one assumes a mean velocity of 50 km/s, the close encounter between -10,000 km and 10,000 km distance, which is already very far away, will only last 400 seconds or 6.7 minutes. After the flyby, the data will be transmitted and the mission ends.

Although the science case of the Comet Interceptor mission is not fully comparable to the proposed

Trojan Flyby mission, it also demonstrates that scientifically valuable data can be gathered during comparatively brief observation periods. In contrast to Comet Interceptor, a flyby of the Martian Trojans could be combined with a mission to Mars with a very low demand for additional Δv. It is therefore advisable to propose such a mission in the next few years.

In addition, I also analyzed alternative ways of exploring the Martian Trojans. One option could be placing a spacecraft in the Lagrangian point L5 in the Mars-Sun system. The spacecraft in this case could move within the stable areas of the L5 region and intersect several passes of the Trojan asteroids when they pass through the orbital plane of Mars. For that case, electric propulsion could be used, as relatively small Δv changes are required over longer time scales. In this concept, the high flyby velocities that occur when the Trojans pass through the ecliptic are also very high and comparable to the proposed scenario. Nevertheless, this concept may still be investigated in the future in more detail, as it allows investigating more than just one Trojan.

The second option is a mission concept for a rendezvous mission. The very high demand for Δv of such a mission could be met with an electric propulsion system. Due to the slow resulting thrust of these propulsion systems, this scenario would also lead to very long transfer times. We proposed such a mission scenario as part of ESA's Cosmic Vision F-call in 2018 and named the mission MarsTAstE (Oberst et al., 2018b).

ESA's evaluation team confirmed an 'interesting science case that could contribute to expanding our understanding of the populations of minor bodies in the Solar System.' However, the mission wasn't selected for further investigation, mainly because the concept wouldn't fit within the constraints of an 'F' (Fast) mission (Anonymous, 2018). Nevertheless, the idea could be reconsidered and proposed as a larger mission, such as an M-class.

Additionally, it should be mentioned again that a mission to the Trojans of Jupiter was already launched in 2021 and is currently on its way to reach its final target in 2033. This mission, 'Lucy', has already performed a first flyby at the main belt asteroid Dinkinesh (see Section 2.2.2 and Figure 2.9) and will perform flybys of six Jupiter Trojans, including one binary. In this case, the spacecraft will also move relatively fast relative to the Trojans, with velocities between approximately $6 - 9$ $^{km}/_{s}$. These values are comparable to those of the proposed Martian Trojan flyby scenario.

Also, the Trojans of Mars are of high interest, and the number of detections is still increasing. In 2023, a new small body was discovered and named 2023 FM_{14}. After its discovery, de la Fuente Marcos et al. (2024) analyzed the orbit of this body in detail and confirmed that 2023 FM14 is the second Trojan of Mars located at Lagrangian point L_4. However, this Trojan cannot be considered for a flyby scenario. As written in section 6.4.3, bodies located at L_4 require significantly higher Δvs compared to bodies located at L_5. Thus, flyby scenarios as proposed in Wickhusen et al. (2023) are not feasible for this newly discovered Trojan.

8.3 Missions to Asteroids

Several missions to asteroids have been announced in the last decades, and several of them are still to come. Asteroids have been of high interest in recent years, and nominal remote sensing missions, sample return missions, and even impact missions have already been flown or will be launched in the next years. Prominent examples among these missions are Hayabusa 1 and 2 (Tsuda et al., 2013), OSIRIS-REx (Lauretta et al., 2017), the aforementioned Lucy mission (Jones et al., 2024), as well as the AIDA DART and Hera missions (Michel et al., 2024).

Asteroids are of high interest due to several reasons. According to Binzel et al. (2015), the main reason for this high interest is the potentially hazardous, even civilization-threatening impact they might pose. On the other hand, their relatively close distance allows easier access for space missions. Additionally, these rocky bodies are considered remnants from the formation of the solar system, which occurred approximately 4.6 billion years ago (Michel et al., 2015). All these reasons make these bodies excellent targets for investigation.

Frequent coverage of asteroids in mainstream media is an additional factor that raises public interest. Besides the possibility of 'asteroid mining,' especially civilization-threatening impacts have been the main topic in several publications over the last decades. Maybe also the theory that dinosaurs were made extinct by an asteroid has sensitized several people to this risk. By coincidence, in March 2024, while I was writing this text, newspaper articles popped up, asking whether the 'dangerous asteroid (99942) Apophis' could still hit Earth in 2029 (Banner, 2024).

Articles like this, along with the strong science case and their accessibility, are probably the main reasons why the scientific community and the general public are interested in asteroids and why several missions to these bodies are planned to be launched in the next years.

The Double Asteroid Redirection Test (DART) mission is dedicated to demonstrating the feasibility of asteroid-deflection techniques. It was launched in 2021 to collide with a near-Earth binary asteroid (65803) Didymos. This mission is the first part of the Asteroid Impact and Deflection Assessment (AIDA), which is an international cooperation program for asteroid deflection between ESA and NASA (Michel et al., 2024).

In September 2022, DART successfully collided with Dimorphos, the small secondary of (65803) Didymos. The main purpose of the mission was to analyze possible methods for asteroid deflection via a kinetic impact (Thomas et al., 2023).

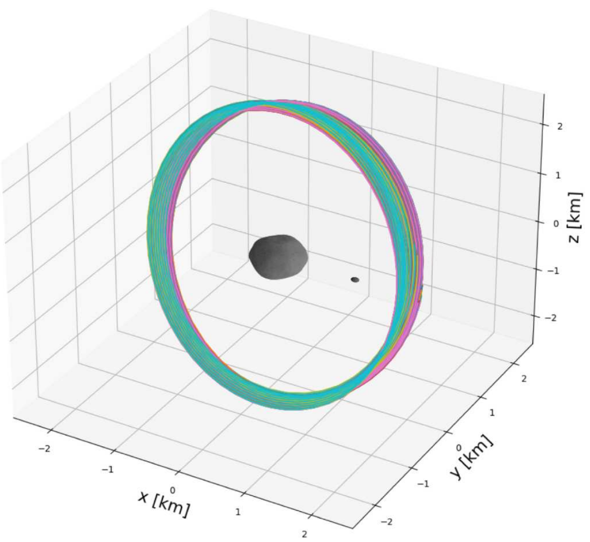

Figure 8.2: Simulated terminator orbit of the Juventas cubesat about the binary asteroid (65803) Didymos. Juventas is a 12 kg 6U cubesat on-board the HERA spacecraft. Credit:(Fodde et al., 2023)

The secondary body Dimorphos was selected to analyze this kinetic impact. A change in the orbital period of this secondary body around the primary allowed a very detailed analysis of the orbital period from ground-based observations (Cheng et al., 2018).

Several pre-impact ground-based observations determined the orbital period of the secondary to be 11.921 hours. If the incident momentum of the impacting spacecraft had been transferred directly to the orbit of the secondary, a change of roughly −7 minutes in the orbital period would have been expected. Surprisingly, the effect on the orbital period was significantly higher and actually changed it by approximately −33 minutes to 11.37 hours (Thomas et al., 2023).

In October 2024, the second part of the mission is planned to be launched. The Hera spacecraft will fly to (65803) Didymos again and investigate the results of the impact. According to Michel et al. (2024), it will be the first rendezvous mission with a binary asteroid.

Already in 2012, I analyzed possible Self-Stabilized Terminator Orbit (SSTO) about 1996 FG_3 for the Marco-Polo-R mission (Hussmann et al., 2012). The size of this near-Earth binary asteroid is comparable to the near-Earth binary

Didymos, which the Hera spacecraft will visit. The Hera spacecraft will release a small 6-unit cubesat called Juventas, which will be the first spacecraft to fly in a SSTO about a binary asteroid (Fodde et al., 2023). The results of the mission analysis are comparable to our results. Such an example terminator orbit about (65803) Didymos is shown in Figure 8.2.

Although this effect was already predicted and simulated by Scheeres (1999), the Osiris-Rex mission was the very first mission to enter a Self-Stabilized Terminator orbit about a small asteroid in 2019. This mission also proved our results from the research in Wickhusen et al. (2012) and show the importance of our orbit analysis for the ASTER mission.

"The officially planned launch date of the ASTER mission will not occur in 2024 or 2026. Nevertheless, the first mission to a triple asteroid is still of high scientific interest. The investigation of such an asteroid will shed light on the complex evolution of binary and triple asteroids and may prove that the BYORP effect, as proposed by Walsh and Jacobson (2015) and Margot et al. (2015), can also lead to triple asteroid systems. Alternatively, different theories might be needed to explain the evolution of such a system.

With our work on orbit stability, we proved that terminator orbits about the triple asteroid 2001 SN_{263} are possible for a spacecraft as proposed for the ASTER mission. Analysis of orbits about this triple asteroid had already been done before. Prado (2014); Araujo et al. (2012, 2015) investigated possible orbits and found several stable regions around the asteroid system. For our simulations, we considered a more complex model, included gravity potentials of all three asteroid bodies, and took the constraints of the ASTER mission into account. As a result, we showed a wide range of stable orbital solutions depending on the initial distance, eccentricity, inclination, and the longitude of ascending node. Additionally, we also analyzed the possible surface coverage of remote sensing instruments and used the proposed laser altimeter as reference payload.

The stable orbit solutions we found allow a very detailed investigation of the asteroids with remote sensing instruments from within the system. The proposed solutions allow remote sensing from different altitudes, i.e., the spacecraft could move from a farther orbit to a closer one over the mission time. When the spacecraft starts at larger distances, it will be able to scan the companion body, which orbits at a larger distance, and then focus on the inner companion and the main body. The terminator orbits also allow full surface coverage of the two inner bodies and precise gravity force determination of this complex system. This will make it possible to understand the interior structure of the asteroid and shed light on the evolution of these systems.

However, the proposed solutions are based on the constraints of the ASTER mission proposal. If the mass and surface area of the spacecraft change significantly during mission development, the stable terminator orbits may differ, but we showed analytically that there will still be a large range of solutions in this case.

The same applies to the rendezvous date of the spacecraft with the asteroid. If the mission is scheduled for a different time, the effect of solar radiation will also differ. With the asteroid's high eccentricity of almost 0.5 in its orbit around the sun, the perihelion and aphelion distances vary between approximately 1 and 3 AU. The resulting acceleration due to solar radiation pressure acting on the spacecraft is therefore approximately 9 times higher at perihelion than at aphelion. Again, this does not affect the existence of the terminator orbits, and the orbits will still be possible in both cases, but the results or initial conditions of the orbit will be different. In these cases, a new detailed study of the location of the terminator orbits will be required. With our knowledge and the tools we developed during the studies, such a new investigation can be done in relatively short time scales, taking the new parameters into account.

Besides the papers included in this thesis, I presented several new concepts that were proposed for exploring bodies of the solar system. The corresponding two publications related to the topic of this thesis were briefly summarized in the relevant section. Some of these new concepts can also be found in upcoming missions, and some may become important in the future when possible missions to the proposed targets are investigated and realized.

I am confident that the investigation of Near-Earth objects will continue and maybe asteroid 2001 SN_{263} will be the first triple asteroid to be investigated by a human space probe.

8.4 Missions to Enceladus

As already mentioned in section 4.4.3, at the end of March 2024, ESA decided to go to Saturn's Moon Enceladus as the first L-class mission of the new Voyage 2050 program. Following the final recommendations from the Voyage 2050 Senior Committee Report three years earlier, ESA issued a call for an Expert Committee for a Large-class (L4) mission covering the science theme 'Moons of the Giant Planets.' The resulting report recommended that this new mission should be sent to Enceladus (Martins et al., 2024).

My work on this body, such as the Enceladus Explorer (EnEx) proposal and the ESA Enceladus ITT, which was finalized in May 2024, may become an important contribution to this new mission. The ESA Report of the Expert Committee states that 'the L4 mission concepts considered in this study, with a launch in the early 2040s, would dramatically improve our understanding of the habitability and the assessment of the presence of biosignatures on Saturn.' Additionally, they note that 'an Enceladus south polar lander with an orbiter and plume sampling system would be the optimum candidate for the L4 mission' (Martins et al., 2024).

Enceladus is considered habitable due to observations performed by the Cassini mission. The exploration of the moon by Cassini revealed active tectonic fractures at Enceladus's south pole, called 'tiger stripes.' These fractures are warmed by internally generated tidal heat and lead to jets of water vapor, the so-called 'plumes,' being ejected into space. A subsurface saltwater sea probably exists under the south pole. Because of the evidence that liquid water is likely present, Enceladus is of great astrobiological interest as a potential habitat for life (Spencer and Nimmo, 2013).

As shown in the previous sections, I was involved in analyzing possible mission scenarios and orbit stability around Enceladus. In the EnEx study, we analyzed possible scenarios for ice-melting probes, and for ESA's 'fractionated sounder' project, I was involved in the search for stable orbits and stability-keeping maneuver strategies for Enceladus (Oberst et al., 2017; Benedikter et al., 2022; Benedikter et al., 2024).

Currently, we are searching for suitable orbits around Enceladus by varying the semi-major axis (350 to 450 km), inclination (40° to 120°), and longitude of ascending node. Moderately inclined orbits (inclination between 45° and 60°) covering the equatorial and mid-latitude regions of Enceladus were found to be stable for several months up to years. In contrast, an example of a highly inclined orbit was found with an inclination of approximately 79.35°, which had an orbital lifetime of 13 days. As we are seeking longer stability, we are currently looking for a suitable strategy of correction maneuvers. Current results show that the overall demand for Δv will be in the range of $< 20 ^m/_s$. This strategy allows coverage of the tiger stripes region and will enable a global characterization of the ocean.

Besides the orbit strategies, on-board power generation will also be a key element for the proposed Enceladus mission in the 2040s. The far distance from the Sun of almost 10 AU leads to approximately only 1% of the radiation energy received on Earth. In Oberst et al. (2017), I analyzed the orbit and illumination conditions of Enceladus between 2020 and 2045. At the end of the 2040s, Jupiter will be at aphelion, which means that the incoming radiation will be at its lower edge. Thus, the typical radiation flux energy will be between $14 - 15 ^W/_{m^2}$.

With these values, it turns out that energy generation with solar cells will hardly be feasible, as a spacecraft would require a solar cell area approximately 100 times larger than that of comparable spacecraft in Earth orbit. For the moment, only Radioisotope Thermoelectric Generators (RTGs) seem to be a possible alternative to solar cells. So far, ESA does not have RTGs that could be used for a mission to Enceladus, but they are currently under development (Ambrosi et al., 2019; Ambrosi et al., 2023). This technology will be a key element for the exploration of Enceladus, and Martins et al. (2024) clearly states that the development of alternative power sources, especially RTGs, will be crucial for a successful mission to the moon.

8.5 Missions to other Solar System Bodies

Besides the above-mentioned mission proposals to the Trojans of Mars, asteroids, and Enceladus, I was also involved in mission proposals to Mars. Additionally, I have made scientific contributions to ongoing missions to other solar system bodies, such as Mercury with BepiColombo and the moons of Jupiter as part of the JUICE mission.

The mission proposal to Mars was published in 2019 as an ESA white paper. In this white paper, we presented the idea of placing a spacecraft in a very low Mars orbit. The target altitude of the spacecraft would be approximately 150 km. At this altitude, the Martian atmosphere already causes significant drag, which would be compensated with an electric propulsion system.

For this proposal, I first calculated the resulting drag force analytically and then simulated the orbit of the spacecraft numerically, using precise database values of the Martian atmosphere (Wickhusen et al., 2018). This analysis presented a completely new scenario for the exploration of Mars, and the results were published in Oberst et al. (2022) and presented in Wickhusen et al. (2022b). This mission proposal could be considered as a mission proposal for ESA's next Medium Size Call (M8), as it received strong positive feedback from the scientific community.

Additionally, I contributed to the exploration of Mercury as part of the BepiColombo mission. Already in 2020, I analyzed the orbit of BepiColombo around Mercury and the impact of Mercury's gravity field on the orbit. We showed that the spacecraft could fall below a critical altitude and come very close to the surface Höschele et al. (2021).

Besides the orbit analysis, I also contribute to the science of the BepiColombo Laser Altimeter (BELA). My contribution is currently mainly focused on operation planning, commanding, data analysis, and tests. A selection of the results can be found in Thomas et al. (2021) and Stark et al. (2021). When BepiColombo enters orbit around Mercury by the end of 2025, it will be the second mission ever to orbit Mercury after Messenger.

In early 2026, the science operation of BELA can begin. At that time, we will see a return pulse of the laser reflected from the surface of Mercury for the first time, and I am looking forward to the new findings we will obtain from these measurements.

Similar to BELA, I am also contributing to the operation planning, data handling, and analysis of the Ganymede Laser Altimeter (GALA) on board the JUICE spacecraft (Enya et al., 2022). In May 2024, we prepared the reference paper for the GALA instruments, which is currently under review. For the paper, I analyzed the orbit in terms of operational times, ground tracks, and laser spot distribution (Hussmann et al., 2024).

JUICE is still on its way to Jupiter but will have a flyby at Earth's moon in August 2024 for an Earth-Moon gravity assist. During the flyby, we will observe an unsimulated return pulse of the laser for the first time, allowing us to perform a precise assessment of GALA's performance.

Then, in July 2031, GALA's science phase will start with a first close flyby of Jupiter's moon Ganymede. After several years of flybys at Ganymede, Callisto, and Europa, JUICE will enter its final, almost circular orbit around Ganymede in 2035. I am confident that our work over the last years will then bear fruit and significantly extend our understanding of the icy moons and the Solar System.

8.6 Synthesis

The goal of this thesis was studying new mission concepts for solar system exploration, with a focus on orbit and trajectory analysis.

In the first research paper, several new orbital solutions for a spacecraft about the asteroid 2001 SN_{263} were found. The solutions enable spacecraft, as proposed in the ASTER mission concept, to perform their close-up mapping phase about the triple asteroid. In contrast to previous analyses, we employed a complex model that included perturbations from the main planets of the solar system, simulated the shape and mass of the ASTER spacecraft, and used geopotential models for all three bodies of the triple asteroid system. Additionally, we accounted for the Solar radiation pressure. The geopotentials of the bodies were modeled as non-spherical shapes with homogeneous mass distribution.

The results show that the solar radiation pressure is the biggest perturbing force in the triple-asteroid system, and only terminator orbits can be considered stable. We demonstrated that stability is achievable over a larger range of distances from the primary body. Furthermore, we showed that the orbits remain stable for at least 1 month, aligning with the designated duration for the close-up mapping phase. The solutions identified in the research were compliant with the requirements and allow exploration of all regions of the primary body with remote sensing instruments such as a laser altimeter, cameras and spectrometers.

The second research article also focused on visiting small asteroids. in this second paper, I explored scenarios that combined a mission to Mars with a fly-by at the Martian Trojan asteroids. These Trojans are of high scientific interest, but a rendezvous mission with them is currently not considered feasible because of their high inclinations relative to the ecliptic. With the results presented in the paper, a mission to Mars - such as the DePhine or the Low Mars Orbiter mission proposals detailed in this thesis - could include a fly-by of one of the Trojans. This approach would allow us to visit these scientifically significant targets at least once, potentially illuminating the formation and evolution of the Eureka Cluster, the asteroid family that includes most Martian Trojans at the Lagrangian point L_5. Additionally, combining a mission to Mars' small moons, Phobos and Deimos, with one to the Trojans could help determine if these bodies are from the same family and whether they originated from similar events, such as a large impact.

In the third research paper, a new mission concept, "DePhine", was presented. This concept aimed to explore the small moons of Mars Deimos and Phobos. The focus of my work was the general mission definition and timeline analysis, which included transfer orbit calculation, as well as the simulation of quasi-satellite orbits about Deimos and Phobos.I searched for the maximal allowable inclinations and defined maneuvers to cover not only the equatorial areas with remote sensing instruments but also the poles. Furthermore, I analyzed trajectories, Δvs, solar irradiance for power generation, the possible data rates for communication with earth and landing scenarios on Phobos and Deimos. At the time of developing this scenario, it was a novel exploration concept, as neither moon had been visited by a human space probe.

I also contributed to follow-up articles which focused on landing a small package on Phobos. The results obtained from the third research paper served as a starting point for the trajectory analysis and landing scenario. The reference Quasi-Satellite orbit of the Dephine and PhoDex proposals was used as initial orbit, and I calculated maneuvers for close fly-bys and landing package deliveries.

Currently the MMX mission is planned to be launched in 2026 with Phobos as primary target and Deimos as secondary target. If successful, it will be the first mission which has the moons of Mars as primary target. In the discussion (Section 8.1), I compared this mission with our proposals, DePhine and PhoDEx, and showed that MMX developed similar strategies. MMX also plans Quasi-Satellite Orbit phases, close flyby phases and landing a small package on the surface of Phobos.

Furthermore, we also developed scenarios for a Low-Mars-Orbiter. In our concept we planned to fly a spacecraft on a circular orbit about Mars within the Martian Atmosphere. My simulations demonstrated that the atmospheric drag of Mars can be compensated with an electric propulsion system down to altitudes of 150 km.

In addition to these main targets, I also highlighted my contributions to significant findings in scientific publications related to the main topic of this thesis. In peer-reviewed articles we presented the results from our studies of orbital evolution of spacecraft about larger bodies. For Enceladus, we demonstrated that stable resonant orbits are possible even at higher inclinations of over 60°. For BepiColombo, we we revealed that the pericenter distance to Mercury's surface could become critical during the extended mission phase.

A main focus of this thesis was the search for stable orbits about small bodies. Besides simulating Self-Stabilized Terminator orbits around the triple asteroid 2001 SN_{263}, I also modeled orbits about the binary asteroid 1996 FG_3. In our publication, we presented the result and demonstrated that these orbits are also feasible for a binary asteroid. At the time of our publication these orbits were still a theoretical concept. In 2019 the OSIRIS-REx spacecraft became the first artificial satellite which entered such an orbit. However, to date, no mission has yet flown in a Self-Stabilized Terminator orbit about a binary or ternary asteroid.

All bodies of interest presented in this thesis may become important targets in future Solar System exploration missions. Scientific analysis of these bodies may shed light on the open questions of the evolution of the Solar System and the universe. The results presented in this thesis can help in planning, developing and carrying out missions to these targets in the future.

Bibliography

Acton, C., Bachman, N., Semenov, B., and Wright, E. (2018). A look towards the future in the handling of space science mission geometry. *Planetary and Space Science*, 150:9–12.

Acton, C. H. (1996). Ancillary data services of NASA's Navigation and Ancillary Information Facility. *Planetary and Space Science*, 44(1):65–70.

Acuna, M. H., Connerney, J. E. P., Ness, N. F., Lin, R. P., Mitchell, D., Carlson, C. W., McFadden, J., Anderson, K. A., Reme, H., Mazelle, C., Vignes, D., Wasilewski, P., and Cloutier, P. (1999). Global Distribution of Crustal Magnetization Discovered by the Mars Global Surveyor MAG/ER Experiment. *Science*, 284:790.

Albee, A. L., Arvidson, R. E., Palluconi, F., and Thorpe, T. (2001). Overview of the mars global surveyor mission. *Journal of Geophysical Research: Planets*, 106(E10):23291–23316.

Ambrosi, R., Tinsley, T., Barco, A., Mesalam, R., Watkinson, E. J., Sargeant, H., Bicknell, C., Crawford, T., Sanderson, R., White, J., Sarsfield, M., Hanigan, N., Magistrati, G., Fongarland, C., Landgraf, M., Simpson, K., Tuley, R., Perkinson, M.-C., Hopton, R., and Slater, P. (2023). The european radioisotope power systems program: Endure – european devices using radioisotope energy. *Nuclear and Emerging Technologies for Space (NETS 2023)*, pages 282–286.

Ambrosi, R. M., Williams, H., Watkinson, E. J., Barco, A., Mesalam, R., Crawford, T., Bicknell, C., Samara-Ratna, P., Vernon, D., Bannister, N., Ross, D., Sykes, J., Perkinson, M.-C., Burgess, C., Stroud, C., Gibson, S., Godfrey, A., Slater, R. G., Reece, M. J., Chen, K., Simpson, K., Tuley, R., Sarsfield, M., Tinsley, T. P., Stephenson, K., Freis, D., Vigier, J.-F., Konings, R. J. M., Fongarland, C., Libessart, M., Merrifield, J., Kramer, D. P., Byrne, J., and Foxcroft, B. (2019). European Radioisotope Thermoelectric Generators (RTGs) and Radioisotope Heater Units (RHUs) for Space Science and Exploration. *Space Science Reviews*, 215(8):55.

Andert, T. P., Remus, S., Simpson, R. A., Pätzold, M., Asmar, S. W., Kahan, D. S., Bird, M. K., Häusler, B., and Tellmann, S. (2015). First Rosetta Radio Science Bistatic Radar Observations of 67P/Churyumov-Gerasimenko. In *EGU General Assembly Conference Abstracts*, EGU General Assembly Conference Abstracts, page 9760.

Andert, T. P., Rosenblatt, P., Pätzold, M., Häusler, B., Dehant, V., Tyler, G. L., and Marty, J. C. (2010). Precise mass determination and the nature of Phobos. *Geophysical Research Letters*, 37(9):L09202.

Anonymous (2018). F-class evaluation (phase 1): Feedback to proposers. Technical report, European Space Agency.

Araujo, R. A. N., Winter, O. C., and Prado, A. F. B. A. (2015). Stable retrograde orbits around the triple system 2001 sn263. *Monthly Notices of the Royal Astronomical Society*, 449(4):4404–4414.

Araujo, R. A. N., Winter, O. C., Prado, A. F. B. A., and Sukhanov, A. A. (2012). Stability regions around the components of the triple system 2001 sn263. *Monthly Notices of the Royal Astronomical Society*, 423(4):3058–3073.

Arianespace (2016). *Ariane 6: User's Manual.* Arianespace.

Asphaug, E. and Melosh, H. J. (1993). The Stickney Impact of Phobos: A Dynamical Model. *Icarus*, 101(1):144–164.

Auster, H.-U., Apathy, I., Berghofer, G., Fornacon, K.-H., Remizov, A., Carr, C., Güttler, C., Haerendel, G., Heinisch, P., Hercik, D., Hilchenbach, M., Kührt, E., Magnes, W., Motschmann, U., Richter, I., Russell, C. T., Przyklenk, A., Schwingenschuh, K., Sierks, H., and Glassmeier, K.-H. (2015). The nonmagnetic nucleus of comet 67P/Churyumov-Gerasimenko. *Science*, 349(6247):1.5102.

Avanesov, G., Zhukov, B., Ziman, Y., Kostenko, V., Kuzmin, A., Muravev, V., Fedotov, V., Bonev, B., Mishev, D., Petkov, D., Krumov, A., Simeonov, S., Boycheva, V., Uzunov, Y., Weide, G. G., Halmann, D., Possel, W., Head, J., Murchie, S., Schkuratov, Y. G., Berghanel, R., Danz, M., Mangoldt, T., Pihan, U., Weidlich, U., Lumme, K., Muinonen, K., Peltoniemi, J., Duxbury, T., Murray, B., Herkenhoff, K., Fanale, F., Irvine, W., and Smith, B. (1991). Results of TV imaging of phobos (experiment VSK-FREGAT). *Planetary and Space Science*, 39(1-2):281–295.

Banaszkiewicz, M. and Ip, W. H. (1991). A statistical study of impact ejecta distribution around Phobos and Deimos. *Icarus*, 90(2):237–253.

Banner, T. (2024). Forscher rechnen nach: Könnte der gefährliche Asteroid Apophis doch die Erde treffen? *Merkur.de*. accessed: 29-March-2024.

Barlow, N. (2009). *Mars: An Introduction to its Interior, Surface and Atmosphere*. Cambridge University Press.

Barucci, M. A., Cheng, A., Michel, P., Benner, L., Binzel, R., Bland, P., Böhnhardt, H., Brucato, J., Bagatin, A. C., Cerroni, P., Dotto, E., Fitzsimmons, A., Franchi, I., Green, S., Lara, L.-M., Licandro, J., Marty, B., Muinonen, K., Nathues, A., Oberst, J., Rivkin, A., Robert, F., Saladino, R., Trigo-Rodriguez, J., Ulamec, S., and Zolensky, M. (2012). Marcopolo-r near earth asteroid sample return mission. *Experimental Astronomy*, 33(2-3):645 – 684.

Basilevsky, A. T., Lorenz, C. A., Shingareva, T. V., Head, J. W., Ramsley, K. R., and Zubarev, A. E. (2014). The surface geology and geomorphology of Phobos. *Planetary and Space Science*, 102:95–118.

Baumgärtel, K., Sauer, K., Dubinin, E., Tarrasov, V., and Dougherty, M. (1998). "Phobos events"—Signatures of solar wind interaction with a gas torus? *Earth, Planets and Space*, 50(5):453–462.

Becker, T. M., Howell, E. S., Nolan, M. C., Magri, C., Pravec, P., Taylor, P. A., Oey, J., Higgins, D., Vilagi, J., Kornos, L., Galad, A., Gajdos, S., Gaftonyuk, N. M., Krugly, Y. N., Molotov, I. E., Hicks, M. D., Carbognani, A., Warner, B. D., Vachier, F., Marchis, F., and Pollock, J. T. (2015). Physical modeling of triple near-earth asteroid (153591) 2001 sn263 from radar and optical light curve observations. *Icarus*, 248:499–515.

Becker, T. M., Howell, E. S., Nolan, M. C., Magri, C., Pravec, P., Taylor, P. A., Oey, J., Higgins, D., Vilagi, J., Kornos, L., Galad, A., Gajdos, S., Gaftonyuk, N. M., Krugly, Y. N., Molotov, I. E., Hicks, M. D., Carbognani, A., Warner, B. D., Vachier, F., Marchis, F., and Pollock, J. T. (2017). Shape model of Asteroid (153591) 2001 SN263 V1.0. *NASA Planetary Data System*.

Becker, T. M., Nolan, M., Howell, E., and Magri, C. (2009). Physical Modeling of Triple Near-Earth Asteroid 153591 (2001 SN263). In *American Astronomical Society Meeting Abstracts #213*, volume 213 of *American Astronomical Society Meeting Abstracts*, page 401.10.

Benedikter, A., Matar, J., Gallonetto, D., Rodriguez-Cassola, M., Krieger, M., Hussmann, H., Parihar, T., Stark, A., Wickhusen, K., Nagai, M., Otto, T., and Hartmann, F. (2024). FRACTIONATED SUB-SURFACE SOUNDER CONFIGURATIONS FOR GIANT PLANETS SATELLITES EXPLORATION. Technical report, ESA.

Benedikter, A., Wickhusen, K., Hussmann, H., Stark, A., Damme, F., Rodriguez-Cassola, M., and Krieger, G. (2022). Periodic orbits for interferometric and tomographic radar imaging of Saturn's moon Enceladus. *Acta Astronautica*, 191:326–345.

Berdeu, A., Langlois, M., and Vachier, F. (2022). First observation of a quadruple asteroid. detection of a third moon around (130) elektra with sphere ifs. *Astronomy and Astrophysics*, 658:L4.

Berlin, P. (2014). *Satellite Platform Design*. Lulea University of Technology.

Bhardwaj, A., Dhanya, M. B., Alok, A., Barabash, S., Wieser, M., Futaana, Y., Wurz, P., Vorburger, A., Holmström, M., Lue, C., Harada, Y., and Asamura, K. (2015). A new view on the solar wind interaction with the Moon. *Geoscience Letters*, 2:10.

Bills, B. G. and Comstock, R. L. (2005). Spatial and temporal patterns of solar eclipses by Phobos on Mars. *Journal of Geophysical Research (Planets)*, 110(E4):E04004.

Binzel, R. P., Reddy, V., and Dunn, T. L. (2015). The Near-Earth Object Population: Connections to Comets, Main-Belt Asteroids, and Meteorites. In *Asteroids IV*, pages 243–256. University of Arizona Press.

Biscani, F. and Izzo, D. (2019). esa/pagmo2: pagmo 2.10.

Biscani, F., Izzo, D., and Yam, C. H. (2010). A Global Optimisation Toolbox for Massively Parallel Engineering Optimisation. *arXiv e-prints*, page arXiv:1004.3824.

Blagonravov, A. A. (1954). COLLECTED WORKS OF K. E. TSIOLKOVSKIY. Technical Report NASA TT F-237, Academy of Sciences USSR.

Bolles, D. (2024). Asteroids. https://science.nasa.gov/solar-system/asteroids/. accessed: 19-Feb-2024.

Bookless, J. and McInnes, C. (2006). Dynamics and Control of Displaced Periodic Orbits Using Solar-Sail Propulsion. *Journal of Guidance Control Dynamics*, 29(3):527–537.

Borderies, N. and Yoder, C. F. (1990). Phobos' gravity field and its influence on its orbit and physical librations. *Astronomy and Astrophysics*, 233(1):235–251.

Bowell, E., Holt, H. E., Levy, D. H., Innanen, K. A., Mikkola, S., and Shoemaker, E. M. (1990). 1990 MB: the first Mars Trojan. In *Bulletin of the American Astronomical Society*, volume 22, page 1357.

Britt, D. T., Yeomans, D., Housen, K., and Consolmagno, G. (2002). Asteroid Density, Porosity, and Structure. In *Asteroids III*, pages 485–500. University of Arizona Press.

Broschart, S. B., Scheeres, D. J., and Villac, B. F. (2010). New families of multi-revolution terminator orbits near small bodies. *Advances in the Astronautical Sciences*, 135:,1685–1702.

Brozović, M., Benner, L. A. M., Taylor, P. A., Nolan, M. C., Howell, E. S., Magri, C., Scheeres, D. J., Giorgini, J. D., Pollock, J. T., Pravec, P., Galád, A., Fang, J., Margot, J.-L., Busch, M. W., Shepard, M. K., Reichart, D. E., Ivarsen, K. M., Haislip, J. B., LaCluyze, A. P., Jao, J., Slade, M. A., Lawrence, K. J., and Hicks, M. D. (2011). Radar and optical observations and physical modeling of triple near-Earth Asteroid (136617) 1994 CC. *Icarus*, 216(1):241–256.

Brum, A. G. V. and Cruz, F. C. (2017). Reviewed plan of the ALR, the laser rangefinder for the ASTER deep space mission to the triple asteroid 2001-SN263. *Journal of Physics: Conf. Ser.*, 911(012016).

Brum, A. G. V., Hetem Jr, A., and Cruz, F. C. (2015a). ALR – Laser altimeter for the ASTER deep space mission. Simulated operation above a surface with crater. *Journal of Physics: Conf. Ser.*, 641(012007).

Brum, A. G. V., Hetem Jr, A., Cruz, F. C., and Rodrigues, A. P. (2015b). ALR - A laser altimeter for the first Brazilian deep space mission. Modeling and simulation of the instrument and its operation. *Journal of Computational and Applied Mathematics*, 34(2):557–569.

Brum, A. G. V., Hetem Jr, A., Rego, I. S., Francisco, C. P. F., Fenili, A., Madeira, F., Cruz, F. C., and Assafin, M. (2011). Preliminary development plan of the ALR, the laser rangefinder for the ASTER deep space mission to the 2001 SN263 asteroid. *Journal of Aerospace Tech and Management*, 3(3):331–338.

Brum, A. G. V., Hussmann, H., Wickhusen, K., and Stark, A. (2021). Encounter trajectories for Deep Space Mission ASTER to the triple Near Earth Asteroid 2001-SN263. The laser altimeter (ALR) point of view. *Advances in Space Research*.

Burke, L., Falck, R., and McGuire, M. (2010). Interplanetary mission design handbook: Earth-to-mars mission opportunities 2026 to 2045. *NASA STI/Recon Technical Report N*.

Burmeister, S., Willner, K., and Oberst, J. (2014). Phobos' Rotational Elements From Control Point Network Analysis: A New Analytic Approach. In *European Planetary Science Congress*, volume 9, pages EPSC2014–326.

Burns, J. A. (1978). The dynamical evolution and origin of the Martian moons. *Vistas in Astronomy*, 22(2):193–210.

Burns, J. A. (1992). Contradictory clues as to the origin of the Martian moons. In George, M., editor, *Mars*, pages 1283–1301. University of Arizona Press.

Cavalca, M., Prado, A. F. B. A., Formiga, J., and Gomes, V. (2017). Searching for orbits around the triple asteroid 2001sn 263. *Journal of Physics: Conference Series*, 9111:012008.

Chappaz, L., Melosh, H. J., Vaquero, M., and Howell, K. C. (2012). Material Transfer from the Surface of Mars to Phobos and Deimos. In *43rd Annual Lunar and Planetary Science Conference*, Lunar and Planetary Science Conference, page 1422.

Cheng, A. F., Barnouin, O. S., Ernst, C. M., and Kahn, E. G. (2012). Efficient Calculation of Effective Potential and Gravity on Small Bodies. In *Asteroids, Comets, Meteors 2012*, volume 1667 of *LPI Contributions*, page 6447.

Cheng, A. F., Rivkin, A. S., Michel, P., Atchison, J., Barnouin, O., Benner, L., Chabot, N. L., Ernst, C., Fahnestock, E. G., Kueppers, M., Pravec, P., Rainey, E., Richardson, D. C., Stickle, A. M., and Thomas, C. (2018). AIDA DART asteroid deflection test: Planetary defense and science objectives. *Planetary and Space Science*, 157:104–115.

Chicarro, A., Martin, P., and Trautner, R. (2004). The Mars Express mission: an overview. In Wilson, A. and Chicarro, A., editors, *Mars Express: the Scientific Payload*, volume 1240 of *ESA Special Publication*, pages 3–13.

Chobotov, V. A. (2002). Orbital mechanics, Third Edition.

Chodas, P., Chamberlin, A., and Khudikyan, S. (2024). Neos discovery statistics. https://cneos.jpl.nasa.gov/stats/totals.html. accessed: 24-Feb-2024.

Christou, A. A., Borisov, G., Dell'Oro, A., Cellino, A., and Bagnulo, S. (2017). Is the Eureka cluster a collisional family of Mars Trojan asteroids? *Icarus*, 293:243–258.

Christou, A. A., Oberst, J., Lupovka, V., Dmitriev, V., and Gritsevich, M. (2014). The meteoroid environment and impacts on Phobos. *Planetary and Space Science*, 102:164–170.

Citron, R. I., Genda, H., and Ida, S. (2015). Formation of Phobos and Deimos via a giant impact. *Icarus*, 252:334–338.

Constable, C. G. and Constable, S. C. (2004). Satellite magnetic field measurements: Applications in studying the deep Earth. *Geophysical Monograph Series*, 150:147–159.

Craddock, R. A. (2011). Are Phobos and Deimos the result of a giant impact? *Icarus*, 211(2):1150–1161.

Ćuk, M. and Burns, J. A. (2005). Effects of thermal radiation on the dynamics of binary NEAs. *Icarus*, 176(2):418–431.

Ćuk, M., Christou, A. A., and Hamilton, D. P. (2015). Yarkovsky-driven spreading of the Eureka family of Mars Trojans. *Icarus*, 252:339–346.

Cunningham, C. (2021). *Asteroids*. Kosmos (London). Reaktion Books.

Curtis, H. D. (2010). Chapter 6 - orbital maneuvers. In Curtis, H. D., editor, *Orbital Mechanics for Engineering Students (Second Edition)*, Aerospace Engineering, pages 319–390. Butterworth-Heinemann, Boston, second edition edition.

Davis, D., Durda, D., Marzari, F., Campo Bagatin, A., and Gil-Hutton, R. (2002). Collisional evolution of small-body populations. *Asteroids III*.

Davis, D. R., Housen, K. R., and Greenberg, R. (1981). The unusual dynamical environment of Phobos and Deimos. *Icarus*, 47(2):220–233.

de la Fuente Marcos, R., de León, J., de la Fuente Marcos, C., Alarcon, M. R., Licandro, J., Serra-Ricart, M., Geier, S., and Cabrera-Lavers, A. (2024). Dynamics of 2023 FW_{14}, the second L_4 Mars trojan, and a physical characterization using the 10.4 m Gran Telescopio Canarias. *Astronomy & Astrophysics*, 683:L14.

de la Torre Sangrà, D. and Fantino, E. (2021). Review of Lambert's problem. *arXiv e-prints*, page arXiv:2104.05283.

DeMeo, F. E. and Carry, B. (2014). Solar System evolution from compositional mapping of the asteroid belt. *Nature*, 505(7485):629–634.

Dotto, E., Emery, J. P., Barucci, M. A., Morbidelli, A., and Cruikshank, D. P. (2008). De Troianis: The Trojans in the Planetary System. In Barucci, M. A., Boehnhardt, H., Cruikshank, D. P., Morbidelli, A., and Dotson, R., editors, *The Solar System Beyond Neptune*, pages 383–395. University of Arizona Press.

Dubinin, E. M., Lundin, R., Pissarenko, N. F., Barabash, S. V., Zakharov, A. V., Koskinen, H., Schwingenshuh, K., and Yeroshenko, Y. G. (1990). Indirect evidences for a gas/dust torus along the Phobos orbit. *Geophysical Research Letters*, 17(6):861–864.

Dubinin, E. M., Pissarenko, N., Barabash, S. V., Zacharov, A. V., Lundin, R., Koskinen, H., Schwingenschuh, K., and Yeroshenko, Y. G. (1991). Tails of Phobos and Deimos in the solar wind and in the Martian magnetosphere. *Planetary and Space Science*, 39(1-2):123–130.

Duxbury, T. C. (1974). Phobos: Control Network Analysis. *Icarus*, 23(2):290–299.

Duxbury, T. C. (1991). An analytic model for the Phobos surface. *Planetary and Space Science*, 39(1-2):355–376.

Duxbury, T. C. and Callahan, J. D. (1989). PHOBOS and Deimos astrometric observations from Mariner 9. *Astronomy and Astrophysics*, 216(1-2):284–293.

Duxbury, T. C., Zakharov, A. V., Hoffmann, H., and Guinness, E. A. (2014). Spacecraft exploration of phobos and deimos. *Planetary and Space Science*, 102:9–17. Phobos.

Ekers, R. and Gingerich, O. (2006). The path to defining planets. *Dissertatio cum Nuncio Sidereo*.

Elphic, R. C., Lee, P., Zolensky, M. E., Mittlefehldt, D. W., Lim, L. F., and Colaprete, A. (2016). Neutron Spectroscopy Can Constrain the Composition and Provenance of Phobos and Deimos. In *47th Annual Lunar and Planetary Science Conference*, Lunar and Planetary Science Conference, page 2957.

Enya, K., Kobayashi, M., Kimura, J., Araki, H., Namiki, N., Noda, H., Kashima, S., Oshigami, S., Ishibashi, K., Yamawaki, T., Tohara, K., Saito, Y., Ozaki, M., Mizuno, T., Kamata, S., Matsumoto, K., Sasaki, S., Kuramoto, K., Sato, Y., Yokozawa, T., Numata, T., Mizumoto, S., Mizuno, H., Nagamine, K., Sawamura, A., Tanimoto, K., Imai, H., Nakagawa, H., Kirino, O., Green, D., Fujii, M., Iwamura, S., Fujishiro, N., Matsumoto, Y., Lingenauber, K., Kallenbach, R., Althaus, C., Behnke, T., Binger, J., Daurskikh, A., Eisenmenger, H., Heer, U., Hüttig, C., Lara, L. M., Lichopoj, A., Lötzke, H.-G., Lüdicke, F., Michaelis, H., Pablo Rodriguez Garcia, J., Rösner, K., Stark, A., Steinbrügge, G., Thabaut, P., Thomas, N., del Togno, S., Wahl, D., Wendler, B., Wickhusen, K., Willner, K., and Hussmann, H. (2022). The Ganymede Laser Altimeter (GALA) for the Jupiter Icy Moons Explorer (JUICE): Mission, science, and instrumentation of its receiver modules. *Advances in Space Research*, 69(5):2283–2304.

ESA (2014). Call for a Medium-size mission opportunity in ESA's Science Programme for a launch in 2025 (M4). Technical report, European Space Agency.

ESA (2021). CALL FOR A MEDIUM-SIZE AND A FAST MISSION OPPORTUNITY IN ESA'S SCIENCE PROGRAMME - TECHNICAL ANNEX. Technical Report ESA-SCI-F-MGT-MAN-001, European Space Agency, Future Missions Department (SCI-F) Directorate of Science.

ESA Media Relations (2024). Saturn's moon enceladus top target for esa. https://www.esa.int/Science_Exploration/Space_Science/Saturn_s_moon_Enceladus_top_target_for_ESA. [Online; accessed 26-March-2024].

ESA Public Relations Division (1999). Esa information note n° 22-1999. https://www.esa.int/Newsroom/Press_Releases/Europe_is_going_to_Mars. [Online; accessed 21-March-2023].

Falkner, P., Peacock, A., and Schulz, R. (2007). Instrumentation for Planetary Exploration Missions. In Schubert, G., editor, *Planets and Moons*, volume 10, pages 595–641. Elsevier Science.

Fanale, F. P. and Salvail, J. R. (1989). Loss of water from Phobos. *Geophysical Research Letters*, 16(4):287–290.

Fang, J. and Margot, J.-L. (2012). The Role of Kozai Cycles in Near-Earth Binary Asteroids. *The Astronomical Journal*, 143(3):59.

Fasoulas, S. and Messerschmid, E. (2009). *Raumfahrtsysteme: Eine Einführung mit Übungen und Lösungen*. Springer.

Faure, G. and Mensing, T. (2007). *Introduction to Planetary Science: The Geological Perspective*. Springer Netherlands.

Feldman, W. C., Ahola, K., Barraclough, B. L., Belian, R. D., Black, R. K., Elphic, R. C., Everett, D. T., Fuller, K. R., Kroesche, J., Lawrence, D. J., Lawson, S. L., Longmire, J. L., Maurice, S., Miller, M. C., Prettyman, T. H., Storms, S. A., and Thornton, G. W. (2004). Gamma-Ray, Neutron, and Alpha-Particle Spectrometers for the Lunar Prospector mission. *Journal of Geophysical Research (Planets)*, 109(E7):E07S06.

Fisher, D. and Erickson, R. (2013). *Solar System: The Moon and Other Small Bodies*. Salem Press.

Fodde, I., Feng, J., Riccardi, A., and Vasile, M. (2023). Robust stability and mission performance of a CubeSat orbiting the Didymos binary asteroid system. *Acta Astronautica*, 203:577–591.

Folkner, W. M., Williams, J. G., Boggs, D. H., Park, R. S., and Kuchynka, P. (2014). The Planetary and Lunar Ephemerides DE430 and DE431. *Interplanetary Network Progress Report*, 42-196:1–81.

Fornasier, S., Wargnier, A., Hasselmann, P. H., Tirsch, D., Matz, K.-D., Doressoundiram, A., Gautier, T., and Barucci, M. A. (2024). Phobos photometric properties from mars express hrsc observations. *Astronomy & Astrophysics*, 686:A203.

Fortescue, P., Stark, J., and Swinerd, G. (2005). *Spacecraft Systems Engineering*. Wiley.

Fraeman, A. A., Arvidson, R. E., Murchie, S. L., Rivkin, A., Bibring, J. P., Choo, T. H., Gondet, B., Humm, D., Kuzmin, R. O., Manaud, N., and Zabalueva, E. V. (2012). Analysis of disk-resolved OMEGA and CRISM spectral observations of Phobos and Deimos. *Journal of Geophysical Research (Planets)*, 117:E00J15.

Fraeman, A. A., Murchie, S. L., Arvidson, R. E., Clark, R. N., Morris, R. V., Rivkin, A. S., and Vilas, F. (2014). Spectral absorptions on Phobos and Deimos in the visible/near infrared wavelengths and their compositional constraints. *Icarus*, 229:196–205.

Franz, H. B., Trainer, M. G., Wong, M. H., Mahaffy, P. R., Atreya, S. K., Manning, H. L. K., and Stern, J. C. (2015). Reevaluated martian atmospheric mixing ratios from the mass spectrometer on the Curiosity rover. *Planetary and Space Science*, 109:154–158.

Freedman, D., Pisani, R., and Purves, R. (2007). Statistics (international student edition). *Pisani, R. Purves, 4th edn. WW Norton & Company, New York*.

Fujimoto, M., Miyamoto, H., and Kuramoto, K. (2017). JAXA's Martian Moons eXplortaion, MMX. In *European Planetary Science Congress*, pages EPSC2017–136.

Fujiwara, A. and Asada, N. (1983). Impact fracture patterns on phobos ellipsoids. *Icarus*, 56(3):590–602.

Futaana, Y., Barabash, S., Holmström, M., Fedorov, A., Nilsson, H., Lundin, R., Dubinin, E., and Fränz, M. (2010). Backscattered solar wind protons by Phobos. *Journal of Geophysical Research (Space Physics)*, 115(A10):A10213.

Gendrin, A., Mangold, N., Bibring, J.-P., Langevin, Y., Gondet, B., Poulet, F., Bonello, G., Quantin, C., Mustard, J., Arvidson, R., and Le Mouélic, S. (2005). Sulfates in Martian Layered Terrains: The OMEGA/Mars Express View. *Science*, 307(5715):1587–1591.

Giancotti, M., Campagnola, S., Tsuda, Y., and Kawaguchi, J. (2014). Families of periodic orbits in Hill's problem with solar radiation pressure: application to Hayabusa 2. *Celestial Mechanics and Dynamical Astronomy*, 120(3):269–286.

Giuranna, M., Roush, T. L., Duxbury, T., Hogan, R. C., Carli, C., Geminale, A., and Formisano, V. (2011). Compositional interpretation of PFS/MEx and TES/MGS thermal infrared spectra of Phobos. *Planetary and Space Science*, 59(13):1308–1325.

Goldsten, J. O., Rhodes, E. A., Boynton, W. V., Feldman, W. C., Lawrence, D. J., Trombka, J. I., Smith, D. M., Evans, L. G., White, J., Madden, N. W., Berg, P. C., Murphy, G. A., Gurnee, R. S., Strohbehn, K., Williams, B. D., Schaefer, E. D., Monaco, C. A., Cork, C. P., Del Eckels, J., Miller, W. O., Burks, M. T., Hagler, L. B., Deteresa, S. J., and Witte, M. C. (2007). The MESSENGER Gamma-Ray and Neutron Spectrometer. *Space Science Reviews*, 131(1-4):339–391.

Gondet, B., Bibring, J. P., and Langevin, Y. (2010). Phobos observations by OMEGA/Mars Expres hyperspectral imager. In *European Planetary Science Congress 2010*, page 548.

Goossens, S., Rowlands, D. D., Mazarico, E., Liounis, A. J., Small, J. L., Highsmith, D. E., Swenson, J. C., Lyzhoft, J. R., Ashman, B. W., Getzandanner, K. M., Leonard, J. M., Geeraert, J. L., Adam, C. D., Antreasian, P. G., Barnouin, O. S., Daly, M. G., Seabrook, J. A., and Lauretta, D. S. (2021). Mass and shape determination of (101955) bennu using differenced data from multiple osiris-rex mission phases. *The Planetary Science Journal*, 2(6):219.

Goretov, V., Lipatov, A., and Linkin, V. (2018). Description of the spacecraft on the EJP for near-earth and planetary research. Technical Report IKI-ASTER-DS-01, Space Research Institute of the Russian Academy of Sciences.

Grebowsky, J. M., Moses, J. I., and Pesnell, W. D. (2002). Meteoric Material-An Important Component of Planetary Atmospheres. *Geophysical Monograph Series*, 130:235.

Grimm, C. D., Witte, L., Schröder, S., and Wickhusen, K. (2020). Size matters - The shell lander concept for exploring medium-size airless bodies. *Acta Astronautica*, 173:91–110.

Gritzner, C., Dürfeld, K., Kasper, J., and Fasoulas, S. (2006). The asteroid and comet impact hazard: risk assessment and mitigation options. *Naturwissenschaften*, 93(8):361–373.

Herique, A., Agnus, B., Asphaug, E., Barucci, A., Beck, P., Bellerose, J., Biele, J., Bonal, L., Bousquet, P., Bruzzone, L., Buck, C., Carnelli, I., Cheng, A., Ciarletti, V., Delbo, M., Du, J., Du, X., Eyraud, C., Fa, W., Gil Fernandez, J., Gassot, O., Granados-Alfaro, R., Green, S. F., Grieger, B., Grundmann, J. T., Grygorczuk, J., Hahnel, R., Heggy, E., Ho, T. M., Karatekin, O., Kasaba, Y., Kobayashi, T., Kofman, W., Krause, C., Kumamoto, A., Küppers, M., Laabs, M., Lange, C., Lasue, J., Levasseur-Regourd, A. C., Mallet, A., Michel, P., Mottola, S., Murdoch, N., Mütze, M., Oberst, J., Orosei, R., Plettemeier, D., Rochat, S., RodriguezSuquet, R., Rogez, Y., Schaffer, P., Snodgrass, C., Souyris, J. C., Tokarz, M., Ulamec, S., Wahlund, J. E., and Zine, S. (2018). Direct observations of asteroid interior and regolith structure: Science measurement requirements. *Advances in Space Research*, 62(8):2141–2162.

Herčík, D., Auster, H.-U., Blum, J., Fornaçon, K.-H., Fujimoto, M., Gebauer, K., Güttler, C., Hillenmaier, O., Hördt, A., Liebert, E., Matsuoka, A., Nomura, R., Richter, I., Stoll, B., Weiss, B. P., and Glassmeier, K.-H. (2017). The MASCOT Magnetometer. *Space Science Reviews*, 208(1-4):433–449.

Hesar, S. G., Scheeres, D. J., and McMahon, J. W. (2017). Sensitivity Analysis of the OSIRIS-REx Terminator Orbits to Maneuver Errors. *Journal of Guidance Control Dynamics*, 40(1):81–95.

Ho, T.-M., Baturkin, V., Grimm, C., Grundmann, J. T., Hobbie, C., Ksenik, E., Lange, C., Sasaki, K., Schlotterer, M., Talapina, M., Termtanasombat, N., Wejmo, E., Witte, L., Wrasmann, M., Wübbels, G., Rößler, J., Ziach, C., Findlay, R., Biele, J., Krause, C., Ulamec, S., Lange, M., Mierheim, O., Lichtenheldt, R., Maier, M., Reill, J., Sedlmayr, H.-J., Bousquet, P., Bellion, A., Bompis, O., Cenac-Morthe, C., Deleuze, M., Fredon, S., Jurado, E., Canalias, E., Jaumann, R., Bibring, J.-P., Glassmeier, K. H., Hercik, D., Grott, M., Celotti, L., Cordero, F., Hendrikse, J., and Okada, T. (2017). MASCOT—The Mobile Asteroid Surface Scout Onboard the Hayabusa2 Mission. *Space Science Reviews*, 208(1-4):339–374.

Höschele, M. (2022). Design of an exploration mission in very low mars orbit using electric thrusting for compensation of atmospheric drag. Master's thesis, Technical University of Berlin, Department of Aeronautics and Astronautics.

Höschele, M., Stark, A., Wickhusen, K., Hussmann, H., and Oberst, J. (2021). Orbital evolution of the BepiColombo Mercury Planetary Orbiter (MPO) in the gravity field of Mercury. *Planetary and Space Science*, 200.

Hui, M.-T., Wiegert, P. A., Tholen, D. J., and Föhring, D. (2021). The Second Earth Trojan 2020 XL_5. *The Astrophysical Journal Letters*, 922(2):L25.

Hussmann, H., Lingenauber, K., Stark, A., Enya, K., Thomas, N., Lara, L., Althaus, C., Hiroshi, A., Behnke, T., Binger, J., Breuer, D., Casotto, S., Castro, J., Choblet, G., Christensen, U., Coppoolse, W., Eisenmenger, H., Ferraz-Mello, S., Fujii, M., Fujishiro, M., Gallina, G., Gwinner, K., Hauber, E., Heer, U., Henkelmann, R., Herran, M., Hüttig, C., Iwamura, S., Jimenez, J., Kimura, O., Kirino, J., Kobayashi, M., Kurita, K., Lainey, V., Leikert, T., Lichopoj, A., Lötzke, H., Lüdicke, F., Martınez-Navajas, I., Michaelis, H., Nakagawa, H., Namiki, N., Nishiyama, G., Hirotomo, N., Oberst, J., Oshigami, S., Pommerol, A., Rech, M., Rodrigo, R., Rodriguez, A., Rösner, K., Touhara, K., Saito, Y., Sasaki, S., Sato, Y., Schmidt, F., Schreiber, U., Schulze-Walewski, S., Sohl, F., Spohn, T., Steinbrügge, G., Stephan, K., Tanimoto, K., Thabaut, P., del Togno, S., Vermeersen, L., Wegner, H., Weidlich, K., Wendler, B., Wickhusen, K., Wieczorek, M., Willner, K., Wolff, F., Yokozawa, T., and Yseboodt, M. (2024). The Ganymede Laser Altimeter (GALA) on the Jupiter Icy Moons Explorer (JUICE) Mission. *Planetary and Space Science - Special issue*. Paper under review.

Hussmann, H., Oberst, J., Wickhusen, K., Shi, X., Damme, F., Lüdicke, F., Lupovka, V., and Bauer, S. (2012). Stability and evolution of orbits around the binary asteroid 175706 (1996 FG3): Implications for the MarcoPolo-R mission. *Planetary and Space Science*, 70(1):102–113.

IAU, T. I. A. U. (2022a). List Of Martian Trojans, The International Astronomical Union - Minor Planet Center. https://minorplanetcenter.net/iau/lists/MarsTrojans.html. [Online; accessed Dec-2022 to Mar-2024].

IAU, T. I. A. U. (2022b). Minor Planet Center. https://minorplanetcenter.net/. [Online; accessed 11-April-2022].

IAU, T. I. A. U. (2024). Minor Planet Center. https://www.minorplanetcenter.net/data. [Online; accessed 19-Feb-2024].

Ip, W. H. and Banaszkiewicz, M. (1990). On the dust/gas tori of Phobos and Deimos. *Geophysical Research Letters*, 17(6):857–860.

Ishimoto, H. and Mukai, T. (1994). Phobos dust rings. *Planetary and Space Science*, 42(8):691–697.

Izzo, D. (2015). Revisiting Lambert's problem. *Celestial Mechanics and Dynamical Astronomy*, 121(1):1–15.

Jacobson, R. A. (2010). The Orbits and Masses of the Martian Satellites and the Libration of Phobos. *The Astronomical Journal*, 139(2):668–679.

Jacobson, R. A. (2022). The orbits of the main saturnian satellites, the saturnian system gravity field, and the orientation of saturn's pole*. *The Astronomical Journal*, 164(5):199.

Jacobson, S. A. and Scheeres, D. J. (2011). Evolution of Small Near-Earth Asteroid Binaries. In *EPSC-DPS Joint Meeting 2011*, volume 2011, page 647.

Jakosky, B. M., Lin, R. P., Grebowsky, J. M., Luhmann, J. G., Mitchell, D. F., Beutelschies, G., Priser, T., Acuna, M., Andersson, L., Baird, D., Baker, D., Bartlett, R., Benna, M., Bougher, S., Brain, D., Carson, D., Cauffman, S., Chamberlin, P., Chaufray, J. Y., Cheatom, O., Clarke, J., Connerney, J., Cravens, T., Curtis, D., Delory, G., Demcak, S., DeWolfe, A., Eparvier, F., Ergun, R., Eriksson, A., Espley, J., Fang, X., Folta, D., Fox, J., Gomez-Rosa, C., Habenicht, S., Halekas, J., Holsclaw, G., Houghton, M., Howard, R., Jarosz, M., Jedrich, N., Johnson, M., Kasprzak, W., Kelley, M., King, T., Lankton, M., Larson, D., Leblanc, F., Lefevre, F., Lillis, R., Mahaffy, P., Mazelle, C., McClintock, W., McFadden, J., Mitchell, D. L., Montmessin, F., Morrissey, J., Peterson, W., Possel, W., Sauvaud, J. A., Schneider, N., Sidney, W., Sparacino, S., Stewart, A. I. F., Tolson, R., Toublanc, D., Waters, C., Woods, T., Yelle, R., and Zurek, R. (2015). The Mars Atmosphere and Volatile Evolution (MAVEN) Mission. *Space Science Reviews*, 195(1-4):3–48.

Jaumann, R., Neukum, G., Behnke, T., Duxbury, T. C., Eichentopf, K., Flohrer, J., Gasselt, S. v., Giese, B., Gwinner, K., Hauber, E., Hoffmann, H., Hoffmeister, A., Köhler, U., Matz, K. D., McCord, T. B., Mertens, V., Oberst, J., Pischel, R., Reiss, D., Ress, E., Roatsch, T., Saiger, P., Scholten, F., Schwarz, G., Stephan, K., Wählisch, M., and HRSC Co-Investigator Team (2007). The high-resolution stereo camera (HRSC) experiment on Mars Express: Instrument aspects and experiment conduct from interplanetary cruise through the nominal mission. *Planetary and Space Science*, 55(7-8):928–952.

Johnson, J. (2017). *Sputnik and the Space Race*. The Cold War Chronicles. Cavendish Square Publishing.

Johnston, R. (2019). (5261) Eureka –discovery and notes. http://www.johnstonsarchive.net/astro/astmoons/am-05261.html. [Online; accessed 11-Feb-2019].

Johnston, R. (2024). Asteroids with Satellites. https://www.johnstonsarchive.net/astro/asteroidmoons.html. [Online; accessed 18-Aug-2024].

Jones, G. and Snodgrass, C. (2019). Comet Interceptor: A proposed ESA Mission to a Dynamically New Comet. In *EGU General Assembly Conference Abstracts*, EGU General Assembly Conference Abstracts, page 15361.

Jones, G. H., Snodgrass, C., Tubiana, C., Küppers, M., Kawakita, H., Lara, L. M., Agarwal, J., André, N., Attree, N., Auster, U., Bagnulo, S., Bannister, M., Beth, A., Bowles, N., Coates, A., Colangeli, L., Corral van Damme, C., Da Deppo, V., De Keyser, J., Della Corte, V., Edberg, N., El-Maarry, M. R., Faggi, S., Fulle, M., Funase, R., Galand, M., Goetz, C., Groussin, O., Guilbert-Lepoutre, A., Henri, P., Kasahara, S., Kereszturi, A., Kidger, M., Knight, M., Kokotanekova, R., Kolmasova, I., Kossacki, K., Kührt, E., Kwon, Y., La Forgia, F., Levasseur-Regourd, A.-C., Lippi, M., Longobardo, A., Marschall, R., Morawski, M., Muñoz, O., Näsilä, A., Nilsson, H., Opitom, C., Pajusalu, M., Pommerol, A., Prech, L., Rando, N., Ratti, F., Rothkaehl, H., Rotundi, A., Rubin, M., Sakatani, N., Sánchez, J. P., Simon Wedlund, C., Stankov, A., Thomas, N., Toth, I., Villanueva, G., Vincent, J.-B., Volwerk, M., Wurz, P., Wielders, A., Yoshioka, K., Aleksiejuk, K., Alvarez, F., Amoros, C., Aslam, S., Atamaniuk, B., Baran, J., Barciński, T., Beck, T., Behnke, T., Berglund, M., Bertini, I., Bieda, M., Binczyk, P., Busch, M.-D., Cacovean, A., Capria, M. T., Carr, C., Castro Marín, J. M., Ceriotti, M., Chioetto, P., Chuchra-Konrad, A., Cocola, L., Colin, F., Crews, C., Cripps, V., Cupido, E., Dassatti, A., Davidsson, B. J. R., De Roche, T., Deca, J., Del Togno, S., Dhooghe, F., Donaldson Hanna, K., Eriksson, A., Fedorov, A., Fernández-Valenzuela, E., Ferretti, S., Floriot, J., Frassetto, F., Fredriksson, J., Garnier, P., Gaweł, D., Génot, V., Gerber, T., Glassmeier, K.-H., Granvik, M., Grison, B., Gunell, H., Hachemi, T., Hagen, C., Hajra, R., Harada, Y., Hasiba, J., Haslebacher, N., Herranz De La Revilla, M. L., Hestroffer, D., Hewagama, T., Holt, C., Hviid, S., Iakubivskyi, I., Inno, L., Irwin, P., Ivanovski, S., Jansky, J., Jernej, I., Jeszenszky, H., Jimenéz, J., Jorda, L., Kama, M., Kameda, S., Kelley, M. S. P., Klepacki, K., Kohout, T., Kojima, H., Kowalski, T., Kuwabara, M., Ladno, M., Laky, G., Lammer, H., Lan, R., Lavraud, B., Lazzarin, M., Le Duff, O., Lee, Q.-M., Lesniak, C., Lewis, Z., Lin, Z.-Y., Lister, T., Lowry, S., Magnes, W., Markkanen, J., Martinez Navajas, I., Martins, Z., Matsuoka, A., Matyjasiak, B., Mazelle, C., Mazzotta Epifani, E., Meier, M., Michaelis, H., Micheli, M., Migliorini, A., Millet, A.-L., Moreno, F., Mottola, S., Moutounaick, B., Muinonen, K., Müller, D. R., Murakami, G., Murata, N., Myszka, K., Nakajima, S., Nemeth, Z., Nikolajev, A., Nordera, S., Ohlsson, D., Olesk, A., Ottacher, H., Ozaki, N., Oziol, C., Patel, M., Savio Paul, A., Penttilä, A., Pernechele, C., Peterson, J., Petraglio, E., Piccirillo, A. M., Plaschke, F., Polak, S., Postberg, F., Proosa, H., Protopapa, S., Puccio, W., Ranvier, S., Raymond, S., Richter, I., Rieder, M., Rigamonti, R., Ruiz Rodriguez, I., Santolik, O., Sasaki, T., Schrödter, R., Shirley, K., Slavinskis, A., Sodor, B., Soucek, J., Stephenson, P., Stöckli, L., Szewczyk, P., Troznai, G., Uhlir, L., Usami, N., Valavanoglou, A., Vaverka, J., Wang, W., Wang, X.-D., Wattieaux, G., Wieser, M., Wolf, S., Yano, H., Yoshikawa, I., Zakharov, V., Zawistowski, T., Zuppella, P., Rinaldi, G., and Ji, H. (2024). The Comet Interceptor Mission. *Space Science Reviews*, 220(1):9.

Jordan, J. F. (1964). The Application of Lambert's Theorem to the Solution of Interplanetary Transfer Problems. Technical Report Technical Report No.35-521, Jet Propulsion Laboratory.

JPL (2022). Horizon Web Interface. https://ssd.jpl.nasa.gov/?horizons. [Online; accessed 11-Dec-2022].

JPL-SBD (2024). JPL Small Body Database Lookup. https://ssd.jpl.nasa.gov/tools/sbdb_lookup.html#/. [Online; accessed Feb/Mar-2024].

Juhasz, A. and Horanyi, M. (1995). Dust torus around Mars. *Journal of Geophysical Research*, 100(E2):3277–3284.

Khan, M., Witasse, O., Martens, W., and Boutonnet, A. (2023). Design of an in-situ science mission to a Jupiter Trojan. *Planetary and Space Science*, 225:105610.

Kholshevnikov, K. V., Krivov, A. V., Sokolov, L. L., and Titov, V. B. (1993). The Dust Torus around Phobos Orbit. *Icarus*, 105(2):351–362.

Koehn, B. W., Bowell, E. G., Skiff, B. A., Sanborn, J. J., McLelland, K. P., Pravec, P., and Warner, B. D. (2014). Lowell Observatory Near-Earth Asteroid Photometric Survey (NEAPS) - 2009 January through 2009 June. *Minor Planet Bulletin*, 41(4):286–300.

Konstantinidis, K., Flores Martinez, C., Dachwald, B., Ohndorf, A., Dykta, P., Bowitz, P., Rudolph, M., Digel, I., Kowalski, J., Voigt, K., and Förstner, R. (2014). A lander mission to probe subglacial water on saturns moon enceladus for life. *Acta Astronautica*, 106.

Kozai, Y. (1962). Secular perturbations of asteroids with high inclination and eccentricity. *Astronomical Journal*, 67:591–598.

Krasinsky, G., Pitjeva, E., Vasilyev, M., and Yagudina, E. (2002). Hidden mass in the asteroid belt. *Icarus*, 158(1):98–105.

Krivov, A. V., Feofilov, A. G., and Dikarev, V. V. (2006). Search for the putative dust belts of Mars: The late 2007 opportunity. *Planetary and Space Science*, 54(9-10):871–878.

Krivov, A. V. and Hamilton, D. P. (1997). Martian Dust Belts: Waiting for Discovery. *Icarus*, 128(2):335–353.

Kuramoto, K., Kawakatsu, Y., Fujimoto, M., Araya, A., Barucci, M. A., Genda, H., Hirata, N., Ikeda, H., Imamura, T., Helbert, J., Kameda, S., Kobayashi, M., Kusano, H., Lawrence, D. J., Matsumoto, K., Michel, P., Miyamoto, H., Morota, T., Nakagawa, H., Nakamura, T., Ogawa, K., Otake, H., Ozaki, M., Russell, S., Sasaki, S., Sawada, H., Senshu, H., Tachibana, S., Terada, N., Ulamec, S., Usui, T., Wada, K., Watanabe, S.-i., and Yokota, S. (2022). Martian moons exploration MMX: sample return mission to Phobos elucidating formation processes of habitable planets. *Earth, Planets and Space*, 74(1):12.

Kuramoto, K., Kawakatsu, Y., Fujimoto, M., and MMX Study Team (2017). Martian Moons Exploration (MMX) Conceptual Study Results. In *48th Annual Lunar and Planetary Science Conference*, Lunar and Planetary Science Conference, page 2086.

Lainey, V., Dehant, V., and Pätzold, M. (2007). First numerical ephemerides of the Martian moons. *Astronomy and Astrophysics*, 465(3):1075–1084.

Lainey, V., Pasewaldt, A., Robert, V., Rosenblatt, P., Jaumann, R., Oberst, J., Roatsch, T., Willner, K., Ziese, R., and Thuillot, W. (2021). Mars moon ephemerides after 14 years of Mars Express data. *Astronomy and Astrophysics*, 650:A64.

Lancaster, E. R. and Blanchard, R. (1969). A UNIFIED FORM OF LAMBERT'S THEOREM. Technical Report NASA Technical Note D-5368, Goddard Space Flight Center.

Lauretta, D. S., Balram-Knutson, S. S., Beshore, E., Boynton, W. V., Drouet d'Aubigny, C., DellaGiustina, D. N., Enos, H. L., Golish, D. R., Hergenrother, C. W., Howell, E. S., Bennett, C. A., Morton, E. T., Nolan, M. C., Rizk, B., Roper, H. L., Bartels, A. E., Bos, B. J., Dworkin, J. P., Highsmith, D. E., Lorenz, D. A., Lim, L. F., Mink, R., Moreau, M. C., Nuth, J. A., Reuter, D. C., Simon, A. A., Bierhaus, E. B., Bryan, B. H., Ballouz, R., Barnouin, O. S., Binzel, R. P., Bottke, W. F., Hamilton, V. E., Walsh, K. J., Chesley, S. R., Christensen, P. R., Clark, B. E., Connolly, H. C., Crombie, M. K., Daly, M. G., Emery, J. P., McCoy, T. J., McMahon, J. W., Scheeres, D. J., Messenger, S., Nakamura-Messenger, K., Righter, K., and Sandford, S. A. (2017). OSIRIS-REx: Sample Return from Asteroid (101955) Bennu. *Space Science Reviews*, 212(1-2):925–984.

Lawrence, D. J., Feldman, W. C., Goldsten, J. O., Maurice, S., Peplowski, P. N., Anderson, B. J., Bazell, D., McNutt, R. L., Nittler, L. R., Prettyman, T. H., Rodgers, D. J., Solomon, S. C., and Weider, S. Z. (2013). Evidence for Water Ice Near Mercury's North Pole from MESSENGER Neutron Spectrometer Measurements. *Science*, 339(6117):292.

Leem, Jung Woo Jun, D.-H., Heo, J., Park, W.-K., Park, J.-H., Cho, W. J., Kim, D. E., and Yu, J. S. (2013). Single-material zinc sulfide bi-layer antireflection coatings for GaAs solar cells. *Optics Express*, 21(S5):A821.

Levison, H. (2024). The discovery of a contact-binary satellite of the asteroid (152830) dinkinesh by the lucy mission. Paper under review.

Levison, H. F., Olkin, C. B., Noll, K. S., Marchi, S., Bell, James F., I., Bierhaus, E., Binzel, R., Bottke, W., Britt, D., Brown, M., Buie, M., Christensen, P., Emery, J., Grundy, W., Hamilton, V. E., Howett, C., Mottola, S., Pätzold, M., Reuter, D., Spencer, J., Statler, T. S., Stern, S. A., Sunshine, J., Weaver, H., and Wong, I. (2021). Lucy Mission to the Trojan Asteroids: Science Goals. *The Planetary Science Journal*, 2(5):171.

Ley, W., Wittmann, K., and Hallmann, W. (2009). *Handbook of Space Technology.* John Wiley and Sons, Ltd.

Li, J., Xia, Z. J., Yoshida, F., Georgakarakos, N., and Li, X. (2023). Asymmetry in the number of L4 and L5 Jupiter Trojans driven by jumping Jupiter. *Astronomy & Astrophysics*, 669:A68.

Longobardo, A., Palomba, E., De Sanctis, M. C., Zinzi, A., Scully, J. E. C., Capaccioni, F., Tosi, F., Zambon, F., Ammannito, E., Combe, J.-P., Raymond, C. A., and Russell, C. T. (2015). Mineralogical and spectral analysis of Vesta's Gegania and Lucaria quadrangles and comparative analysis of their key features. *Icarus*, 259:72–90.

Macau, E. E. N., Winter, O. C., Velho, H. F. C., Sukhanov, A. A., Brum, A. G. V., Ferreira, J. L., Hetem, A., and Sandonato, G. M. (2011). The ASTER mission: exploring for the first time a triple system asteroid. In *Proceedings of the 62nd International Astronautical Congress*, Cape Town, SA.

Margot, J. L., Nolan, M. C., Benner, L. A. M., Ostro, S. J., Jurgens, R. F., Giorgini, J. D., Slade, M. A., and Campbell, D. B. (2002). Binary asteroids in the near-earth object population. *Science*, 296(5572):1445–1448.

Margot, J.-L., Pravec, P., Taylor, P., Carry, B., and Jacobson, S. (2015). *Asteroid Systems Binaries, Triples, and Pairs*, pages 355–374. University of Arizona Press.

Martins, Z., Bunce, E., Grasset, O., Hamp, R., Jones, G., Le Gall, A., Lucchetti, A., Postberg, F., Prieto-Ballesteros, O., Roth, L., Tortora, P., and Vorburger, A. (2024). Report of the Expert Committee for the Large-class mission in ESA's Voyage 2050 plan covering the science theme 'Moons of the Giant Planets'. Technical report, European Space Agency.

Masago, B. Y. P. L., Prado, A. F. B. A., Chiaradia, A. P. M., and Gomes, V. M. (2016). Developing the precessing inclined bi-elliptical four-body problem with radiation pressure to search for orbits in the triple asteroid 2001sn263. *Advances in Space Research*, 57(4):962–982.

McInnes, C. R. (1997). The Existence and Stability of Families of Displacement Two-Body Orbits. *Celestial Mechanics and Dynamical Astronomy*, 67(2):167–180.

Meeus, J. (1997). *More mathematical astronomy morsels*. Willmann-Bell.

Menne, K. (2023). Asteroid Dinkinesh, nicht einer, nicht zwei, sondern drei! *Spektrum der Wissenschaft*. accessed: 26-Feb-2024.

Michel, P., DeMeo, F. E., and Bottke, W. F. (2015). *Asteroids IV*. University of Arizona Press.

Michel, P., Küppers, M., Martino, P., and Carnelli, I. (2024). The ESA Hera Mission to the Binary Asteroid (65803) Didymos: Ready for Launch in October 2024. In *LPI Contributions*, volume 3040 of *LPI Contributions*, page 1575.

Michel, P., Ulamec, S., Böttger, U., Grott, M., Murdoch, N., Vernazza, P., Sunday, C., Zhang, Y., Valette, R., Castellani, R., Biele, J., Tardivel, S., Groussin, O., Jorda, L., Knollenberg, J., Grundmann, J. T., Arrat, D., Pont, G., Mary, S., Grebenstein, M., Miyamoto, H., Nakamura, T., Wada, K., Yoshikawa, K., and Kuramoto, K. (2022). The MMX rover: performing in situ surface investigations on Phobos. *Earth, Planets and Space*, 74(1):2.

Mikkola, S. and Innanen, K. (1997). Orbital Stability of Planetary Quasi-Satellites. In Dvorak, R. and Henrard, J., editors, *The Dynamical Behaviour of our Planetary System*, page 345.

Mikkola, S., Innanen, K., Muinonen, K., and Bowell, E. (1994). A preliminary analysis of the orbit of the Mars Trojan asteroid (5261) Eureka. *Celestial Mechanics and Dynamical Astronomy*, 58(1):53–64.

Millour, E., Forget, F., Lopez-Valverde, M., Lefevre, F., Gonzalez-Galindo, F., Lewis, S., Chaufray, J.-Y., Montabone, L., Zakharov, V., Spiga, A., and Vals, M. (2018). Exploring the interannual variablitity of the Martian atmosphere with the Mars Climate Database v5.3. In *42nd COSPAR Scientific Assembly*, volume 42, pages C4.3–6–18.

Mizuno, T., Kase, T., Shiina, T., Mita, M., Namiki, N., Senshu, H., Yamada, R., Noda, H., Kunimori, H., Hirata, N., Terui, F., and Mimasu, Y. (2017). Development of the laser altimeter (lidar) for hayabusa2. *Space Science Reviews*, 208(1):33–47.

Molina-Cuberos, G. J., Witasse, O., Lebreton, J.-P., Rodrigo, R., and López-Moreno, J. J. (2003). Meteoric ions in the atmosphere of Mars. *Planetary and Space Science*, 51(3):239–249.

Montenbruck, O. and Gill, E. (2000). *Satellite orbits : models, methods, and applications*. Springer.

Morley, T., Budnik, F., MacKenzie, R., and Faehling, N. (2004). Mars Express Navigation for Beagle 2 Separation and Mars Orbit Insertion. In *18th International Symposium on Space Flight Dynamics*, volume 548 of *ESA Special Publication*, page 189.

Mostaza Prieto, D., Graziano, B. P., and Roberts, P. C. E. (2014). Spacecraft drag modelling. *Progress in Aerospace Sciences*, 64:56–65.

Mottola, S., Arnold, G., Grothues, H.-G., Jaumann, R., Michaelis, H., Neukum, G., and Bibring, J.-P. (2007). The Rolis Experiment on the Rosetta Lander. *Space Science Reviews*, 128(1-4):241–255.

Mottola, S., Denk, T., Marchi, S., Binzel, R. P., Noll, K. S., Spencer, J. R., and Levison, H. F. (2023). Characterizing asteroid (152830) Dinkinesh in preparation for the encounter with the NASA Lucy mission: a photometric study. *Monthly Notices of the Royal Astronomical Society: Letters*, 524(1):L1–L4.

Murchie, S. and Erard, S. (1996). Spectral Properties and Heterogeneity of PHOBOS from Measurements by PHOBOS 2. *Icarus*, 123(1):63–86.

Murchie, S. L., Britt, D. T., Head, J. W., Pratt, S. F., Fisher, P. C., Zhukov, B. S., Kuzmin, A. A., Ksanfomality, L. V., Zharkov, A. V., Nikitin, G. E., Fanale, F. P., Blaney, D. L., Bell, J. F., and Robinson, M. S. (1991). Color heterogeneity of the surface of Phobos: relationships to geologic features and comparison to meteorite analogs. *Journal of Geophysical Research*, 96:5925–5945.

Murchie, S. L., Britt, D. T., and Pieters, C. M. (2014). The value of Phobos sample return. *Planetary and Space Science*, 102:176–182.

Murchie, S. L., Choo, T., Humm, D., Rivkin, A. S., Bibring, J. P., Langevin, Y., Gondet, B., Roush, T. L., Duxbury, T., and CRISM Team (2008). MRO/CRISM Observations of Phobos and Deimos. In *39th Annual Lunar and Planetary Science Conference*, Lunar and Planetary Science Conference, page 1434.

Murchie, S. L., Thomas, P. C., Rivkin, A. S., and Chabot, N. L. (2015). Phobos and Deimos. In *Asteroids IV*, pages 451–467. University of Arizona Press.

Murray, C. and Dermott, S. (1999). *Solar System Dynamics*. Cambridge University Press.

Murray, J. B. and Heggie, D. C. (2014). Character and origin of Phobos' grooves. *Planetary and Space Science*, 102:119–143.

Murray, J. B. and Iliffe, J. C. (2011). Morphological and geographical evidence for the origin of Phobos' grooves from HRSC Mars Express images. *Geological Society of London Special Publications*, 356(1):21–41.

NAIF (2019). SPICE generic Kernels. https://naif.jpl.nasa.gov/pub/naif/generic_kernels/spk/. [Online; accessed 12-Mar-2019].

NASA (2024). Asteroids: Facts. https://science.nasa.gov/solar-system/asteroids/facts/. [Online; accessed 15-Feb-2024].

Nicholson, S. B. (1961). The Trojan Asteroids. *Leaflet of the Astronomical Society of the Pacific*, 8(381):239.

Nolan, M. C., Howell, E. S., Becker, T. M., Magri, C., Giorgini, J. D., and Margot, J. L. (2008). Arecibo Radar Observations of 2001 SN_{263}: A Near-Earth Triple Asteroid System. In *AAS/Division for Planetary Sciences Meeting Abstracts #40*, volume 40 of *AAS/Division for Planetary Sciences Meeting Abstracts*, page 25.04.

Oberst, J., Hussmann, H., Giese, B., Sohl, F., Shoji, D., Stark, A., Wickhusen, K., and Wählisch, M. (2017). Enceladus geodetic framework. In *International Archives of the Photogrammetry, Remote Sensing and Spatial Information Sciences - ISPRS Archives*, volume XLII-3, pages 113–118.

Oberst, J., Lainey, V., Poncin-Lafitte, C. L., Dehant, V., Rosenblatt, P., Ulamec, S., Biele, J., Spurmann, J., Kahle, R., Klein, V., Schreiber, U., Schlicht, A., Rambaux, N., Laurent, P., Noyelles, B., Foulon, B., Zakharov, A., Gurvits, L., Uchaev, D., Murchie, S., Reed, C., Turyshev, S. G., Gil, J., Graziano, M., Willner, K., Wickhusen, K., Pasewaldt, A., Wählisch, M., and Hoffmann, H. (2012). GETEMME—a mission to explore the Martian satellites and the fundamentals of solar system physics. *Experimental Astronomy*, 34.

Oberst, J., Schwarz, G., Behnke, T., Hoffmann, H., Matz, K. D., Flohrer, J., Hirsch, H., Roatsch, T., Scholten, F., Hauber, E., Brinkmann, B., Jaumann, R., Williams, D., Kirk, R., Duxbury, T., Leu, C., and Neukum, G. (2008). The imaging performance of the SRC on Mars Express. *Planetary and Space Science*, 56(3-4):473–491.

Oberst, J., Wickhusen, K., Gwinner, K., Hauber, E., Stark, A., Elgner, S., Grott, M., Fanara, L., Hussmann, H., Steinbrügge, G., Lewis, S., Balme, M., Maugeri, M., Diolaiuti, G., Karlsson, N., Johnsson, A., Ivanov, A., and Hiesinger, H. (2022). Planetary polar explorer - the case for a next-generation remote sensing mission to low Mars orbit. *Experimental Astronomy*.

Oberst, J., Wickhusen, K., Ho, T.-M., Willner, K., Gläser, P., Witte, L., Golkar, A., Herique, A., Zakharov, A., Groussin, O., Barabash, S., Pätzold, M., Hübers, H.-W., Seidensticker, K., Josset, J.-L., Rosenblatt, P., Lainey, V., Cremonese, G., Christou, A., and Orosei, R. (2014). PhoDEx - a Mission to Explore the Origin and Evolution of the Martian Satellites. Technical report, German Aerospace Center.

Oberst, J., Wickhusen, K., Willner, K., Gwinner, K., Spiridonova, S., Kahle, R., Coates, A., Herique, A., Plettemeier, D., Díaz-Michelena, M., Zakharov, A., Futaana, Y., Pätzold, M., Rosenblatt, P., Lawrence, D. J., Lainey, V., Gibbings, A., and Gerth, I. (2018a). DePhine - The Deimos and Phobos Interior Explorer. *Advances in Space Research*, 62(8):2220–2238.

Oberst, J., Wickhusen, K., Willner, K., Ulamec, S., Biele, J., Damme, F., Topputo, F., Speretta, S., Börner, A., Böttger, U., Grott, M., Ho, T.-M., Herique, A., Beck, P., Plettemeier, D., Thomas, N., Mall, U., Helbert, J., Gwinner, K., Adeli, S., Dirkx, D., Vermeersen, B., Stark, A., Rauer, H., Christou, A., Michel, P., Kührt, E., Hviid, S., and Vincent, J.-B. (2018b). Mars TAstE - a F-Class Mission Proposal for ESA's Cosmic Vision Program. Technical report, German Aerospace Center.

Oberst, J., Wickhusen, K., Zakharov, A., Willner, K., Futaana, Y., Spiridonova, S., Pätzold, M., Kahle, R., Rosenblatt, P., Gwinner, K., Lawrence, D., Coates, A., Lainey, V., Herique, A., Gibbings, A., Plettemeier, D., Gerth, I., and Diaz Michelena, M. (2016). DePhine - a M-Class Mission Proposal for ESA's Cosmic Vision Program. Technical report, German Aerospace Center.

Obrecht, G., Cowan, K., and de Almeida Prado, A. F. (2020). Applicability of evolutionary algorithms for orbit optimization in the strongly perturbed environment of the 2001 SN263 triple asteroid system. *Proceedings of the 2nd IAA/AAS SciTech Forum 2019 (SciTech Forum on Space Flight Mechanics and Space Structures and Materials), Moscow, Russia, 25 June 2019*, 174:205–225.

Øieroset, M., Brain, D. A., Simpson, E., Mitchell, D. L., Phan, T. D., Halekas, J. S., Lin, R. P., and Acuña, M. H. (2010). Search for Phobos and Deimos gas/dust tori using in situ observations from Mars Global Surveyor MAG/ER. *Icarus*, 206(1):189–198.

Osterhage, W. (2021). *Die Geschichte der Raumfahrt*. Springer Berlin Heidelberg.

Paral, J., Trávníček, P. M., Rankin, R., and Schriver, D. (2010). Sodium ion exosphere of Mercury during MESSENGER flybys. *Geophysical Research Letters*, 37(19):L19102.

Pätzold, M., Andert, T., Jacobson, R., Rosenblatt, P., and Dehant, V. (2014a). Phobos: Observed bulk properties. *Planetary and Space Science*, 102:86–94.

Pätzold, M., Andert, T. P., Asmar, S. W., Anderson, J. D., Barriot, J. P., Bird, M. K., Häusler, B., Hahn, M., Tellmann, S., Sierks, H., Lamy, P., and Weiss, B. P. (2011). Asteroid 21 Lutetia: Low Mass, High Density. *Science*, 334(6055):491.

Pätzold, M., Andert, T. P., Tyler, G. L., Asmar, S. W., Häusler, B., and Tellmann, S. (2014b). Phobos mass determination from the very close flyby of Mars Express in 2010. *Icarus*, 229:92–98.

Peet, M. M. (2023). *Spacecraft Dynamics and Control*. Arizona State University.

Peplowski, P. N., Bazell, D., Evans, L. G., Goldsten, J. O., Lawrence, D. J., and Nittler, L. R. (2015). Hydrogen and major element concentrations on 433 Eros: Evidence for an L- or LL-chondrite-like surface composition. *Meteoritics & Planetary Science*, 50(3):353–367.

Peplowski, P. N., Lawrence, D. J., Rhodes, E. A., Sprague, A. L., McCoy, T. J., Denevi, B. W., Evans, L. G., Head, J. W., Nittler, L. R., Solomon, S. C., Stockstill-Cahill, K. R., and Weider, S. Z. (2012). Variations in the abundances of potassium and thorium on the surface of Mercury: Results from the MESSENGER Gamma-Ray Spectrometer. *Journal of Geophysical Research (Planets)*, 117:E00L04.

Perna, D., Alvarez-Candal, A., Fornasier, S., Kaňuchová, Z., Giuliatti Winter, S. M., Vieira Neto, E., and Winter, O. C. (2014). The triple near-Earth asteroid (153591) 2001 SN263: an ultra-blue, primitive target for the Aster space mission. *Astronomy and Astrophysics*, 568:L6.

Picardi, G., Biccari, D., Seu, R., Marinangeli, L., Johnson, W. T. K., Jordan, R. L., Plaut, J., Safaenili, A., Gurnett, D. A., Ori, G. G., Orosei, R., Calabrese, D., and Zampolini, E. (2004). Performance and surface scattering models for the Mars Advanced Radar for Subsurface and Ionosphere Sounding (MARSIS). *Planetary and Space Science*, 52:149–156.

Pieters, C. M., Murchie, S., Thomas, N., and Britt, D. (2014). Composition of Surface Materials on the Moons of Mars. *Planetary and Space Science*, 102:144–151.

Pieters, C. M., Taylor, L. A., Noble, S. K., Keller, L. P., Hapke, B., Morris, R. V., Allen, C. C., McKay, D. S., and Wentworth, S. (2000). Space weathering on airless bodies: Resolving a mystery with lunar samples. *Meteoritics & Planetary Science*, 35(5):1101–1107.

Pincock, S. and Frary, M. (2008). *Der Ursprung des Universums für Dummies*. Wiley.

Plettemeier, D., Hahnel, R., Hegler, S., Safaeinili, A., Orosei, R., Cicchetti, A., Plaut, J., and Picardi, G. (2009). Simulation of Radar-Backscattering from Phobos - A Contribution to the Experiment MARSIS aboard MarsExpress. In *EGU General Assembly Conference Abstracts*, EGU General Assembly Conference Abstracts, page 3763.

Podbregar, N. and Lohmann, D. (2014). *Im Fokus: Sonnensystem: Eine Reise durch unsere kosmische Heimat*. Naturwissenschaften im Fokus. Springer Berlin Heidelberg.

Polishook, D., Jacobson, S. A., Morbidelli, A., and Aharonson, O. (2017). A martian origin for the mars trojan asteroids. *Nature Astronomy*, 1.

Poppe, A. R., Curry, S. M., Fatemi, S., McFadden, J. P., and Delory, G. T. (2015). Modeling the Phobos and Deimos Neutral Gas Tori: Implications for Detection by MAVEN. In *46th Annual Lunar and Planetary Science Conference*, Lunar and Planetary Science Conference, page 1399.

Prado, A. F. B. A. (2014). Mapping orbits around the asteroid 2001sn263. *Advances in Space Research*, 53(5):877–889.

Pravec, P., Scheirich, P., Kušnirák, P., Šarounová, L., Mottola, S., Hahn, G., Brown, P., Esquerdo, G., Kaiser, N., Krzeminski, Z., Pray, D. P., Warner, B. D., Harris, A. W., Nolan, M. C., Howell, E. S., Benner, L. A. M., Margot, J. L., Galád, A., Holliday, W., Hicks, M. D., Krugly, Y. N., Tholen, D., Whiteley, R., Marchis, F., DeGraff, D. R., Grauer, A., Larson, S., Velichko, F. P., Cooney, W. R., Stephens, R., Zhu, J., Kirsch, K., Dyvig, R., Snyder, L., Reddy, V., Moore, S., Gajdoš, Š., Világi, J., Masi, G., Higgins, D., Funkhouser, G., Knight, B., Slivan, S., Behrend, R., Grenon, M., Burki, G., Roy, R., Demeautis, C., Matter, D., Waelchli, N., Revaz, Y., Klotz, A., Rieugné, M., Thierry, P., Cotrez, V., Brunetto, L., and Kober, G. (2006). Photometric survey of binary near-Earth asteroids. *Icarus*, 181(1):63–93.

Ramsley, K. R. and Head, J. W. (2013a). Mars impact ejecta in the regolith of Phobos: Bulk concentration and distribution. *Planetary and Space Science*, 87:115–129.

Ramsley, K. R. and Head, J. W. (2013b). The origin of Phobos grooves from ejecta launched from impact craters on Mars: Tests of the hypothesis. *Planetary and Space Science*, 75:69–95.

Rivkin, A. S., Brown, R. H., Trilling, D. E., Bell, J. F., and Plassmann, J. H. (2002). Near-Infrared Spectrophotometry of Phobos and Deimos. *Icarus*, 156(1):64–75.

Roa, J. (2017). *10. Lambert's problem with generalized logarithmic spirals*, pages 233–260. De Gruyter, Berlin, Boston.

Robutel, P. and Souchay, J. (2010). An Introduction to the Dynamics of Trojan Asteroids. In Souchay, J. and Dvorak, R., editors, *Lecture Notes in Physics*, volume 790, pages 195–227. Berlin Springer Verlag.

Rosenblatt, P. (2011). The origin of the Martian moons revisited. *The Astronomy and Astrophysics Review*, 19:44.

Rosenblatt, P. and Charnoz, S. (2012). On the formation of the martian moons from a circum-martian accretion disk. *Icarus*, 221(2):806–815.

Rosenblatt, P., Charnoz, S., Dunseath, K. M., Terao-Dunseath, M., Trinh, A., Hyodo, R., Genda, H., and Toupin, S. (2016). Accretion of Phobos and Deimos in an extended debris disc stirred by transient moons. *Nature Geoscience*, 9(8):581–583.

Rosenblatt, P., Lainey, V., Le Maistre, S., Marty, J. C., Dehant, V., Pätzold, M., Van Hoolst, T., and Häusler, B. (2008). Accurate Mars Express orbits to improve the determination of the mass and ephemeris of the Martian moons. *Planetary and Space Science*, 56(7):1043–1053.

Rosenblatt, P., Marty, J., Le Maistre, S., Dehant, V. M., and Karatekin, O. (2009). Assessing the precision on the determination of the Martian CO2 seasonal mass budget from time-variable gravity observations. In *AGU Fall Meeting Abstracts*, volume 2009, pages P23A–1240.

Rubincam, D. P. (2000). Radiative Spin-up and Spin-down of Small Asteroids. *Icarus*, 148(1):2–11.

Rubincam, D. P., Chao, B. F., and Thomas, P. C. (1995). The Gravitational Field of Deimos. *Icarus*, 114(1):63–67.

Rumpf, C. M., Lewis, H. G., and Atkinson, P. M. (2017). Asteroid impact effects and their immediate hazards for human populations. *Geophysical Research Letters*, 44(8):3433–3440.

Rödel, E. (2014). *Sputnik: Aufbruch ins All*. Motorbuch.

Safronov, V. S. and Vitjazev, A. V. (1986). The Origin and Early Evolution of the Terrestrial Planets. In Saxena, S. K., editor, *Chemistry and Physics of Terrestrial Planets*, volume 6, page 1.

Saito, Y., Yokota, S., Tanaka, T., Asamura, K., Nishino, M. N., Fujimoto, M., Tsunakawa, H., Shibuya, H., Matsushima, M., Shimizu, H., Takahashi, F., Mukai, T., and Terasawa, T. (2008). Solar wind proton reflection at the lunar surface: Low energy ion measurement by MAP-PACE onboard SELENE (KAGUYA). *Geophysical Research Letters*, 35(24):L24205.

Sanchez, D. M. and Prado, A. F. B. A. (2019). Searching for less-disturbed orbital regions around the near-earth asteroid 2001 sn263. *Journal of Spacecraft and Rockets*, 56(6):1775–1785.

Sánchez, J. P., Morante, D., Hermosin, P., Ranuschio, D., Estalella, A., Viera, D., Centuori, S., Jones, G., Snodgrass, C., Levasseur-Regourd, A. C., and Tubiana, C. (2021). ESA F-Class Comet Interceptor: Trajectory design to intercept a yet-to-be-discovered comet. *Acta Astronautica*, 188:265–277.

Santana-Ros, T., Micheli, M., Faggioli, L., Cennamo, R., Devogèle, M., Alvarez-Candal, A., Oszkiewicz, D., Ramírez, O., Liu, P. Y., Benavidez, P. G., Campo Bagatin, A., Christensen, E. J., Wainscoat, R. J., Weryk, R., Fraga, L., Briceño, C., and Conversi, L. (2022). Orbital stability analysis and photometric characterization of the second Earth Trojan asteroid 2020 XL_5. *Nature Communications*, 13:447.

Saunders, R. S., Arvidson, R. E., Badhwar, G. D., Boynton, W. V., Christensen, P. R., Cucinotta, F. A., Feldman, W. C., Gibbs, R. G., Kloss, C., J., Landano, M. R., Mase, R. A., McSmith, G. W., Meyer, M. A., Mitrofanov, I. G., Pace, G. D., Plaut, J. J., Sidney, W. P., Spencer, D. A., Thompson, T. W., and Zeitlin, C. J. (2004). 2001 Mars Odyssey Mission Summary. *Space Science Reviews*, 110(1):1–36.

Scheeres, D. (2012). *Orbital Motion in Strongly Perturbed Environments: Applications to Asteroid, Comet and Planetary Satellite Orbiters*. Springer Praxis Books. Springer Berlin Heidelberg.

Scheeres, D., Sutter, B., and Rosengren, A. (2013). Design, dynamics and stability of the osiris-rex sun-terminator orbits. *Advances in the Astronautical Sciences*, 148:3263–3282.

Scheeres, D. J. (1999). Satellite dynamics about small bodies: Averaged solar radiation pressure effects. *Journal of the Astronautical Sciences*, 47(1):25–46.

Schefter, J. (2000). *The Race: The Complete True Story of How America Beat Russia to the Moon*. Anchor.

Schenk, P., Clark, R., Howett, C., Verbiscer, A., and Waite, J. (2018). *Enceladus and the Icy Moons of Saturn*. Space Science Series. University of Arizona Press.

Schmadel, L. D. (2012). *Dictionary of Minor Planet Names*. Springer Berlin, Heidelberg.

Schmeidler, F. (1998). *Kommentar zu "De revolutionibus"*. Gesamtausgabe / Nicolaus Copernicus. Akademie Verlag.

Scholl, H., Marzari, F., and Tricarico, P. (2005). Dynamics of Mars Trojans. *Icarus*, 175(2):397–408.

Scully, J. E. C., Yin, A., Russell, C. T., Buczkowski, D. L., Williams, D. A., Blewett, D. T., Ruesch, O., Hiesinger, H., Le Corre, L., Mercer, C., Yingst, R. A., Garry, W. B., Jaumann, R., Roatsch, T., Preusker, F., Gaskell, R. W., Schröder, S. E., Ammannito, E., Pieters, C. M., and Raymond, C. A. (2014). Geomorphology and structural geology of Saturnalia Fossae and adjacent structures in the northern hemisphere of Vesta. *Icarus*, 244:23–40.

Seidelmann, P. K., Archinal, B. A., A'Hearn, M. F., Conrad, A., Consolmagno, G. J., Hestroffer, D., Hilton, J. L., Krasinsky, G. A., Neumann, G., Oberst, J., Stooke, P., Tedesco, E. F., Tholen, D. J., Thomas, P. C., and Williams, I. P. (2007). Report of the IAU/IAG Working Group on cartographic coordinates and rotational elements: 2006. *Celestial Mechanics and Dynamical Astronomy*, 98(3):155–180.

Sergeyevsky, A. and Cunniff, R. (1987). Interplanetary mission design handbook. Volume 1, Part 5: Mars-to-Earth ballistic mission opportunities, 1992-2007.

Serio, G., Manara, A., and Sicoli, P. (2002). Giuseppe piazzi and the discovery of ceres. *Asteroids III*.

Shi, X., Oberst, J., and Willner, K. (2016). Mass wasting on Phobos triggered by an evolving tidal environment. *Geophysical Research Letters*, 43(24):12,371–12,379.

Sierks, H., Keller, H. U., Jaumann, R., Michalik, H., Behnke, T., Bubenhagen, F., Büttner, I., Carsenty, U., Christensen, U., Enge, R., Fiethe, B., Gutiérrez Marqués, P., Hartwig, H., Krüger, H., Kühne, W., Maue, T., Mottola, S., Nathues, A., Reiche, K. U., Richards, M. L., Roatsch, T., Schröder, S. E., Szemerey, I., and Tschentscher, M. (2011). The Dawn Framing Camera. *Space Science Reviews*, 163(1-4):263–327.

Silva Neto, J. B., Sanchez, D. M., Prado, A. F. B. A., Formiga, J. K. S., Zanetti, R., Russell, R. P., Ozimek, M. T., and Bowes, A. L. (2016). Using solar radiation pressure to maneuver a spacecraft in the triple asteroid 2001sn(263). *Spaceflight Mechanics*, 158:3789–3804.

Simonelli, D. P., Thomas, P. C., Carcich, B. T., and Veverka, J. (1993). The Generation and Use of Numerical Shape Models for Irregular Solar System Objects. *Icarus*, 103(1):49–61.

Soter, S. L. (1971). *The Dust Belts of Mars*. PhD thesis, Cornell University, New York.

Spencer, J. R. and Nimmo, F. (2013). Enceladus: An Active Ice World in the Saturn System. *Annual Review of Earth and Planetary Sciences*, 41:693–717.

Spiridonova, S., Wickhusen, K., Kahle, R., and Oberst, J. (2017). Quasi-satellite orbits around deimos and phobos motivated by the dephine mission proposal. In *Proceedings of the 26th International Symposium on Space Flight Dynamics*.

Spohn, T., Sohl, F., and Breuer, D. (1998). Mars. *Astronomy and Astrophysics Review*, 8:181–235.

Stark, A., Hussmann, H., Wickhusen, K., Lüdicke, F., Hüttig, C., Gwinner, K., Thomas, N., Lara, L. M., and the BELA Team (2021). In-cruise checkouts of the BepiColombo Laser Altimeter (BELA): Implications for performance and operations at Mercury. In *European Planetary Science Congress*, pages EPSC2021–648.

Steinbrügge, G., Stark, A., Hussmann, H., Wickhusen, K., and Oberst, J. (2018). The performance of the BepiColombo Laser Altimeter (BELA) prior launch and prospects for Mercury orbit operations. *Planetary and Space Science*, 159:84–92.

Stickle, A. M., Schultz, P. H., and Crawford, D. A. (2015). Subsurface failure in spherical bodies: A formation scenario for linear troughs on Vesta's surface. *Icarus*, 247:18–34.

Sukhanov, A. A., Velho, H. F. C., Macau, E. E. N., and Winter, O. C. (2010). The Aster project: Flight to a near-Earth asteroid. *Cosmic Research*, 48(5):443–450.

Takahashi, S. and Scheeres, D. J. (2020). Higher-Order Corrections for Frozen Terminator Orbit Design. *Journal of guidance, control and dynamics*, 43(9):1642–1655.

Tholen, D. J. (1989). Asteroid taxonomic classifications. In Binzel, R. P., Gehrels, T., and Matthews, M. S., editors, *Asteroids II*, pages 1139–1150. University of Arizona Press.

Thomas, C. A., Naidu, S. P., Scheirich, P., Moskovitz, N. A., Pravec, P., Chesley, S. R., Rivkin, A. S., Osip, D. J., Lister, T. A., Benner, L. A. M., Brozović, M., Contreras, C., Morrell, N., RoŻek, A., Kušnirák, P., Hornoch, K., Mages, D., Taylor, P. A., Seymour, A. D., Snodgrass, C., Jørgensen, U. G., Dominik, M., Skiff, B., Polakis, T., Knight, M. M., Farnham, T. L., Giorgini, J. D., Rush, B., Bellerose, J., Salas, P., Armentrout, W. P., Watts, G., Busch, M. W., Chatelain, J., Gomez, E., Greenstreet, S., Phillips, L., Bonavita, M., Burgdorf, M. J., Khalouei, E., Longa-Peña, P., Rabus, M., Sajadian, S., Chabot, N. L., Cheng, A. F., Ryan, W. H., Ryan, E. V., Holt, C. E., and Agrusa, H. F. (2023). Orbital period change of Dimorphos due to the DART kinetic impact. *Nature*, 616(7957):448–451.

Thomas, N., Hussmann, H., Spohn, T., Lara, L. M., Christensen, U., Affolter, M., Bandy, T., Beck, T., Chakraborty, S., Geissbuehler, U., Gerber, M., Ghose, K., Gouman, J., HosseiniArani, S., Kuske, K., Peteut, A., Piazza, D., Rieder, M., Servonet, A., Althaus, C., Behnke, T., Gwinner, K., Hüttig, C., Kallenbach, R., Lichopoj, A., Lingenauber, K., Lötzke, H. G., Lüdicke, F., Michaelis, H., Oberst, J., Schrödter, R., Stark, A., Steinbrügge, G., del Togno, S., Wickhusen, K., Castro, J. M., Herranz, M., Rodrigo, J., Perplies, H., Weigel, T., Schulze-Walewski, S., Blum, S., Casciello, A., Rugi-Grond, E., Coppoolse, W., Rech, M., Weidlich, K., Leikert, T., Henkelmann, R., Trefzger, B., and Metz, B. (2021). The BepiColombo Laser Altimeter. *Space Science Reviews*, 217(1):25.

Thomas, N., Stelter, R., Ivanov, A., Bridges, N. T., Herkenhoff, K. E., and McEwen, A. S. (2011a). Spectral heterogeneity on Phobos and Deimos: HiRISE observations and comparisons to Mars Pathfinder results. *Planetary and Space Science*, 59(13):1281–1292.

Thomas, P., Veverka, J., Bell, J., Lunine, J., and Cruikshank, D. (1992). Satellites of Mars: geologic history. In George, M., editor, *Mars*, pages 1257–1282. University of Arizona Press.

Thomas, P. C. (1989). The shapes of small satellites. *Icarus*, 77(2):248–274.

Thomas, P. C. (1993). Gravity, Tides, and Topography on Small Satellites and Asteroids: Application to Surface Features of the Martian Satellites. *Icarus*, 105(2):326–344.

Thomas, P. C., Adinolfi, D., Helfenstein, P., Simonelli, D., and Veverka, J. (1996). The Surface of Deimos: Contribution of Materials and Processes to Its Unique Appearance. *Icarus*, 123(2):536–556.

Thomas, P. C., Parker, J. W., McFadden, L. A., Russell, C. T., Stern, S. A., Sykes, M. V., and Young, E. F. (2005). Differentiation of the asteroid Ceres as revealed by its shape. *Nature*, 437(7056):224–226.

Thomas, P. C., Tajeddine, R., Tiscareno, M. S., Burns, J. A., Joseph, J., Loredo, T. J., Helfenstein, P., and Porco, C. (2016). Enceladus's measured physical libration requires a global subsurface ocean. *Icarus*, 264:37–47.

Thomas, P. C., Veverka, J., Sullivan, R., Simonelli, D. P., Malin, M. C., Caplinger, M., Hartmann, W. K., and James, P. B. (2000). Phobos: Regolith and ejecta blocks investigated with Mars Orbiter Camera images. *Journal of Geophysical Research*, 105(E6):15091–15106.

Thomas, V. C., Makowski, J. M., Brown, G. M., McCarthy, J. F., Bruno, D., Cardoso, J. C., Chiville, W. M., Meyer, T. F., Nelson, K. E., Pavri, B. E., Termohlen, D. A., Violet, M. D., and Williams, J. B. (2011b). The Dawn Spacecraft. *Space Science Reviews*, 163(1-4):175–249.

Todd, M., Tanga, P., Coward, D., and Zadnik, M. (2013). Predictions for the detection of earth and mars trojan asteroids by the gaia satellite. *Monthly Notices of the Royal Astronomical Society*.

Tsuda, Y., Yoshikawa, M., Abe, M., Minamino, H., and Nakazawa, S. (2013). System design of the Hayabusa 2 - Asteroid sample return mission to 1999 JU3. *Acta Astronautica*, 91:356–362.

Ulamec, S., Michel, P., Grott, M., Schröder, S., Hübers, H. W., Cho, Y., Prieto-Ballesteros, O., Murdoch, N., Vernazza, P., Biele, J., Tardivel, S., and Miyamoto, H. (2024). IDEFIX, the MMX Rover — In-Situ Science on Phobos. In *LPI Contributions*, volume 3040 of *LPI Contributions*, page 1878.

Urban, K. (2017). Abschied von der habitablen Zone. *Spektrum der Wissenschaft*. accessed: 30-aug-2023.

Veselovsky, I. S. (2004). Is Phobos Magnetized? *Solar System Research*, 38(3):188–193.

Walsh, K. J. and Jacobson, S. A. (2015). *Formation and Evolution of Binary Asteroids*, pages 375–393. University of Arizona Press.

Walsh, K. J., Richardson, D. C., and Michel, P. (2008). Rotational breakup as the origin of small binary asteroids. *Nature*, 454:188.

Watanabe, S., Hirabayashi, M., Hirata, N., Hirata, N., Noguchi, R., Shimaki, Y., Ikeda, H., Tatsumi, E., Yoshikawa, M., Kikuchi, S., Yabuta, H., Nakamura, T., Tachibana, S., Ishihara, Y., Morota, T., Kitazato, K., Sakatani, N., Matsumoto, K., Wada, K., Senshu, H., Honda, C., Michikami, T., Takeuchi, H., Kouyama, T., Honda, R., Kameda, S., Fuse, T., Miyamoto, H., Komatsu, G., Sugita, S., Okada, T., Namiki, N., Arakawa, M., Ishiguro, M., Abe, M., Gaskell, R., Palmer, E., Barnouin, O. S., Michel, P., French, A. S., McMahon, J. W., Scheeres, D. J., Abell, P. A., Yamamoto, Y., Tanaka, S., Shirai, K., Matsuoka, M., Yamada, M., Yokota, Y., Suzuki, H., Yoshioka, K., Cho, Y., Tanaka, S., Nishikawa, N., Sugiyama, T., Kikuchi, H., Hemmi, R., Yamaguchi, T., Ogawa, N., Ono, G., Mimasu, Y., Yoshikawa, K., Takahashi, T., Takei, Y., Fujii, A., Hirose, C., Iwata, T., Hayakawa, M., Hosoda, S., Mori, O., Sawada, H., Shimada, T., Soldini, S., Yano, H., Tsukizaki, R., Ozaki, M., Iijima, Y., Ogawa, K., Fujimoto, M., Ho, T.-M., Moussi, A., Jaumann, R., Bibring, J.-P., Krause, C., Terui, F., Saiki, T., Nakazawa, S., and Tsuda, Y. (2019). Hayabusa2 arrives at the carbonaceous asteroid 162173 ryugu—a spinning top–shaped rubble pile. *Science*, 364(6437):268–272.

Werner, R. A. and Scheeres, D. J. (1996). Exterior gravitation of a polyhedron derived and compared with harmonic and mascon gravitation representations of asteroid 4769 Castalia. *Celestial Mechanics and Dynamical Astronomy*, 65:313–344.

Wickhusen, K., de Brum, A. G. V., Damme, F., Stark, A., Vincent, J.-B., Hussmann, H., and Oberst, J. (2022a). Terminator orbits around the triple asteroid 2001-SN263 in application to the deep space mission ASTER. *Acta Astronautica*, 198:631–641.

Wickhusen, K., Hussmann, H., Oberst, J., and Luedicke, F. (2012). Orbital stability during the mapping and approach phases of the MarcoPolo-R spacecraft. In *European Planetary Science Congress 2012*.

Wickhusen, K., Oberst, J., Christou, A., and Damme, F. (2023). Trajectory analysis for combined missions to mars and its Trojan Asteroids. *Planetary and Space Science*, 228.

Wickhusen, K., Oberst, J., and Damme, F. (2018). A Proposed Mission to Very Low Mars Orbit - Supported by an Electric Propulsion System. In *European Planetary Science Congress*.

Wickhusen, K., Oberst, J., Gwinner, K., Hauber, E., Stark, A., Fanara, L., Höschele, M., Xiao, H., Su, S., Hussmann, H., and Steinbrügge, G. (2022b). Planetary polar explorer - the case for a next generation remote sensing mission to low Mars orbit. In *44th COSPAR Scientific Assembly. Held 16-24 July*, volume 44, page 427.

Wickhusen, K., Oberst, J., Hussmann, H., Shi, X., and Damme, F. (2011). Stability and Evolution of Orbits around Binary Asteroids: Applications to the Marco Polo Mission Scenario. In *EPSC-DPS Joint Meeting 2011*, volume 2011, page 1085.

Wieczorek, M. A. and Meschede, M. (2018). Shtools: Tools for working with spherical harmonics. *Geochemistry, Geophysics, Geosystems*, 19(8):2574–2592.

Wiegert, P., Innanen, K., and Mikkola, S. (2000). The Stability of Quasi Satellites in the Outer Solar System. *THE ASTRONOMICAL JOURNAL*, 119(4):1978–1984.

Wieser, M. and Barabash, S. (2016). A family for miniature, easily reconfigurable particle sensors for space plasma measurements. *Journal of Geophysical Research (Space Physics)*, 121(12):11,588–11,604.

Wieser, M., Barabash, S., Futaana, Y., Holmström, M., Bhardwaj, A., Sridharan, R., Dhanya, M. B., Wurz, P., Schaufelberger, A., and Asamura, K. (2009). Extremely high reflection of solar wind protons as neutral hydrogen atoms from regolith in space. *Planetary and Space Science*, 57(14-15):2132–2134.

Williams, D. R. (2023). Mars fact sheet. https://nssdc.gsfc.nasa.gov/planetary/factsheet/marsfact.html. accessed: 07-Jul-2023.

Willner, K. (2009). *The martian moon Phobos : a geodetic analysis of its motion, orientation, shape, and physical parameters*. PhD thesis, Technical University of Berlin, Germany.

Willner, K., Oberst, J., Hussmann, H., Giese, B., Hoffmann, H., Matz, K. D., Roatsch, T., and Duxbury, T. (2010). Phobos control point network, rotation, and shape. *Earth and Planetary Science Letters*, 294(3-4):541–546.

Willner, K., Shi, X., and Oberst, J. (2014). Phobos' shape and topography models. *Planetary and Space Science*, 102.

Winter, O. C., Valvano, G., Moura, T. S., Borderes-Motta, G., Amarante, A., and Sfair, R. (2020). Asteroid triple-system 2001 SN263: surface characteristics and dynamical environment. *Monthly Notices of the Royal Astronomical Society*, 492(3):4437–4455.

Woolley, R. C. and Whetsel, C. W. (2013). On the nature of Earth-Mars porkchop plots.

Wynn-Williams, G. (2016). *Surveying the Skies*. Springer.

Yano, H., Kubota, T., Miyamoto, H., Okada, T., Scheeres, D., Takagi, Y., Yoshida, K., Abe, M., Abe, S., Barnouin-Jha, O., Fujiwara, A., Hasegawa, S., Hashimoto, T., Ishiguro, M., Kato, M., Kawaguchi, J., Mukai, T., Saito, J., Sasaki, S., and Yoshikawa, M. (2006). Touchdown of the Hayabusa Spacecraft at the Muses Sea on Itokawa. *Science*, 312(5778):1350–1353.

Zakharov, A., Horanyi, M., Lee, P., Witasse, O., and Cipriani, F. (2014). Dust at the Martian moons and in the circummartian space. *Planetary and Space Science*, 102:171–175.

Acknowledgments

Acknowledgments

I would like to say a warm thank-you to my department heads, Hauke Hußmann and Jürgen Oberst. Your steady help, good advice, and constant belief in me kept this work moving forward, even on the toughest days.
My thanks also go to all my colleagues. Stephan Elgner, your door was always open for a friendly chat that cleared my head. Konrad Willner, your guidance in the final stretch made sure everything came together. To the rest of the team—every quick answer, shared laugh, and extra pair of eyes mattered more than you know.
I am deeply grateful to my parents and to my sister and her family for cheering me on from start to finish. Above all, I thank my wife and our children. We faced every hurdle side by side and turned each problem into something we solved together. This dissertation carries a piece of all of you.

Appendices

Appendix A

Glossary

Δv delta-v.

BELA BepiColombo Laser Altimeter.

CDF Concurrent Design Facility.

CNEOS Center for Near-Earth Object Studies.

CNES Centre national d'études spatiales.

DePhine Deimos and Phobos Interior Explorer.

DLR German Aerospace Center.

EnEx Enceladus Explorer.

ESA European Space Agency.

GEO Geostationary Orbit.

GETEMME Gravity, Einstein's Theory, and Exploration of the Martian Moons' Environment.

IAU International Astronomical Union.

JAXA Japan Aerospace Exploration Agency.

JUICE Jupiter Icy Moons Explorer.

LEO Low Earth Orbit.

MarsTAstE Mars' Trojan Asteroids Explorer.

MCD Mars Climate Database.

MEX Mars Express.

MMX Martian Moons eXploration.

MOI Mars Orbit Insertion.

MPC Minor Planet Center.

MPO Mercury Planetary Orbiter.

NAIF Navigation and Ancillary Information Facility.

NASA National Aeronautics and Space Administration.

NEA Near-Earth Asteroid.

NEO Near-Earth Object.

PhoDEx Phobos and Deimos Explorer.

QS Quasi Satellite.

QSO Quasi Satellite Orbit.

RTGs Radioisotope Thermoelectric Generators.

S/C Spaceraft.

SRP Solar Radiation Pressure.

SSTO Self-Stabilized Terminator Orbit.

TOF Time of Flight.

Appendix B

Verwendete KI-Tools

In dieser Arbeit habe ich KI-Tools ausschließlich zur sprachlichen Überprüfung verwendet. Ich habe dabei den gesamten Text bereits vorgeschrieben und die KI-Engine dann den Text auf sprachliche Fehler überprüfen lassen. Der Hauptprompt sowie zwei zufällige Beispiele der Anwendung sind im Folgenden aufgeführt.

Die sprachliche Überprüfung des Textes wurde dabei nicht auf die eingebundenen wissenschaftlichen Manuskripte (Kapitel 5, 6, 7) angewendet. Diese Manuskripte wurden nicht verändert und so belassen, wie sie veröffentlicht wurden.

Das verwendete KI-Tool ist dabei GPT von der Firma OpenAI in den Versionen 3.5, 4 und 4o, wobei die Version 4o am häufigsten zum Einsatz kam.

B.1 Hauptprompt

Der folgende Prompt ist der Hauptpromt, der die Aufgabe definiert und für alle Textblöcke gilt. Die darauf folgenden zwei Beispiele zeigen dann zwei zufällig gewählte Textblöcke, die überprüft wurden und für die Vorschläge zur Verbesserung gemacht wurden.

input: *Du sollst für mich englisches "proof reading" einer wissenschaftlichen Arbeit machen. Ich werde dir immer ein paar Teile Text geben. Du sollst lediglich das Englisch überprüfen.*
Wichtig: du sollst nicht jeden kleinen Fehler verändern und nicht jede Formulierung optimieren. Du sollst nur schwere Fehler anmerken und dann Verbesserungen vorschlagen. Verifiziere und verbessere dabei ausschließlich die englische Sprache, keinen Inhalt.
Verwende dabei immer so viel wie möglich von meiner Struktur, meinem Satzbau und meiner Wortwahl. Wenn aber grobe Fehler drin sind, schlage mir Verbesserungen vor.
Ich werde dir Latex Blöcke geben. Behalte das Latex Format bei. Wenn der Text größtenteils OK ist, dann schreibe nur "Text ist OK, kann so bleiben". Wenn noch grobe Fehler drin sind, mache Verbesserungsvorschläge

B.2 Beispiel 1

input: *During the Dephine and PhoDEx concept development and also during the research in Grimm et al. (2020), I focused on possible delivery options. The question was how the landing package could be delivered to the surface of either Phobos or Deimos. During my research, the proposal team agreed on a free fall delivery. The challenging aspect was always the trade of between the release height and the risk of damaging or losing the spacecraft by getting to close to the surface of the moon.*

output:

Dein Text ist größtenteils korrekt, aber es gibt ein paar kleine grammatikalische und stilistische Anpassungen, die ihn verbessern können. Hier ist die überarbeitete Version:

"During the Dephine and PhoDEx concept development and also during the research in Grimm et al. (2020), I focused on possible delivery options. The question was how the landing package could be delivered to the surface of either Phobos or Deimos. During my research, the proposal team agreed on a free-fall delivery. The challenging aspect was always the trade-off between the release height and the risk of damaging or losing the spacecraft by getting too close to the surface of the moon."

Spezifische Anpassungen:

- Rechtschreibung: "free fall" zu "free-fall" für Konsistenz.
- Bindestrich: "trade of" zu "trade-off".
- Klarheit und Präzision: "getting to close" zu "getting too close".

Text ist jetzt grammatikalisch korrekt und gut für eine wissenschaftliche Arbeit geeignet.

B.3 Beispiel 2

input: *In the following years, more objects were found in the region and until 1807, a total number of 4 asteroids was discovered. The three new objects were called (2) Pallas, (3) Juno and (4) Vesta. Until 1851, a total number of 15 minor planets had been discovered and this number increased to more than 50 until 1858 (Schmadel, 2012). Since then, more and more asteroids have been discovered over the years, and with better sensors, computers, and spacecrafts, it was possible to detect smaller bodies with diameters of only a few tens of meters. Today in February 2024 NASA and the MPC state that more than 1.3 Million asteroids have been detected and are listed in their databases (Bolles, 2024; IAU, 2024).*

output:

Your passage is informative and captures the history of asteroid discovery well. However, a few minor adjustments can enhance the grammatical correctness and flow:

- Plural agreement: The term "asteroids" should be used with "were" rather than "was".
- Consistency and clarification: "Until 1851" and "until 1858" might confuse readers about the sequence of discoveries. Clarifying these transitions can improve comprehension.
- Terminology: "spacecrafts" should be corrected to "spacecraft".
- Stylistic consistency: Ensure that all terms and numerical expressions are used consistently for clarity and professionalism.

Here's the revised version of your text:

"In the following years, more objects were found in the region, and by 1807, a total of four asteroids had been discovered. The three new objects were named (2) Pallas, (3) Juno, and (4) Vesta. By 1851, a total of 15 minor planets had been discovered, and this number increased to more than 50 by 1858 (Schmadel, 2012). Since then, the discovery of asteroids has continued to accelerate, and with advancements in sensors, computers, and spacecraft, it has become possible to detect smaller bodies with diameters of only a few tens of meters. As of February 2024, NASA and the MPC report that more than 1.3 million asteroids have been detected and are listed in their databases (Bolles, 2024; IAU, 2024)."

This version corrects grammatical errors, clarifies historical details, and enhances the overall readability of your text.